High-fidelity numerical simulations of compressible turbulence and mixing generated by hydrodynamic instabilities

by

Pooya Movahed

A dissertation submitted in partial fulfillment
of the requirements for the degree of
Doctor of Philosophy
(Mechanical Engineering)
in the University of Michigan
2014

Doctoral Committee:

Assistant Professor Eric Johnsen, Chair
Professor David R. Dowling
Professor R. Paul Drake
Professor Kenneth G. Powell

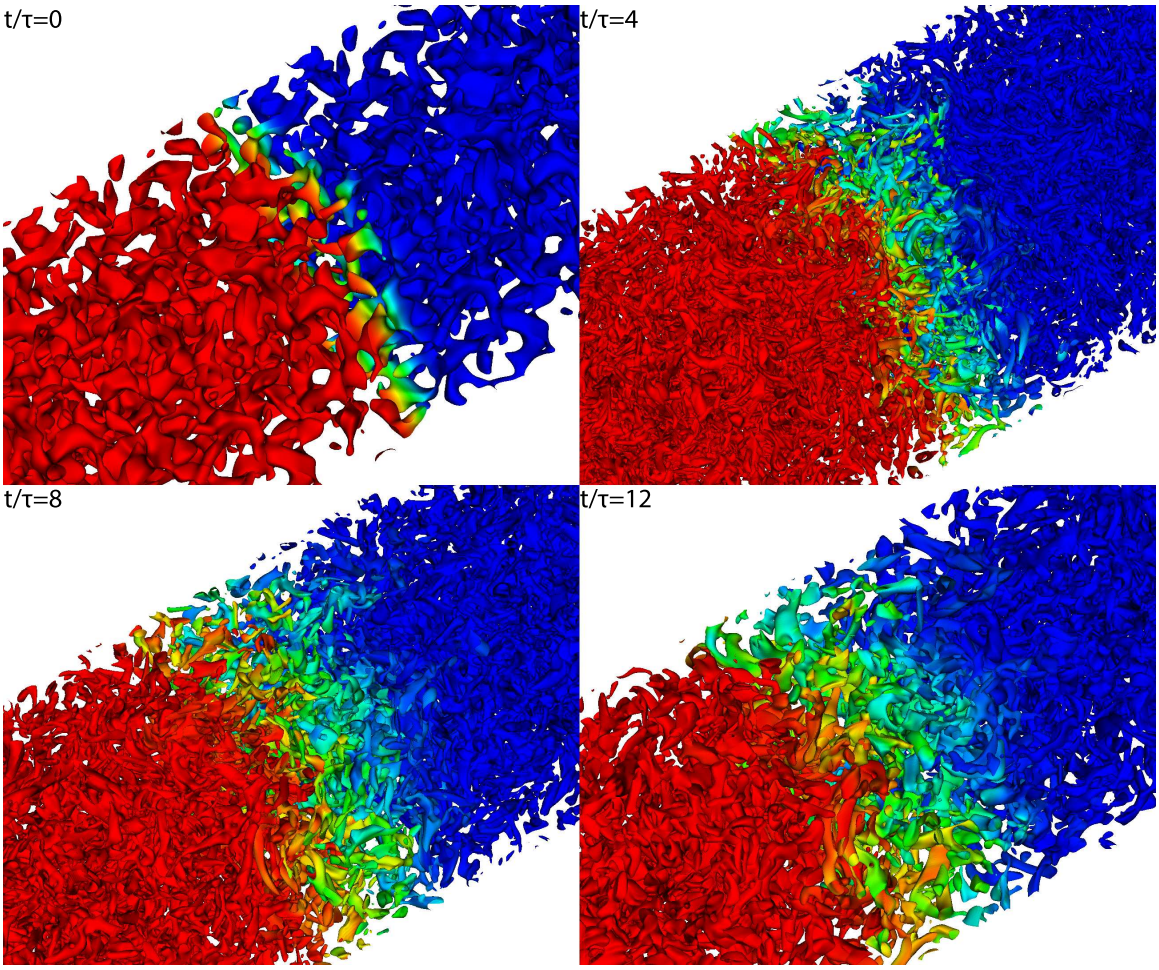
t/τ=0
t/τ=4
t/τ=8
t/τ=12

Dedicated to my parents

ACKNOWLEDGEMENTS

First and foremost, I would like to thank my advisor, Professor Eric Johnsen, for giving me the opportunity to pursue my own ideas and providing me guidance as needed. My experience of working with Eric, particularly as his first Ph.D. student, was rewarding. I was able to stop by his office at any time and he was always willing to listen patiently and to discuss research. In addition, I would like to thank him for involving me in writing research proposals.

I would like to thank Professors David Dowling, Paul Drake, and Ken Powell for accepting to be on my committee and providing useful comments. I am thankful to Prof. Dowling for insightful conversations on turbulence and teaching me advanced fluid mechanics. I wish to acknowledge Prof. Drake for introducing me to the field of high energy density physics and helping me understand of the big picture of my research. I would like to thank Prof. Schultz, Dr. Fryxell, Dr. Myra, Sreenivas Varadan and Marc T. Henry de Frahan for useful conversations.

I would like to thank my parents for their endless support while I pursued my academic dream. Special thanks goes to my mother for helping me in my courses when I was a kid, inspiring me to pursue a Ph.D. in the United States, and being always there for me. A special thanks to Parham and Nasim who supported me despite the distance. I would like also to thank my high school physics teachers who interested me in physics in the first place.

Many thanks to my friends Sreenivas, Chengyun, Koohyar, Dana, Mostafa, Marc, Brandon, Max, Aditya, Yashar, Shahab, Joel, Harish, Adeleena, Shima, Mauro,

Sheng, Amirreza, Sina, Reza... for making this Ph.D. more than an academic experience. Thanks to Brock Palen at the Center for Advanced Computing, University of Michigan, for teaching me how to use a cluster and for providing advice on parallel programming. I wrote most of my thesis in the new branch of Starbucks on Plymouth Road. I would like to thank all the staff for their hospitality.

This effort was supported in part by the DOE NNSA/ASC under the Predictive Science Academic Alliance Program by Grant No. DEFC5208NA28616. This work used the Extreme Science and Engineering Discovery Environment (XSEDE), which is supported by National Science Foundation grant number OCI-1053575.

TABLE OF CONTENTS

LIST OF FIGURES

Figure

LIST OF TABLES

Table

LIST OF APPENDICES

Appendix

LIST OF ABBREVIATIONS

ICF Inertial Confinement Fusion

NIF National Ignition Facility

RANS Reynolds-Averaged Navier-Stokes

LES Large Eddy Simulation

DNS Direct Numerical Simulation

RM Richtmyer-Meshkov

RMI Richtmyer-Meshkov instability

RT Rayleigh-Taylor

RTI Rayleigh-Taylor instability

KH Kelvin-Helmholtz

ILES Implicit LES

MPI Message Passing Interface

WENO weighted essentially non-oscillatory

NSF National Science Foundation

XSEDE Extreme Science and Engineering Discovery Environment

ABSTRACT

High-fidelity numerical simulations of compressible turbulence and mixing generated by hydrodynamic instabilities

by

Pooya Movahed

Chair: Eric Johnsen

High-speed flows are prone to hydrodynamic interfacial instabilities that evolve to turbulence, thereby intensely mixing different fluids and dissipating energy. The lack of knowledge of these phenomena has impeded progress in a variety of disciplines. In science, a full understanding of mixing between heavy and light elements after the collapse of a supernova and between adjacent layers of different density in geophysical (atmospheric and oceanic) flows remains lacking. In engineering, the inability to achieve ignition in inertial fusion and efficient combustion constitute further examples of this lack of basic understanding of turbulent mixing. In this work, my goal is to develop accurate and efficient numerical schemes and employ them to study compressible turbulence and mixing generated by interactions between shocked (Richtmyer-Meshkov) and accelerated (Rayleigh-Taylor) interfaces, which play important roles in high-energy-density physics environments.

To accomplish my goal, a hybrid high-order central/discontinuity-capturing finite difference scheme is first presented. The underlying principle is that, to accurately and efficiently represent both broadband motions and discontinuities, non-dissipative

methods are used where the solution is smooth, while the more expensive and dissipative capturing schemes are applied near discontinuous regions. Thus, an accurate numerical sensor is developed to discriminate between smooth regions, shocks and material discontinuities, which all require a different treatment. The interface capturing approach is extended to central differences, such that smooth distributions of varying specific heats ratio can be simulated without generating spurious pressure oscillations. I verified and validated this approach against a stringent suite of problems including shocks, interfaces, turbulence and two-dimensional single-mode Richtmyer-Meshkov instability simulations. The three-dimensional code is shown to scale well up to 4000 cores.

Using a novel set-up, I perform direct numerical simulations of freely decaying turbulent multi-material mixing starting from an unperturbed material interface between two fluids in a pre-existing isotropic turbulent velocity field in the presence and absence of gravity. In the absence of gravity, the energy dissipation rate is matched in each fluid, such that anisotropy in the initial set-up solely comes from the density gradient. At large scales, the mixing region grows self-similarly after an initial transient period; a one-dimensional turbulence diffusion model in conjunction with Prandtl's mixing length theory is applied to describe the growth of the mixing region. In this regime, the growth of the mixing regions scales as time to the power of 2/7 for Batchelor turbulence, as predicted by energy budget arguments for large Reynolds numbers. At small scales, flow isotropy and intermittency are measured. Results suggest that a large density ratio between the two fluids is required to produce anisotropy at the Taylor microscale, while the flow remains isotropic at the dissipation (Kolmogorov) scales.

Having identified the role of density gradient alone, I revisit the problem in the presence of gravity in a Rayleigh-Taylor unstable configuration. Now, the baroclinic vorticity due to the gravitational field provides energy that drives the initially decay-

ing turbulent field. Flow dynamics are characterized by the two important competing time scales of the problem, corresponding to the decay of the initial turbulent field and the Rayleigh-Taylor development. The resulting turbulence is found to be anisotropic across all scales. The velocity field is highly intermittent at the bubble and spike fronts.

CHAPTER I

Introduction

The current chapter provides an introduction to turbulence and mixing generated by hydrodynamic instabilities. First, the concept of hydrodynamic instability is explained, with an emphasis on the Richtmyer-Meshkov and Rayleigh-Taylor instabilities. Then, a brief discussion on turbulence is provided, including different numerical approaches to simulate turbulence. Next, different concepts such as the mixing transition and mixing classification are explained. The chapter ends with an overview of the thesis.

1.1 Hydrodynamic instabilities

The field of hydrodynamic instabilities is an important branch of fluid dynamics that has been studied for decades starting with the work of Helmholtz (Swinney & Gollub, 1985). In general, stability of a system can be defined as the quality of being prone to amplification of small disturbances present in an environment. In unstable configurations, the disturbances grow and their amplification can lead to a chaotic behavior of the system. Small disturbances exist in any system in nature, including systems made of fluids. The Navier-Stokes equations governing fluid motion are nonlinear partial differential equations for which few analytical solutions exist. Linear theory has been used as a tool to study hydrodynamic instabilities and particularly

to investigate early time response of flows subject to small perturbations. At later stages for flows in which perturbations grow, the flow exhibits a chaotic behavior and becomes turbulent. This process is highly nonlinear such that theoretical analysis is limited. Generally, experiments and numerical simulations are needed to investigate turbulence and mixing in these flows.

1.1.1 Motivation

In high-energy-density physics (Drake, 2006), including astrophysics (Kifonidis *et al.*, 2006) and Inertial Confinement Fusion (ICF) (Lindl, 1995), and supersonic combustion (Yang *et al.*, 1993), hydrodynamic instabilities can trigger the evolution of a laminar flow to turbulent multi-material mixing regions. In these applications, three main hydrodynamic instabilities are known to occur at perturbed interfaces between different fluids, namely the Richtmyer-Meshkov (RM) (Richtmyer, 1960; Meshkov, 1969), Rayleigh-Taylor (RT) (Taylor, 1950) and Kelvin-Helmholtz (KH) (Thomson, 1871; Helmholtz, 1868) instabilities. In these instabilities, initial perturbations along the interface can grow due to interactions with shocks (RM), acceleration fields (RT) or shear (KH). Due to the high Reynolds numbers in these flows, viscous effects may be neglected for early time analysis (Drake, 2006). Consequently, the Euler equations are often used to model these flows. The hydrodynamic instabilities occurring in systems that obey the Euler equations are invariant under scale transformation ranging from astrophysical applications to small-scales instabilities in ICF (Ryutov *et al.*, 1999; Drake, 2006). This allows us apply the same concepts to study these hydrodynamic instabilities regardless of their scales.

At large scales, many astrophysical phenomena such as core-collapse supernovae, astrophysical jets, stellar formation, etc., can be broken down into a simplistic, yet insightful, sequence of events: large density gradients interact with shock waves or are accelerated, thus leading to hydrodynamic instabilities (figure 1.1). Physics of

Figure 1.1: Logarithm of the density of a Type-II supernova explosion (1987A) from numerical simulation. From Kifonidis *et al.* (2003), reproduced with permission © ESO.

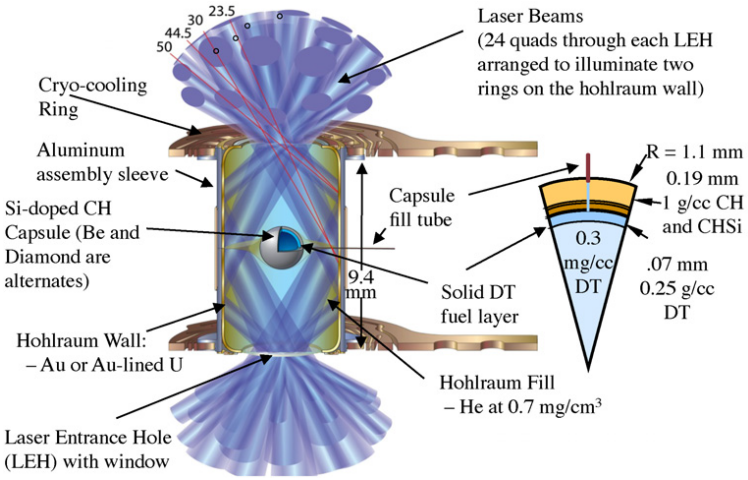

Figure 1.2: Schematic of National Ignition Campaign indirect-drive hohlraum and capsule. From Landen *et al.* (2012), © IOP publishing. Reproduced by permission of IOP Publishing. All rights reserved.

thermonuclear burning involves predicting the mode of propagation (e.g., detonation, deflagration) and the speed of the flame front. Accurate modeling of hydrodynamic instabilities is a requirement for supernova models since scenarios for thermonuclear burning are coupled to hydrodynamics.

At small scales, hydrodynamic instabilities play a dominant role in the implosion of the deuterium-tritium capsule in ICF. Achieving fusion requires extremely high pressures and temperatures and has been so far limited to the cores of planets and stars and nuclear weapons. As shown in figure 1.2, the energy of 192 laser beams

directed inside a hohlraum, is used at the National Ignition Facility (NIF) to compress a tiny capsule inside the hohlraum and achieve fusion. The interaction of the waves with perturbations present at different layers of the fuel inside the capsule leads to hydrodynamic instabilities, e.g., RT and RM and reduces the efficiency of compression by mixing the ablator with the fuel, making it more challenging to achieve the extreme conditions required at the center of the capsule to initiate ignition.

1.1.2 The Richtmyer-Meshkov instability

The Richtmyer-Meshkov instability (RMI) occurs when a shock interacts with a perturbed interface separating fluids of different densities (Richtmyer, 1960; Meshkov, 1969). The mis-alignment of the density gradient across the interface and the pressure gradient across the shock wave leads to baroclinic vorticity generation along the interface, which is the basic mechanism for the amplification of any perturbations initially present along the interface (Brouillette, 2002). The vorticity evolution equation for the compressible inviscid flows simplifies to

$$\frac{D\omega}{Dt} = \frac{\partial \omega}{\partial t} + u \cdot \nabla(\omega) = (\omega \cdot \nabla) u - \omega \nabla \cdot u + \frac{1}{\rho^2}(\nabla \rho \times \nabla p) \tag{1.1}$$

where ρ is the density, p the pressure, u the velocity, and $\omega = \nabla \times u$ is the vorticity vector. The first term on the right-hand side only appears in three-dimensional flows and is called vortex stretching. The second term, called vortex compression, takes in to account compressibility effects. The last term is the baroclinic vorticity generation term and is the main mechanism for vorticity generation in the RMI.

The shock wave initially compresses the perturbations existing along the interface. As the shock traverses the interfaces, a vortex sheet is created by the baroclinic vorticity and induces different velocities at each point relative to the unperturbed interface (figure 1.3). The relative motion along the interface causes the lighter gas to penetrate into the heavier gas, thus forming a bubble, and the heavier gas to

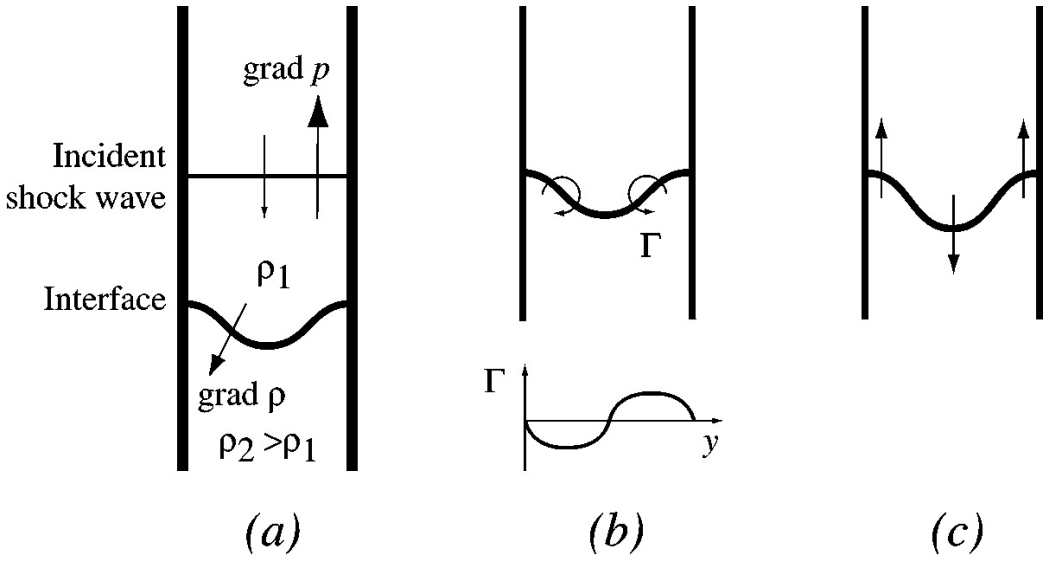

Figure 1.3: Vorticity deposition at a light/heavy interface. (a) Initial configuration. (b) Circulation deposition and intensity of vortex sheet. (c) Subsequent deformation of the interface. From Brouillette (2002). Reproduced by permission.

rise into the lighter gas and roll-up forming a spike. The heavy/light configuration ($\nabla p \cdot \nabla \rho > 0$), which is Rayleigh-Taylor stable (i.e., for a continuous acceleration), is also unstable in the RMI and the amplitude will grow after a phase inversion. Secondary instabilities, such as Rayleigh-Taylor and Kelvin-Helmholtz also occur at later times and help the roll-up process at the spike leading to the appearance of mushroom-like structures.

The initial growth of the single-mode RMI can be predicted analytically. Impulsive models for the amplitude growth rate such as the Richtmyer model (Richtmyer, 1960) and the Meyer-Blewett model (Meyer & Blewett, 1972) are derived by substituting the constant acceleration in the Rayleigh-Taylor instability models with an impulsive acceleration. These models predict a constant amplitude growth rate, which is applicable only for very early times while the flow is still in the linear regime. The post-shock Richtmyer velocity $\dot{h}_0^+$ and the non-dimensional time τ are used for scaling

purposes and are defined as

$$\tau = k\dot{h}_0^+, \quad \dot{h}_0^+ = kA^+h_0^+\Delta u, \qquad \text{where } A = \frac{\rho_2 - \rho_1}{\rho_2 + \rho_1}, \tag{1.2}$$

where h the amplitude, h_0^+ the post-shock amplitude, k the wave number, A the Atwood number, A^+ the post-shock Atwood number, and Δu is the velocity of the unperturbed interface. Perturbation models such as the Zhang-Sohn model (Zhang & Sohn, 1997), using a Pade expansion approximation, and the Sadot et al. model (Sadot *et al.*, 1998), which are based on the asymptotic expansion of the linear perturbation equations, agree well with the experimental results. The Zhang-Sohn model does not predict the $1/t$ asymptotic growth rate at late times while the Sadot et al. model predicts the correct growth $1/t$ asymptotic growth rate.

Similarly, analytical models can be used to predict the initial vorticity distribution along the interface. The interaction of shocks and interfaces results in vorticity deposition along the interface. For sufficiently small perturbation amplitude, linear stability theory for incompressible flows can be used to evaluate the strength of the vortex sheet in the linear stage (Jacobs & Sheeley, 1996). The vorticity distribution, Ω, can be written as

$$\Omega\left(y\right) = 2\dot{h}\sin\left(ky\right). \tag{1.3}$$

Integrating equation 1.3 over one half wave length yields

$$\Gamma = \int_0^{\pi/k} \Omega\left(y\right) dy = \frac{4}{k}\dot{h}_0^+. \tag{1.4}$$

where Γ is the circulation. In another approach, Samtaney and Zabusky (Samtaney & Zabusky, 1994) used shock polar analysis to calculate the circulation deposition on shock-accelerated interfaces. Retaining only the first-order term, the

non-dimensionalized vorticity distribution becomes

$$\Omega\left(y\right) = \Gamma_1' a_0^+ k \sin\left(ky\right), \tag{1.5}$$

where

$$\Gamma_1' = \frac{2\gamma^{1/2}}{1+\gamma}\left(1-\eta^{-1/2}\right)\left(1-Ma^{-1}+2Ma^{-2}\right)\left(Ma-1\right)\left(Ma-1\right), \tag{1.6}$$

here, Ma is the Mach number, $\eta = \rho_2/\rho_1$, and γ is the specific heats ratio.

The RMI occurs in different configurations (planar, cylindrical, and spherical) based on the application. Although cylindrical and spherical configurations are more representative of practical applications, most of the work in the literature has been performed in a planar geometry with single or multi-mode perturbations for simplicity. In the planar case, the geometry may be such that, after the shock has passed through the interface, it reflects off the end wall and impinges upon the distorted interface again (re-shock) (Collins & Jacobs, 2002; Schilling *et al.*, 2007; Schilling & Latini, 2010). Complex small-scale features appear right after re-shock and enhance the mixing rate. Secondary baroclinic vorticity is generated and affects the small-scale features responsible for the increase in circulation on each side of the interface (Aure & Jacobs, 2008*a*). The mixing region eventually becomes turbulent and molecularly mixed at late times. Vortex stretching effects that are not present in two-dimensional simulations play a dominant role in the interface behavior especially after re-shock when the flow becomes turbulent. In the absence of re-shock, vorticity is deposited at the interface only once due to the interaction between the shock and the interface. The interface evolves and gets distorted due to the initial vorticity field. This is in contrast with the Rayleigh-Taylor instability, where vorticity is deposited continuously inside the mixing region. As the energy source available for the growth of the instability is restricted to the initial energy deposited by the shock at the interface, the initial

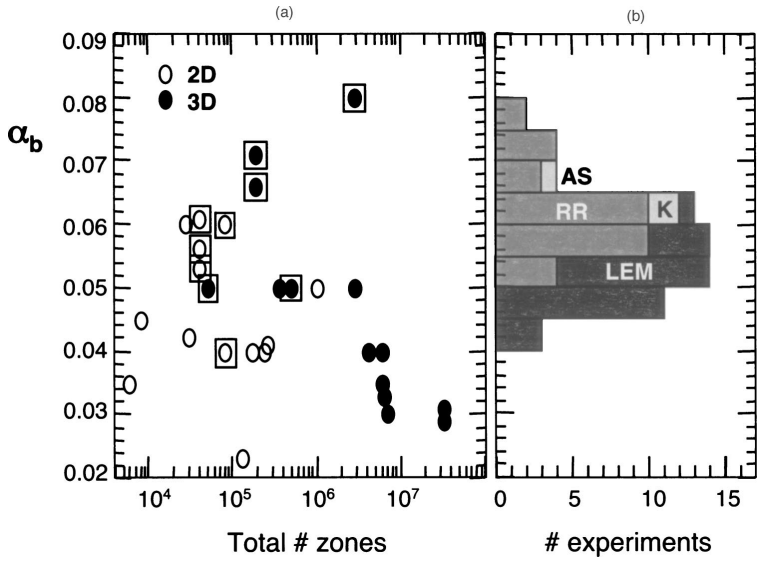

Figure 1.4: (a) α_b vs. total number of zones from previously published simulations. Square indicate simulations with interface reconstruction. (b) Histogram from previous experiments. Reprinted with premission from Dimonte *et al.* (2004). Copyright 2004, AIP Publishing LLC.

growth of the instability is linear rather than exponential as for the Rayleigh-Taylor instability, where kinetic energy is produced continuously.

1.1.3 The Rayleigh-Taylor instability

The Rayleigh-Taylor instability (RTI) occurs when a heavy fluid is accelerated into a light one or, alternatively, when the light fluid supports the heavy fluid in the presence of gravity. Taylor (1950) used linear theory to show that the initial growth of an interfacial perturbation is exponential until its amplitude becomes comparable to its wavelength. After an initial transition period, interface perturbations evolve to a turbulent mixing region. Initial potential energy of the system provides the energy required for the mixing region to grow and for the turbulence intensity to increase, while energy gets dissipated at the same time due to diffusion. For miscible fluids, molecular diffusion tends to reduce the local density differences, thus, reducing the local rate of baroclinic vorticity generation.

In the nonlinear regime, bubbles of the light fluid penetrate into the heavy fluid

while spikes of the heavy fluid rise into the light fluid. For a constant acceleration, g, the growth is quadratic in time

$$h_b(t) \simeq \alpha_b A g t^2, \quad h_s(t) \simeq \alpha_s A g t^2 \tag{1.7}$$

where b and s correspond to bubbles and spikes, and α_b and α_s are model constants. The quadratic growth in time is in agreement with models based on dimensional analysis as well as models viewing the growth as a result of a buoyancy force (Cook & Dimotakis, 2001). A large body of experimental and computational work in the last decades has sought to measure the model constants (Read, 1984; Dimonte & Schneider, 2000; Duff *et al.*, 1962; Dalziel *et al.*, 1999). Previous studies show that the bubble and spike growth becomes increasingly asymmetric as the Atwood number increases. Particularly, α_s approaches 0.5 as A goes to 1 (free fall) (Ramaprabhu *et al.*, 2006, 2012). While researchers hoped for a universal value, α_b was found to be sensitive to the initial conditions ranging between 0.01 and 0.08 (figure 1.4) (Dimonte *et al.*, 2004).

Turbulence dynamics inside the mixing region at different scales is of great interest for modeling purposes. Modeling RT turbulence is challenging as the density gradient across the mixing region and the presence of a gravitational field result in large-scale anisotropies in the mixing region. High-resolution numerical simulations have been used to study flow isotropy in different directions (Cook & Dimotakis, 2001; Cabot & Cook, 2006; Cabot & Zhou, 2013). These simulations suggest that the flow becomes anisotropic in the direction of gravity at the Taylor microscale while flow remains isotropic at the Kolmogorov microscale, where diffusion acts.

1.2 Turbulent multi-material mixing

1.2.1 What is turbulence?

Reynolds was the first to point out that flow inside a pipe transitions to a different regime as a certain non-dimensional parameter (thereafter called the *Reynolds number*) exceeds a threshold in 1883 (Davidson, 2004). The Reynolds number for a flow inside a pipe is defined as $Re = ud/\nu$, where d is the pipe diameter, u the mean flow inside the pipe, and ν the kinematic viscosity. This dimensionless quantity is representative of the relative importance of inertial forces compared to viscous forces. At low Re, the viscous forces are dominant and any initial perturbation in the system, which can potentially lead to a chaotic behavior, gets damped by viscous diffusion. As Re increases, viscous forces become less important and flow can potentially start to transition to a chaotic and random system, in which case the flow consists of eddies of different sizes. While turbulent flows possess many different features based on many factors such as initial conditions and geometry, common characteristics of all of these flows categorizing them as a turbulent flow are (Davidson, 2004):

- Velocity fluctuations are randomly distributed in both space and time, and exhibit a wide range of length scales particularly at high Re.
- Any minute change in any of flow properties might lead to a substantial large change in the whole domain resulting in an unpredictable field.

A common idea in turbulence in agreement with empirical observations is that turbulent flows consist of eddies of a wide range of scales. For high-Re flows, the viscous effects are expected to be negligble at large scales and inertia plays the dominant role.

Richardson (1926) envisioned the idea of an inviscid energy cascade from large scales to small scales driven by inertial forces. Large-scale eddies, which are generated by instabilities, extract energy from the mean flow. The large-scale eddies are also

themselves subject to instabilities that result in breakup to smaller eddies. Through this multi-stage, essentially inviscid process, energy is transferred from the large scales to small scales, where it is dissipated by viscous diffusion. For an inviscid cascade, the rate at which energy per unit mass is passed down the cascade Π scales as

$$\Pi \sim \frac{u^2}{l/u} \sim \frac{u^3}{l}, \tag{1.8}$$

where l and u are the diameter and velocity of the large-scale eddies, u^2 represents the turbulent kinetic energy and l/u is the eddy turn-over time. The above assumption is validated in wind tunnel experiments (Comte-Bellot & Corrsin, 1966; Krogstad & Davidson, 2010) that show that

$$\frac{du^2}{dt} \sim -\frac{u^3}{l}. \tag{1.9}$$

Viscous dissipation is expected to occur at the small scales. Some common arguments made to justify that dissipation occurs at small scales are as follows (Davidson, 2004):

- The rate of kinetic energy dissipation per unit mass in a fluid is $\epsilon = 2\nu S_{ij} S_{ij}$ where $S_{ij} = 1/2\left(\partial u_i/\partial x_j + \partial u_j/\partial x_i\right)$ is the strain-rate tensor. Thus, high dissipation occurs in regions with high velocity gradients (small scales).
- Vorticity is concentrated at small scales in turbulent flows based on empirical observations and a measure of the turbulent kinetic energy dissipation can be related to the vorticity as $\nu < \omega^2 >$. This suggests that viscous dissipation occurs at small scales, where vorticity is concentrated.
- The Reynolds number for an eddy can be defined as $Re = ul/\nu$ where u is the characteristic velocity of the eddy, and l is the characteristic length scale of the eddy. Large Re for large eddies suggests that viscous forces are negligible (almost no dissipation) and inertial forces are dominant. On the other hand,

most of dissipation is expected to occur at scales where $Re \sim 1$. For small eddies, $Re \sim 1$ suggesting that dissipation occurs at small scales.

1.2.2 Numerical approaches to simulate turbulence

With the increase in computing power, numerical simulation have become a promising approach to investigate turbulent flows. The three most common approaches are: Reynolds-Averaged Navier-Stokes (RANS), Large Eddy Simulation (LES), and Direct Numerical Simulation (DNS). The RANS approach is based on averaging the governing equations and solving for the mean quantities, while a closure is needed for the Reynolds stresses. The Reynolds stresses are modeled using either a turbulent viscosity hypothesis or directly with transport equations. These models typically include several tunable parameters and are used in industry due to their simplicity, robustness, and computationally least expensive, used in practice for design purposes. High-fidelity numerical results are not expected for hydrodynamic instability simulations with RANS as such models are not well suited for unsteady flows.

In LES, the goal is to resolve the large unsteady motions while the small-scale dynamics are modeled. In this approach, a filtering operation is performed to decompose each variable into the sum of a filtered (or resolved) component and a residual (or subgrid-scale) component (Pope, 2000). Each filter introduces a cut-off and flow features with length scales smaller than the cut-off are modeled. In LES, the filter and grid need to be sufficiently fine to resolve 80% of the energy (Pope, 2000). Thus, LES is more expensive than RANS. The filtered Navier-Stokes equations contain the subgrid-scale stress tensor that needs to be modeled for closure. Since the large-scale unsteady motions, which are typically anisotropic and depend on the geometry and boundaries, are resolved, the subgrid-scale models are required to model only small-scale motions. A fundamental assumption is that these dynamics are universal, e.g., based on K41 theory. Closure models have been developed mainly for incompressible

flows and direct implementation for compressible turbulence is not expected to yield good results (Lesieur & Metais, 1996). Furthermore, in transitional flows, the turbulence evolves spatially and temporally, so that the models must be applied at the correct locations and times (Stolz *et al.*, 2005). There are two different approaches in modeling the residual stress tensor for compressible turbulence:

- Explicit LES: physics-based models are used for closure. For instance, the stretched-vortex subgrid-scale model by Misra & Pullin (1997) was extended to compressible multicomponent flows in Lombardini *et al.* (2011) and was used to perform Richtmyer-Meshkov instability simulations under re-shock conditions. For this framework, it is critical to minimize the numerical dissipation in the resolved scales, in order to represent the energy transfer across scales accurately (Park *et al.*, 2004).
- Implicit LES (ILES): this approach has widely been used over the past three decades for simulating hydrodynamic instabilities (Youngs, 1991; Dimonte *et al.*, 2004; Thornber *et al.*, 2011). ILES relies on numerical dissipation playing the role of the subgrid-scale model to dissipate energy. In practice, this approach is numerically robust and is capable of modeling early-time behavior of hydrodynamic instabilities accurately. The numerical dissipation in this approach scales with the grid size, such that refining or coarsening a given grid changes the Reynolds number. Thus, one serious downside is that numerical convergence cannot be obtained particularly for problems in which the physical growth of the small scale features (either physical or due to numerical errors) can affect the transition significantly. A good example is the evolution of an interface in the Richtmyer-Meshkov instability after re-shock (Movahed & Johnsen, 2013*a*).

In summary, there should be a mechanism either physical or numerical to dissipate energy in LES. In high-speed flows, different features such as shock waves, rarefaction

waves, and turbulent mixing regions may be present. In order to ensure numerical stability, shock-capturing (ILES approach) is necessary close to some of these structures, particularly shock waves. Since the scheme reduces to first-order accuracy there, the numerical dissipation will be dominant in these regions and designing/optimizing an explicit subgrid-scale model in these regions is may not be feasible. On the other hand, in other parts of the flow field, particularly in regions where turbulent multi-material mixing occurs, the numerical dissipation added through the ILES approach does not represent the physical diffusion correctly and is often found too dissipative for turbulent simulations as well. This results in unphysical features reported in very high-resolution simulations (i.e., high Reynolds number simulations) of even canonical problems such as the decaying isotropic turbulence problem (Grinstein *et al.*, 2007).

Direct numerical simulation (DNS) involves solving the Navier-Stokes equations on such a fine grid such that all the scales present in broadband turbulence are resolved and no modeling is required. The grid resolution is typically required to be of the order of the Kolmogorov length scale. Since this scale is orders of magnitude smaller than the integral scale, and since high-order non-dissipative methods are required to prevent small-scale features to be damped by the numerical dissipation, the computations are very expensive. This approach is not followed in industry for design as the computational cost is prohibitive. DNS is well suited as a research tool at the current time to investigate some fundamental questions regarding turbulence in simplified geometries and at relatively low Reynolds numbers. DNS results are in principle not affected by numerical errors or approximations present in any subgrid-scale model and can thus be considered to be *exact* solutions to the equations of motion (given appropriate initial and boundary conditions), as long as the method converges. DNS results can be used in particular to assess the performance and even improve subgrid-scale models in LES and Reynolds average stress models in RANS.

1.2.3 Mixing transition and classification

Fluid motion is always subject to instabilities and can transition to turbulence in the absence of enough viscous dissipation to suppress these instabilities. Transition in fluid behavior is observed in gas- and liquid-phase shear layers (Koochesfahani & Dimotakis, 1986), jets (Dowling & Dimotakis, 1990), pipe flow (Bakewell Jr & Lumley, 2004), boundary layers (Sayadi *et al.*, 2013), bluff-body wakes (Prasad & Williamson, 1997), grid turbulence (Comte-Bellot & Corrsin, 1966), Couette-Taylor flow (Dong, 2007), and Richtmyer-Meshkov instability (Jacobs & Sheeley, 1996). This transition manifests itself as an increase in the spectrum of eddying scales and emergence of a near -5/3 power-law regime in the velocity spectrum as proposed by Kolmogorov theory (Kolmogorov, 1962). Dimotakis (2000) suggests that this transition to a fully-developed turbulence state occurs approximately at

$$Re_{tr} \approx 10^4, \quad Re_{tr,\lambda} \approx 100, \tag{1.10}$$

where Re_{tr} is the local (outer) transition Reynolds number and $Re_{tr,\lambda}$ is the transition Reynolds number based on the Taylor microscale. The Re-dependence of different phenomena is expected to decrease as the Reynolds number increases beyond Re_{tr}. At higher Reynolds numbers, sufficient scale separation occurs between the inner dissipation scale and the Liepmann-Taylor scale for the quasi-inviscid motion of the eddies in the inertial range responsible for the non-dissipative cascade of energy from large scales to small scales (Dimotakis, 2005).

Figure 1.5 shows how mixing is enhanced in shear layers as Reynolds number is increased. A turbulent flow is composed by eddies of different sizes and these eddies are capable of transporting and dispersing fluid across a large range of scales up to the diffusion scales, where molecular diffusion acts, and this results in effective mixing of fluids by turbulent flows with several consequences in nature and engineering. This

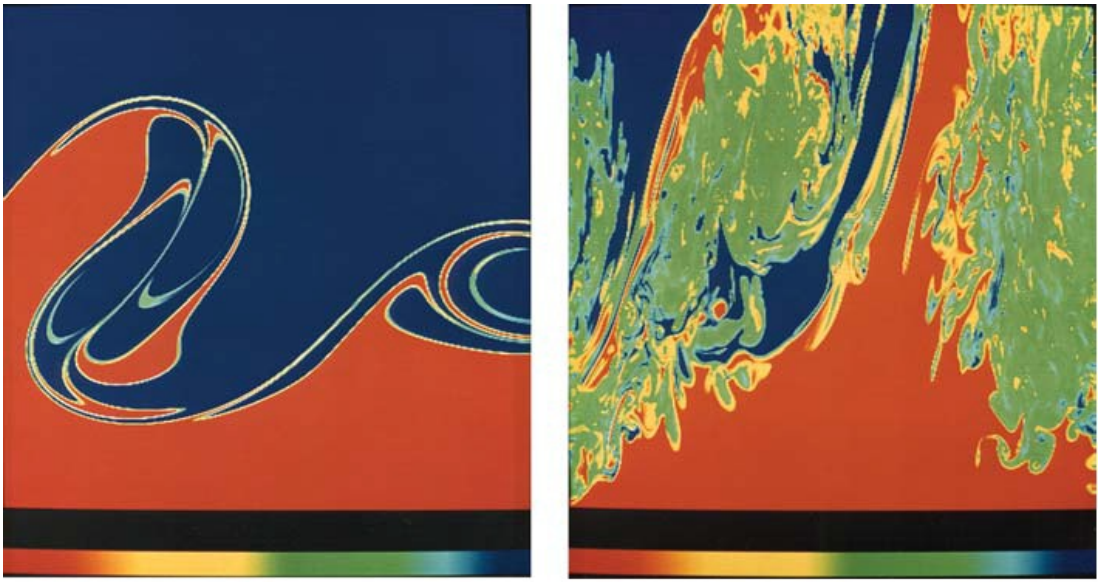

Figure 1.5: Liquid-phase shear-layer slices of passive scalar field. Color codes high-speed fluid mole fraction. Left: $Re_\delta \cong 1.75^3$, right: $Re_\delta \cong 2.3 \times 10^4$. From Koochesfahani & Dimotakis (1986), reproduced with permission.

process consists of three stages: entrainment, dispersion, and diffusion. Viscosity and mass diffusion introduce two different scales at which diffusion acts, namely the Kolmogorov scale (λ_K) and the Batchelor scale (λ_B), respectively. Classical turbulence theoriy suggests that

$$\lambda_B \approx C_B \lambda_K Sc^{-1/2} \tag{1.11}$$

where Sc is the Schmidt number and C_B is of order unity (Batchelor, 1959). According to Dimotakis (2005), mixing occurs at three different levels:

- Level I: Mixing and flow dynamics are decoupled. Examples include mixing of density-matched gases, and the dispersion and mixing of nonreacting trace markers, such as pollutants.

- Level II: Mixing is coupled to flow dynamics. For instance, at unstably stratified interfaces the misalignment of the density and the pressure gradients generates baroclinic vorticity and the amount of vorticity production is directly related to how different flows mix with each other at these interfaces.

- Level III: Mixing is coupled to the dynamics by modifying the fluid(s). The change can be in composition, density, pressure, or enthalpy. Mixing in supernova explosions occur at this level.

Most of the research in the literature on turbulent mixing has mostly been confined to level I. Level II mixing has been mostly studied in the context of the multi-mode Rayleigh-Taylor instability and the Richtmyer-Meshkov instability. While these flows become anisotropic at large scales, it is still not clear whether the flow becomes isotropic at small scales.

1.3 Dissertation outline

The goal of this thesis is to develop numerical methods suitable to simulate the RMI and the RTI and employ them to conduct high-fidelity simulations to study the physics of compressible multi-material turbulent mixing generated by these instabilities. In the first part of my work, a new solution-adaptive method is proposed for inviscid and viscous simulations of the RMI (Chapter II). The proposed scheme takes advantage of a hybrid high-order central/discontinuity-capturing finite difference framework. The underlying principle is that, to accurately and efficiently represent both broadband motions and discontinuities, non-dissipative methods are used where the solution is smooth, while the more expensive and dissipative capturing schemes are applied near discontinuous regions. Thus, an accurate sensor is developed to discriminate between smooth regions, shocks and material discontinuities, which all require a different treatment.

I implemented the hybrid algorithm into my own FORTRAN compressible Navier-Stokes solver. Given that our largest runs take take tens of thousands of processor-hours and generate up to one terabyte of data, I have parallelized my code using the Message Passing Interface (MPI) library and parallel HDF5 library is implemented

in the code as well for efficient parallel input/output (Appendix A). This also allows us to visualize our data in parallel using the VisIt software package. The code has successfully been run on different clusters, including Nyx and Flux at the University of Michigan and Ranger, Lonestar, and Stampede at the Texas Advanced Computing Center.

Following rigorous verification and validation (including the two-dimensional single-mode RM instability with re-shock), it is shown that the new approach is computationally less expensive and preserves small-scale features in turbulent mixed regions better than pure shock-capturing approach. Different key quantities such as circulation, enstrophy, total turbulent kinetic energy, anisotropy of the velocity field are reported and effects of physical viscosity on the evolution of the interface are investigated (Chapter II).

In the second part of my work, a novel set-up is proposed to investigate turbulent mixing between two adjacent fluids in the presence and absence of gravity, with application to the Rayleigh-Taylor instability. Fluids of different densities lie next to each other, and a random velocity field extending in the entire domain is used to initialize the problem. In order to analyze the relevance of each of the possible factors causing anisotropy at later stages, we start with the simplest case and make the problem progressively more complicated.

- The evolution of an interface under the presence of physical mass diffusion with no velocity perturbation is considered. It is shown that a velocity depending on the material interface profile should be prescribed initially to prevent the generation of unphysical waves in the presence of physical mass diffusion (Chapter III).

- Decaying isotropic turbulence is considered in detail and different quantities measuring flow intermittency and integral quantities are reported. This problem provides a baseline for the isotropic evolution of an isotropic field (Chapter IV).

- I consider a new set-up where the initial interface separates the light and heavy fluids in an existing turbulent velocity field extending in approximately the whole domain in each fluid in the absence of an acceleration field. The focus is on how two fluids of different density mix in the absence of gravity due to turbulence diffusion. The growth rate due to turbulence diffusion decreases as the kinetic energy of the initial turbulent field decays. Different arguments are proposed to describe the observed growth rate in the self-similar regime. Directional Taylor microscale and Kolmogorov microscale are defined and measured to investigate flow isotropy at different scales. The skewness and kurtosis of velocity derivatives are measured to quantify flow intermittency at small scales (Chapter IV).

- Finally, I revisit the problem in the presence of a gravitational field. The initial fluctuating velocity field perturbs the interface and the baroclinic vorticity generated by the Rayleigh-Taylor instability provides energy for the mixing region. By comparing the results of simulations with and without gravity, the role of gravity on isotropy of turbulence and flow intermittency inside the mixing region are highlighted. Effects of the initial most energetic wave number and the Reynolds number on the mixing region growth are also investigated (Chapter V).

Concluding remarks and further extensions for the present work are provided in the last chapter, Chapter VI.

CHAPTER II

A solution-adaptive method for efficient compressible multifluid simulations, with application to the Richtmyer-Meshkov instability

2.1 Introduction

In a number of high-speed flows with multiple fluid components, laminar initial conditions evolve to turbulent multi-material mixing regions[1]. For instance, the RMI consists of a shock interacting with a perturbed interface separating different fluids (Brouillette, 2002). The baroclinic vorticity deposited along the interface during the interaction drives the growth of the perturbation, which may eventually evolve into a turbulent mixing region. The initial behavior is dominated by shocks and interfaces, while at late times the flow is characterized by multi-material turbulence. Theoretical and experimental studies of the physics of such flows, particularly under high-energy-density conditions (Drake, 2006) important in the context of ICF (Lindl, 1995) and supernova collapse (Kifonidis *et al.*, 2006), remain challenging. High-fidelity simulations (DNS and LES) would provide a wealth of data to help understand the underlying physics. However, such shock-accelerated turbulence poses computational

[1]This chapter is adapted from Movahed, P. & Johnsen, E. 2013*a* A solution-adaptive method for efficient compressible multifluid simulations, with application to the Richtmyer-Meshkov instability. *J. Comput. Phys.* **239**, 166–186.

challenges, due to the transient nature of the process, to the possibile "physical" growth of numerical errors and to the presence of both discontinuities (shocks, interfaces, contacts) and broadband turbulence at different stages in the problem. Shock- and interface-capturing schemes rely on numerical dissipation to stabilize the solution, while such artificial diffusion must be prevented to represent turbulence accurately (Johnsen *et al.*, 2010). Although discontinuity-capturing schemes could be used to simulate such flows, the computational cost for the required resolutions is generally prohibitive. Furthermore, special care must be taken with material discontinuities (contacts and interfaces) across which the specific heats ratios γ varies, as spurious pressure oscillations may be generated (Abgrall, 1996), evolve based on the physical instability and affect the resulting turbulence. It has been shown that, for high-order shock-capturing schemes like weighted essentially non-oscillatory (WENO) schemes (Liu *et al.*, 1994; Jiang & Shu, 1996), a finite volume approach in which the primitive variables are reconstructed preserves the pressure equilibrium (Johnsen & Colonius, 2006). However, high-order three-dimensional finite volume shock-capturing schemes are computationally expensive. Additionally, standard finite difference implementations for multi-material flows typically lead to errors, unless a finite volume-like approach is followed (Nonomura *et al.*, 2012). The approach of Abgrall (1996) has yet to be extended to central schemes, which could be used to efficiently simulate smooth variations of γ in multi-material turbulence, *e.g.*, after interfaces have sufficiently diffused.

To address these difficulties, a hybrid high-order central/discontinuity-capturing finite difference scheme is presented. The underlying principle is that, to accurately and efficiently represent both broadband motions and discontinuities, non-dissipative methods are used where the solution is smooth, while the more expensive and dissipative capturing schemes are applied near discontinuous regions. Thus, an accurate sensor is required to discriminate between smooth regions, shocks and material

discontinuities, which all require a different treatment. Although many pure shock-capturing studies exist, such solution-adaptive schemes have been used previously to simulate single-fluid compressible turbulence problems: shock-turbulence interaction (Larsson & Lele, 2009), compressible isotropic turbulence (Johnsen *et al.*, 2010), shock-turbulent boundary layer interaction (Bernardini *et al.*, 2011). Two-dimensional RMI simulations have been performed with high-order WENO schemes for a single fluid (Schilling *et al.*, 2007). Multifluid turbulence resulting from the RMI has also been studied through large-eddy simulation (Lombardini *et al.*, 2011; Ward & Pullin, 2011), although it was not shown explicitly that spurious interfacial oscillations are prevented; this latter approach relies on the properties of the subgrid-scale model to dissipate any such errors.

The original contributions of this chapter are as follows. First, we extend the approach of Abgrall (1996) to central schemes, such that smooth distributions of varying γ can be simulated. This procedure is further extended to kinetic energy-preserving central schemes (Honein & Moin, 2004), which stabilize the solution by decreasing aliasing errors; in particular, it is shown that Blaisdell's approach (Blaisdell *et al.*, 1996) must be followed to prevent spurious pressure oscillations for varying γ. The present analysis is shown to apply to both finite difference and finite volume schemes, and to hybrid central/shock-capturing schemes. Finally, a new discontinuity sensor is presented, which discriminates between smooth and discontinuous regions. Section 2.2 decsribes the physical model. The full numerical method is presented in Section 2.3. One-dimensional multifluid problems with smooth/discontinuous variations in γ and shocks, and two-dimensional problems (single-mode Richtmyer-Meshkov instability) are used to verify the proposed algorithm in Section 2.4. Additional comments on symmetry-breaking issues are made in the appendix B.

2.2 Physical model

The focus of this chapter is on flows of two gases with different specific heats ratios γ. The Navier-Stokes equations are considered:

$$\frac{\partial \rho}{\partial t} + \frac{\partial}{\partial x_j}\left(\rho u_j\right) = 0, \tag{2.1a}$$

$$\frac{\partial (\rho u_i)}{\partial t} + \frac{\partial}{\partial x_j}\left(\rho u_i u_j + p\delta_{ij}\right) = \frac{\partial \tau_{ij}}{\partial x_j}, \tag{2.1b}$$

$$\frac{\partial E}{\partial t} + \frac{\partial}{\partial x_j}\left[u_j(E+p)\right] = \frac{\partial}{\partial x_j}(u_i\tau_{ij}) + \frac{\partial}{\partial x_j}\left[k\frac{\partial T}{\partial x_j}\right], \tag{2.1c}$$

where ρ is the density, p the pressure, u_i the velocity, E the total energy per unit volume, T is the temperature, μ is the viscosity and k is the thermal conductivity. For $\mu = 0$ and $k = 0$, the equations reduce to the Euler equations. The viscous stress tensor τ_{ij} is given by

$$\tau_{ij} = \mu\left(\frac{\partial u_i}{\partial x_j} + \frac{\partial u_j}{\partial x_i}\right) - \frac{2}{3}\mu\frac{\partial u_k}{\partial x_k}\delta_{ij}, \tag{2.2}$$

where μ is the viscosity, and the bulk viscosity is ignored. The gases are assumed ideal, with

$$\frac{p}{\gamma - 1} = \rho e = E - \frac{1}{2}\rho u_i u_i, \tag{2.3}$$

where e is the internal energy and the specific heats ratio γ may depend on composition but not temperature. For multicomponent problems, an additional transport equation must be solved to describe the fluid composition. In the present work, the γ-based model of Abgrall (1996) is followed, in which the transport equation is solved in non-conservative (advection) form for $1/(\gamma - 1)$:

$$\frac{\partial}{\partial t}\left(\frac{1}{\gamma - 1}\right) + u_j\frac{\partial}{\partial x_j}\left(\frac{1}{\gamma - 1}\right) = 0. \tag{2.4}$$

It should be noted that, although diffusion of momentum (viscosity) and energy (thermal conductivity) is included, the limit of zero molecular mass diffusion is considered at this time. For a binary system, the mass fractions, molecular masses and γ are related as follows:

$$Y_1 = 1 - Y_2, \tag{2.5a}$$

$$\frac{1}{M} = \frac{Y_1}{M_1} + \frac{Y_2}{M_2}, \tag{2.5b}$$

$$\frac{1}{\gamma - 1} = \frac{Y_1}{\gamma_1 - 1}\frac{M}{M_1} + \frac{Y_2}{\gamma_2 - 1}\frac{M}{M_2}, \tag{2.5c}$$

where M is the molecular mass and Y is the mass fraction.

2.3 Hybrid shock-capturing/central difference methodology

For simplicity, the semi-discrete form of the Euler equations is considered in one dimension for the analysis:

$$\frac{d}{dt}\tilde{q}_i + \frac{\hat{f}_{i+1/2} - \hat{f}_{i-1/2}}{\Delta x} = 0, \tag{2.6}$$

where q is the vector of conserved variables and f is the flux vector. The tilde denotes pointwise value for finite difference and the cell-average value for finite volume; the hat represents the high-order numerical flux at the cell edge. It is straightforward to extend the following analysis to multiple dimensions. Multi-dimensional problems are solved dimension by dimension; for finite volume schemes, appropriate quadratures must be performed in the directions tangential to the cell edges (Titarev & Toro, 2004). A third-order accurate strong stability preserving (SSP) Runge-Kutta scheme is used for explicit time marching (Gottlieb & Shu, 1998).

In the hybrid formulation, the numerical flux is written

$$\hat{f}_{i+1/2} = (1 - \eta_{i+1/2})\hat{f}^{(central)}_{i+1/2} + \eta_{i+1/2}\hat{f}^{(shock-capturing)}_{i+1/2}, \tag{2.7}$$

where $\eta_{i+1/2} \in [0, 1]$ is a switching function defined at each cell edge based on the local flow smoothness such that a sixth-order central scheme is used in smooth regions and fifth-order WENO shock capturing is applied near discontinuities in a stable fashion (Larsson & Gustafsson, 2008). To minimize the computational cost, it is preferred to set η exactly equal to either zero or one by introducing a cut-off. Given an appropriate switching function (or shock sensor), the difficulty is to determine the discrete version of the transport equation, *e.g.*, equation (2.4), such that high-order accuracy is retained and no spurious pressure oscillations occur for central schemes when considering flows with smoothly varying γ. Since the procedure is known for shock capturing (Johnsen & Colonius, 2006) and due to the linearity of equation (2.7), proving that a purely central scheme is high-order accurate and prevents pressure oscillations ensures that the corresponding hybrid method does as well. The three elements of the hybrid framework are described in the rest of this section. A detailed analysis of the central fluxes is presented in Section 2.3.1, to show how to solve the transport equation to prevent spurious pressure oscillations for smoothly varying γ. In Section 2.3.2, the shock-capturing component of the hybrid scheme is explained briefly. No special treatment is required for low Mach number flows (Thornber *et al.*, 2008*a*,*b*) since the central scheme is expected to be used in those regions. Finally, a novel discontinuity sensor based on the difference between WENO and ideal weights is introduced in Section 2.3.3.

Form	Divergence	Non-conservative	Split
$\frac{\partial f}{\partial x}$	$\frac{\partial}{\partial x}(uv)$	$u\frac{\partial v}{\partial x} + v\frac{\partial u}{\partial x}$	$\frac{1}{2}\frac{\partial}{\partial x}(uv) + \frac{1}{2}\left(u\frac{\partial v}{\partial x} + v\frac{\partial u}{\partial x}\right)$

Table 2.1: Definitions of convective fluxes consisting of the product of two variables, u and v.

2.3.1 Central fluxes

In this section, a stable and accurate discretization of the convective terms is sought such that no spurious pressure oscillations are generated in regions of (smoothly) varying γ; abrupt changes in γ are flagged by the discontinuity sensor, such that shock capturing (Abgrall, 1996; Johnsen & Colonius, 2006) is used. We anticipate the need for using a split form of the convective terms for stable turbulence simulations (Pirozzoli, 2011) and thus follow this general viewpoint in the analysis; the traditional divergence form is a special case thereof.

Here, a convective flux consisting of the multiplication of two variables u and v is written in one of three forms (table 2.1): divergence, non-conservative and split. Although all three forms are equivalent in the continuous case, a Fourier analysis of the discrete expressions shows that the amplitude of the aliasing errors is reduced when using the split form (Blaisdell *et al.*, 1996). The convective terms in the mass, momentum and energy equations are in the form $\frac{\partial}{\partial x}(\rho u \phi)$, where $\phi = (1, u, (E + p)/\rho)^T$. This cubic term is expanded by Feiereisen *et al.* (1981) as follows in the momentum equations:

$$\frac{\partial}{\partial x}(\rho u \phi) = \frac{1}{2}\frac{\partial}{\partial x}(\rho u \phi) + \frac{1}{2}\phi\frac{\partial}{\partial x}(\rho u) + \frac{1}{2}\rho u\frac{\partial \phi}{\partial x}, \tag{2.8}$$

while Blaisdell *et al.* (1996) expanded the convective terms in the momentum and energy equations as such:

$$\frac{\partial}{\partial x}(\rho u \phi) = \frac{1}{2}\frac{\partial}{\partial x}(\rho u \phi) + \frac{1}{2}u\frac{\partial}{\partial x}(\rho \phi) + \frac{1}{2}\rho\phi\frac{\partial u}{\partial x}. \tag{2.9}$$

The Feiereisen form (Feiereisen *et al.*, 1981) ensures that both ρu_i and $\rho u_i u_i$ are conserved in the limits of incompressibility and zero viscosity on a periodic domain using summation by parts, thus the terminology "kinetic-energy preserving", despite not being strictly applicable for the compressible case. The Blaisdell form (Blaisdell *et al.*, 1996) results in a more robust scheme and less unphysical pile-up of energy at high wave numbers associated with aliasing errors. It is possible to develop a split form that is skew-symmetric in the strict sense, i.e., the integral of kinetic energy is preserved in time in the incompressible limit (Morinishi, 2010). Additional robustness can be obtained by fully expanding the cubically nonlinear convective terms (Kennedy & Gruber, 2008):

$$\begin{aligned}\frac{\partial}{\partial x}(\rho u\phi) =& a\frac{\partial}{\partial x}(\rho u\phi) + b\left[\rho\frac{\partial}{\partial x}(u\phi) + u\frac{\partial}{\partial x}(\rho\phi) + \phi\frac{\partial}{\partial x}(\rho u)\right] + \\ & (1-a-2b)\left(\rho u\frac{\partial\phi}{\partial x} + \rho\phi\frac{\partial u}{\partial x} + u\phi\frac{\partial\rho}{\partial x}\right),\end{aligned} \tag{2.10}$$

where a and b are parameters to be set to minimize aliasing errors. A high-order accurate conservative formulation of the convective terms in these different forms can be developed for both finite difference and finite volume formulations (Ducros *et al.*, 2000). It can be shown that solving for the total energy instead of the internal energy decreases the robustness of the scheme (Nagarajan *et al.*, 2003), and the generalized finite difference formulation was summarized recently by Pirozzoli (2010). On the other hand, solving for the internal energy does not conserve the total energy, which is problematic for flows with shocks. This discrepancy was addressed by combining update equations for the kinetic and internal energy to obtain (Honein & Moin, 2004):

$$\frac{\partial E}{\partial t} + \frac{u}{2}\frac{\partial}{\partial x}\left(\rho u^2\right) + \frac{\rho u^2}{2}\frac{\partial u}{\partial x} + \frac{\partial}{\partial x}(\rho e u) + p\frac{\partial u}{\partial x} + u\frac{\partial p}{\partial x} = 0. \tag{2.11}$$

The spatial derivatives can then be discretized by any of the forms described above. For the multicomponent Euler equations, it is shown below that the $\frac{\partial}{\partial x}(\rho e u)$ term

must be treated in a special fashion to prevent spurious pressure oscillations.

In the following analysis, we consider the advection of a smooth distribution in γ and ρ at velocity u and pressure p. Following the approach of Abgrall (Abgrall, 1996), the Euler equations can be marched forward by one time step or substep:

$$\rho_i^{n+1} = \rho_i^n - \frac{\Delta t}{\Delta x} D_i \left(\rho u\right), \tag{2.12a}$$

$$\left(\rho u\right)_i^{n+1} = \left(\rho u\right)_i^n - \frac{\Delta t}{\Delta x} \left[D_i \left(\rho u^2\right) + D_i \left(p\right)\right], \tag{2.12b}$$

$$\left(\rho e + \frac{\rho u^2}{2}\right)_i^{n+1} = \left(\rho e + \frac{\rho u^2}{2}\right)_i^n - \frac{\Delta t}{\Delta x} \left[D_i \left(\rho u e\right) + D_i \left(\frac{\rho u^3}{2}\right) + D_i \left(up\right)\right], \tag{2.12c}$$

where D_i is a linear difference operator. Equations (2.12a) and (2.12b) can be combined to obtain the required velocity equilibrium, $u_i^{n+1} = u_i^n = u$. However, the energy equation depends on which split form is chosen. For the divergence and Blaisdell *et al.* (1996) forms, equation (2.12c) simplifies to

$$\left(\rho e\right)_i^{n+1} = \left(\rho e\right)_i^n - \frac{u \Delta t}{\Delta x} D_i \left(\rho e\right). \tag{2.13}$$

For the Feiereisen *et al.* (1981) form, equation (2.12c) simplifies to

$$\left(\rho e\right)_i^{n+1} = \left(\rho e\right)_i^n - \frac{u \Delta t}{2 \Delta x} \left[D_i \left(\rho e\right) + e_i^n D_i \left(\rho\right) + \rho_i^n D_i \left(e\right)\right]. \tag{2.14}$$

From equation (2.3), a constant pressure implies that equation (2.13) simplifies to

$$\left(\frac{1}{\gamma - 1}\right)_i^{n+1} = \left(\frac{1}{\gamma - 1}\right)_i^n - \frac{u_i^n \Delta t}{\Delta x} D_i \left(\frac{1}{\gamma - 1}\right), \tag{2.15}$$

which is the consistent discrete version of equation (2.4). Thus, the divergence and Blaisdell *et al.* (1996) forms both preserve the pressure equilibrium, $p_i^{n+1} = p_i^n = p$. On the other hand, for the Feiereisen *et al.* (1981) form , equation (2.4) cannot be obtained, since the following numerical discretization does not hold: $D_i \left(\rho e\right)^n =$

$e_i^n D_i(\rho) + \rho_i^n D_i(e)^n$. Thus, given that equation (2.15) must hold, the Feiereisen *et al.* (1981) form leads to spurious pressure oscillations for flows with variable γ. Similar arguments for the split form and spurious oscillations for flows of variable γ hold for finite volume schemes.

2.3.2 Discontinuity capturing

The sensor described in the next section discriminates between smooth and discontinuous regions, including those where the composition (γ) varies sharply. For shocks and contacts in single-fluid regions, finite difference WENO is used with Roe flux-splitting with entropy fix (Jiang & Shu, 1996). At material interfaces, primitive variables are interpolated (Johnsen & Colonius, 2006) using WENO along with Roe's solver (Roe, 1981; Shyue, 1998). Although a standard finite difference WENO (Jiang & Shu, 1996) is preferred, the approach of Johnsen & Colonius (2006) is necessary to prevent spurious pressure oscillations at interfaces. In the present context, this latter approach constitutes a second-order approximation to the standard finite difference WENO. Since this procedure is applied at material discontinuities only, where the scheme's accuracy is expected to be first order at best, this second-order approximation is not detrimental.

Fifth-order accurate WENO reconstruction, required for the discontinuity sensor and the shock- and interface-capturing schemes, is summarized here. A function $p(x)$ may be approximated at the cell edge $x_{i+1/2}$ to fifth order by convexly combining three third-order accurate polynomials $v^{(1)}(x)$, $v^{(2)}(x)$ and $v^{(3)}(x)$:

$$p_{i+1/2} = p(x_{i+1/2}) = \omega_1 v_{i+1/2}^{(1)} + \omega_2 v_{i+1/2}^{(2)} + \omega_3 v_{i+1/2}^{(3)} + O(\Delta x^5), \tag{2.16}$$

where the polynomials at $x_{i+1/2}$ are functions of the cell averages:

$$\begin{aligned} v_{i+1/2}^{(1)} &= \frac{1}{3}\bar{v}_{i-2} - \frac{7}{6}\bar{v}_{i-1} + \frac{11}{6}\bar{v}_i \\ v_{i+1/2}^{(2)} &= -\frac{1}{6}\bar{v}_{i-1} + \frac{5}{6}\bar{v}_i + \frac{1}{3}\bar{v}_{i+1}. \\ v_{i+1/2}^{(3)} &= \frac{1}{3}\bar{v}_i + \frac{5}{6}\bar{v}_{i+1} - \frac{1}{6}\bar{v}_{i+2} \end{aligned} \tag{2.17}$$

The WENO weights ω_i

$$\omega_i = \frac{\alpha_i}{\alpha_1 + \alpha_2 + \alpha_3}, \qquad \alpha_i = \frac{d_i}{(\beta_i + \epsilon)^2}, \qquad \epsilon = 10^{-6}, \tag{2.18}$$

are modifications of the ideal weights d_i

$$d_1 = \frac{1}{10}, \qquad d_2 = \frac{3}{5}, \qquad d_3 = \frac{3}{10}. \tag{2.19}$$

The smoothness indicators β_i are designed to emphasize smooth stencils:

$$\begin{aligned} \beta_1 &= \frac{13}{12}\left(\bar{v}_{i-2} - 2\bar{v}_{i-1} + \bar{v}_i\right)^2 + \frac{1}{4}\left(\bar{v}_{i-2} - 4\bar{v}_{i-1} + 3\bar{v}_i\right)^2 \\ \beta_2 &= \frac{13}{12}\left(\bar{v}_{i-1} - 2\bar{v}_i + \bar{v}_{i+1}\right)^2 + \frac{1}{4}\left(\bar{v}_{i-1} - \bar{v}_{i+1}\right)^2 \\ \beta_3 &= \frac{13}{12}\left(\bar{v}_i - 2\bar{v}_{i+1} + \bar{v}_{i+2}\right)^2 + \frac{1}{4}\left(\bar{v}_i - 4\bar{v}_{i+1} + \bar{v}_{i+2}\right)^2 \end{aligned} \quad , \tag{2.20}$$

such that the WENO weights are nonlinear functions of the cell averages.

2.3.3 Discontinuity sensor

The performance of a hybrid central/shock-capturing scheme strongly depends on the ability of the sensor to discriminate between discontinuous and smooth regions (Johnsen *et al.*, 2010). For fully-developed compressible isotropic turbulence, the Ducros sensor (Ducros *et al.*, 2000) exhibits excellent performance. However, it is not designed to handle contact or material discontinuities, and is not well suited

to laminar flow or spatially evolving turbulence; given that all these regimes are of interest, another approach is required. The present discontinuity sensor consists of two steps: first, smooth regions are discriminated from discontinuous regions. Then, material interfaces are identified. Inspired by (Hill & Pullin, 2004; Ward & Pullin, 2011; Taylor *et al.*, 2007), I define a switching function by considering the deviation of WENO weights from ideal weights. This procedure is performed for density only, as it provides a good representation of weak solutions of the Euler equations, including shocks, contact discontinuities and rarefaction waves. A function g, based on the first norm deviation of the ideal weights from the WENO weights, is defined as

$$g = |\tilde{\omega}_1 - d_1| + |\tilde{\omega}_2 - d_2| + |\tilde{\omega}_3 - d_3|, \tag{2.21}$$

where

$$\tilde{\omega}_i = \frac{\tilde{\alpha}_i}{\tilde{\alpha}_1 + \tilde{\alpha}_2 + \tilde{\alpha}_3}, \qquad \tilde{\alpha}_i = \frac{d_i}{(\beta_i + \tilde{\epsilon})^2}, \qquad \tilde{\epsilon} = 10^{-8}. \tag{2.22}$$

In smooth regions, WENO weights are close to ideal weights, such that g is small. Beyond a certain threshold, the solution will not be stable with a purely central scheme. Since $\sum_i \tilde{\omega}_i = \sum_i d_i = 1$ with $0 \leq \tilde{\omega}_j, d_j \leq 1$, g is a bounded function between 0 to 1.8 for fifth-order WENO; for third- and seventh-order accurate WENO, g takes the maximum of 4/3 and 68/35, respectively. When using shock capturing, a discontinuity is smeared across a certain number of points, which does not vary significantly from one grid size to another. This indicates that g remains almost constant near a discontinuity as the discontinuity becomes sharper on finer grids, such that the same threshold can be used for measuring smoothness on different grids. On the other hand, in smooth regions, g is $O(\Delta x^2)$ and fewer cells are flagged as the flow features become smoother on finer resolutions. Based on empirical tests, the threshold is set to 1.5 for fifth-order WENO and sixth-order central difference; if g exceeds this threshold, shock capturing (WENO) must be used. In the WENO

procedure ϵ is a dimensional quantity that introduces a lower bound on the effective smoothness indicators, $(\beta_i + \epsilon)$, where β is $O(\bar{v}^2)$ (Fedkiw *et al.*, 2000; Henrick *et al.*, 2005). The value of ϵ in equation (2.18) is set to 10^{-8} here to make the sensor sensitive to variations as small as $O(10^{-4})$ in the density field. The computational cost of the present sensor is not particularly high, *e.g.*, compared to that of Hill & Pullin (2004), given that the only additional computed quantity is $\tilde{\alpha}$.

The next step is to identify material interfaces, such that the appropriate WENO interpolation is used. In the discontinuous regions detected by the sensor, we measure the total variation of $1/(\gamma - 1)$:

$$TV\left(\frac{1}{\gamma-1}\right)_{i+1/2} = \sum_{r=-3}^{2}\left(\frac{1}{\gamma-1}\right)_{i+r} - \frac{1}{2}\left[\left(\frac{1}{\gamma-1}\right)_{i-1} + \left(\frac{1}{\gamma-1}\right)_{i}\right]. \tag{2.23}$$

If the total variation is smaller than an empirically determined threshold (10^{-3}), we use standard finite difference WENO (Jiang & Shu, 1996). A total variation greater than 10^{-3} implies that we are close to a material interface; to prevent spurious pressure oscillation, we follow the procedure of Johnsen & Colonius (2006). In the problems of interest, the material discontinuity must be captured accurately on the given resolutions. If not, unphysical structures are produced along the interface due to the lack of dissipation, though the calculations remain stable. This problem is resolved by combining the present sensor with a contact discontinuity detector based on the strength of the contact in characteristic space (Varadan & Johnsen, 2014). In our two-dimensional simulations, this sensor is applied along the 45° and 135° directions as well, to detect contacts not aligned with the mesh.

After identifying the discontinuous cells, it is important to ensure that the cells flagged by the sensor do not lie inside the stencil used by the central scheme. In practice, small numerical errors may be generated at interfaces between smooth and discontinuous regions where the scheme switches between a central and a shock-

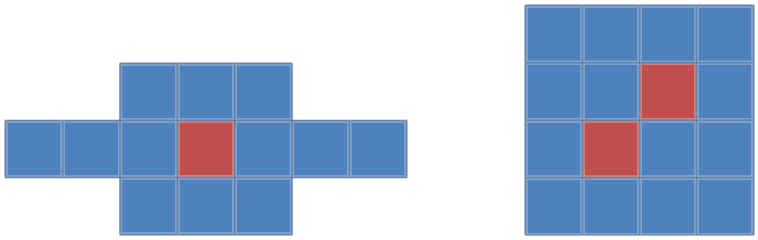

(a) Horizontal sweep. (b) 45^o sweep.

Figure 2.1: Schematic of the application of the sensor. Additional cells (blue) are flagged as discontinous when a cell (red) is flagged as discontinous by the sensor.

capturing scheme. Adding extra dissipation by flagging more points around the cells identified by the sensor is helpful in mitigating such errors. To overcome these difficulties, a sufficient number of points are flagged as the sensor is applied independently in each spatial direction, as shown in figure 2.1. Similar approaches in which flagging extra points in a radius of 2-4 points have also been previously followed (Hill & Pullin, 2004; Larsson & Lele, 2009; Johnsen *et al.*, 2010). In addition to identifying extra points, the application of standard high-order spatial filters in shock-free regions to remove dispersion errors and high-frequency spurious numerical noise is discussed in Section 2.3.4. Figure 2.2 summarizes the hybrid algorithm used for calculating the advection fluxes of equation (2.1).

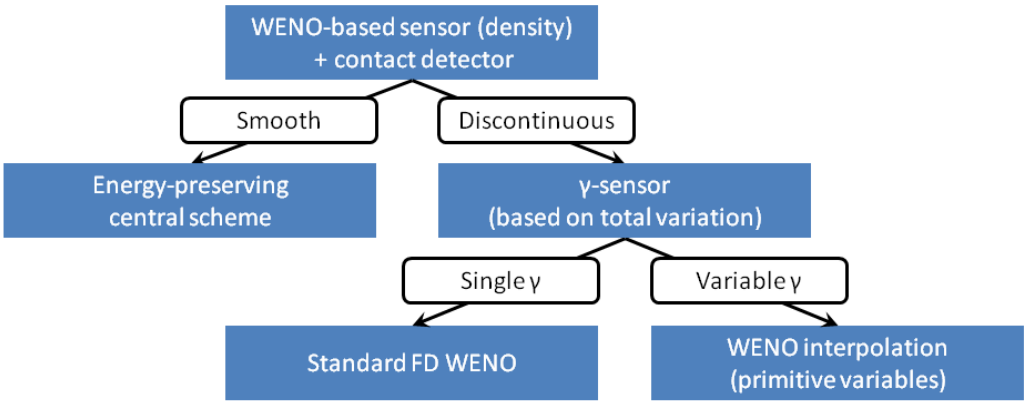

Figure 2.2: Summary of the proposed hybrid scheme for calculating the advection fluxes of equation (2.1).

2.3.4 Spatial filter

Even though an energy-preserving central scheme is used, dispersion errors may be generated and contaminate the solution. These errors reduce the ability to resolve high wavenumbers with increasing order and thus lead to high-frequency spurious noise. This issue is problematic with high-order central schemes, which nominally provide no numerical dissipation. Such errors can be corrected using a spatial filter whose order is higher than that of the base scheme. In hybrid schemes, additional small errors may be generated at interfaces between smooth and discontinuous regions, where the scheme switches between central and shock capturing. Thus, in smooth regions, there is no dissipation mechanism to damp such spurious errors. To address this problem, background numerical dissipation can be applied to damp these errors using a spatial filter of order higher than the base scheme. In this work, a standard tenth-order explicit spatial filter is applied to the conservative variables at the end of each Runge-Kutta time step. The filtered value, $\hat{u}$ can be expressed as

$$\hat{u}_i = \sum_{j=-5}^{5} a_j u_{i+j}, \tag{2.24}$$

where the coefficients a_j can be found in (Vasilyev *et al.*, 1998; Bogey & Bailly, 2004). The filtering procedure does not introduce any phase error by enforcing the symmetry property $a_j = a_{-j}$. While applying the spatial filter in smooth regions was found useful to remove numerical noise, applying the filter in discontinuous regions introduces large overshoots, as observed in (Lo *et al.*, 2010). Therefore, the filtering procedure is only applied if all the cells inside the filtering stencil are flagged "smooth" by the sensor.

2.4 Results

Several test problems are used to assess the performance of the proposed numerical method. First, a single-fluid problem with a shock and smooth structures (Shu-Osher problem) is considered to evaluate the discontinuity sensor. Then, the advection of a smooth distribution in γ is used to validate the analysis for kinetic energy-preserving central schemes. A multifluid shock-tube problem is then presented to show that isolated discontinuities are well captured. The one-dimensional tests end with a multifluid extension of the Shu-Osher problem, which includes smooth and sharp changes in γ. Finally, detailed two-dimensional results for the Richtmyer-Meshkov instability are presented.

2.4.1 Single-fluid Shu-Osher problem

The Shu-Osher problem (Shu & Osher, 1989) consists of a one-dimensional spatially varying density field of a fluid with constant $\gamma = 1.4$ interacting with a shock. This problem is used to evaluate the performance of the proposed discontinuity sensor. The initial conditions (figure 2.3) correspond to a $M = 3$ right-moving shock wave interacting with a perturbed density field on the domain $x \in [0, 10]$, with:

$$[\rho, u, p, \gamma] = \begin{cases} [3.857143, 2.629369, 10.3333, 1.4], & \text{if } x \leq 1, \\ [1 + 0.2\sin(5(x-5)), 0, 1, 1.4], & \text{otherwise.} \end{cases} \tag{2.25}$$

The hybrid and pure WENO schemes are run on a uniform mesh with 300 grid points and a CFL of 0.8. Figure 2.4 shows the pressure, density, entropy and shock sensor at $t = 1.8$. Results obtained using WENO with $N = 6400$ grid points constitute the reference solution. As observed in Johnsen *et al.* (2010), the pressure field is accurately represented with both schemes, but the density and entropy fields exhibit excessive dissipation with WENO. The switching function η shows the actual points

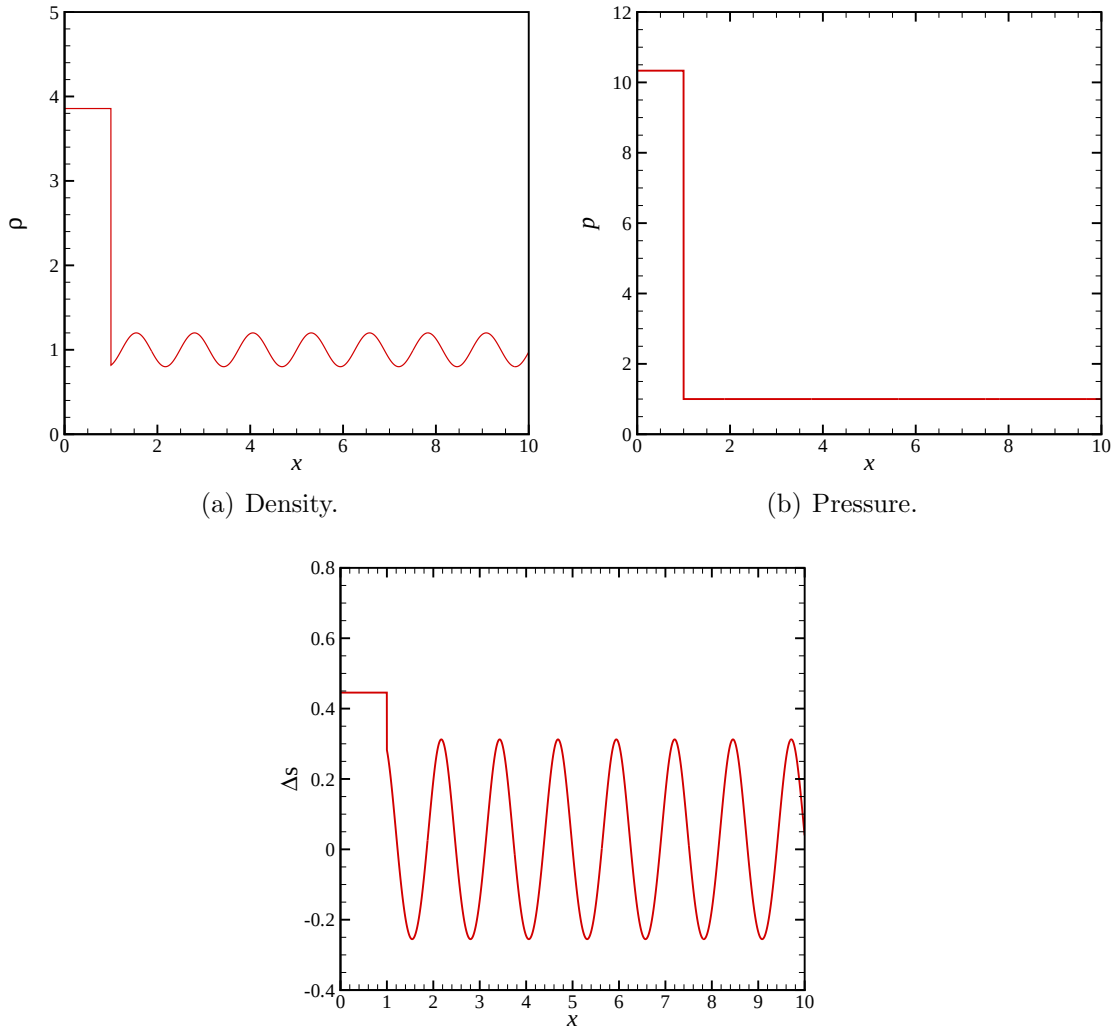

(a) Density.

(b) Pressure.

(c) Entropy.

Figure 2.3: Initial conditions for the Shu-Osher problem.

where each scheme is used. The acoustic waves are strong enough at $t = 1.8$ to steepen into weak shocks, such that shock-capturing must be used. The current WENO-based sensor identifies the appropriate regions in which the central scheme can be applied. As a result, the entropy waves are more accurately represented. The function g is small in smooth regions, while values beyond the threshold are achieved close to the shocks.

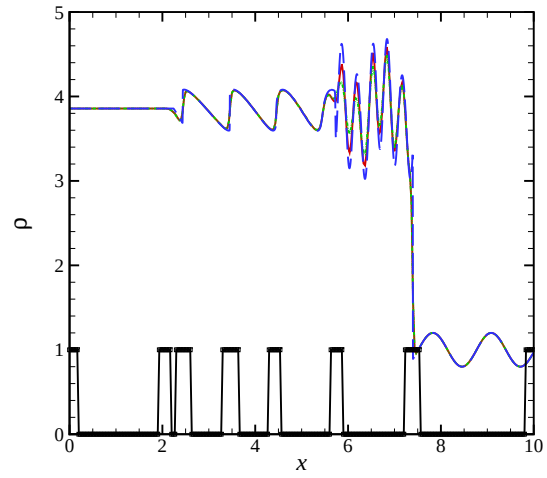

(a) Density. The black line on the bottom of the density field shows the switching function η.

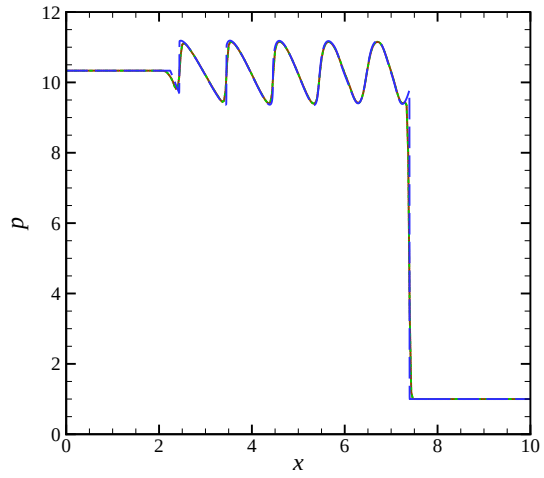

(b) Pressure.

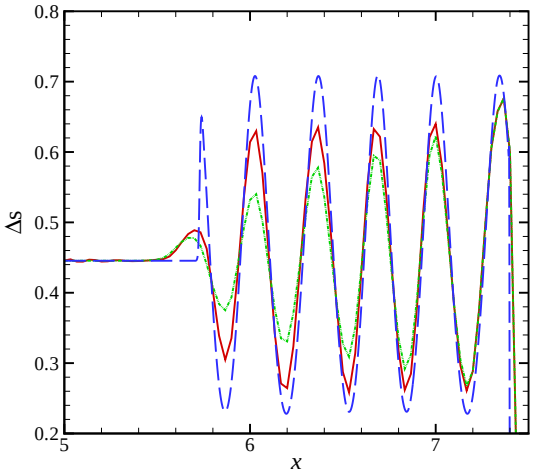

(c) Entropy (zoomed in).

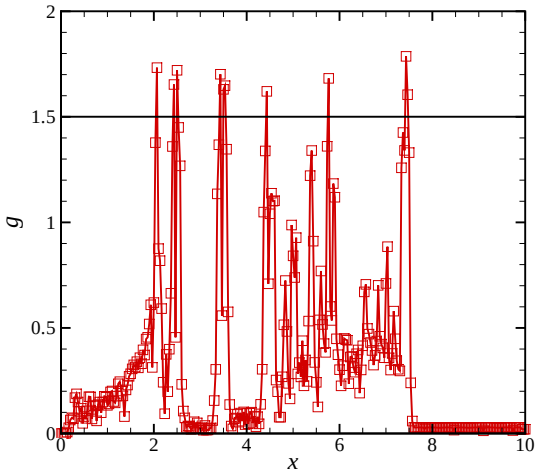

(d) Shock sensor function.

Figure 2.4: Solution to the Shu-Osher problem at $t = 1.8$ with $N = 300$ points. Dashed blue: reference solution (WENO5, $N = 6400$); solid red: hybrid solution; dotted green: pure WENO.

2.4.2 Advection of a smooth γ distribution

The advection of a smooth distribution of density and γ is computed to validate the analysis presented in Section 2.3.1 for kinetic energy-preserving central schemes. The following initial conditions are used:

$$\left[\rho, u, p, \frac{1}{\gamma - 1}\right] = \left[2 + \sin(2\pi x), 1, 1, 2.5 + \sin(2\pi x)\right]. \tag{2.26}$$

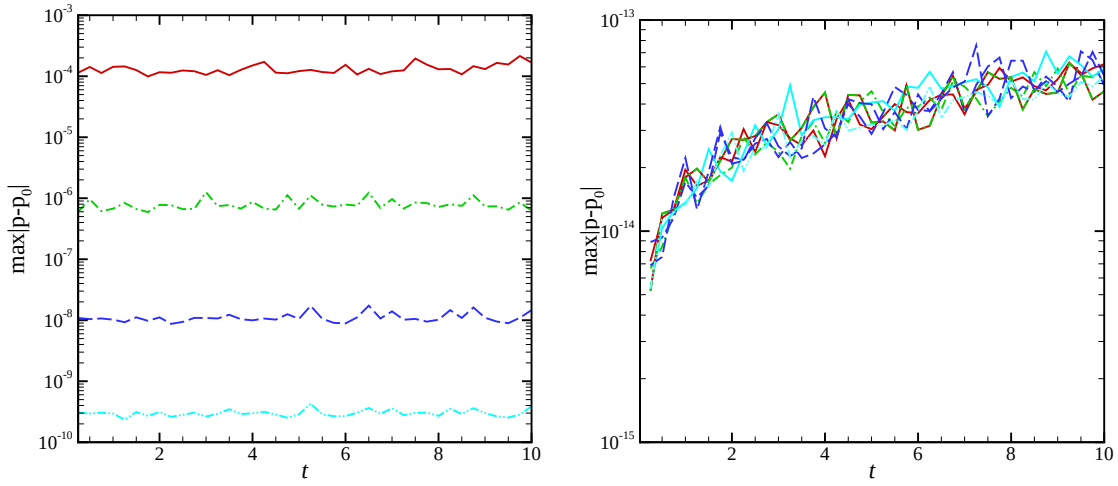

(a) Feiereisen form (Feiereisen *et al.*, 1981).

(b) Blaisdell (Blaisdell *et al.*, 1996) and divergence forms.

Figure 2.5: Time evolution of the L_∞ pressure error for the advection of a smooth variable-γ fluid with $N = 100$ points. Solid red: second order; dash-dotted green: fourth order; long-dashed blue: sixth order; dash-dot-dotted cyan: eighth order.

The domain is periodic with 100 points. Sufficiently smooth profiles in density and γ are chosen to ensure that the simulations are stable with central differences for the given time marching. Simulations are performed for 10 periods. Figure 2.5 shows the L_∞ pressure error for the Blaisdell *et al.* (1996), Feiereisen *et al.* (1981) and the divergence form. In agreement with the analysis of Section 2.3.1, spurious oscillations are observed with the Feiereisen *et al.* (1981) form. These errors remain essentially constant with time and decrease with order of accuracy. The errors produced by the divergence and Blaisdell *et al.* (1996) forms remain bounded near round-off level for the entire simulation, thus validating the analysis.

2.4.3 Sod shock tube problem

A multifluid modification (Abgrall & Karni, 2001) of the Sod shock tube (Sod, 1978) problem is considered to show that isolated discontinuities are captured with

the present scheme. The initial conditions are

$$[\rho, \gamma, u, p]_L = [1, 1.4, 0, 1]\,, \qquad [\rho, \gamma, u, p]_R = [0.125, 1.6, 0, 0.1]\,. \tag{2.27}$$

Figure 2.6 shows the density, pressure, velocity and $1/(\gamma - 1)$ results at $t = 0.2$ using 200 points. The computed solution agrees well with the exact solution in all fields. Uniform pressure and velocity are maintained across the material discontinuity. The flagging mechanism for the sensor produces additional dissipation specifically at locations that connect the shock and contact with the constant regions in between them. This extra dissipation is found useful to remove numerical noise generated by the switch between the central and shock-capturing schemes at material discontinuities.

2.4.4 Multifluid Shu-Osher problem

A variation in γ is introduced into the initial flow field of the original Shu-Osher problem described in Section 2.4.1. The initial conditions correspond to a $M = 3$ shock in air interacting with a sharp material interface followed by perturbed density and γ fields on the domain $x \in [0, 10]$, with initial conditions:

$$\left[\rho, u, p, \frac{1}{\gamma - 1}\right] = \begin{cases} [3.857143, 2.629369, 10.3333, 2.5]\,, & \text{if } x \leq 1, \\ [1 + 0.2\sin(5\,(x-5))\,, 0, 1, 1.33 + 0.2\sin(5\,(x-5))]\,, & \text{otherwise.} \end{cases} \tag{2.28}$$

The same computational parameters are used as in Section 2.4.1. Figure 2.7 shows the pressure, velocity, density and $1/(\gamma-1)$ profiles at $t = 1.8$. Results obtained using the WENO scheme of Johnsen & Colonius (2006) with $N = 6400$ grid points constitute the reference solution. Overall, the hybrid scheme matches the reference solution well. Pressure oscillations are prevented and the initial distribution in γ maintains its amplitude just downstream of the shock region (entropy waves region) as the waves are compressed by the shock. The $1/(\gamma - 1)$ distribution remains constant in

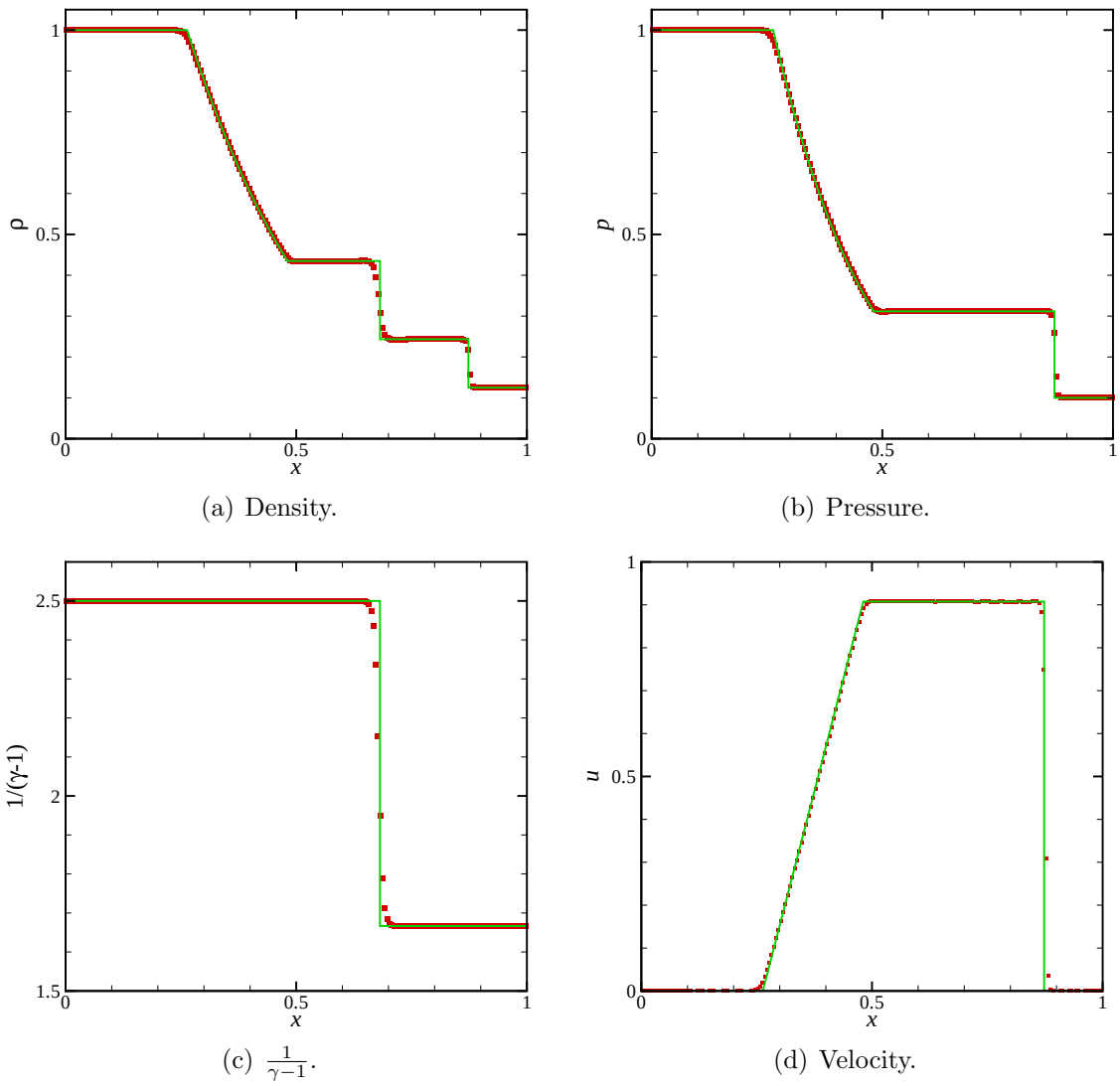

(a) Density. (b) Pressure.

(c) $\frac{1}{\gamma-1}$. (d) Velocity.

Figure 2.6: Multifluid Sod shock tube problem at $t = 0.2$ with $N = 200$ points. Red squares: hybrid; solid green: exact solution.

the acoustic region, which is separated from the entropy waves region by the original sharp interface.

2.5 Planar single-mode Richtmyer-Meshkov instability

Planar (two-dimensional) single-mode Richtmyer-Meshkov instability (RMI) experiments with re-shock (Collins & Jacobs, 2002) are considered to validate the hybrid algorithm described in the previous chapter, assess its performance and determine the

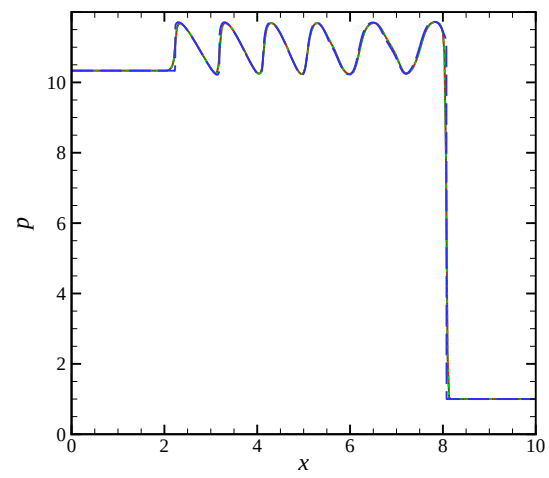

(a) Pressure.

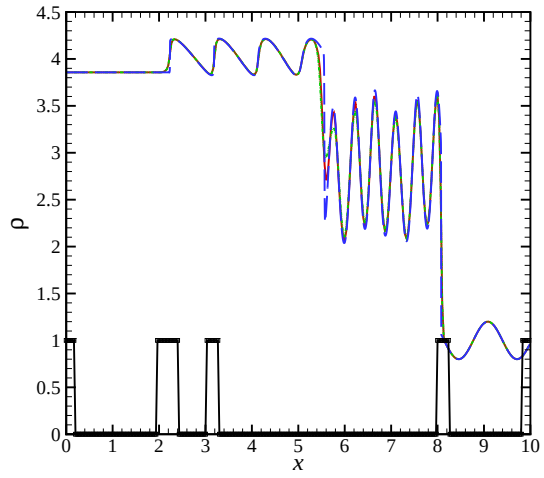

(b) Density. The black line on the bottom of the density field shows the switching function η.

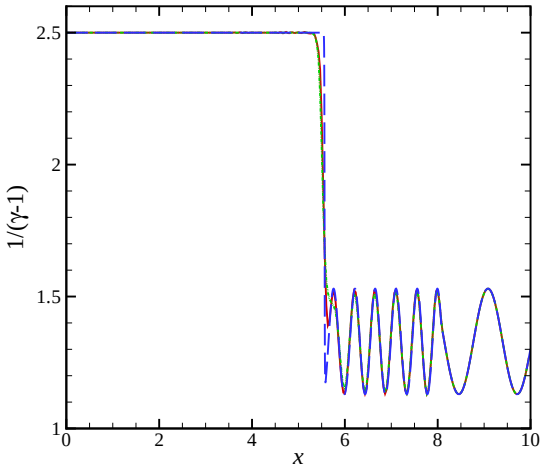

(c) $1/(\gamma - 1)$.

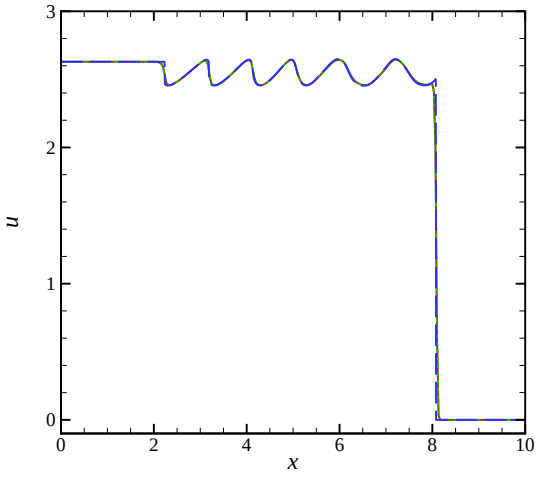

(d) Velocity.

Figure 2.7: Numerical solution to the multifluid Shu-Osher problem at $t = 1.8$ with $N = 300$ points. Dashed blue: reference solution (WENO5, $N = 6400$); solid red: hybrid; dotted green: pure WENO.

feasibility of resolved viscous calculations. This problem has been investigated numerically, *e.g.*, by Latini *et al.* (2007); Schilling *et al.* (2007) with constant γ, and Houim & Kuo (2011) with a method that does not conserve the total energy. The present computations are set up to match the experiments as closely as possible. A Mach 1.21 shock interacts with an interface separating air and SF_6. The interface is initialized as a diffuse sinusoidal perturbation where the initial amplitude, wavelength

and diffusion thickness are 0.183 cm, 5.93 cm and 0.50 cm. An exponential diffusion function (Latini *et al.*, 2007) is used to compute the initial volume fraction in the mixing region in a thermodynamically consistent fashion. The shock is initialized from a corresponding one-dimensional simulation to avoid start-up errors (Jin & Liu, 1996; Johnsen, 2013). Inflow and reflecting boundary conditions are used at the entrance and end of the shock tube, and periodic boundary conditions are set along the sides. A base pressure of 10^4 Pa is used for non-dimensionalization and a tenth-order spatial filter is employed to minimize the numerical noise. No special care is taken to prevent potential temperature errors, e.g., temperature spikes at material interfaces relevant to viscous simulations, which could be addressed following (Johnsen & Ham, 2012). Inviscid calculations are first presented, followed by viscous simulations.

2.5.1 Inviscid calculations

Since the majority of past simulations have focused on the Euler equations, inviscid results are emphasized. Figure 2.8/ 2.9 shows temporal sequences of density, vorticity and the sensor fields before/after re-shock on a grid with 512 cells per wavelength with the present hybrid scheme. The deposition of baroclinic vorticity along the interface, the penetration of spikes of SF_6 into the air and bubbles of air into SF_6 and the resulting mushroom-like structure are well represented. The roll-up rate is enhanced due to the Kelvin-Helmholtz instability in the vorticity bilayer region, thus resulting in the formation of more small-scale features. At the instant of re-shock, the amplitude is much larger and more perturbed than initially, such that a broad distribution of scales can be observed after the shock interaction. Due to the set-up, phase inversion occurs. At late times, the results lose their symmetry (Appendix B). The sensor performance suggests that the interface is accurately detected during the evolution of the instability. In the current problem, the vorticity is frozen along the captured interface, such that the baroclinic vorticity slightly diffuses numerically.

With the Ducros sensor (Ducros *et al.*, 2000), a central scheme would result in large errors. The bubble and spike locations, x_b and x_s, are defined as the position where $\bar{X} \leq 0.99$ and $\bar{X} \geq 0.01$, respectively, where $\bar{X}$ is the spatially-averaged volume fraction of SF_6 in the spanwise direction (Latini *et al.*, 2007). The amplitude of the mixing layer is defined as $(x_b - x_s)/2$. The time evolution of the amplitude, bubbles and spikes is shown in figure 2.10. The growth rate of the amplitude decreases monotonically as the resolution is increased before re-shock, in good agreement with the experiments (Collins & Jacobs, 2002). The time evolution of the bubble and spike positions shows convergence in an integral sense before re-shock; after re-shock ($t = 0.008$ s) and interaction with the rarefaction ($t = 0.011$ s), there are discrepancies depending on the resolution, thus suggesting that the instability is sensitive to the precise conditions at re-shock. In inviscid simulations, there exists no physical cut-off length scale to prevent the production of unphysical small-scale features. Furthermore, the solution before re-shock will always be affected by grid-level perturbations, such that the precise conditions before re-shock vary with mesh size. Thus, a full grid-independent solution cannot be achieved with grid refinement. Convergence is expected for fully resolved viscous simulations as the grid is refined and is discussed in the next section. In the experiments (Collins & Jacobs, 2002), the driver-based expansion wave generated by the diaphragm rupture starts to interact with the mixing region at $t \approx 0.0045$ s and decelerates the contact while expanding the mixing layer. These effects, along with boundary layers present in the experiments, are not considered here and may explain the small discrepancy after 0.0045 s.

Given the critical role of vorticity, related quantities such as circulation and enstrophy are considered. The vorticity is calculated from the velocity field numerically using second-order central differences. The circulation and mass-weighted enstrophy are calculated by integrating the vorticity distribution in a box around the interface

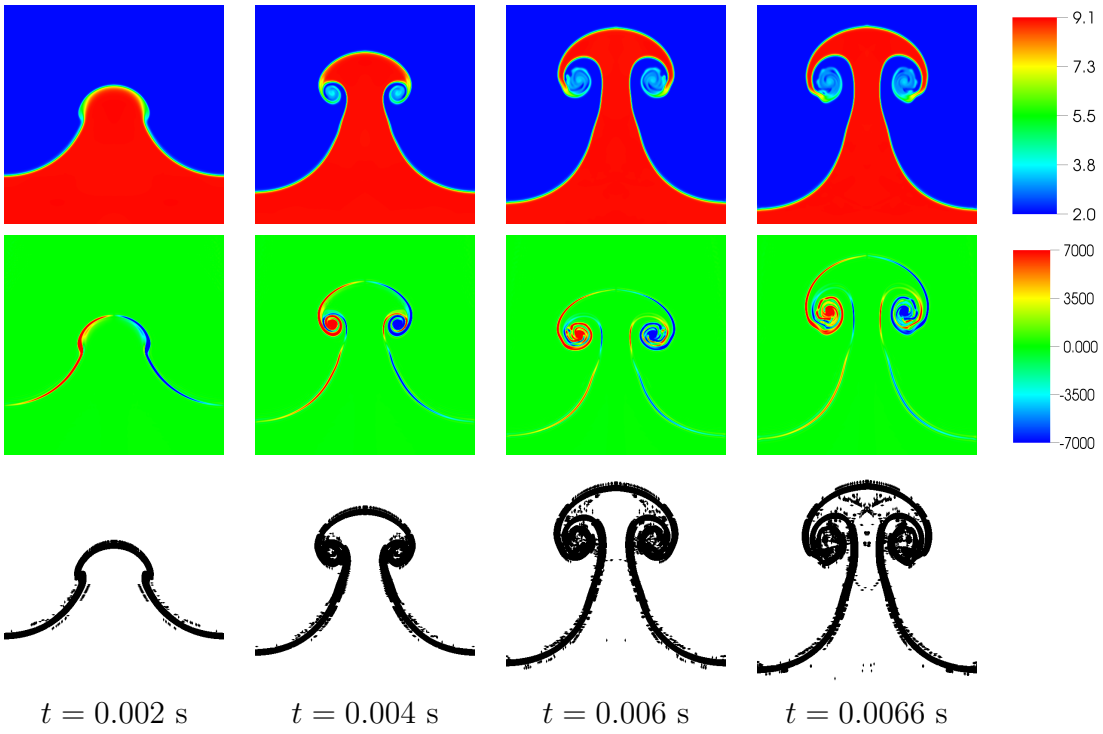

Figure 2.8: Time evolution of the inviscid Richtmyer-Meshkov instability (before reshock) with $N = 512$ points per wavelength. Top: density; middle: vorticity; bottom: sensor.

over half of the domain and the full domain, respectively (Aure & Jacobs, 2008*b*)

$$\Gamma = \int \nabla \times \mathbf{u} dxdy, \qquad \Omega = \int \rho \left(\nabla \times \mathbf{u}\right)^2 dxdy. \tag{2.29}$$

Figure 2.11 represents the time evolution of the positive, negative and total circulation, and enstrophy. The passage of the shock causes a jump in circulation due to baroclinic vorticity. The absolute value of positive and negative circulation each increases monotonically as the grid refinement is performed, in agreement with the amount of small scales resolved on each grid. The magnitude of the total circulation appears to converge in the integral sense and increases due to secondary baroclinic vorticity generation (Peng *et al.*, 2003). Enstrophy, a good measure of the generation of small-scale features, shows a behavior qualitatively similar to that of circulation: it first increases due to the initial shock interaction, then again significantly after re-

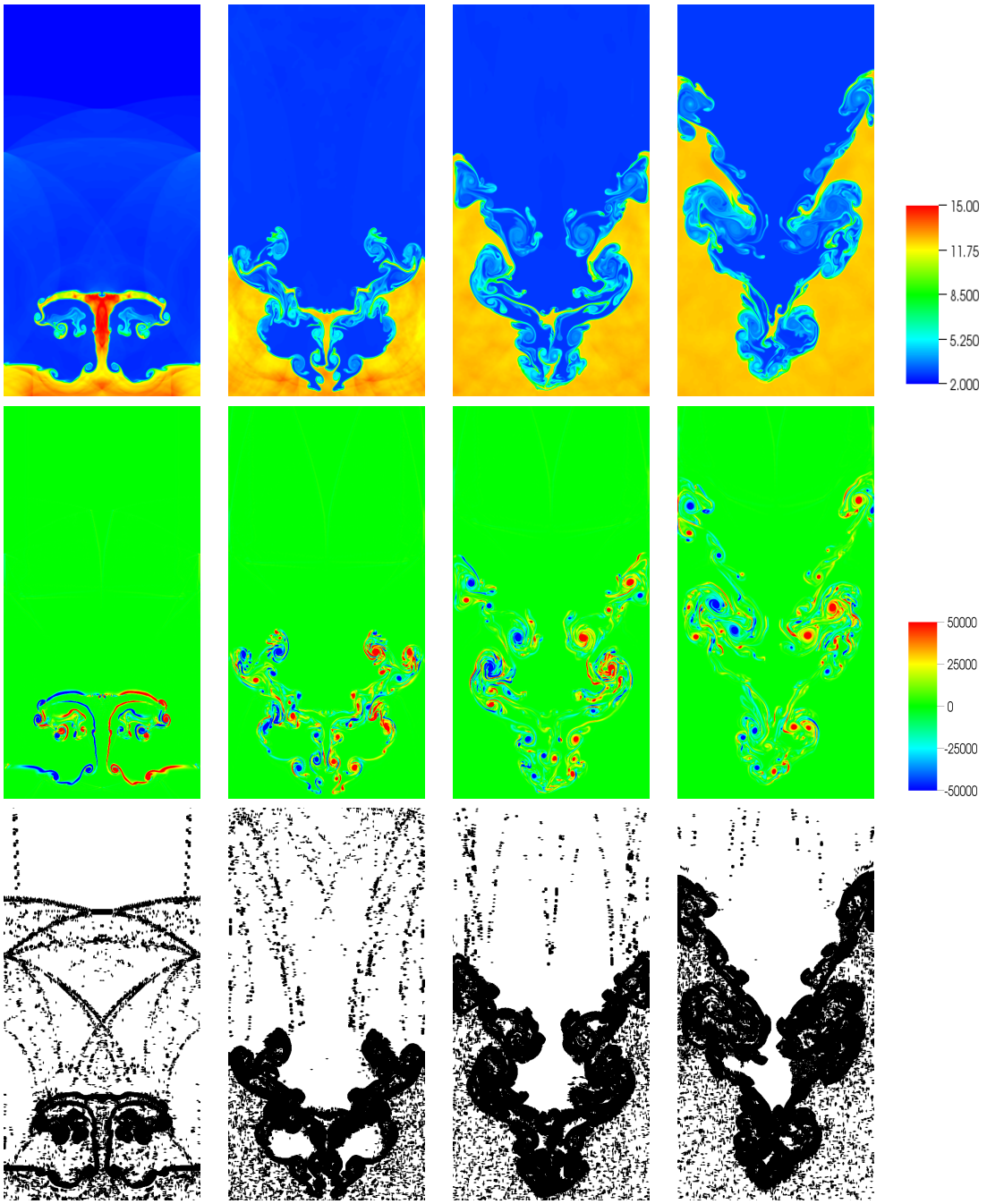

Figure 2.9: Time evolution of the inviscid Richtmyer-Meshkov instability (After reshock) with $N = 512$ points per wavelength. Top: density; middle: vorticity; bottom: sensor.

shock. Higher enstrophy is achieved on finer grids because the numerical dissipation is lower.

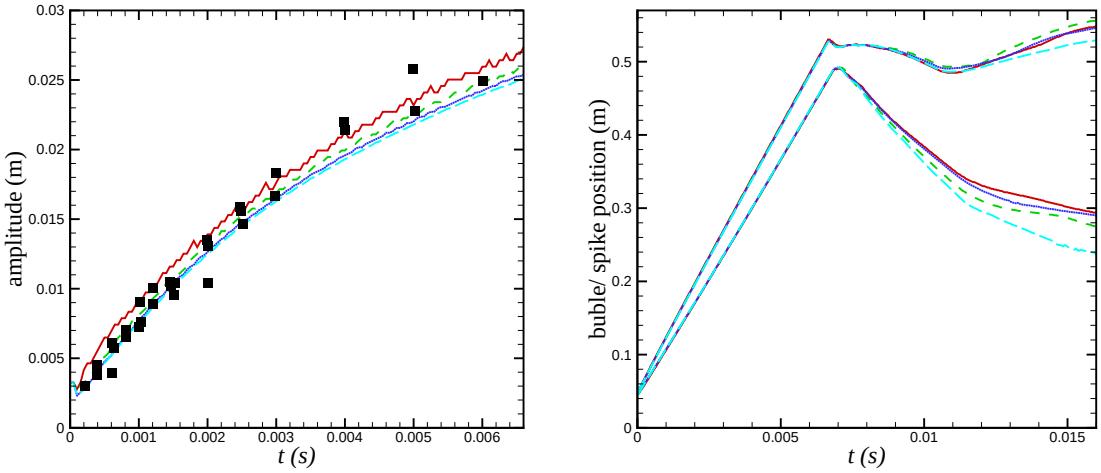

(a) Amplitude of the perturbation vs. time.

(b) Bubble and spike position vs. time.

Figure 2.10: Time evolution of the amplitude, bubbles and spikes for the inviscid Richtmyer-Meshkov instability with N points per wavelength. Solid red: $N = 64$; dashed green: $N = 128$; dotted blue: $N = 256$; long dashed cyan: $N = 512$. Black squares: experiments (Collins & Jacobs, 2002).

In anticipation of three-dimensional turbulent simulations, the energy associated with small-scale motions can be quantified by computing the "turbulent kinetic energy" (TKE). Although the present simulations are two-dimensional and not fully turbulent, such a quantity is a measure of the intensity of the small-scale velocity fluctuations. At each cross-section, the mean velocities, $\hat{u}$ and $\hat{v}$ are defined as

$$\hat{u} = \langle \rho u \rangle \,/\, \langle \rho \rangle \,, \quad \hat{v} = \langle \rho v \rangle \,/\, \langle \rho \rangle \,, \tag{2.30}$$

where the brackets $\langle\rangle$ represent the mean average operator in the spanwise direction. The total turbulent kinetic energy in the mixing region is defined as

$$TKE = \int \left[\frac{1}{2} \rho \left((u - \hat{u})^2 + (v - \hat{v})^2 \right) \right] dxdy, \tag{2.31}$$

where the integral is taken over the mixing region. This quantity is shown in figure 2.12. TKE is initially generated after the first shock interaction. Before re-shock, the

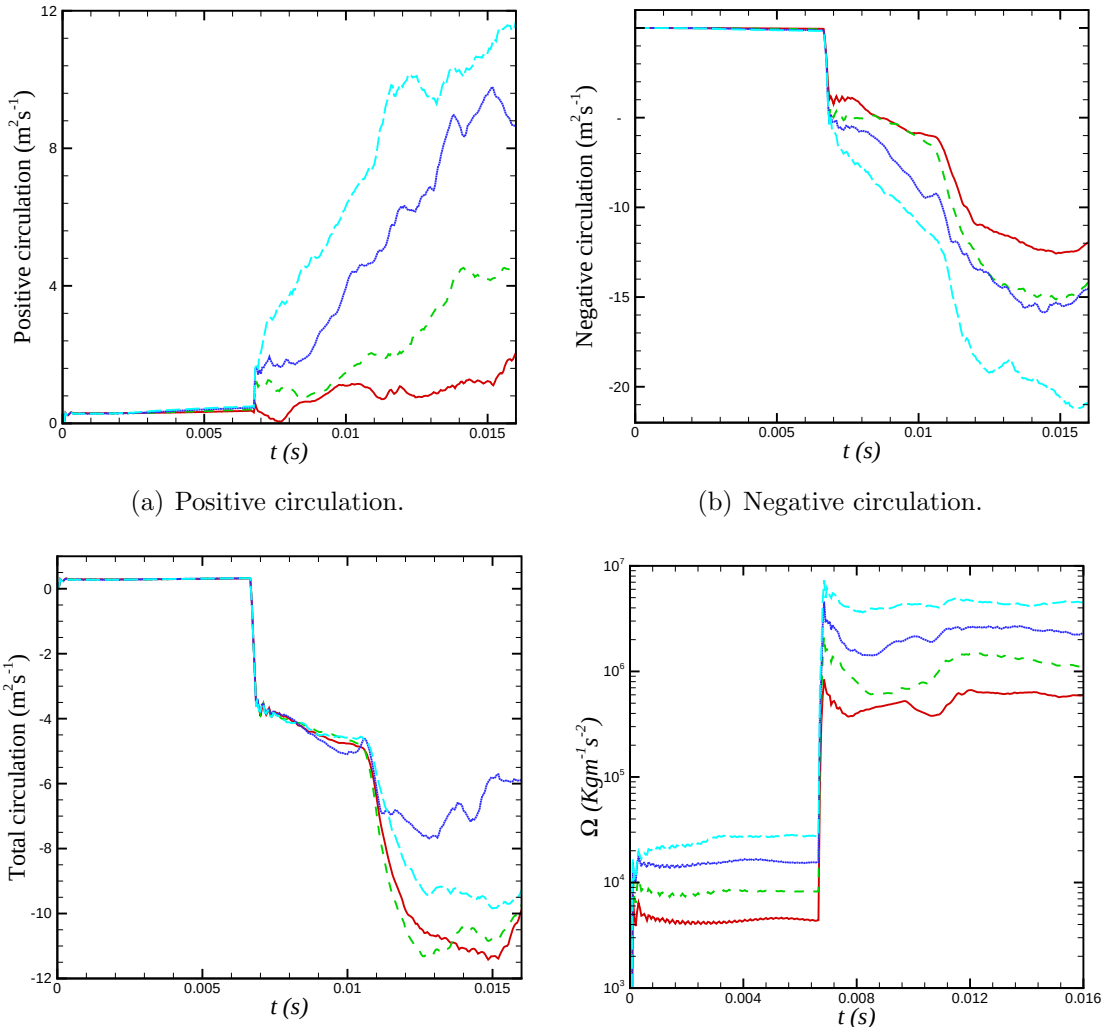

(a) Positive circulation.

(b) Negative circulation.

(c) Total circulation.

(d) Enstrophy.

Figure 2.11: Time evolution of circulation and enstrophy in the mixing region for the inviscid Richtmyer-Meshkov instability with N points per wavelength. Solid red: $N = 64$; dashed green: $N = 128$; dotted blue: $N = 256$; long dashed cyan: $N = 512$.

interface is much more distorted, thus resulting in more baroclinic vorticity deposition on the interface. This interaction produces an increase in TKE by two orders of magnitude. After the interaction with the reflected rarefaction, TKE increases again. The time evolution of the ratio of streamwise to spanwise TKE is a measure of isotropy. This ratio is over-predicted at low resolutions, which emphasizes the effect of numerical dissipation on the isotropy of the small-scale motions. This anisotropy

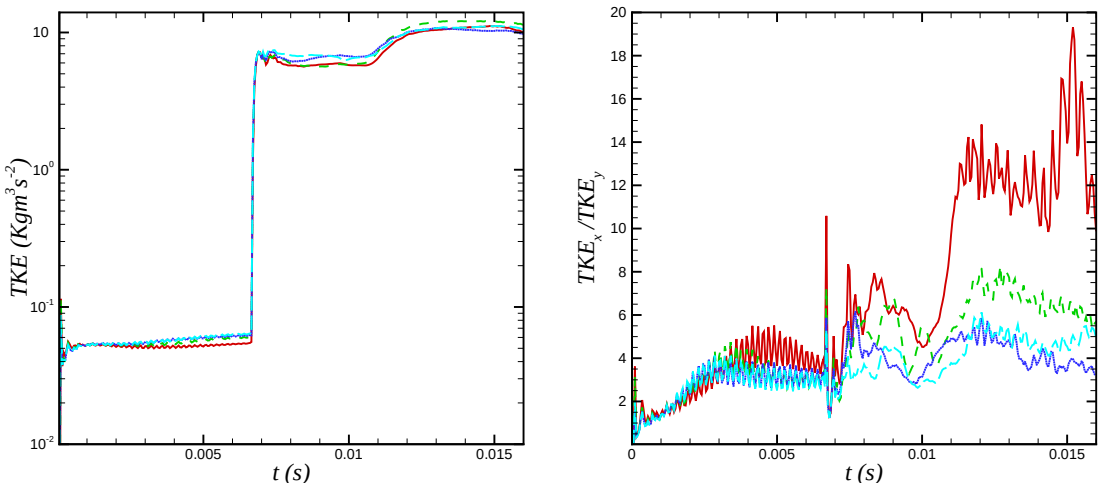

(a) TKE. (b) Ratio of the streamwise and spanwise TKE.

Figure 2.12: Time evolution of TKE in the mixing region for the inviscid Richtmyer-Meshkov instability with N points per wavelength. Solid red: $N = 64$; dashed green: $N = 128$; dotted blue: $N = 256$; long dashed cyan: $N = 512$.

remains, even long after re-shock.

The efficiency of the hybrid framework can be quantified by monitoring the CPU time. The code was run on the Nyx cluster at the Center for Advanced Computing at the University of Michigan. For each simulation, 160 processors were used. Table 2.2 compares the performance of the hybrid code to that of pure WENO in terms of the total CPU time. The advantages of the hybrid framework over pure shock-capturing schemes are twofolds: better resolution properties for broadband motions and reduced computational cost. The former is minor at early times, since large scales dominate; thus, the hybrid and pure WENO solutions are very similar. Thus, the advantage of the hybrid scheme lies primarily in compute time early on, and improves with resolution. Significant savings are achieved until re-shock, where shock-capturing is only used sparingly in well-defined regions. After re-shock, load balancing becomes more important. This issue is expected to be less relevant for resolved viscous calculations of the RMI where enough resolution is provided to resolve the contact without any artificial numerical dissipation. For instance, resolved

Resolution (points per wavelength)	128	256	512	1024
Before re-shock	0.87	0.77	0.68	0.63
Full simulation	0.96	0.93	0.83	0.79

Table 2.2: Efficiency of the hybrid scheme compared to pure WENO, defined as t_{hybrid}/t_{WENO}, for the inviscid Richtmyer-Meshkov instability.

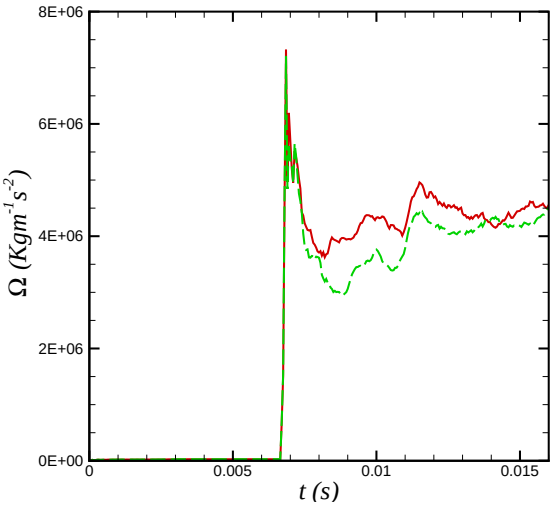

Figure 2.13: Time evolution of the enstrophy for the hybrid (red) and pure WENO (green) results on $N = 512$ points per wavelength.

simulations of one-dimensional unsteady detonations were recently reported (Romick *et al.*, 2012) where it was showed that it is not necessary to use capturing to stably simulate the advection part of equation (2.1). Still, for sufficiently fine resolutions, the advantages of using the hybrid framework remain significant, especially given that finer scales can be represented on the grid, as illustrated by the enstrophy plot in figure 2.13.

2.5.2 Viscous simulations

Viscous calculations are performed to discuss limitations of inviscid simulations and resolution requirements for resolved calculations. The diffusive terms are discretized in non-conservative form with sixth-order central differences. The heat conduction and viscosity coefficients of the mixture are determined from Herning and Zipper approximation for binary mixing and the temperature-dependent pure com-

ponent transport properties (Reid *et al.*, 1987). It is well-known that Euler simulations do not exhibit pointwise convergence (Samtaney & Pullin, 1996): the numerical dissipation scales with the grid size, thus resulting in more small-scale features and higher levels of enstrophy with mesh refinement. Navier-Stokes simulations on a sufficiently fine grid where diffusive effects can be captured are expected to produce a resolved solution, since diffusion introduces a cut-off length. Although not shown here, Navier-Stokes simulations with 512 points per wavelength and viscosities and thermal conductivities matching the experiments show very similar results to Euler calculations, thus implying that physical diffusion (*i.e.*, the experimental Reynolds number) cannot be resolved on these grids. Slight differences in viscous calculations after re-shock were observed, which are attributed to the sensitivity of the instability to the initial conditions, rather than to the physical mechanisms.

Instead, for the present purpose, simulations performed at a Reynolds number 100 times lower than in the experiment are considered. Figure 2.14 shows the density fields at $t = 0.0066$ s (before re-shock) and $t = 0.0086$ s (after re-shock). Although the spike morphology is almost identical before re-shock, the viscous results exhibit vastly different behavior thereafter. As expected, the smallest scales are larger than those observed in the inviscid case. Although pointwise convergence is not achieved in the viscous case, certain convergence patterns are clearly discernable at this Reynolds number. Enstrophy is compared in figure 2.15. Other than the maximum value, viscous simulations exhibit enstrophy levels that remain on the same order with increasing mesh resolution, unlike the inviscid calculations. At the time of re-shock, scales much smaller than the initial perturbation are present and compressed by the shock, such that the resolution requirements of the problem changes dramatically. Physical diffusion is well represented at the present resolution for the given Reynolds number, at least in an integral sense.

In the inviscid case, much more small-scale features are produced when increas-

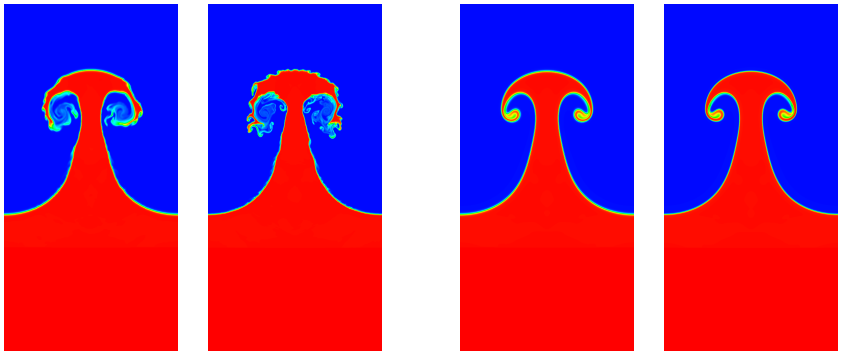

(a) $N = 512$ (inviscid). (b) $N = 1024$ (inviscid). (c) $N = 512$ (viscous). (d) $N = 1024$ (viscous).

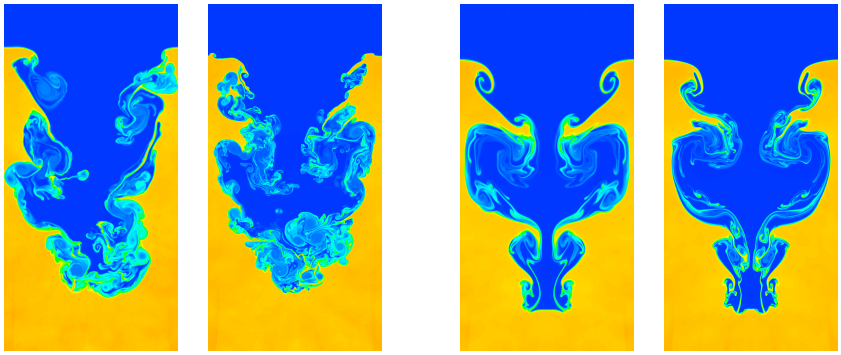

(e) $N = 512$ (inviscid). (f) $N = 1024$ (inviscid). (g) $N = 512$ (viscous). (h) $N = 1024$ (viscous).

Figure 2.14: Density contours before re-shock at $t = 0.0066$ s (top) and after re-shock at $t = 0.0086$ s (bottom) for different resolutions (N: number of cells per wavelength) for the inviscid and viscous Richtmyer-Meshkov simulations.

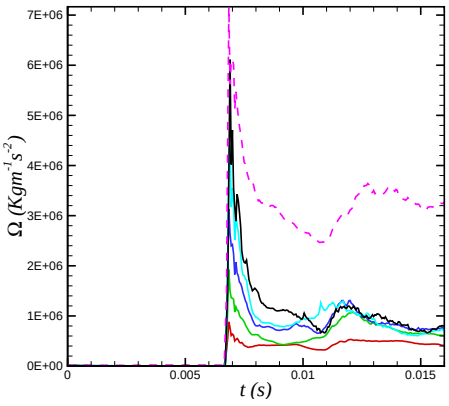

Figure 2.15: Time evolution of enstrophy for the viscous Richtmyer-Meshkov instability. Red: $N = 64$; green: $N = 128$; blue: $N = 256$; cyan: $N = 512$; black: $N = 1024$; magenta (dotted): $N = 512$ (inviscid).

ing the resolution, and it becomes more difficult to identify common large scale features. In the absence of a regularizing factor (physical dissipation) small-scale Kelvin-Helmholtz roll-ups develop due to grid-dependent perturbations at 1024 points per wavelength suggesting that a converged grid-independent solution cannot be achieved as the grid is further refined. The discrepancy in enstrophy shows that the physics for Euler calculations (implicit large-eddy simulation or ILES) at these resolutions with the present methods must be interpreted with care, as the small-scale features are greatly exaggerated. Although ILES may be advantageous for certain problems, it is unclear how one might reconcile that approach with viscous results. In sufficiently high-resolution viscous simulations, a physical cut-off length scale is expected to damp the physical growth of grid-level perturbations, such that a grid-independent (converged) solution is achieved.

The use of appropriate non-reflecting boundary conditions is necessary for the viscous case. Following Thompson (1987) for modeling the non-reflecting boundary conditions at the entrance of the tube, the wave speeds, in particular that of the interface, remain the same for both the viscous and the inviscid cases (figure 2.14). On the other hand, applying a zero-gradient boundary condition, as was done in the original article (Movahed & Johnsen, 2013*a*), results in reflection of waves from the entrance. In this latter case, the reflected shock incoming shock off of the interface is reflected again at the entrance, when the imperfect zero-gradient boundary condition was originally applied. The wave reflected off of the entrance subsequently interacts with the interface and reduces its speed before re-shock. This effect is more pronounced for the viscous case, as shown in figure 2.16.

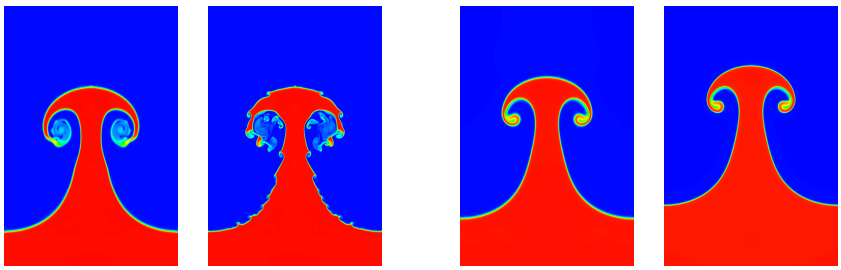

(a) $N = 512$ (inviscid). (b) $N = 1024$ (inviscid). (c) $N = 512$ (viscous). (d) $N = 1024$ (viscous).

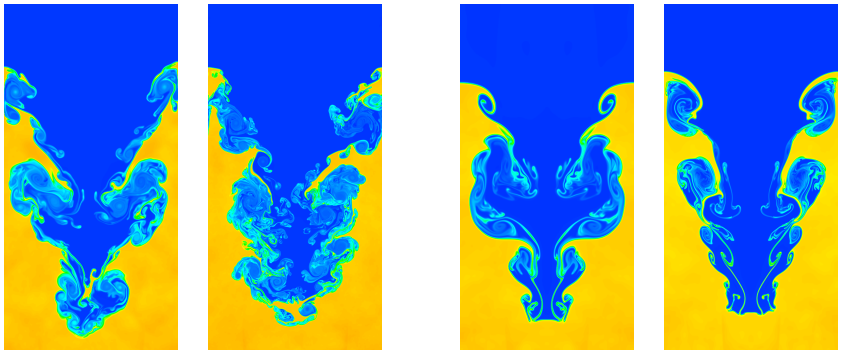

(e) $N = 512$ (inviscid). (f) $N = 1024$ (inviscid). (g) $N = 512$ (viscous). (h) $N = 1024$ (viscous).

Figure 2.16: Density contours before re-shock at $t = 0.0066$ s (top) and after re-shock at $t = 0.0085$ s (bottom) for different resolutions (N: number of cells per wavelength) for the inviscid and viscous Richtmyer-Meshkov simulations. A zero-gradient approximation is used to model the non-reflecting boundary condition at the entrance.

CHAPTER III

On the treatment of material interfaces in the presence of finite mass physical diffusion

3.1 Introduction

In this chapter, we are interested in investigating suitable initial conditions for starting numerical simulations of transient evolution of a material interface in the presence of diffusion processes (mass, momentum and energy). A material interface corresponds to a discontinuity in the mass fraction and density between two different fluids. In compressible high Reynolds number flows, diffusion terms are often neglected and the Euler equations are considered instead. In the absence of diffusion, the pressure and velocity should remain uniform across an isolated material interface and the interface is simply advected by the flow. Preserving these correct boundary conditions requires an appropriate numerical scheme (Johnsen, 2011).

With the advancements of computational resources, direct numerical simulation is becoming plausible where the Navier-Stokes equations are considered. In Navier-Stokes solvers, physical diffusion terms, including Fickian diffusion, are included. Due to the presence of physical mass diffusion, the initial material interface profile starts to diffuse. For the Navier-Stokes equations, if the same initial conditions as those used for the Euler are applied, transient waves are produced, which propagate away

from the interface. These waves may get reflected at the boundaries and interact with the interface again, thus affecting the dynamics. If gravity is present, these waves can also disturb the initial hydrostatic pressure field. The following analysis shows that an initial velocity should be prescribed at the interface to prevent these spurious waves when including physical mass diffusion. This initial velocity distribution corresponds to the steady-state profile achieved in the presence of physical mass diffusion. This result indicates that those transient waves are unphysical and should be prevented in numerical simulations by initializing the problem in a consistent manner.

3.2 The incompressible problem

In this section, the work of Sandoval (1995) on initializing the velocity field in variable-density flows consisting of two incompressible miscible fluids is summarized. The continuity equation is

$$\frac{\partial \rho}{\partial t} + \frac{\partial \left(\rho u_j\right)}{\partial x_j} = 0. \tag{3.1}$$

The transport equation for the mass fraction of the first fluid, Y_1, assuming Fickian diffusion reads

$$\frac{\partial \left(\rho Y_1\right)}{\partial t} + \frac{\partial \left(\rho u_j Y_1\right)}{\partial x_j} = \frac{\partial}{\partial x_j}\left(\rho D \frac{\partial Y_1}{\partial x_j}\right). \tag{3.2}$$

The mass fraction and the density fields are related as

$$\frac{1}{\rho} = \frac{Y_1}{\rho_1} + \frac{1 - Y_1}{\rho_2}, \tag{3.3}$$

where ρ_1 and ρ_2 are the denisty of the first and second fluids, respectively. Taking partial derivative of both sides of equation 3.3 results in

$$-\frac{d\rho}{\rho^2} = dY_1 \left(\frac{1}{\rho_1} - \frac{1}{\rho_2}\right). \tag{3.4}$$

Equations 3.1 and 3.2 can be combined to obtain the transport equation in the non-conservative form

$$\rho \left[\frac{\partial Y_1}{\partial t} + u_j \frac{\partial Y_1}{\partial x_j} \right] = \frac{\partial}{\partial x_j} \left(\rho D \frac{\partial Y_1}{\partial x_j} \right). \tag{3.5}$$

Using equations 3.4 and 3.5, the partial derivatives of Y_1 can be replaced with corresponding partial derivatives of ρ to obtain

$$\frac{\partial \rho}{\partial t} + u_j \frac{\partial \rho}{\partial x_j} = \rho \frac{\partial}{\partial x_j} \left(\frac{D}{\rho} \frac{\partial \rho}{\partial x_j} \right). \tag{3.6}$$

Comparing equations 3.6 and 3.1 implies that the velocity field is no longer divergence-free in regions where there exists a gradient in the mass fraction and when mass diffusion is present. In fact, the divergence of the velocity is

$$\frac{\partial u_j}{\partial x_j} = -\frac{\partial}{\partial x_j} \left(\frac{D}{\rho} \frac{\partial \rho}{\partial x_j} \right). \tag{3.7}$$

Thus, to satisfy equation 3.7, the initial velocity field in a variable-density flow consisting of two miscible fluids must be given by

$$u_i = -\frac{D}{\rho} \frac{\partial \rho}{\partial x_i}. \tag{3.8}$$

This velocity must be added at a material interface for consistency in numerical simulations of material interfaces in the presence of physical mass diffusion. Otherwise, transient waves are produced until the velocity profile achieves the appropriate form. This approach has been used previously to perform DNS of the decay of isotropic, variable-density turbulence in Sandoval (1995) and also to investigate transition stages of the Rayleigh-Taylor instability between miscible incompressible fluids in Cook & Dimotakis (2001). The present interest lies in extending this idea to

compressible flows. The above analysis is expected to hold for the compressible case only when the pure density of both fluids, ρ_1 and ρ_2, remain uniform in the domain and are not a function of pressure. In this case, the density variations in the domain are solely due to variations in composition. Thus equation 3.4 is valid and the same procedure can be followed to obtain as that given by equation 3.8. The above analysis fails when the density of each fluid changes due to the pressure variations, for instance in the case of Rayleigh-Taylor flows (see chapter V). A different approach is proposed in Section 3.4 for this case.

3.3 The compressible problem with no gravity

In this section, we will numerically study effects of different initial conditions on the temporal evolution of a material interface in the absence of gravity. The initial conditions are

$$\rho_1 = \mu_1 = 1, \quad \frac{\rho_2}{\rho_1} = \frac{\mu_2}{\mu_1} = \frac{M_2}{M_1} = 3, \quad \gamma_1 = \gamma_2 = 1.4, \tag{3.9a}$$

$$L = 20\pi, \quad u = 0, \quad p = T = (2\pi)^2 (\rho_1 + \rho_2), \quad Re = 100, \quad Sc = 1. \tag{3.9b}$$

where ρ is the density, μ the kinematic viscosity, M the molecular weight, γ the specific heats ratio, L the domain length, u the velocity, p the pressure, T the temperature, Re the scaled Reynolds number and Sc the Schmidt number. A diffuse profile is considered and equation 3.3 is used to obtain the density field.

$$Y_1(z) = 1 - \frac{1}{2}\left[1 + \operatorname{erf}\left(\frac{z - z_0}{H}\right)\right], \tag{3.10}$$

where $z_0 = 0$ is the mid-plane location separating the two fluids corresponding to $Y_1 = 0.5$, and $H = \frac{8}{128}2\pi$. In the absence of physical diffusion terms ($Re \to \infty$), the pressure, velocity, and temperature remain uniform in the whole domain as ex-

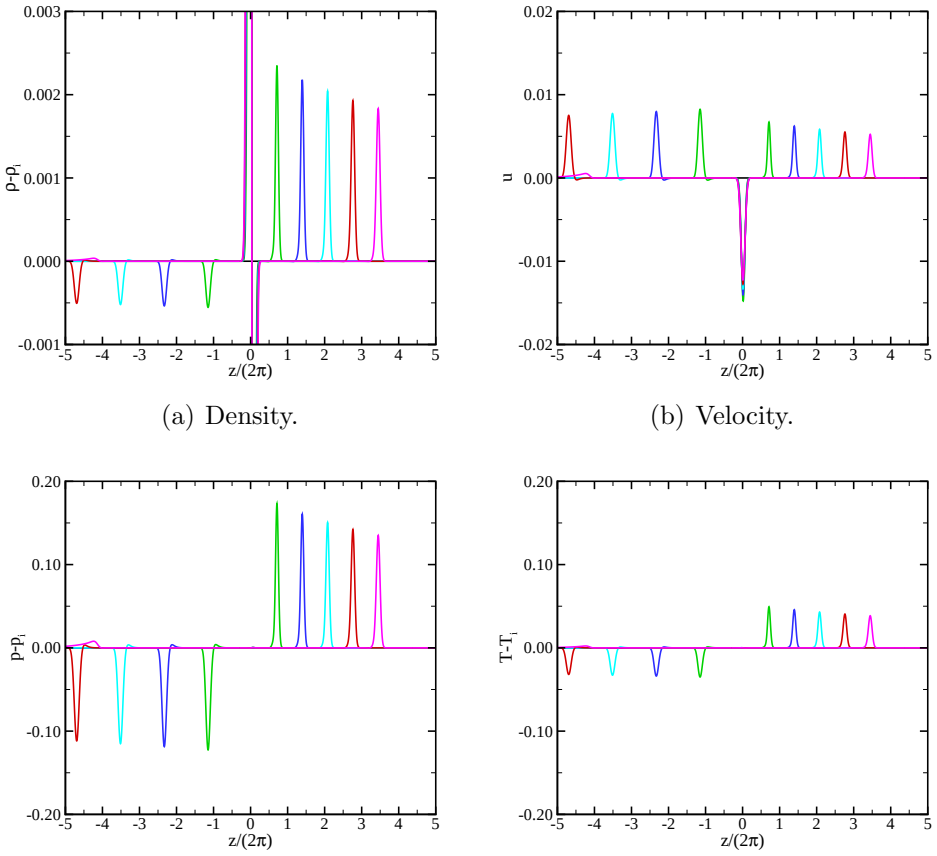

(a) Density. (b) Velocity.

(c) Pressure. (d) Temperature.

Figure 3.1: Time evolution of different quantities in the diffusion of one fluid into the other for $N = 2560$; $t = 0.0$ (black), 0.5 (green), 1.0 (blue), 1.5 (cyan), 2.0 (red), 2.5 (purple).

pected (not shown here). The pressure, velocity, and temperature equilibria are also maintained when only viscous and Fourier heat diffusion terms are considered (but no mass diffusion).

Next, we consider Navier-Stokes simulations with mass diffusion in the absence of a prescribed velocity. Figure 3.1 shows the time evolution of different quantities. The obvious observations are: (i) the velocity profile at the interface takes a profile similar to that of equation 3.8, (ii) two waves moving to the left/right in the light/heavy fluid are generated. The left-moving wave travels faster due to the higher speed of sound in the light fluid. A grid-refinement study reveals that the waves generated at the interface are not a numerical artifact. As the number of points per domain length

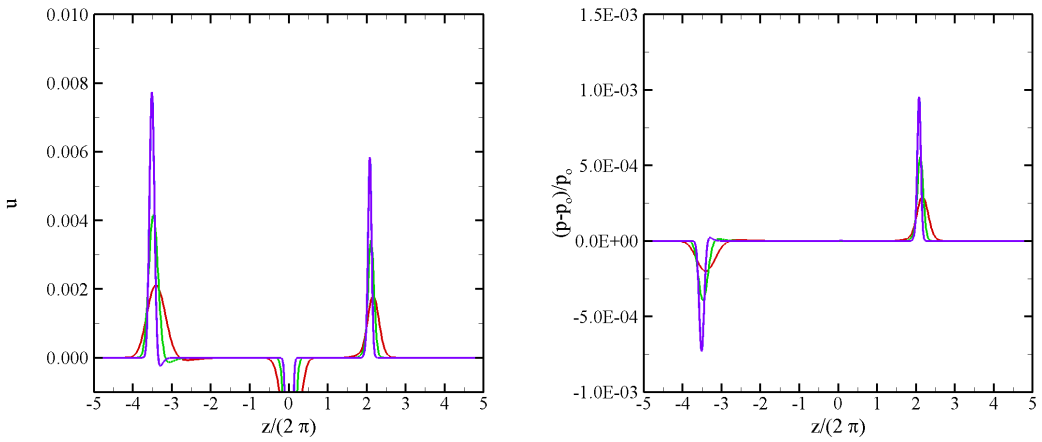

(a) Velocity. (b) Pressure.

Figure 3.2: The relative error for the diffusion of two fluids of different compositions at $t = 1.5$ on different resolutions, N cells per domain length; $N = 320$ (red), 640 (green), 1280 (blue), 2560 (purple).

increases, the amplitude of the generated waves increases while the width of each wave decreases (figure 3.2). These waves, which have different amplitudes and speeds, in practice may get reflected at non-reflecting boundaries and affect the results by either resulting in a net drift or by interacting with dynamical flow features, such as modes in a turbulent field existing in the domain in more complicated set-ups such as the one described in Chapter IV. These issues may deteriorate the quality of DNS results.

Next, we reconsider the same problem with a prescribed initial velocity of

$$u_i = -\frac{1}{ReSc}\frac{1}{\rho}\frac{\partial \rho}{\partial x_i}, \tag{3.11}$$

following Sandoval (1995). Figure 3.3 shows different fields with and without the initial prescribed velocity at $t = 1.5$. Although it appears that this approach eliminates the spurious waves, a more careful inspection indicates that these errors are still present. However, their amplitude is three orders of magnitude smaller. The underlying reason can be understood by considering the momentum equation. By

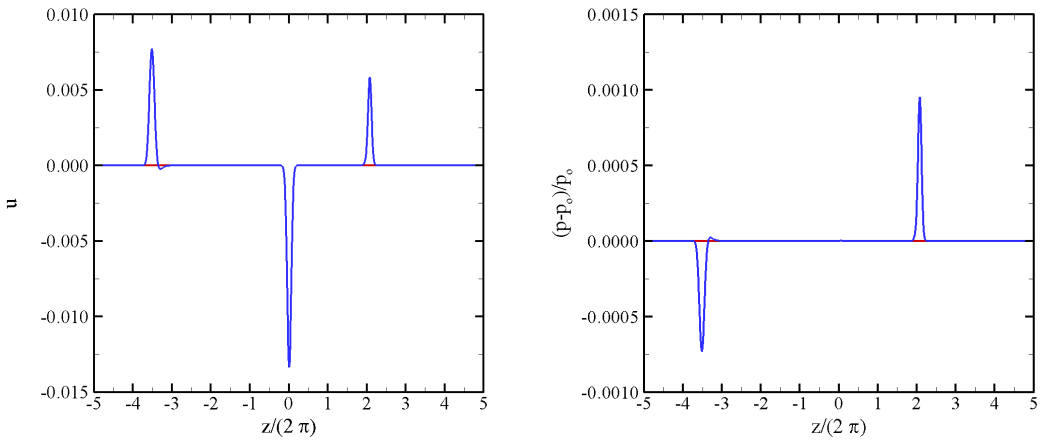

(a) Velocity.

(b) Pressure.

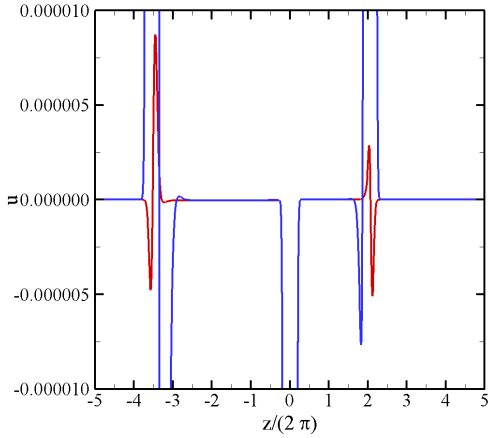

(c) Velocity (zoomed in).

Figure 3.3: The relative error for the diffusion of two fluids of different compositions at $t = 1.5$ for $N = 2560$; Red: with prescribed velocity, blue: without prescribed velocity.

taking the divergence of the momentum equation, one obtains

$$\frac{\partial}{\partial t}\left(\frac{\partial\left(\rho u_j\right)}{\partial x_j}\right)+\frac{\partial}{\partial x_j}\left[\frac{\partial}{\partial x_i}\left(\rho u_i u_j\right)\right]+\frac{\partial^2 p}{\partial x_j \partial x_j}=\frac{\partial}{\partial x_j}\left[\frac{\partial}{\partial x_i}\left(\mu\frac{\partial u_j}{\partial x_i}\right)\right]. \tag{3.12}$$

The first and last terms are identically zero from the continuity equation for single-fluid incompressible flows and one obtains a Poissson equation for pressure. These two terms are not zero for the multiple-fluid compressible case. This suggests that unless the initial pressure field cancels the second and fourth terms, the initial

prescribed velocity generates momentum in the j direction. Therefore, it is expected than an initial varying pressure field must also be prescribed between the two fluids. Considering the problem in one dimension and integrating equation 3.12 twice yields

$$p = p_0 - \rho u^2 + \frac{4}{3Re}\mu\frac{\partial u}{\partial x}. \tag{3.13}$$

where u in this case is the velocity prescribed in equation 3.11. Replacing u from equation 3.11 results in

$$p = p_0 - \frac{1}{\rho}\left(\frac{1}{ReSc}\frac{\partial \rho}{\partial x}\right)^2 - \frac{4}{3Re^2Sc}\mu\frac{\partial}{\partial x}\left(\frac{1}{\rho}\frac{\partial \rho}{\partial x}\right). \tag{3.14}$$

The errors in pressure with prescribing the above pressure field remains at the same level without it (not shown here). Thus we decided to pursue our investigation without adding any prescribed pressure perturbation initially.

3.4 The compressible problem with gravity

Here, we consider the same set-up in the presence of gravity. The mass fraction and density are the same as before. The pressure field is obtained by integrating

$$\frac{dp}{dz} = -\rho g, \tag{3.15}$$

where $g = 1$ is the gravity. The pressure at the mid-plane is set to $(2\pi)^2(\rho_1 + \rho_2)$ as the reference pressure. Similar to the case without gravity, prescribing a velocity in the form of equation 3.11 prevents the generation of unphysical acoustic waves as shown in figure 3.4.

Now, we focus on a material interface in hydrostatic equilibrium in the presence of gravity in an isothermal set-up. An isothermal field is chosen such that heat conduction does not affect hydrostatic equilibrium. The following equations are combined

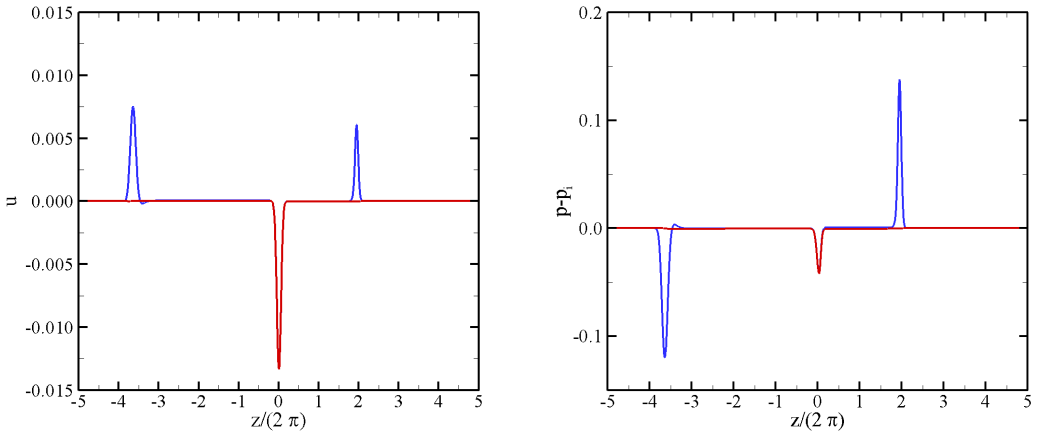

(a) Velocity. (b) Pressure.

Figure 3.4: The profile of different quantities in the diffusion of one fluid into the other at $t = 1.5$ in the presence of gravity for $N = 2560$; Red: with prescribed velocity, blue: without prescribed velocity.

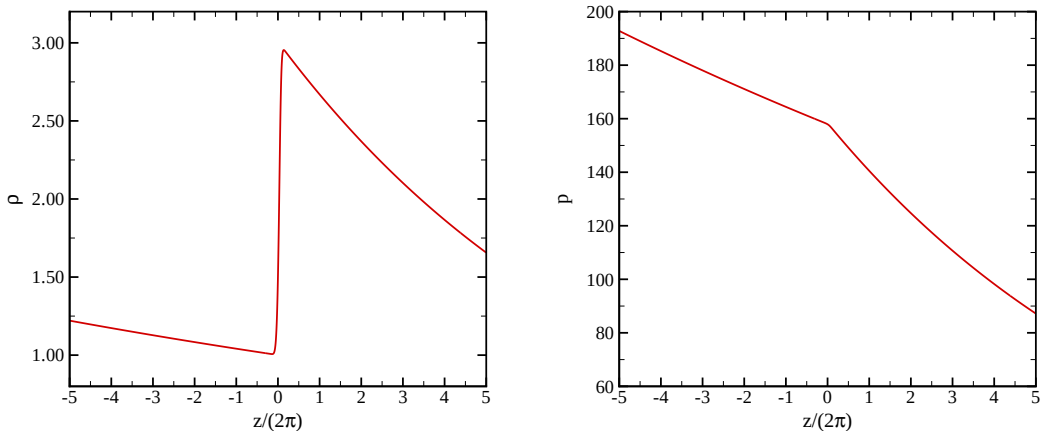

(a) Density. (b) Pressure.

Figure 3.5: Initial profile of (a) density, and (b) pressure in hydrostatic equilibrium.

to obtain the pressure and density in both fluids (Mellado *et al.*, 2005; Olson & Cook, 2007),

$$R = R_0 \sum_{i=1}^{2} \frac{Y_i}{M_i}, \qquad p = \rho R T, \qquad \frac{dp}{dz} = -\rho g. \tag{3.16}$$

The two fluids are modeled as ideal gases with same properties as equation 3.9. The initial density and pressure profiles are shown in figure 3.5. To verify that the boundary conditions are implemented correctly, simulations were performed in the

absence of finite physical diffusion ($Sc \to \infty$) to ensure that the interface remains unperturbed. Figure 3.6 shows that issues similar to those discussed above also arise for the case with gravity. The main differences are (i) the velocity becomes negative/positive between the interface and the left/right moving waves, (ii) temperature increases slightly between the left and right moving waves, (iii) pressure increases slightly between the left and right moving waves and takes a similar profile as velocity at the interface. Generation of these waves can be prevented by prescribing an initial velocity as shown in figure 3.7. For the current set-up with gravity, a velocity in the form of equation 3.17 is considered,

$$u_i = -\frac{1}{ReSc}\frac{1}{M}\frac{\partial M}{\partial x_i}. \tag{3.17}$$

Equation 3.11 cannot be used for the current set-up as the pressure variations here due to the gravity result in corresponding changes in the density. Thus, density variations exist away from the initial mid-plane, where the composition is not expected to change. Using equation 3.11 therefore results in velocity perturbations away from the initial interface. The derivation presented in section 3.2 is no longer valid since ρ_1 and ρ_2 are variable in this set-up due to the changes in the pressure; in particular, equation 3.4 is no longer valid. Instead of the density in equation 3.11, we use the molecular weight as similar relations between the mass fraction and density (equation 3.3) are valid between the molecular weight and the mass fraction (equation 3.18) and since changes in the pressure do not result in any change in the molecular weight,

$$\frac{1}{M} = \frac{1}{M_1} + \frac{1}{M_2}. \tag{3.18}$$

In addition, the velocity perturbations are restricted to the mixing region, unlike equation 3.11 for the current set-up. At a fixed pressure and temperature, $\rho_2/\rho_1 = M_2/M_1$ for two different ideal gases, and equations 3.18 and 3.3 become identical.

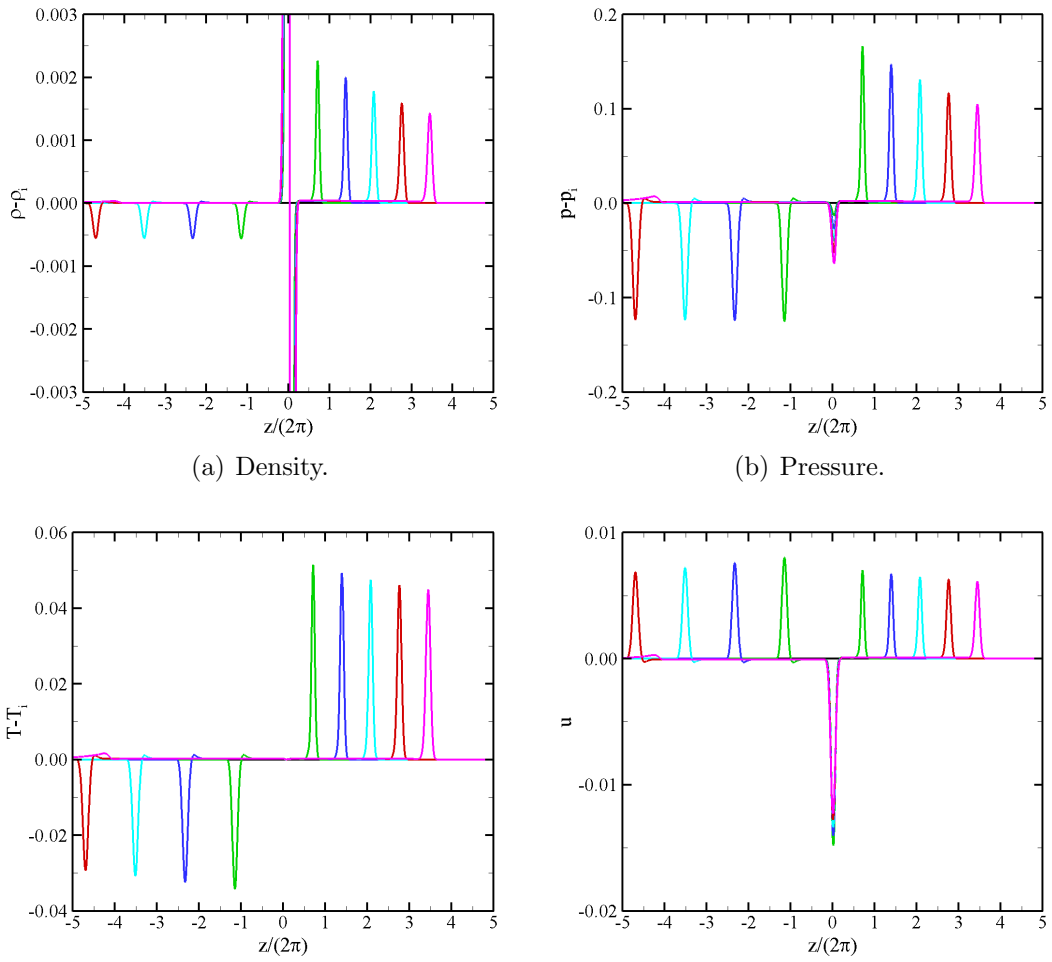

(a) Density.

(b) Pressure.

(c) Temperature.

(d) Velocity.

Figure 3.6: Time evolution of different quantities in the diffusion of one fluid into the other; $t = 0.0$ (black), 0.5 (green), 1.0 (blue), 1.5 (cyan), 2.0 (red), 2.5 (purple) for $N = 2560$. The reference profiles for density and pressure are shown in figure 3.5.

Thus equation 3.17 proposed here for the isothermal set-up reduces to equation 3.11 for the previous set-up considered initially.

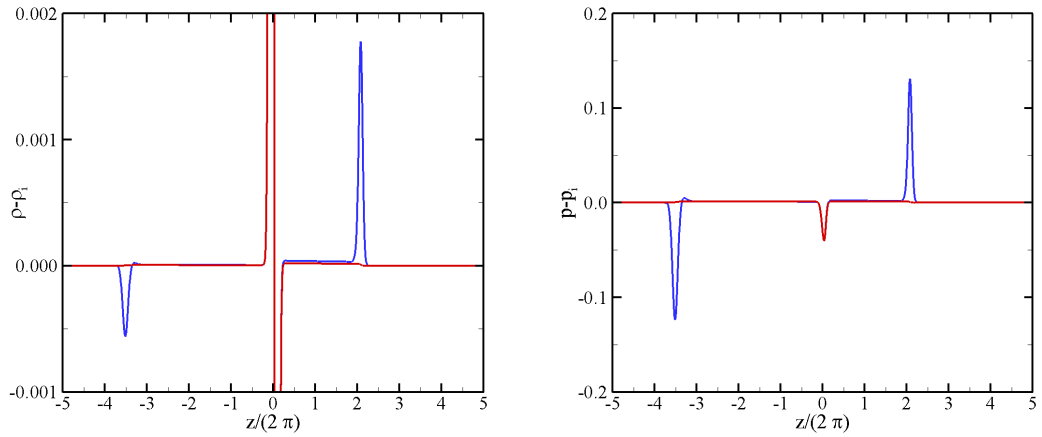

(a) Density.

(b) Pressure.

(c) Temperature.

(d) Velocity.

Figure 3.7: The profile of different quantities in the diffusion of one fluid into the other at $t = 1.5$ for $N = 2560$; with prescribed velocity (red), without prescribed velocity (blue).

CHAPTER IV

The mixing region in freely decaying variable-density turbulence

4.1 Introduction

Turbulence effectively mixes fluids through a multiscale process (Danckwerts, 1952, 1958; Dimotakis, 2005): fluids are entrained at the largest scales, dispersed by eddies of varying sizes until the length and time scales are sufficiently small for viscous, heat and mass diffusion to dominate[1]. Dimotakis (2005) suggests that turbulent mixing can be categorized into three *levels*. Extensive research has been dedicated to understanding mixing of passive scalars (Level-1), which is decoupled from the fluid dynamics (Warhaft, 2000; Sawford, 2001), specifically in the context of dispersion of collections of small particles in turbulent flows, e.g., pollutants, smoke or under certain circumstances clouds. At the other end of the spectrum, Level-3 mixing is characterised by a strong coupling between the fluid dynamics and the composition of the fluids, such as in combustion processes. A variety of problems in atmospheric, oceanic and astrophysical flows lie in between, where the mixing is coupled to the dynamics (Level-2 mixing), e.g., through variations in density and composition, but with little modification to the fluids themselves. A considerable amount of research in Level-2

[1]This chapter is adapted from Movahed, P. & Johnsen, E. 2014*a* The mixing region in freely decaying variable-density turbulence. *submitted to J. Fluid Mech.* .

mixing, the focus of this work, is concerned with hydrodynamic instabilities at interfaces (Chandrasekhar, 1961) driven by acceleration fields (Rayleigh-Taylor), shear (Kelvin-Helmholtz) or shocks (Richtmyer-Meshkov), which may ultimately evolve to turbulence. At the present time, there is no consensus as to whether the resulting turbulence can be described by Kolmogorov-Obukhov ideas (Soulard & Griffond, 2012) or not (Poujade, 2006; Abarzhi, 2010). The lack of understanding of Level-2 turbulent mixing has impeded progress in a variety of problems, e.g., understanding how heavy and light elements mix after the collapse of a supernova (Kifonidis *et al.*, 2006) and the inability to achieve ignition in inertial confinement fusion (Lindl, 1995; Thomas & Kares, 2012).

One of the main difficulties in Level-2 mixing lies in the realisation that the turbulence is not isotropic at all scales, thus preventing direct application of classical Kolmogorov-Obukhov-Corrsin (KOC) theory (Obukhov, 1949; Corrsin, 1951). From a pragmatic viewpoint, the Rayleigh-Taylor instability is a useful model to study anisotropy in turbulence (Cabot & Cook, 2006; Abarzhi, 2010). Large-scale features such as density variations and an acceleration field break the problem symmetry, thus leading to anisotropy. The misalignment of the (hydrostatic) pressure and density gradients at unstably stratified interfaces generates baroclinic vorticity that feeds the instability, which can subsequently lead to fully mixed turbulence through a multi-stage process (Cook & Dimotakis, 2001; Cabot & Cook, 2006). Anisotropy is observed at the integral and Taylor scales in Rayleigh-Taylor turbulence, although the dynamics at the Kolmogorov microscale remain isotropic (Cabot & Zhou, 2013). In these problems, the occurrence of anisotropy is attributable to both the presence of a large-scale density gradient across the mixing region and of gravity. In Rayleigh-Taylor turbulence, these two potential sources of large-scale anisotropy are always present, such that it is not possible to identify the individual contribution of each one on anisotropy. Furthermore, species diffusion in miscible fluids tends to locally

smoothen the density gradient and consequently reduce the local rate of baroclinic vorticity production ($\sim \nabla\rho \times \nabla p$), compared to the immiscible counterpart. Thus, the dynamics in Rayleigh-Taylor turbulence are directly affected by the mixing process, by contrast to passive scalar (Level 1) mixing. In addition, the kinematic viscosities in each fluid may be different, such that the turbulence decays at different rates in each region, another source of anisotropy (Tordella & Iovieno, 2011). These difficulties present challenges for investigating anisotropy in turbulent mixing through the Rayleigh-Taylor instability.

As our first step toward a better understanding of Level-2 mixing in general and Rayleigh-Taylor turbulence in particular, we seek to isolate the effect of a density gradient from that of gravity on the turbulence. In contrast to past studies of RT mixing, we start by neglecting gravity to consider passive scalar mixing, and superpose a density gradient on the initial isotropic field. Statistics of passive scalar mixing are known from numerical and experimental freely decaying (grid) turbulence studies (Warhaft, 2000; Sawford, 2001). In one such set of wind tunnel experiments, Tong & Warhaft (1994) and Jayesh *et al.* (1994) used a conventional grid to generate an initial turbulent field with $30 \leq Re_\lambda \leq 130$, where Re_λ is the initial Taylor-scale Reynolds number, and imposed a linear mean cross-stream temperature gradient upstream of the grid, such that temperature behaves as a passive scalar in this incompressible flow. The scalar spectra in the inertial range approached the expected $-5/3$ slope sooner than those of velocity, and the scalar dissipation was found to be 20% larger in the direction of the temperature gradient. Mydlarski & Warhaft (1998) investigated higher Re_λ (up to 700) by employing an active grid technique to generate the initial turbulent field. Other passive scalar studies in grid turbulence focused on dispersion of a thermal wake behind a heated wire (Stapountzis *et al.*, 1986; Warhaft, 1984; Anand & Pope, 1983), in which case the mean temperature profile was found to be Gaussian, while the variance was not. The mean thermal wake development was

shown to consist of three stages: molecular diffusive ($h \sim t^{1/2}$), turbulent convective ($h \sim t$) and turbulent diffusive ($h \sim t^{1-n/2}$), where h is the mixing region width and n is the time exponent of the kinetic energy decay rate. However, the tunnel was not sufficiently long to reach the expected growth in the final stage. In the context of stably stratified turbulence, Huq & Britter (1995*a*) studied the role of Schmidt number on passive scalar mixing between two layers of different fluids due to grid-generated turbulence in water tunnel experiments. The scalar Taylor microscales were found to be dependent on the Schmidt number, whereas integral scales were not. Huq & Britter (1995*b*) also investigated the evolution of a mixing region starting from an initially sharp interface between two fluids of different densities. The mixing region grew initially due to turbulence diffusion, similar to the passive case, but at later times decreased because of buoyancy effects. In another related study, Lamriben *et al.* (2011) investigated the role of background rotation on freely decaying turbulence in a water-filled rotating tank. By measuring the anisotropic energy flux density and the energy distribution at different scales, it was shown that the anisotropy caused by rotation (i.e., Coriolis force) results in small-scale anisotropy. This result lies in contrast with anisotropy observed in Rayleigh-Taylor turbulence, where the flow remains isotropic at small scales despite the large-scale anisotropy (Cabot & Zhou, 2013).

Recent advances in numerical algorithms and supercomputers have allowed for the use of direct numerical simulation (DNS) to investigate turbulent mixing and compute flow statistics at relatively high Reynolds numbers. For instance, Livescu *et al.* (2000) performed DNS of the experiments of Warhaft (1984), with an emphasis on characterising the development of the scalar wake. Watanabe & Gotoh (2006, 2007) studied inertial-range intermittency under a mean uniform scalar gradient in forced turbulence, focusing on scaling exponents of the structure functions of scalar increments. In freely decaying turbulence, anisotropy may be introduced by manipulating

the initial distribution of kinetic energy even in the context of passive scalar mixing. For instance, Tordella & Iovieno (2006, 2011, 2012) used a problem set-up similar to that of the present work: two adjacent turbulent fields with the same or different integral scale and kinetic energy. When the energy dissipation rate was different in each field, departures from isotropy were found to be large, with higher intermittency in the direction of the energy gradient. At this time, no such studies of anisotropy caused by a density gradient alone have been reported.

In the present work, we seek to advance the fundamental understanding of Level-2 turbulent mixing, by focusing on anisotropy caused by density and composition gradients alone in a freely decaying turbulent field with zero mean velocity. Our goal is to determine the extent to which the large-scale anisotropy in fluid density/composition modifies the phenomenology of the turbulence at different scales. We conduct DNS, in which all scales are resolved, using a novel set-up inspired by Tordella & Iovieno (2011): starting from passive scalar mixing in freely decaying turbulence with no external body force, we impose a density gradient by juxtaposing two fields with different densities. The key novelty lies in matching the dissipation rate in the two fluids to ensure that the turbulence in the entire domain has the same decay, by contrast to Tordella & Iovieno (2011) who considered constant-density fields with different integral scales and kinetic energy. By doing so, we can isolate the effect of the density gradient alone. Due to the existence of this large-scale density gradient, one expects an initially isotropic turbulence field to eventually become anisotropic. However, the responsible mechanisms are not immediately obvious; possibilities include the momentum of large-scale structures during entrainment and molecular diffusion at the small scales. This chapter is organised as follows. The problem description, including the governing equations, the numerical approach and a discussion on the initial conditions used to generate an isotropic turbulent field are presented in Section 4.2. The large-scale dynamics are first investigated in Section 4.3, followed by a study of

the small-scale dynamics in Section 4.4.

4.2 Problem description

4.2.1 Physical model

The three-dimensional compressible Navier-Stokes equations for a binary system of perfect gases describe the problem under consideration, which we solve numerically:

$$\frac{\partial \rho}{\partial t} + \frac{\partial}{\partial x_j}\left(\rho u_j\right) = 0, \tag{4.1}$$

$$\frac{\partial (\rho u_i)}{\partial t} + \frac{\partial}{\partial x_j}\left(\rho u_i u_j + p\delta_{ij}\right) = \frac{1}{Re}\frac{\partial \tau_{ij}}{\partial x_j}, \tag{4.2}$$

$$\frac{\partial E}{\partial t} + \frac{\partial}{\partial x_j}\left[u_j(E+p)\right] = \frac{1}{Re}\left[\frac{\partial}{\partial x_j}(u_i\tau_{ij}) + \frac{\partial}{\partial x_j}\left(k\frac{\partial T}{\partial x_j}\right) + \frac{1}{Sc}\frac{\partial}{\partial x_j}\left(\rho\frac{\partial Y_i}{\partial x_j}\right)(h_1 - h_2)\right], \tag{4.3}$$

$$\frac{\partial (\rho Y_i)}{\partial t} + \frac{\partial (\rho u_j Y_i)}{\partial x_j} = \frac{1}{ReSc}\frac{\partial}{\partial x_j}\left(\rho\frac{\partial Y_i}{\partial x_j}\right), \tag{4.4}$$

where ρ is the density, p the pressure, u_i the velocity, $E = \rho(e + u_i u_i/2)$ the total energy per unit volume, $e = p/\rho(\gamma - 1)$ the internal energy, T the temperature, Y_i the mass fraction of fluid i, k the thermal conductivity, $h = e + p/\rho$ the enthalpy, Re the scaled Reynolds number, Sc the Schmidt number and δ_{ij} the Kronecker delta. The fluids are assumed Newtonian, with viscous stress tensor

$$\tau_{ij} = \mu\left[\left(\frac{\partial u_i}{\partial x_j} + \frac{\partial u_j}{\partial x_i}\right) - \frac{2}{3}\frac{\partial u_k}{\partial x_k}\delta_{ij}\right], \tag{4.5}$$

where μ is the viscosity. The viscosity and thermal conductivity of the mixture are determined from the Herning and Zipper (Reid *et al.*, 1987) approximation for a binary mixture:

$$\mu = \frac{\mu_1 Y_1 M_1^{-1/2} + \mu_2 Y_2 M_2^{-1/2}}{\mu_1 M_1^{-1/2} + \mu_2 M_2^{-1/2}}, \tag{4.6}$$

where M is the molecular weight. The ideal gas equation for a binary mixture reads

$$\frac{p}{\rho} = \frac{\bar{R}T}{M}, \qquad \text{with } \frac{1}{M} = \frac{Y_1}{M_1} + \frac{Y_2}{M_2}, \tag{4.7}$$

where $\bar{R}$ is the universal gas constant. The two fluids may take on different densities, pressures, temperatures, molecular weights, viscosities, and thermal conductivities. The specific heats ratio γ is set to 1.4 for both fluids. The light-fluid density ρ_1, the length $l = L/(2\pi)$ where L is the computational domain width, the velocity $u_{ref} = 1$, the pressure $p_{ref} = \rho_1 u_{ref}^2$ and the light-fluid gas constant $R_{ref} = R_1$ are used for non-dimensionalisation. The Reynolds, Schmidt and Prandtl numbers are related to the scaled variables by

$$Re = \frac{\rho_1 l u_{ref}}{\mu_1}, \quad Sc = \frac{\mu_1}{\rho_1 D}, \quad Pr = \frac{c_p \mu}{k}, \tag{4.8}$$

where D is the mass diffusivity, and c_p is the specific heat at constant pressure, which can be written in terms of R and γ as

$$c_p = \frac{\gamma}{\gamma - 1} R. \tag{4.9}$$

For simplicity, we set $\mu_1 = 1$ and define the scaled Reynolds number, Re, later in equation 4.14 based on the Taylor-scale Reynolds number.

4.2.2 Numerical method

Our numerical code uses explicit finite differences in space to solve the compressible Navier-Stokes equations for multiple fluids. A sixth-order central scheme in the split form approximates the convective fluxes. No artificial dissipation is necessary since the mesh resolutions are sufficiently high to resolve the steep (but not discontinuous) density and mass fraction gradients, as described below. As shown in Movahed

& Johnsen (2013*a*), the advection terms of equations 4.1 are expanded based on the form of Blaisdell *et al.* (1996):

$$\frac{\partial}{\partial x_j}(\rho u_j \phi) = \frac{1}{2}\frac{\partial}{\partial x_j}(\rho u_j \phi) + \frac{1}{2}u_j \frac{\partial}{\partial x_j}(\rho \phi) + \frac{1}{2}\rho\phi\frac{\partial u_j}{\partial x_j}, \tag{4.10}$$

where $\phi = (1, u_i, (E+p)/\rho, Y_i)$. The flux of Ducros *et al.* (2000) is implemented in the split form, which satisfies summation by parts in periodic domains and is discretely conservative. This approach minimises unphysical pile-up of energy at high wavenumbers due to potential aliasing errors. Diffusive terms are discretised in non-conservative form as

$$\frac{\partial}{\partial x}\left(\mu\frac{\partial u}{\partial x}\right) = \mu\frac{\partial^2 u}{\partial x^2} + \frac{\partial \mu}{\partial x}\frac{\partial u}{\partial x}, \tag{4.11}$$

resulting in better accuracy, robustness, spectral representation of diffusive effects at high wavenumbers, and preventing odd-even decoupling (Pirozzoli, 2011). A third-order accurate strong stability preserving (SSP) Runge-Kutta scheme is used for explicit time marching (Gottlieb & Shu, 1998). This approach has been used to investigate late-time mixing in the Richtmyer-Meshkov instability (Movahed & Johnsen, 2011*b*, 2013*a*).

4.2.3 Single-fluid freely decaying isotropic turbulence

We first describe DNS of decaying isotropic turbulence in a single fluid, which constitutes the basis for the initialisation of our multifluid problem. The initial conditions consist of a random solenoidal velocity field inside a triple periodic box of size $2\pi \times 2\pi \times 2\pi$ that satisfies a Batchelor spectrum $E(k) \approx k^4 \exp\left(\frac{-2k^2}{k_0^2}\right)$, where k_0 is the most energetic wavenumber and $\lambda_0 = 2/k_0$ is the initial Taylor microscale (Lee *et al.*, 1991; Johnsen *et al.*, 2010; Movahed & Johnsen, 2013*c*). The density and pressure fields are initially uniform. The turbulent Mach number and Taylor-scale

Reynolds number are defined as

$$M_t = \frac{\sqrt{\langle u_i u_i \rangle_{vol}}}{\langle c \rangle_{vol}}, \quad Re_\lambda = \frac{\langle \rho \rangle_{vol} \, u_{rms} \lambda}{\langle \mu \rangle_{vol}}, \tag{4.12}$$

where

$$u_{rms} = \sqrt{\frac{\langle u_i u_i \rangle_{vol}}{3}}, \qquad \lambda^2 = \frac{\langle u_i^2 \rangle_{vol}}{\left\langle \left(\frac{\partial u_i}{\partial x_i} \right)^2 \right\rangle_{vol}}. \tag{4.13}$$

Here, c is the sound speed, λ is the time-varying Taylor microscale, and $\langle \cdot \rangle_{vol}$ denotes spatial averages over the whole domain. An important time scale of the problem is the eddy turn-over time defined based on the initial properties, $\tau = \lambda_0 / u_{rms,0}$. We relate the initial Taylor-scale Reynolds number, $Re_{\lambda,o}$, and the scaled Reynolds number, Re, as

$$Re_{\lambda,o} = Re \left[\frac{\rho_0 u_{rms,0} \lambda_0}{\mu} \right]. \tag{4.14}$$

The same approach as that discussed in detail in Johnsen *et al.* (2010) is used to generate the initial random field on the finest grid. For a given k_0, the velocity field is generated on the finest mesh ($N^3 = 512^3$) and filtered spectrally to coarser grids. We show sample results for simulations with $k_0 = 4$, $Re_{\lambda,o} = 60 - 200$, and $M_t = 0.1$ in figure 4.1. The initial conditions are not in acoustic equilibrium; this results in a transition period (up to $t/\tau \approx 2$) during which the energy is redistributed across scales to achieve a state of turbulence. The enstrophy increases as the fluctuations in the thermodynamic variables representing the different turbulent modes (acoustic, vorticity and entropy) reach this equilibrium state (Monin & Yaglom, 1975). The skewness of velocity derivatives, defined as

$$S = \frac{\left\langle \frac{1}{3} \left(\frac{\partial u_i}{\partial x_i} \right)^3 \right\rangle_{vol}}{\left\langle \frac{1}{3} \left(\frac{\partial u_i}{\partial x_i} \right)^2 \right\rangle_{vol}^{1.5}}, \tag{4.15}$$

is a measure of the nonlinear equilibrium of turbulence; in our simulations, it ranges between -0.6 and -0.4 at $Re_{\lambda,o} = 60 - 200$, in agreement with previously reported values for physically realistic turbulence (Sreenivasan & Antonia, 1997). Since there is no external forcing providing energy to the turbulence, the total kinetic energy decays due to viscous diffusion, as exemplified by the decrease in turbulent Mach number. In the present work, the Reynolds numbers over the course of the simulations are not sufficiently high for the flow to be deemed fully mixed based on the definition of Dimotakis (2000), as is the case in many past numerical studies of this problem (Lee *et al.*, 1991; Johnsen *et al.*, 2010; Larsson & Lele, 2009; Bhagatwala & Lele, 2011, 2012). In this sense, we do not expect our results to be Reynolds-number independent. Although shocklets may form at sufficiently high M_t and thus require shock capturing, the present focus is on $M_t < 0.4$. For such turbulent Mach numbers, central differences can be used in a stable fashion everywhere for all time. The turbulent kinetic energy spectra for $Re_{\lambda,o} = 100$, $M_t = 0.1$, and $t = 4\tau$ are shown in figure 4.2 for different grid resolutions. These results confirm that the dynamics of all turbulent scales are accurately represented on a grid of $N^3 = 256^3$, which is used for most of the present simulations.

4.2.4 Initial set-up for the multifluid simulations

4.2.4.1 Domain and initial mass fraction field

The computational domain consists of a rectangular parallelepiped of size $L \times L \times 10L$, with $L = 2\pi$ and N points per L on a uniform Cartesian grid (figure 4.3). The velocity field described in Section 4.2.3 is used to initialise the problem. Taking advantage of periodicity, ten such isotropic boxes are juxtaposed in the z-direction to make up the full domain. Boundary conditions are periodic in the x- and y-directions, and non-reflecting with one-sided differences in the z-direction. Although the approach of Thompson (1987) is followed for non-reflecting conditions, numerical errors may

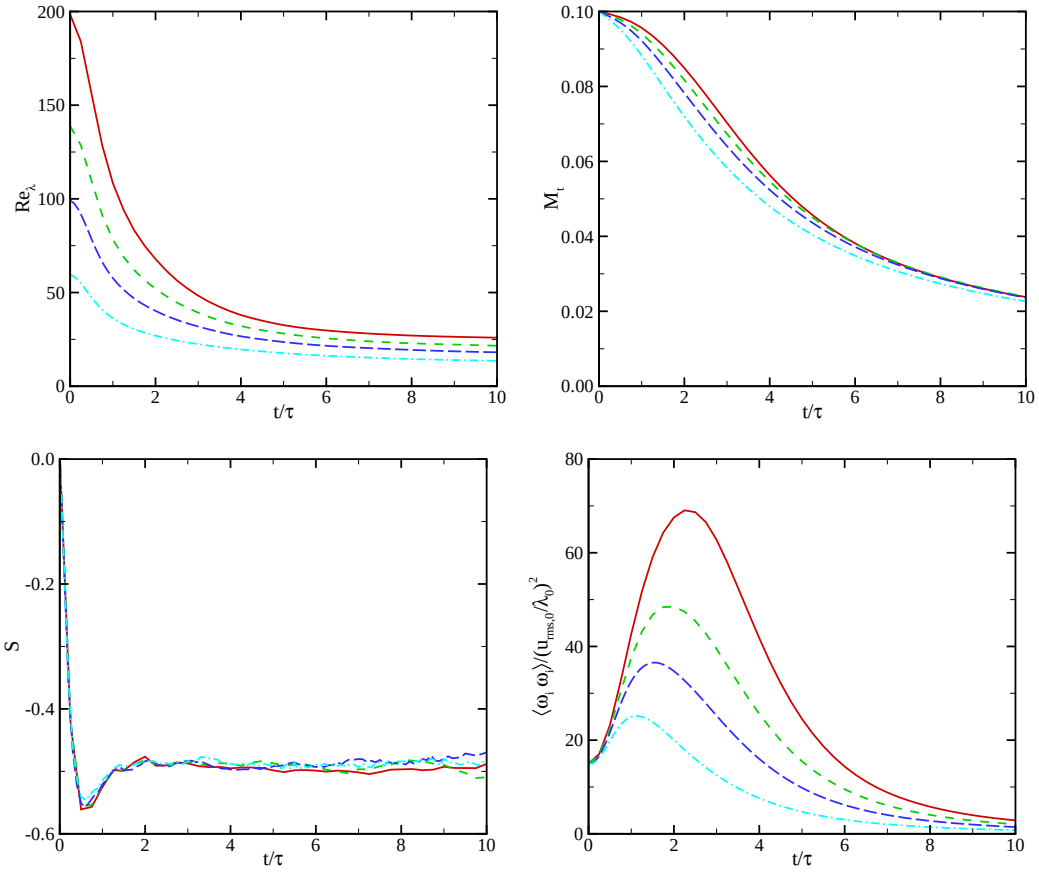

Figure 4.1: Temporal evolution of Re_λ (top left), M_t (top right), skewness (bottom left), and enstrophy (bottom right) for single-fluid decaying isotropic turbulence at $Re_{\lambda,o} = 60$ (cyan), 100 (blue), 140 (green), and 200 (red).

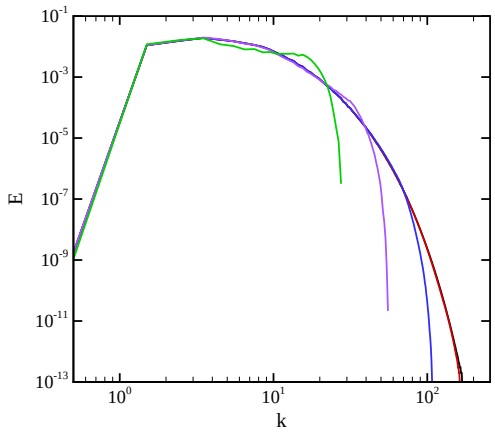

Figure 4.2: Kinetic energy spectra at $Re_{\lambda,o} = 100$, $M_t = 0.1$, $t = 4\tau$, and $N^3 = 32^3$ (green), 64^3 (purple), 128^3 (blue), 256^3 (red), 512^3 (black), where N is the number of grid points per domain width. Note that the red and black curves lie on top of each other.

be generated as turbulence reaches the boundaries. To avoid such difficulties, an error function is used to damp the turbulent fluctuations near the boundaries. The length of the domain ($10L$) in the z-direction was selected to ensure that boundaries have a negligible effect on the evolution of the mixing region near $z = 0$. To prevent generation of unphysical waves at the interface in the presence of finite physical mass diffusion, the following mean velocity is prescribed at the interface (Joseph, 1990; Cook & Dimotakis, 2001),

$$u_i = -\frac{1}{ReSc}\frac{1}{\rho}\frac{\partial \rho}{\partial x_i}. \tag{4.16}$$

While the initial volume-averaged velocity is homogeneous and isotropic, inhomogenity is introduced in the form of composition and density gradients in the z-direction. The initial mass fraction field is generated without any perturbations in the x-y plane:

$$Y_1(z) = \frac{1}{2}\left[1 - \mathrm{erf}\left(\frac{z - z_0}{H}\right)\right], \tag{4.17}$$

where $z_0 = 0$ is the mid-plane location separating the two fluids corresponding to $Y_1 = 0.5$. The value $H = \frac{8}{128}L$ corresponds to the steepest interface profile that

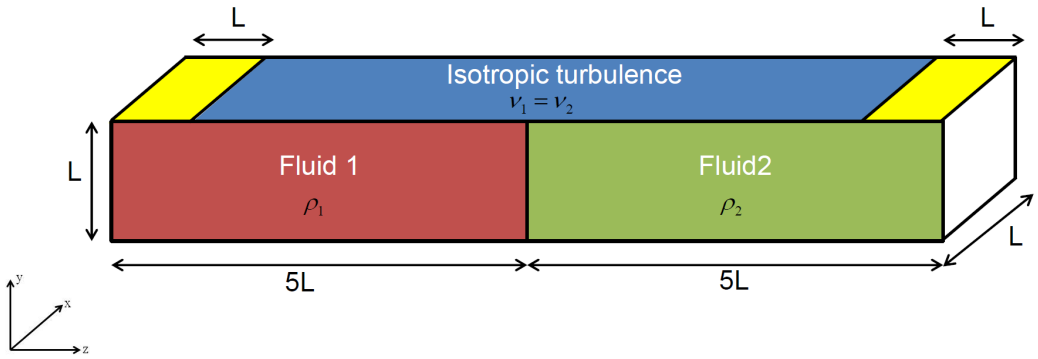

Figure 4.3: Schematic of the initial computational set-up (not to scale). Two fluids of different densities are initially separated by a diffuse unperturbed material interface in the presence of a random initial velocity field that evolves to turbulence.

central differences are capable of resolving in a satisfactory fashion on a $N = 128$ points per L grid, thus avoiding the use of shock capturing and minimising numerical dissipation that would otherwise overwhelm the small turbulent scales (Johnsen *et al.*, 2010). Because of this, the mixing region has a finite initial size. For simplicity, we keep the ratio of the initial thickness of the mixing region to the initial Taylor microscale constant for all simulations. In the current set-up, pressure is uniform initially. To achieve an initially isothermal field and minimise compressibility effects, the properties of the heavy and light fluids are related as follows (Dimonte *et al.*, 2004):

$$\frac{R_2}{R_1} = \frac{M_1}{M_2} = \frac{\rho_1}{\rho_2}, \qquad p_{initial} = T_{initial} = 2\pi L\left(\rho_1 + \rho_2\right). \tag{4.18}$$

In the mixing region, the initial density profile is obtained from the mass fraction field (Cook & Dimotakis, 2001):

$$\frac{1}{\rho} = \frac{Y_1}{\rho_1} + \frac{Y_2}{\rho_2}. \tag{4.19}$$

Figure 4.4 shows the initial mass fraction and density fields for $\rho_2/\rho_1 = 3$.

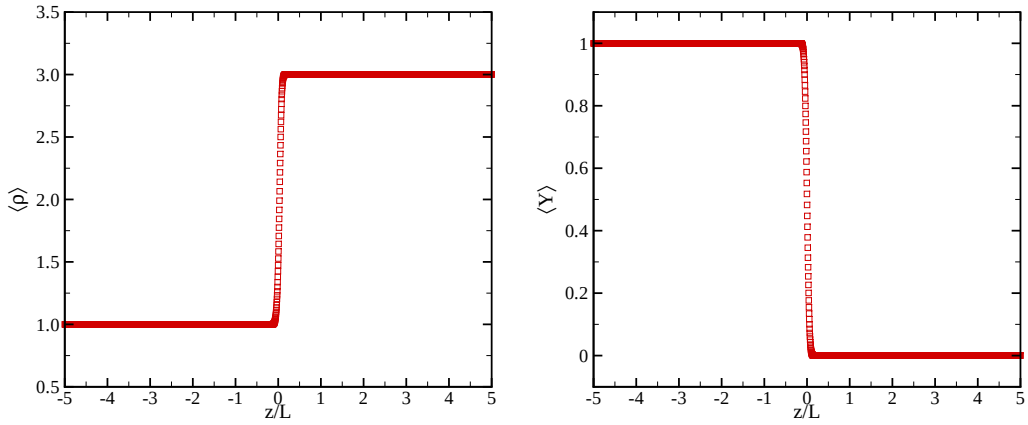

Figure 4.4: Initial mass fraction (left) and density (right) fields for $N = 256$ per L and $\rho_2/\rho_1 = 3$.

4.2.4.2 Matched dissipation rate and key dimensionless parameters

The key turbulent properties in the heavy and light fluids are related as follows:

$$\frac{Re_{\lambda 2}}{Re_{\lambda 1}} = \frac{\rho_2 \mu_1}{\rho_1 \mu_2}, \qquad M_{t2} = M_{t1}\sqrt{\frac{\rho_2}{\rho_1}}, \tag{4.20}$$

with $M_{t1} = 0.1$. Due to the non-dimensionalization, the turbulent Mach number is slightly different in each fluid, but since dilatational dissipation is negligible this discrepancy is not expected to affect the dynamics. Simulations are performed at a Prandtl number of 0.7 and Schmidt number 1.0.

The fluids have different densities and dynamic viscosities, but the density and viscosity ratios are equal such that the kinematic viscosity are the same in both fluids. Since the velocity is initialiased with the same random field in each fluid, the initial Taylor-scale Reynolds numbers are the same in both fluids. Furthermore, we expect the integral quantities representative of the turbulence dynamics, e.g., dissipation rate, enstrophy and turbulent kinetic energy, and relevant length scales (Taylor and Kolmogorov microscales), to evolve in the same way in each fluid, except perhaps in the mixing region (Movahed & Johnsen, 2013*c*; Samtaney *et al.*, 2001). Therefore, the initial condition exhibits anisotropy solely in the composition and density gradients.

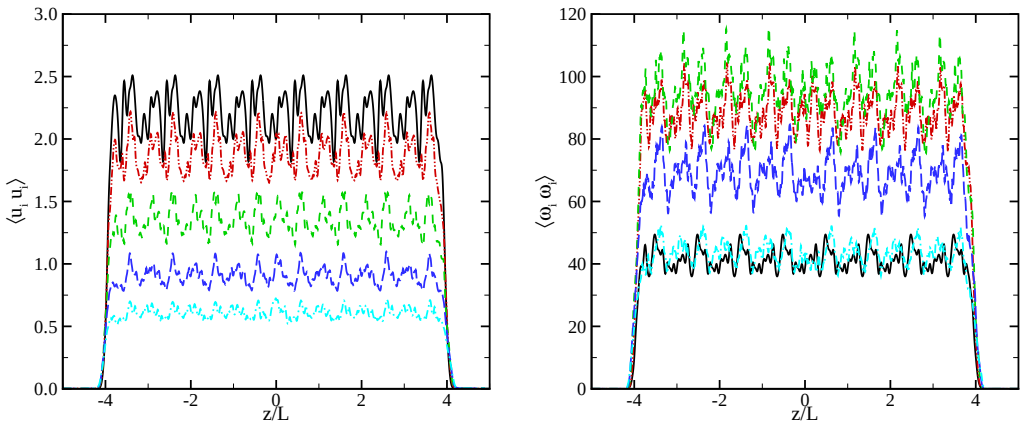

Figure 4.5: Spatial distribution of the average kinetic energy (left) and enstrophy (right) in the x-y plane during the first five eddy turn-over times for $Re_{\lambda,o} = 100$ and $\rho_2/\rho_1 = 3$.

Table 4.1: Summary of the DNS runs with the relevant parameters.

Mixing classification	ρ_2/ρ_1	μ_2/μ_1	k_o	$Re_{\lambda,i}$	N
Level I	1	1	4	60, 100, 120, 140	256
Level I	1	1	4	200	512
Level I	1	1	8	60, 100, 140	512
Level II	3	3	4	60, 100, 120, 140, 200	256
Level II	5	5	4	60, 100	256
Level II	8	8	4	60, 100	256
Level II	12	12	4	60	256
Level II	12	12	4	100	512

Figure 4.5 confirms that the kinetic energy and enstrophy remain nearly uniform in the entire domain apart from slight changes in the mixing region.

The quantities that we vary are the density ratio, $\rho_2/\rho_1 = 1$, 3, 5, 8, and 12, and the initial Reynolds numbers, $Re_{\lambda,o} = 60$, 100, 120, 140, and 200. A density ratio of $\rho_2/\rho_1 = 1$ corresponds to passive scalar mixing, since the other relevant fluid properties are identical. Table 4.1 summarises the simulations runs, along with the relevant parameters.

4.3 Results: dynamics of the large scales in the mixing region

The focus of this section lies in the large-scale dynamics of the mixing region. First, the qualitative behavior is presented (Section 4.3.1). For different density ratios, we consider the evolution of the mixing region width in Section 4.3.2, followed by analysis based on the observation that the growth is self-similar (Section 4.3.3). We finally assess how well mixed the fluids are in Section 4.3.4.

4.3.1 Qualitative behavior of the large scales

We begin by considering the qualitative behavior of the velocity and mass fraction fields. Figure 4.6 shows instantaneous three-dimensional visualisations of the evolution of the turbulent field and mixing region for $\rho_2/\rho_1 = 3$ and $Re_{\lambda,o} = 100$. The normalized Q-criterion is defined as

$$\Lambda = \frac{S^*_{ij}S^*_{ij} - \frac{1}{2}\omega_k\omega_k}{S^*_{ij}S^*_{ij} + \frac{1}{2}\omega_k\omega_k}, \tag{4.21}$$

where $\boldsymbol{\omega} = \nabla \times \mathbf{u}$ is the vorticity and

$$S^*_{ij} = S_{ij} - \frac{\delta_{ij}}{3}S_{kk}, \quad S_{ij} = \frac{1}{2}\left(\frac{\partial u_i}{\partial x_j} + \frac{\partial u_j}{\partial x_i}\right), \tag{4.22}$$

where S_{ij} is the strain-rate tensor. The normalized Q-criterion is used to extract outlines of the turbulent eddies and visualize changes in their morphology. In addition, the eddies are colored by mass fraction to highlight the dynamics and growth of the mixing region. Over the first few eddy turn-over times, ever smaller scales are produced as the initial random field evolves to turbulence. At late times, the smaller eddies have dissipated, leaving the largest ones behind (Pope, 2000). The mixing region grows with time through a turbulent diffusion process, in which heavy eddies near the interface are entrained and dispersed into the light fluid, and vice-versa.

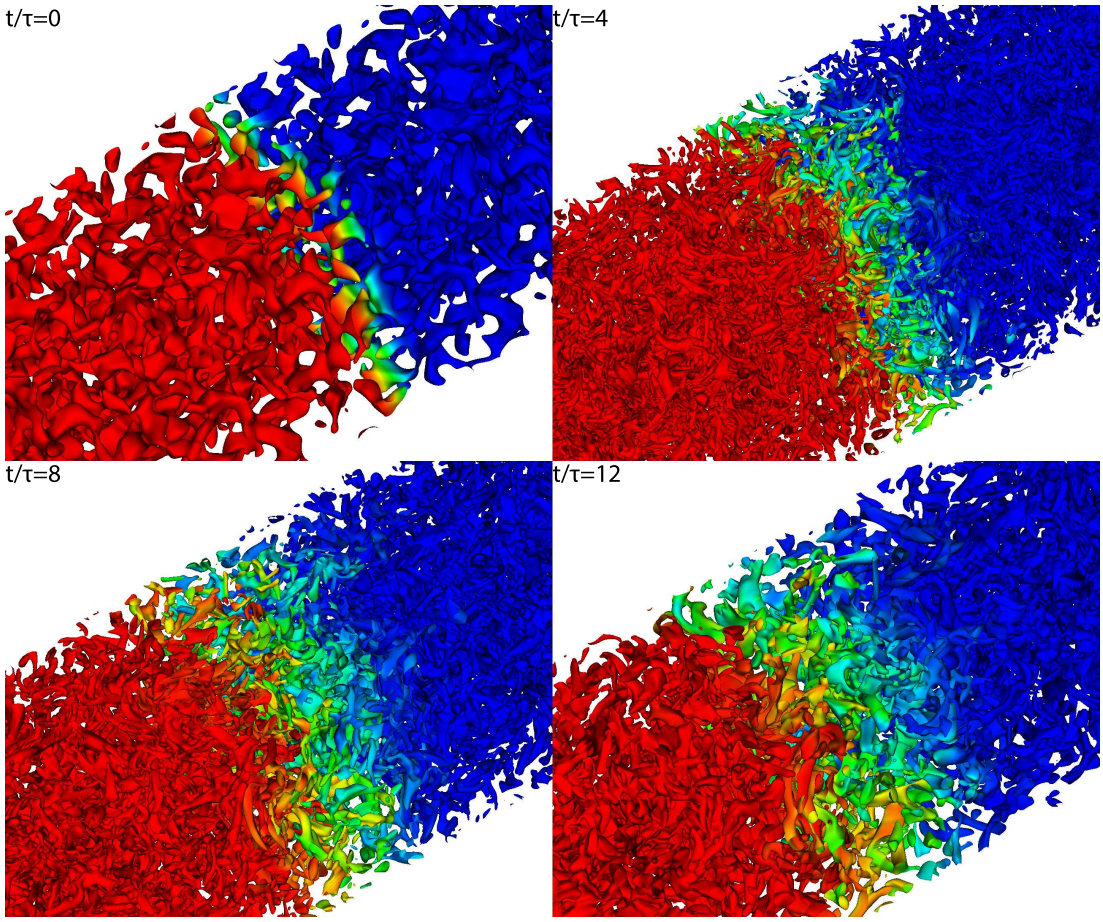

Figure 4.6: Snapshots of turbulent eddies extracted by the normalised Q-criterion colored by mass fraction for $Re_{\lambda,o} = 100$ and $\rho_2/\rho_1 = 3$. Red: light fluid; blue: heavy fluid.

Similar observations can be made by considering instantaneous two-dimensional slices of mass fraction in figures 4.7 and 4.8. As the Reynolds number is increased, smaller-scale features are discernible at a given time; however, it is not immediately clear how the Reynolds number affects the mixing region growth rate. A larger density ratio does not appear to significantly affect the size distribution of the turbulent length scales qualitatively. However, the mean location of the mixing region changes in the plots for different density ratios, i.e., the heavier fluid displaces the lighter; in addition, this process appears to produce a wider mixing region. Although such qualitative results provide useful information, more quantitative measures are necessary, which are investigated in greater detail in the following sections.

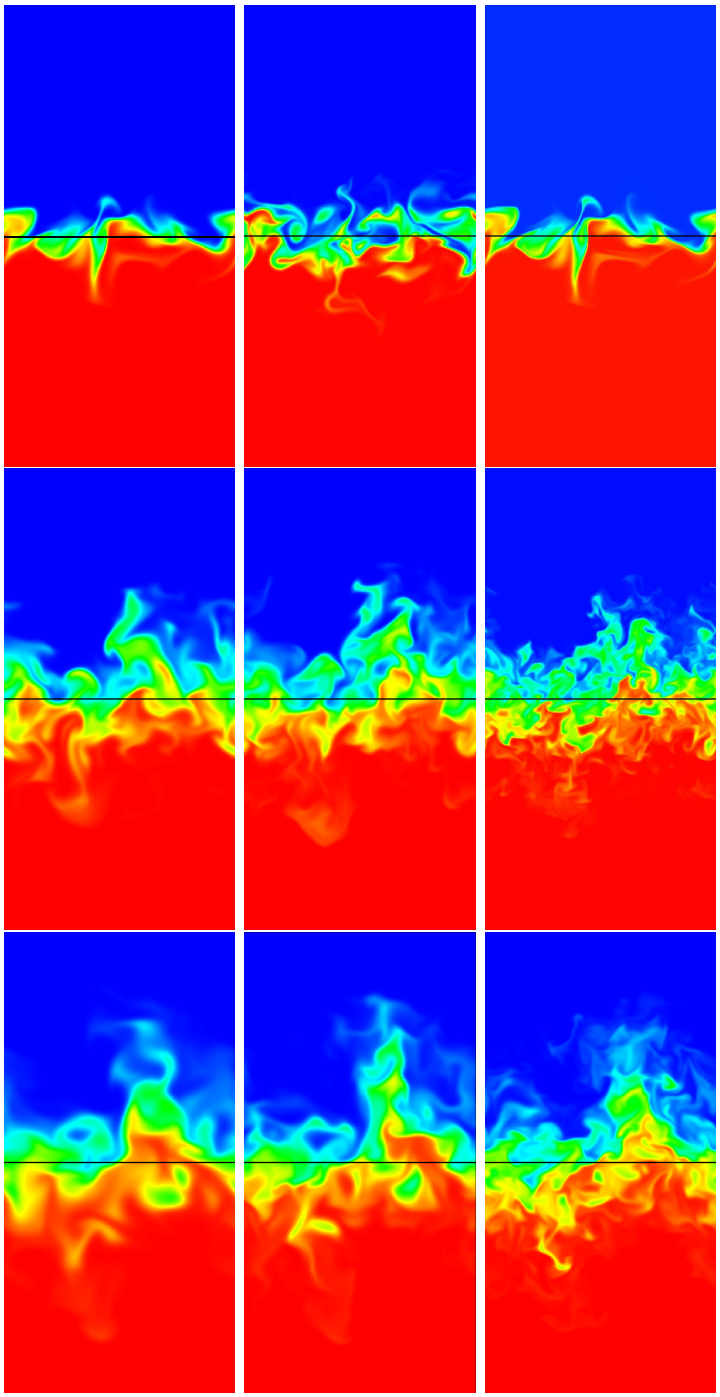

Figure 4.7: Two-dimensional contours of mass fraction in the x-z plane at $t = 1\tau$ (top), $t = 5\tau$ (middle), and $t = 10\tau$ (bottom) for $\rho_2/\rho_1 = 1$ and $Re_{\lambda,o} = 60$ (left), 100 (middle), and 200 (right). The vertical direction corresponds to the direction of anisotropy in the composition (z-direction). Each plot covers an area of $L \times 2L$ and the initial mid-plane ($z = 0$) is located in the middle of the vertical direction. Red: light fluid; blue:heavy fluid.

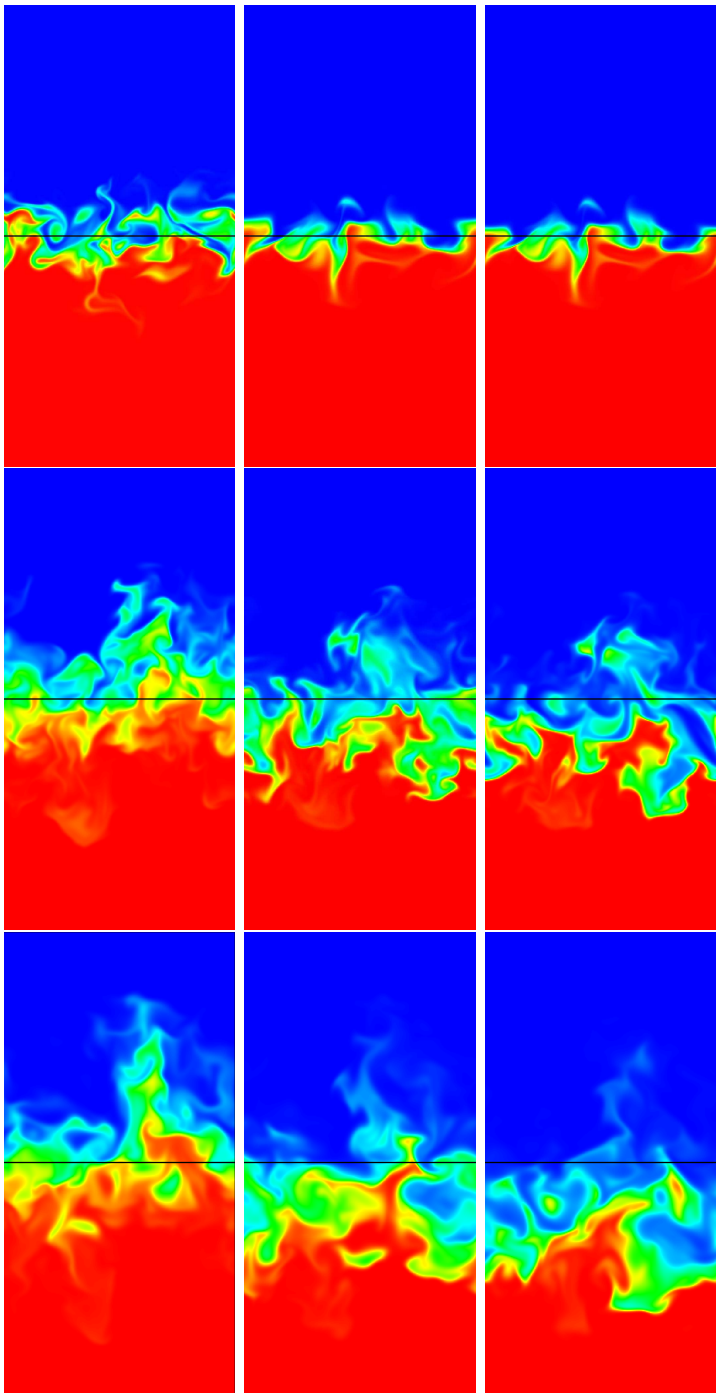

Figure 4.8: Two-dimensional contours of mass fraction in the x-z plane at $t = 1\tau$ (top), $t = 5\tau$ (middle), and $t = 10\tau$ (bottom) for $Re_{\lambda,o} = 100$ and $\rho_2/\rho_1 =$ 1 (left), 5 (middle), and 12 (right). The vertical direction corresponds to the direction of anisotropy in the composition (z-direction). Each plot covers an area of $L \times 2L$ and the initial mid-plane ($z = 0$) is located in the middle of the vertical direction. Red: light fluid; blue:heavy fluid.

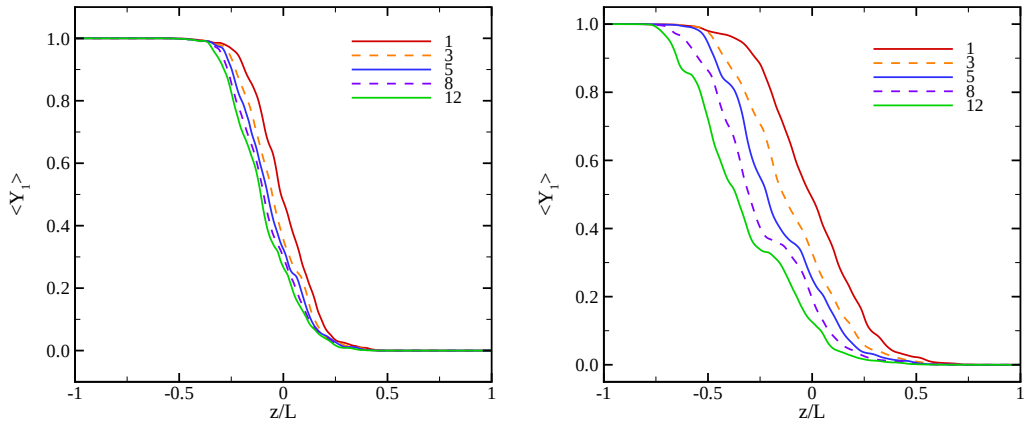

Figure 4.9: Mass fraction profiles at $t = 3\tau$ (left), and $t = 10\tau$ (right) for $Re_{\lambda,o} = 100$, and $\rho_2/\rho_1 = 1$ (red), 3 (orange), 5 (blue), 8 (purple) and 12 (green).

4.3.2 Evolution of the mixing region width

The dynamics in the mixing region are of particular interest. As the fluids mix, the width of the mixing region grows with time. The temporal evolution of the mass fraction varies with density ratio, as shown in figure 4.9. More importantly, the mid-plane corresponding to $\langle Y \rangle = 0.5$, where $\langle \cdot \rangle$ denotes spatial averages in x-y, shifts toward the lighter fluid as the density ratio is increased; we discuss this phenomenon in more detail at the end of this section. This result is important in the context of the Rayleigh-Taylor instability, as the temporal evolution of turbulence statistics is often reported at a fixed location relative to the grid, namely the $z = 0$ plane (Cook & Dimotakis, 2001). The mass fraction is essentially anti-symmetric about $\langle Y \rangle = 0.5$ at low density ratios, but loses this property as the density ratio increases.

We measure the mixing region growth using two approaches. The first, borrowed from Rayleigh-Taylor instability analysis, is based on the notion of spikes/bubbles (masses of heavy/light fluids penetrating the light/heavy fluids). The spike (bubble) amplitude h_s (h_b) is defined as the distance between $\langle Y_1 \rangle \leq 0.99$ ($\langle Y_1 \rangle \geq 0.01$) and the initial mid-plane ($z = 0$). The spikes (bubbles) amplitude growth is due to the penetration of the heavy (light) fluid into the light (heavy) fluid. The amplitude of

the mixing region, h_{amp} is defined as the average of h_b and h_s:

$$h_{amp} = \frac{h_s + h_b}{2}. \tag{4.23}$$

Figure 4.10 shows that over the first two to three eddy turn-over times different density ratios do not produce very different h_s or h_b; bubbles and spikes grow with the evolving velocity field. After that point, the growth of the bubbles and spikes strongly depend on the density ratio. The increase in spike amplitude can be explained via momentum considerations. In the absence of gravity and with increasing ρ_2/ρ_1, an eddy in the heavy fluid has higher momentum than the corresponding volume of light fluid, such that it is easier for the heavy fluid to displace the light fluid and penetrate it. The same dependence on the density ratio (through the Atwood number) has been observed in Rayleigh-Taylor instability (Cook & Dimotakis, 2001). The asymmetry in bubble/spike growth in the absence of gravity suggests that such momentum considerations are important factors in the asymmetric growth observed in Rayleigh-Taylor instability as ρ_2/ρ_1 is increased, rather than gravity effects alone. As a result, the mean position of the interface moves toward the light fluid and is amplified with higher density ratio, an observation confirmed by monitoring the location in z of the $\langle Y \rangle = 0.5$ plane (figure 4.11). To illustrate this point, we extend the analysis of Tordella *et al.* (2008) to variable-density flows. Assuming that the dilatation is small in our problem, the averaged momentum equations can be written:

$$\frac{\partial \overline{\rho u_i}}{\partial t} + \frac{\partial}{\partial x_j}\overline{\rho u_i u_j} = -\frac{\partial \bar{p}}{\partial x_j} + \frac{\partial}{\partial x_j}\overline{\left(\mu \frac{\partial u_i}{\partial x_j}\right)}, \tag{4.24}$$

where the bars denote the mean. Since there is no mean pressure gradient, the z-momentum equation for the mean reduces to:

$$\frac{\partial}{\partial t}\overline{\rho w} = -\frac{\partial}{\partial z}\overline{\rho w^2} + \frac{\partial}{\partial z}\overline{\mu \frac{\partial w}{\partial z}}. \tag{4.25}$$

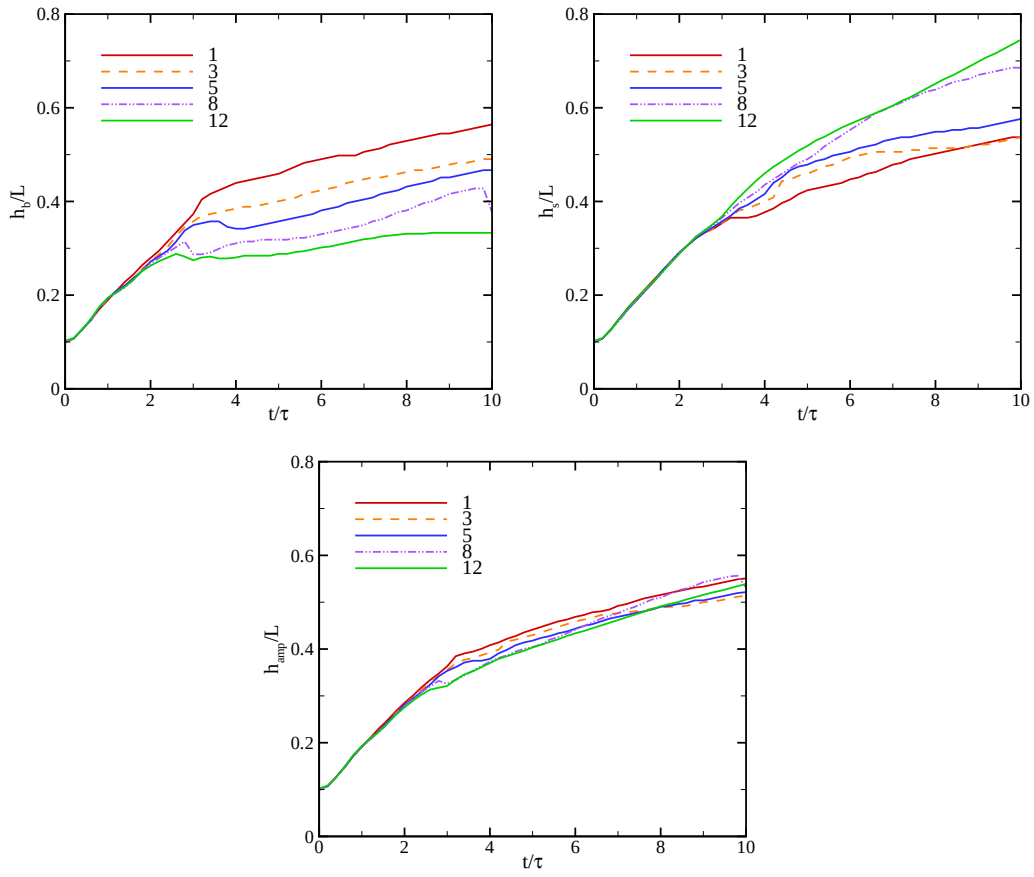

Figure 4.10: Temporal evolution of h_b, h_s and h_{amp} for $Re_{\lambda,o} = 100$, and $\rho_2/\rho_1 = 1$ (red), 3 (orange), 5 (blue), 8 (purple) and 12 (green).

Initially, the mean momentum is zero. Since the last term is diffusive, the mean momentum in the z-direction becomes negative for a positive density gradient, such that the mean interface location moves in the negative z-direction, thus confirming the simulations results. Over the range $1 \lesssim t/\tau \lesssim 4$, the mean interface location appears to move at an approximately constant velocity proportional to the Atwood number, though the explicit dependence is not straightforward. While this motion results in a greater asymmetry in bubble and spike as the density ratio increases, it does not have a clear effect on the total mixing width ($2h_{amp}$) as the asymmetry is deemphasized when averaging the bubble and spike growth in equation 4.23. For $4 \lesssim t/\tau \lesssim 6$, the higher density ratios lead to a smaller h_{amp}; no clear pattern emerges thereafter.

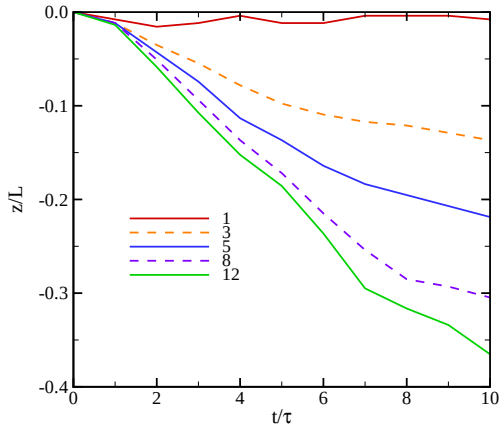

Figure 4.11: Temporal evolution of the $\langle Y \rangle = 0.5$ plane in z for $Re_{\lambda,o} = 100$, and $\rho_2/\rho_1 = 1$ (red), 3 (orange), 5 (blue), 8 (purple) and 12 (green).

The second measure of mixing region width is defined as

$$h = 2 \int_{-\infty}^{\infty} \min\left(\langle Y_1 \rangle, \langle Y_2 \rangle\right) dz, \tag{4.26}$$

and is preferred for analyzing the growth rate compared to equation 4.23 since it has the advantage of avoiding dependence on statistical fluctuations (Cook & Dimotakis, 2001; Cabot & Cook, 2006; Cabot & Zhou, 2013). Figure 4.12 shows h for different ρ_2/ρ_1. In this case, a larger density ratio contributes to a larger mixing region width, consistent with the contour plots in Section 4.3.1. The growth of h defined in equation 4.26 is analysed in the next section.

4.3.3 Self-similarity and scaling of the mixing region width

The scaling of the mixing region width h with time is a quantity of practical engineering importance. With the present problem set-up, turbulent diffusion of a passive scalar, i.e., $\rho_2 = \rho_1$, is expected to be a self-similar process with the same growth rate in each z-direction since the dissipation rate, and thus the turbulence, are identical in each fluid. This behavior is confirmed for all density ratios by plotting the average mass fraction field as a function of the similarity variable $\xi = z/h$ in figure

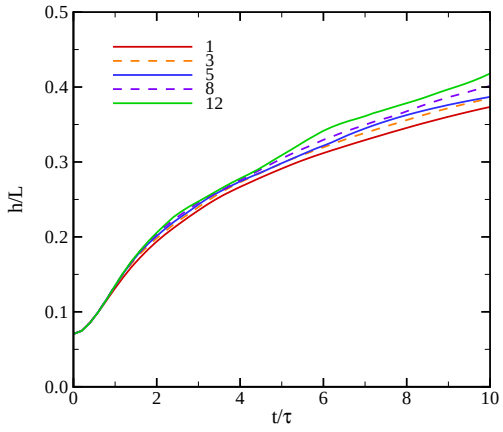

Figure 4.12: Temporal evolution of the mixing region width h based on equation 4.26 for $Re_{\lambda,o} = 100$, and different ρ_2/ρ_1.

4.13. As the density ratio is increased, self-similarity is still observed, though it takes longer to develop and in the most mixed regions ($0.4 \lesssim \langle Y \rangle \lesssim 0.6$) the profiles do not perfectly collapse at the higher density ratios.

We seek to determine the scaling of h with time. This mixing process can be described by one-dimensional (turbulent) diffusion of one fluid into the other:

$$\frac{\partial Y}{\partial t} = \frac{\partial}{\partial z}\left(\kappa \frac{\partial Y}{\partial z}\right), \tag{4.27}$$

where Y is the mass fraction and κ is an effective diffusion coefficient that varies with time and may be Reynolds-number dependent. After integrating equation 4.27 for $z < 0$, and rearranging following Lawrie & Dalziel (2011), we obtain:

$$h\dot{h} = \kappa \left(\frac{\frac{\partial Y}{\partial \xi}\big|_{\xi=0}}{-\int_{-\infty}^{0} Y\,(\xi)\, d\xi} \right). \tag{4.28}$$

Since the expression in parentheses is a constant, $h\dot{h} \sim \kappa$. To determine κ, Prandtl's mixing length theory, $\kappa \sim u_{turb} l_{turb}$, is invoked, where $u_{turb} = u_{rms}$, $l_{turb} = \lambda$ and λ is the Taylor microscale. Since μ/ρ is the same for both fluids, $\kappa \sim Re_\lambda$. Theoretical self-preserving analysis as well as grid turbulence experiments for a decaying isotropic

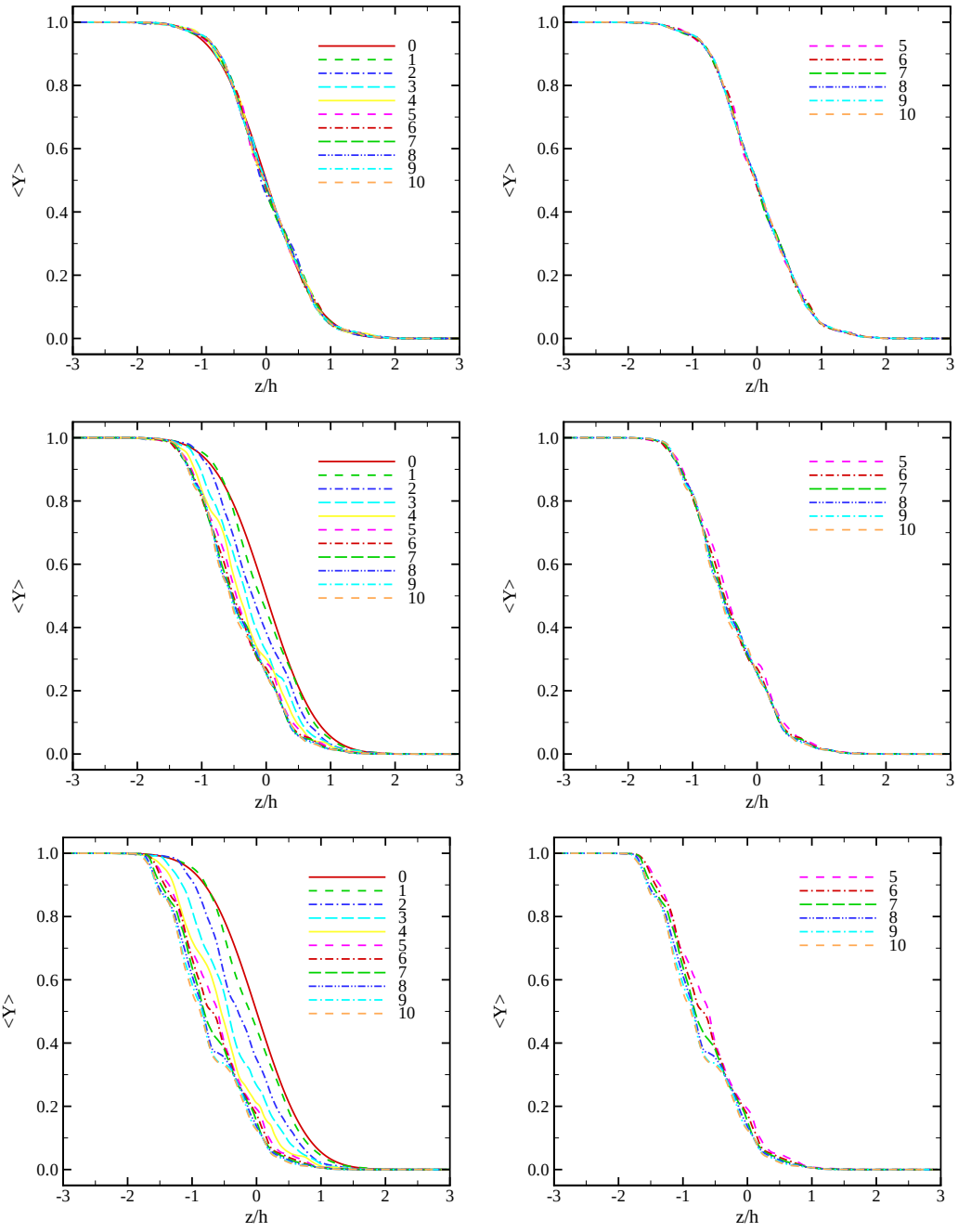

Figure 4.13: Average mass fraction field in the x-y plane at different times for $Re_{\lambda,o} = 100$ and $\rho_2/\rho_1 = 1$ (top), 5 (middle), and 12 (bottom). Left: $0 - 10\tau$. Right: $5 - 10\tau$.

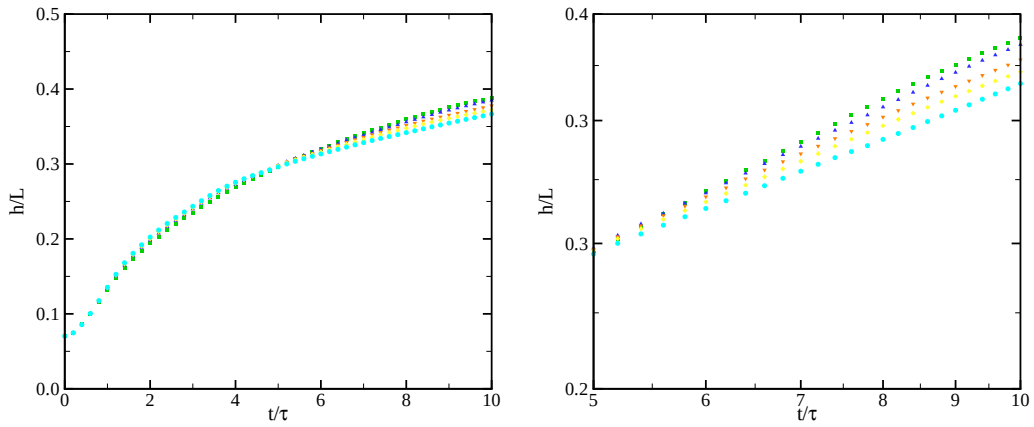

Figure 4.14: Time evolution of the mixing region width (with $\rho_2/\rho_1 = 3$) for $Re_{\lambda,o} =$ 60 (green), 100 (blue), 120 (orange), 140 (yellow), and 200 (cyan). Left: linear-linear; right: log-log.

field (George, 1992) support the following scalings:

$$\lambda \sim t^{1/2}, \qquad u_{rms}^2 \sim t^{-n}. \tag{4.29}$$

Thus, $Re_\lambda \sim t^{(1-n)/2}$. Defining $\alpha = (1-n)/2$, the power law behavior of $Re_\lambda \sim t^\alpha$ yields the following scaling for the mixing region width:

$$h \sim t^{(\alpha+1)/2} \sim t^{1-n/2}. \tag{4.30}$$

We note that according to Dimotakis (2000) the turbulence is not fully developed in the self-similar regime (recall figure 4.1) since Re_λ falls below 100 in our simulations, such that Reynolds-number dependence is expected in this scaling. These observations are confirmed in figure 4.14, although the sensitivity to the Reynolds number is relatively weak. This can be explained by noticing that the difference in Re_λ is less than 25 at any time during the self-similar regime for the present initial Taylor-scale Reynolds numbers ($60 \leq Re_{\lambda,o} \leq 200$). This small change in α does not significantly affect h.

4.3.3.1 High-Reynolds number limit

This analysis can be taken one step further by assuming fully developed turbulence, in which case we can compute the actual exponent based on energy considerations previously used for Rayleigh-Taylor turbulence near bubbles and spikes (Abarzhi *et al.*, 2005). Grid turbulence experiments of decaying homogeneous isotropic turbulence support the following empirical law (Comte-Bellot & Corrsin, 1966) for the velocity fluctuations:

$$\frac{du^2}{dt} \sim -\frac{u^3}{l}, \tag{4.31}$$

where l is the integral scale. A fluid parcel initially at the interface is transported by eddies of different sizes in the fluctuating velocity field u. The largest eddies of size l contribute the most to the growth of the mixing region, thus suggesting a scaling $h \sim l$. This scaling is in agreement with the water tunnel grid-generated turbulence experiments of Huq & Britter (1995*a*). The dynamics of the mixing region can also be related to the fluctuating field as $\dot{h} \sim u$. For the Batchelor spectrum considered here, $u^2 l^5$ is an invariant, which corresponds to conservation of angular momentum (Batchelor & Proudman, 1956). Substituting into equation 4.31 yields:

$$u^2 \sim t^{-10/7}, \qquad h \sim l \sim t^{2/7}. \tag{4.32}$$

This result provides an asymptotic limit for the exponent in fully developed (Reynolds-number independent) turbulence starting from a Batchelor spectrum.

4.3.3.2 Comparison between theory and simulations

The above arguments can be verified by comparing $h(t)$ computed directly from the DNS with that obtained by measuring α from $Re_\lambda(t)$ and substituting into equation 4.30. A power-law least-squares fit to Re_λ in the mixing region is performed to find α at different $Re_{\lambda,o}$. To compute h, we use the regression method of Krogstad &

Davidson (2010). The process relies on a linear best-fit for

$$\ln h = \ln(a) + n \ln(t - t_0), \tag{4.33}$$

where t_0 is the virtual point of origin. Assuming that d_i is the fitted function, for each t_0 the variance can be defined as

$$\sigma^2 = \frac{1}{N-1} \sum_{i=1}^{N} \left[d_i \left(x_i \right) - h \left(x_i \right) \right]^2. \tag{4.34}$$

We consider $t_0/\tau = 0.0$, 0.5, 1.0, 1.5, and 2.0. Since $t_0/\tau = 0.0$ and 0.5 yield the smallest σ^2, we report data corresponding to these two values. As described in Section 4.2.3, it takes approximately 2τ for the initial field to evolve to turbulence; additional time is expected to be required for the mass fraction field to become correlated with the velocity field and result in self-similar growth, as supported by figure 4.13 in which the data collapses well between $5 - 10\tau$. Thus, we pick $t = 5\tau$ as a safe choice for the beginning of the self-similar regime in our analysis and take $t = 10\tau$ as the final time to prevent box-size effects. The growth obtained using the two different approaches (directly from the DNS vs. computing α from Re_λ) is compared in table 4.2 for $\rho_1/\rho_2 = 1$ and table 4.3 for $\rho_1/\rho_2 = 3$, and figure 4.15 shows the exponent of time for different $Re_{\lambda,o}$ and density ratios. Overall, the agreement between the two different approaches to measuring the time exponent is good. The general trend shows that the growth exponent decreases as $Re_{\lambda,o}$ increases, and in fact tends to the asymptotic limit of fully developed turbulence (equation 4.32).[2] The discrepancy

[2]The Batchelor spectrum is commonly used to initialise this problem in numerical simulations and is thus the focus of the present work. Nevertheless, the analysis for fully developed turbulence holds for other spectra, e.g., Saffman's ($E(k) \sim k^2$), in which case $u^2 l^3$ is the flow invariant (Saffman, 1967). Starting from equation 4.31, a Saffman spectrum yields $h \sim l \sim t^{2/5}$. For $Re_{\lambda,o} = 60, 100, 140$ and 200 and a virtual origin of $t_0 = 0$, passive scalar simulations ($\rho_2/\rho_1 = 1$) produce time exponents 0.44, 0.43, 0.39 and 0.37, respectively. Again, similar trends are observed, though the asymptotic limit slightly undershoots the prediction. We note that box-size effects become important earlier due to a more rapid growth with a Saffman spectrum and may thus reduce the measured exponent.

in the growth exponent decreases as $Re_{\lambda,o}$ increases up to 140. The decrease in the growth of the mixing region is related to the higher enstrophy (i.e., dissipation) at higher $Re_{\lambda,o}$ during the self-similar regime. Figure 4.15 suggests that the growth exponent, and thus mixing region width, increases with the density ratio, but the dependence is not absolutely monotonic. As discussed in Section 4.3.2, for a density ratio of one, the mixing region grows symmetrically in both fluids. At higher density ratios, the mixing region grows asymmetrically as an eddy in the heavy fluid has higher momentum than the corresponding volume of light fluid, such that it is easier for the heavy fluid to displace the light fluid and penetrate it. By the same argument, it is more difficult for the light fluid to penetrate the heavy fluid.

Our predicted values are consistent with past results, both experimental and computational. DNS of passive scalar mixing Tordella & Iovieno (2011), in which isotropic turbulent fields with the same Taylor scale but different kinetic energy are juxtaposed, obtained a scaling $h \sim t^{0.33}$ based on multiple simulations with $Re_\lambda = 45 - 150$ after the initial transient (figure 1 of Tordella & Iovieno, 2011). Our set-up is different, since the turbulent fields used here have the same volume-averaged kinetic energy per unit mass $u_{rms}^2/2$ but different kinetic energy per unit volume $\rho u_{rms}^2/2$, which enables us to investigate Level-2 mixing. A $k - \epsilon$ turbulent diffusion model (Anand & Pope, 1983) was used to predict a $t^{0.34}$ growth for experimental wind tunnels studies of the development of a thermal wake in an isotropic grid-generated turbulence behind a heated wire (Warhaft, 1984; Stapountzis *et al.*, 1986) at the last stage of the development of the thermal wake (turbulent diffusive stage). While the model of Anand & Pope (1983) fits the experimental data well, the slope of a power-law fit to the mixing region width does not reach the predicted growth.

Table 4.2: Scaling of h with time for $\rho_2/\rho_1 = 1$, and virtual origins $t_0/\tau = 0.0$, and 0.5. The predicted growth $(\alpha + 1)/2$ is obtained using equation 4.30 by fitting $Re_\lambda \sim t^\alpha$. The observed growth is calculated by performing a direct data fit to h. The same interval $(5 - 10\tau)$ is used in each case to obtain α and the observed growth. The error is defined as (observed growth − predicted growth)/observed growth.

t_0/τ		$Re_{\lambda,o} = 60$	$Re_{\lambda,o} = 100$	$Re_{\lambda,o} = 120$	$Re_{\lambda,o} = 140$	$Re_{\lambda,o} = 200$
0.0	α	-0.420	-0.377	-0.371	-0.371	-0.326
	predicted growth	0.290	0.311	0.314	0.314	0.337
	observed growth	0.383	0.358	0.349	0.327	0.316
	error	24.2%	13.1%	10.0%	4.0%	-6.6%
0.5	α	-0.386	-0.350	-0.345	-0.345	-0.304
	predicted growth	0.307	0.325	0.327	0.327	0.348
	observed growth	0.352	0.333	0.324	0.304	0.293
	error	12.8%	2.4%	-0.9%	-7.5%	−18.8%

Table 4.3: Scaling of h with time for $\rho_2/\rho_1 = 3$, and virtual origins $t_0/\tau = 0.0$, and 0.5. The predicted growth $(\alpha + 1)/2$ is obtained using equation 4.30 by fitting $Re_\lambda \sim t^\alpha$. The observed growth is calculated by performing a direct data fit to h. The same interval $(5 - 10\tau)$ is used in each case to obtain α and the observed growth. The error is defined as (observed growth − predicted growth)/observed growth.

t_0/τ		$Re_{\lambda,o} = 60$	$Re_{\lambda,o} = 100$	$Re_{\lambda,o} = 120$	$Re_{\lambda,o} = 140$	$Re_{\lambda,o} = 200$
0.0	α	-0.409	-0.360	-0.341	-0.353	-0.339
	predicted growth	0.295	0.320	0.329	0.323	0.330
	observed growth	0.393	0.370	0.342	0.325	0.306
	error	24.9%	13.5%	3.8%	0.6%	−7.8%
0.5	α	-0.379	-0.334	-0.317	-0.328	-0.315
	predicted growth	0.310	0.333	0.341	0.336	0.342
	observed growth	0.365	0.344	0.317	0.302	0.284
	error	15.0%	3.2%	−7.6%	−11.3%	−20.4%

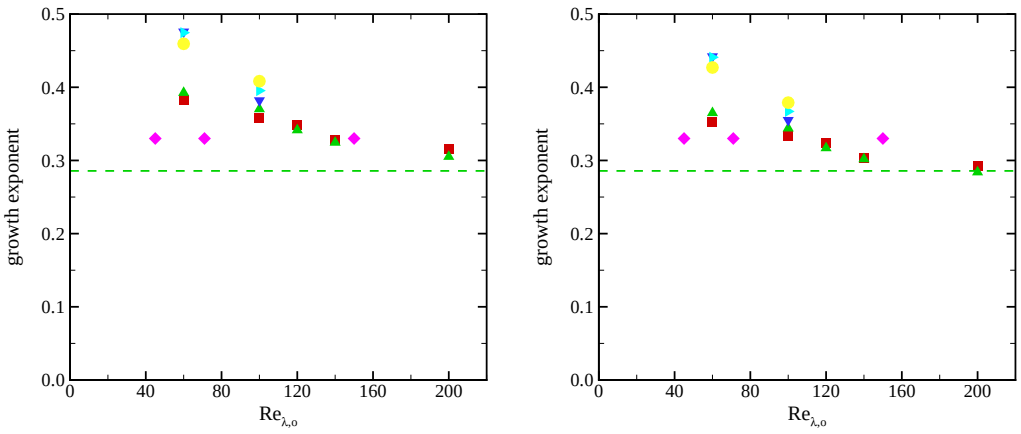

Figure 4.15: Time exponent of the mixing region width computed directly from the DNS: ρ_2/ρ_1= 1 (red), 3 (green), 5 (blue), 8 (cyan), 12 (yellow). Left: $t_0/\tau = 0.0$; right: $t_0/\tau = 0.5$. Purple diamonds: DNS of Tordella & Iovieno (2011); green dashed line: theoretical growth exponent of 2/7 (equation 4.32).

4.3.3.3 Effect of k_o

The ratio of the initial Taylor microscale ($\lambda_o = 2/k_o$) to the domain size L is yet another parameter that enters the problem. In practice, $k_o = 4$ is used commonly in studies of isotropic turbulence (Lee *et al.*, 1991; Johnsen *et al.*, 2010; Larsson & Lele, 2009; Bhagatwala & Lele, 2011, 2012). A higher k_o is desirable to reduce box-size effects, as is sometimes done in Rayleigh-Taylor turbulence (Cabot & Cook, 2006). In addition, putting the initial energy at higher modes allows for a more natural transition to a fully developed state from the initial artificial spectrum, specifically with regards to achieving a spectrum $E(k) \sim k^4$ at low wavenumbers. On the other hand, increasing k_o significantly increases the required grid resolution. We performed most of our simulations with $k_0 = 4$ to resolve all scales on a grid of $N = 256$ per L. Here, we discuss the sensitivity of the results on k_o by considering the passive scalar case ($\rho_2 = \rho_1$) with $k_0 = 8$ and $Re_{\lambda,o} = 60 - 140$ on a grid of $N = 512$ per L. We set the initial thickness of the diffuse interface to be half that used for k_o by doubling H in equation 5.9, such that the ratio of λ_o to the initial mixing thinkness

is the same as for $k_o = 4$. A corresponding self-similar behaviour is also observed for $k_o = 8$, with time exponents 0.335, 0.328, and 0.323 corresponding to $Re_{\lambda,o} =$ 60, 100, and 140, respectively. As for $k_o = 4$, the exponents decrease with increasing $Re_{\lambda,o}$, though at a reduced rate. Compared to the $k_o = 4$ results, the mixing region width at 10τ is half. Furthermore, the self-similar behavior is observed up to 20τ for $k_o = 8$, after which point box-size effects become evident. Thus, if one is interested in studying the problem until times later than 10τ, higher values of k_o should be considered to prevent box-size effects, though at the expense of higher computational cost. The current data fit for $k_0 = 4$ is done for the interval $5\tau < t < 10\tau$ to avoid box size effects and to remain in the self-similar regime. A longer period of self-similar behaviour in time compared to the current work is particularly desirable for a power law fit.

4.3.4 Mixedness

Mixing can be quantified by considering a hypothetical reaction between two pure fluids where the fully mixed fluid is the product corresponding to a stoichiometric mixture of the two fluids (Cook & Dimotakis, 2001). We use mass fraction for convenience instead of volume fraction typically used in the incompressible case. The mass fraction of the mixed fluid is

$$Y_m(Y) = \begin{cases} 2Y & \text{if} \quad Y \leq 0.5, \\ 2(1-Y) & \text{if} \quad Y > 0.5, \end{cases} \tag{4.35}$$

where the stoichiometric coefficient is taken to be 0.5. The mixing region width (entrainment length) is defined as

$$h_m = \int_{-\infty}^{\infty} Y_m(\langle Y \rangle)\, dz, \tag{4.36}$$

where h_m represents the maximum thickness of the product fluid (mixed fluid) if the fluid entrained into the mixing region is perfectly mixed in each x-y plane, thus implying that there are no perturbations from the mean. For a stoichiometric coefficient of 0.5, equation 5.31 reduces to equation 4.26. A measure of mixedness, Ξ, can be defined by comparing the total amount of the product with the maximum possible product as

$$\Xi = \frac{\int_{-\infty}^{\infty} \langle Y_m \rangle \, dz}{h_m}. \tag{4.37}$$

Figure 4.16 shows the temporal evolution of the mixedness in the mixing region. Since no perturbation exists in each x-y plane initially, Ξ starts from unity and decreases as the velocity field perturbs the mass fraction and entrains one fluid into the other, thus creating inhomogeneous regions in x-y. After this transition period, the mass fraction perturbations in x-y decrease. This behavior is due to the decay in the velocity and enstrophy fields, such that the fluid newly entrained into the mixing region is not sufficiently energetic to perturb the mass fraction field. At later times, the variation in Ξ decreases, thus suggesting a balance between molecular diffusion and entrainment from the "edges" of the mixing region. With increasing density ratio, the mixedness decreases owing to the larger density and mass fraction fluctuations. On the other hand, the mixing region width increases because the heavier fluid has a higer momentum (recall figure 4.12). These observations are consistent with the qualitative features of figures 4.7 and 4.8.

4.4 Results: dynamics of the small scales in the mixing region

We now shift our focus to the small scales. To quantify flow isotropy across the different turbulent scales in the mixing region, energy spectra are first considered in Section 4.4.1. Then anisotropy at different length scales is investigated (Section 4.4.2),

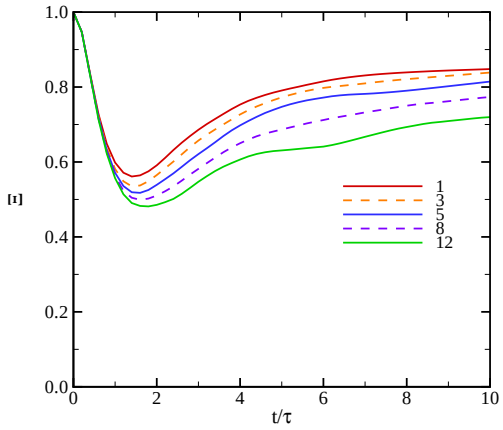

Figure 4.16: Temporal evolution of the mixedness Ξ for $Re_{\lambda,o} = 100$ and different density ratios.

followed by an examination of intermittency in Section 4.4.4. All of the quantities reported in this section are measured well within the mixing zone, in the range $0.25 \leq \langle Y \rangle \leq 0.75$.

4.4.1 Two-dimensional energy spectra

To better understand the energy distribution in the mixing region, the cumulative energy spectra, defined as

$$C_\phi(k) = \frac{\int_0^k E_\phi(k')\,dk'}{\int_0^\infty E_\phi(k')\,dk'}, \tag{4.38}$$

are considered (Mueschke & Schilling, 2009). This quantity measures how the energy is distributed between wavenumbers 0-k, where k is the magnitude of the two-dimensional wave vector k in the x-y plane. At each x-y plane in the mixing region, the two-dimensional energy spectra for each fluctuating field $\phi' = \phi - \langle\phi\rangle$ is calculated and averaged in the z-direction inside the mixing region. Figure 4.17 shows C_ϕ for the velocity, mass fraction, and density fluctuating fields. Since the initial density and mass fraction fields do not contain any perturbations in the x-y planes, C is 1 initially. As turbulence starts to develop from the initial random field, energy gets transferred

to higher wavenumbers. After the initial transition time, the relative distribution of energy between different modes reverses as the turbulence decays.

To determine the effect of the density ratio on the different scales, spectra of density, mass fraction and velocity fluctuations are shown in figure 4.18 for different density ratios at $Re_{\lambda,o} = 100$, and $t = 5\tau$, i.e., during self-similar growth. Increasing the density ratio does not have a significant effect on the mass fraction spectra, but produces larger energies in the density and z-velocity spectra. While the dependence of the z-velocity spectra on the density ratio is due to the different background pressures (equation 5.13), the larger density ratios yield higher density fluctuations across all scales at a given time.

4.4.2 Temporal evolution of the Taylor and Kolmogorov scales

Perhaps the clearest indicator of anisotropy is one based on the calculation of directional length scales in the mixing region, namely Taylor and Kolmogorov scales, λ_i and η_i, respectively, in the ith direction (Cook & Dimotakis, 2001; Cabot & Zhou, 2013):

$$\lambda_i(z,t) = \left[\frac{\langle u_i^2\rangle}{\left\langle\left(\frac{\partial u_i}{\partial x_i}\right)^2\right\rangle}\right]_{mz}^{1/2}, \quad \eta_i(z,t) = \left[\frac{(\nu/Re)^3}{\epsilon_i}\right]_{mz}^{1/4}, \tag{4.39}$$

where

$$\epsilon_i(z,t) = \frac{15\nu}{Re}\left\langle\left(\frac{\partial u_i}{\partial x_i}\right)^2\right\rangle \tag{4.40}$$

is the directional dissipation rate and $[\cdot]_{mz}$ is the average in the z-direction well within the mixing zone, in the range $0.25 \leq \langle Y\rangle \leq 0.75$. In equations 4.39 and 5.34, it is implied that there is no sum in i. By contrast, the overall dissipation is defined

$$\epsilon = \frac{2\nu}{Re}S_{ij}^* S_{ij}^*. \tag{4.41}$$

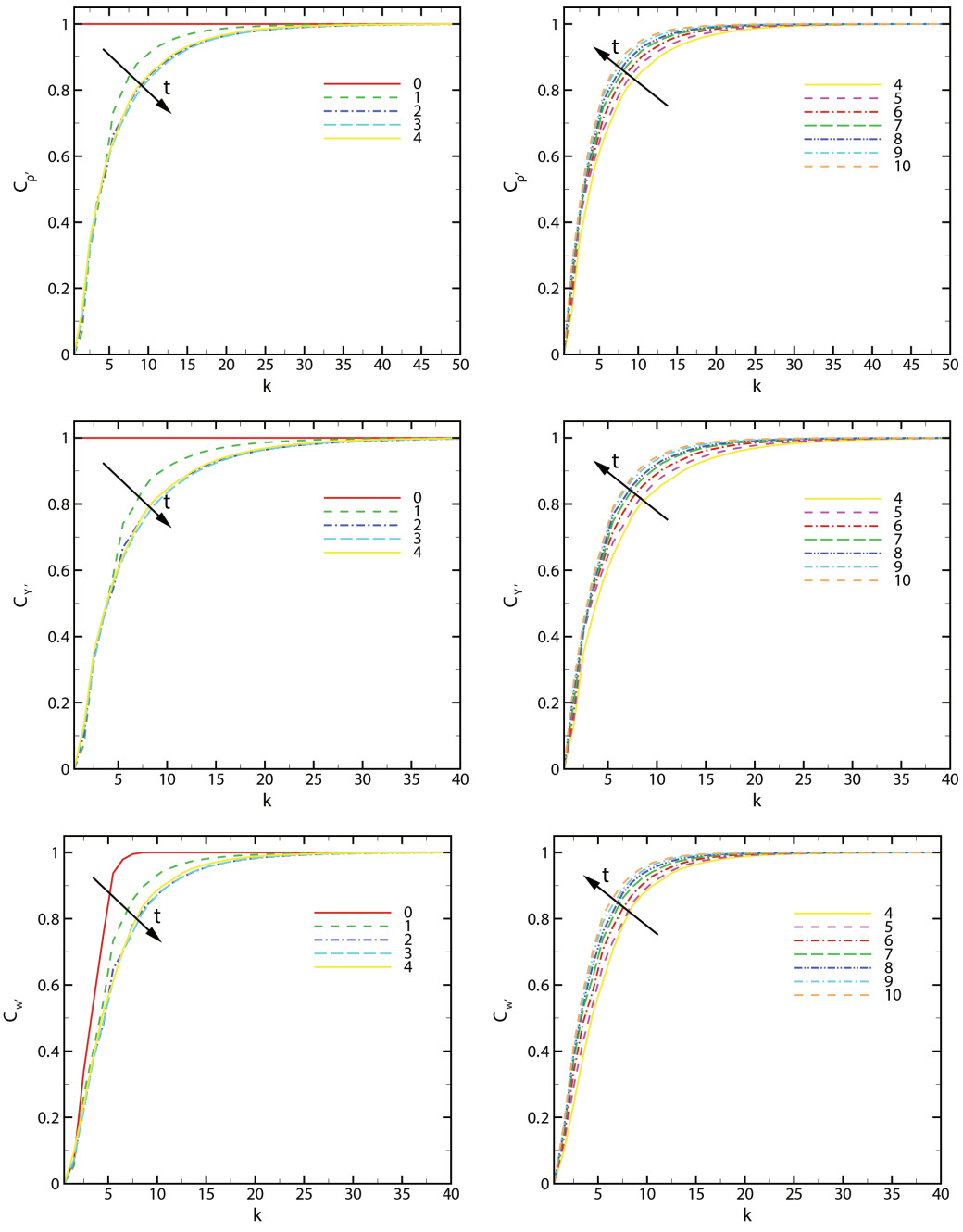

Figure 4.17: Cumulative energy spectra of density, mass fraction, and the vertical velocity fluctuation fields at different times for $Re_{\lambda,o} = 100$ and $\rho_2/\rho_1 = 3$.

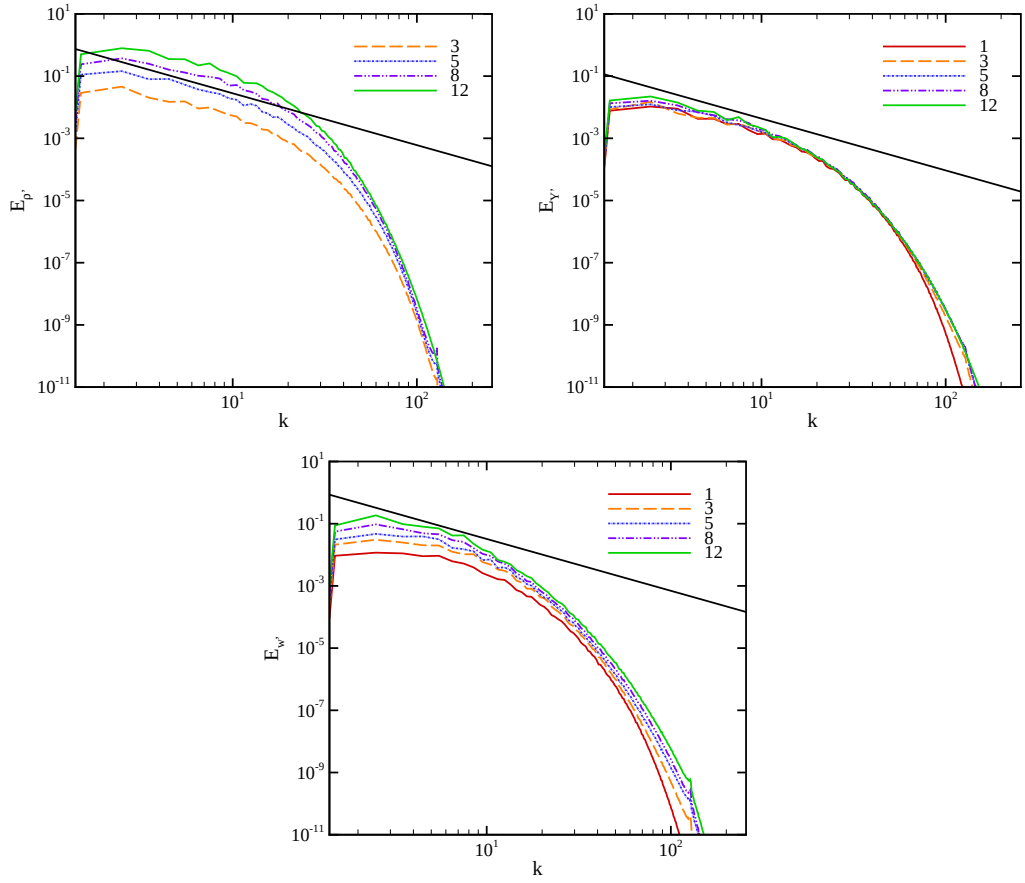

Figure 4.18: Two-dimensional spectra of density, mass fraction and vertical velocity fluctuations for $Re_{\lambda,o} = 100$, $t/\tau = 5$, and $\rho_2/\rho_1 = 1$ (red), 3 (orange), 5 (blue), 8 (purple), 12 (green). The black line corresponds to a -5/3 slope.

Equation 5.34 is commonly used in experiments to measure dissipation as it requires measuring only one of the components of equation 5.35. This definition could raise concerns regarding the accuracy of dissipation measurements, especially in anisotropic fields (Sreenivasan & Antonia, 1997) since equation 5.34 corresponds to equation 5.35, the exact definition of dissipation, only for spherical symmetry in incompressible homogeneous isotropic turbulence. However, this surrogacy issue is not problematic here as equation 5.34 is used solely to measure isotropy at the Kolmogorov scale; the full dissipation is calculated as well.

Figure 4.19 shows the time evolution of the directional Taylor and Kolmogorov scales. During the initial transition period (up to approximately 2τ), the initial energy at large scales gets transferred to the small scales as discussed in the previous section. This energy transfer results in an increase in enstrophy and dissipation, and consequently a decrease in the Taylor and Kolmogorov scales. After the initial transition, the developed turbulent field decays freely, and these length scales increase with time as the smallest scales dissipate the soonest (Pope, 2000).

Considering anisotropy, the general trend in the evolution of the Taylor and Kolmogorov scales are in agreement with grid turbulence experiments and DNS of single-fluid decaying isotropic turbulence. At a modest density ratio ($\rho_2/\rho_1 = 3$), the directional Taylor scales do not exhibit significant anisotropy. As the density ratio increases, the Taylor scale in the z-direction takes higher values relative to the x- and y-directions, representing anisotropy at that scale in the z-direction. This anisotropy also increases with time. The fact that the flow is almost isotropic at the Taylor scale for $\rho_2/\rho_1 = 3$ is particularly important in terms of Rayleigh-Taylor turbulence as many DNS are performed at this density ratio (Cook & Dimotakis, 2001; Cabot & Cook, 2006); typically the anisotropy in the composition/density is considered as one of the main sources of anisotropy in addition to gravity in these flows. At the smallest scales, the turbulence is isotropic despite the large-scale anisotropy in density, as all

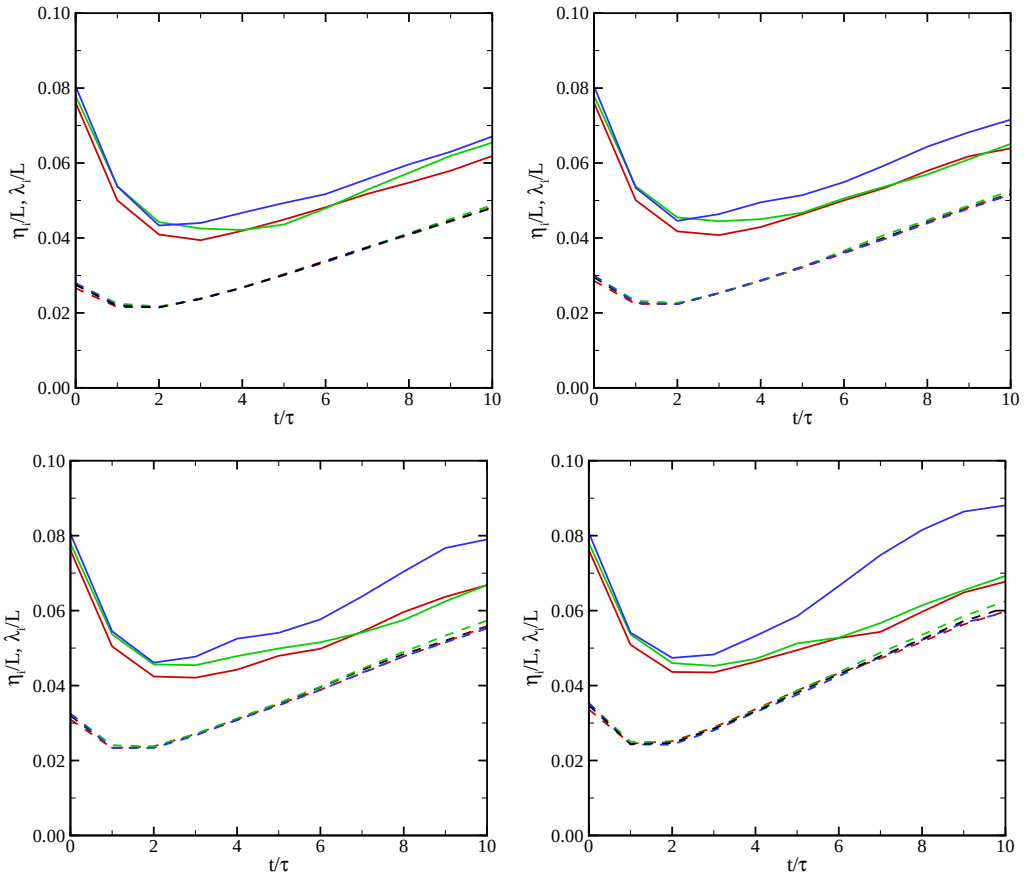

Figure 4.19: Time evolution of the directional Taylor (solid) and Kolmogorov (dashed) scales (solid) for $Re_{\lambda,o} = 100$, $\rho_2/\rho_1 = 3$ (top left), 5 (top right), 8 (bottom left), 12 (bottom (right). Red: x-component; green: y-component; blue: z-component. The Kolmogorov scale used by measuring the full dissipation is also plotted in black.

three curves essentially fall onto each other. In other words, the average dissipation rate is the same in each direction, as expected for an isotropic field.

At the small scales, the growth rate of η_i is essentially the same for all density ratios, thus suggesting that small scales are dissipated at a similar rate. This result is expected since the initial Taylor-scale Reynolds number and dissipation rate are the same across the entire field for all density ratios. The minimum achieved increases slightly with density ratio. Although both sets of length scales increase with time, the growth rate of η_i in time is slightly higher than that of λ_x and λ_y as the density ratio is increased.

Anisotropy of the flow field can be investigated by considering the anisotropy tensor, defined as

$$B_{ij} = \left[\frac{\langle u_i u_j \rangle}{2E} - \frac{1}{3}\delta_{ij} \right]_{mz}, \tag{4.42}$$

where E is the turbulent kinetic energy and $\langle u_i u_j \rangle$ is the ij component of the Reynolds stress tensor. For an isotropic field, $B_{ii} = 0$ since $\langle u^2 \rangle = \langle v^2 \rangle = \langle w^2 \rangle$. For Rayleigh-Taylor turbulence, $B_{11} \approx B_{22} \approx -1/6$ and $B_{33} \approx 1/3$ as $\langle u^2 \rangle \approx \langle v^2 \rangle \approx \langle w^2 \rangle / 4$ (Ramaprabhu *et al.*, 2013). Figure 4.20 shows the temporal evolution of different components of the anisotropy tensor for various density ratios. For a modest density ratio of 3, the three measured components of the tensor remain close to zero, corresponding to a nearly isotropic field. As the density ratio increases, B_{33} also increases, while B_{11} and B_{22} decrease slightly. For a density ratio of 12, B_{33} reaches a high value of 0.17 at late times, representing large-scale anisotropy by the current measure. This behaviour is in agreement with the large-scale anisotropy observed for the directional Taylor microscale in the direction of the initial large-scale anisotropy.

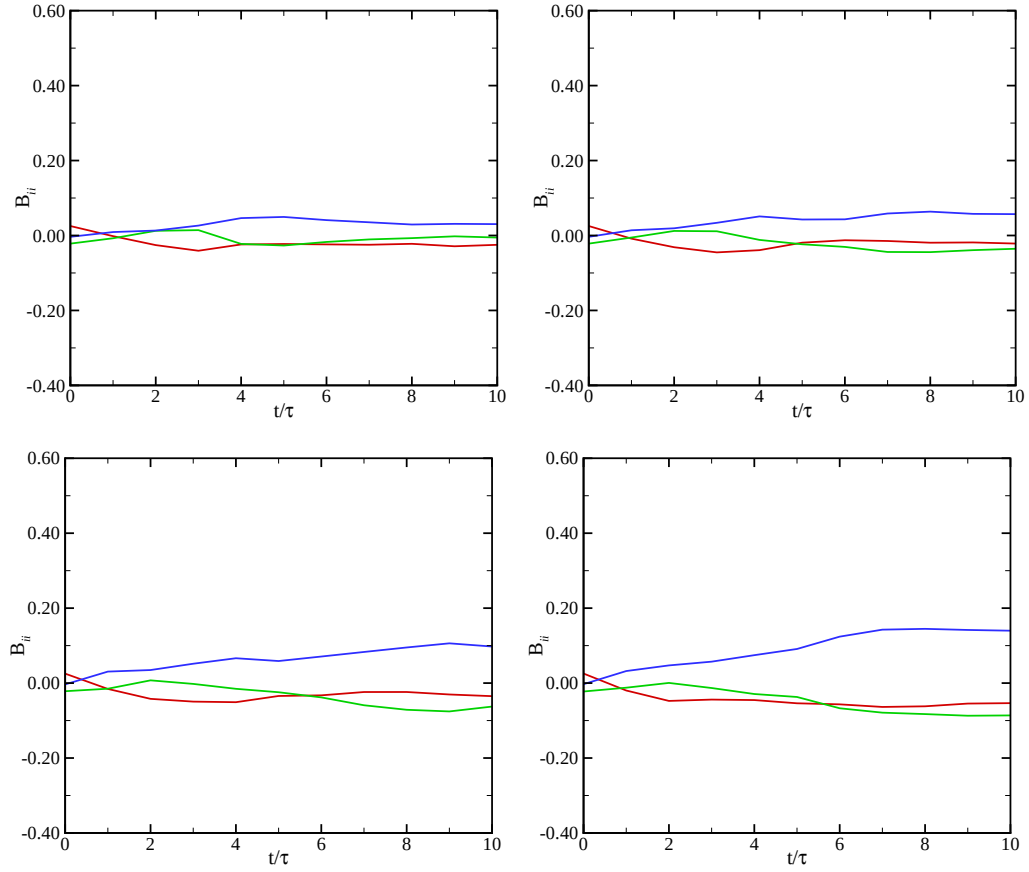

Figure 4.20: Time evolution of the anisotropy tensor for $Re_{\lambda,o} = 100$, $\rho_2/\rho_1 = 3$ (top left), 5 (top right), 8 (bottom left), 12 (bottom (right). Red: x-component; green: y-component; blue: z-component.

4.4.3 Temporal evolution of the relevant length scales in the mass fraction field

Similar ideas can be used to examine isotropy in the mass fraction field. The directional Corrsin scale is given by (Monin & Yaglom, 1975; Antonia *et al.*, 2013):

$$\lambda_i^Y = \left[\frac{\langle Y'^2 \rangle}{\left\langle \left(\frac{\partial Y'}{\partial x_i} \right)^2 \right\rangle} \right]_{mz}^{1/2}, \tag{4.43}$$

and the directional turbulent scalar dissipation is defined as

$$\chi_i = \left[\frac{6}{ReSc} \left\langle \left(\frac{\partial Y'}{\partial x_i} \right)^2 \right\rangle \right]_{mz}. \tag{4.44}$$

Based on dimensional arguments, the corresponding directional dissipation length scale is $\eta_i^Y \sim (ReSc)^{-3/4} \chi_i^{-1/4}$. These quantities are shown in figures 4.21 and 4.22, along with the mass fraction fluctuations in figure 4.23. By contrast to the length scales relevant to the velocity field, the current results suggest that the mass fraction field remains isotropic from the dissipation scale to the Corrsin scale, for a fixed density ratio. Given that the Corrsin microscale represents the large-scale mass fraction fluctuations, higher values are observed as both the mass fraction fluctuations and the mixing region width are larger at higher density ratios. This phenomenon can be explained by the higher mass fraction fluctuations at higher density ratios, which lead to higher dissipation rates. The Corrsin scale is 10 times smaller than the Taylor microscale of the velocity field, which suggests that resolution requirements to resolve the Corrsin microscale accurately are much higher than those for the Taylor microscale.

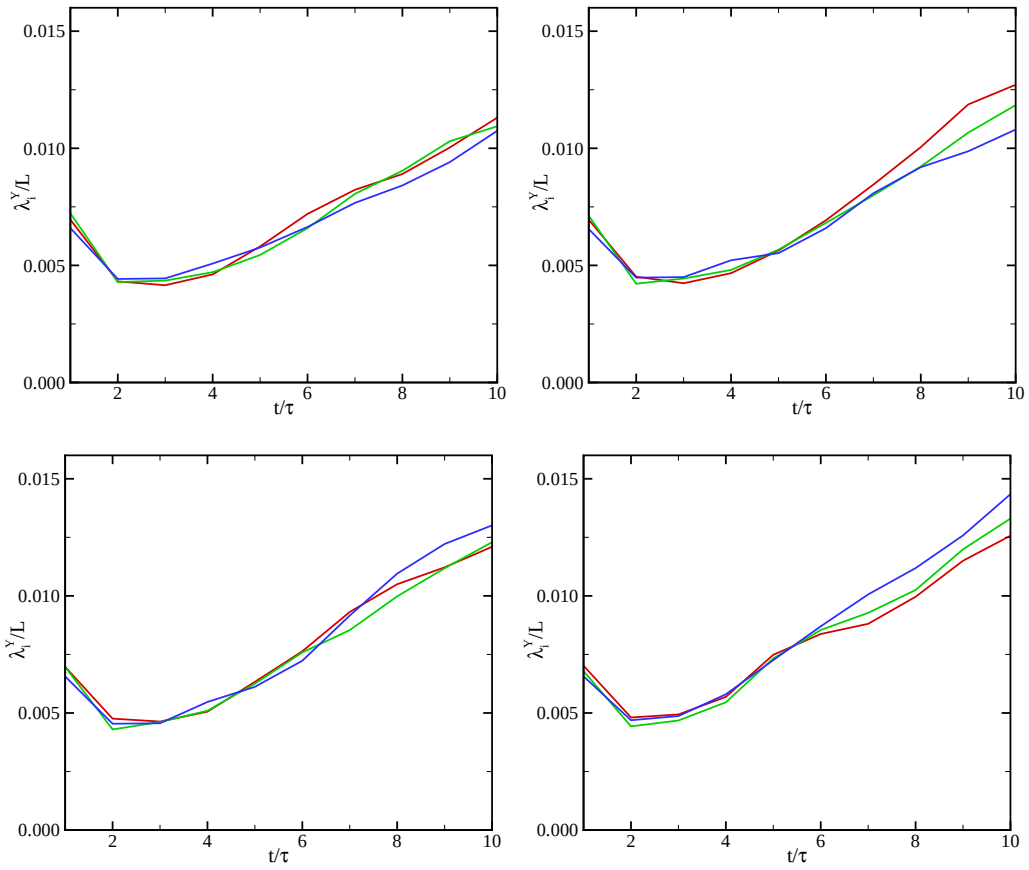

Figure 4.21: Time evolution of the directional Corrsin microscale for $Re_{\lambda,o} = 100$, and $\rho_2/\rho_1 = 3$ (top left), 5 (top right), 8 (bottom left) and 12 (bottom right). Red: x-component; green: y-component; blue: z-component.

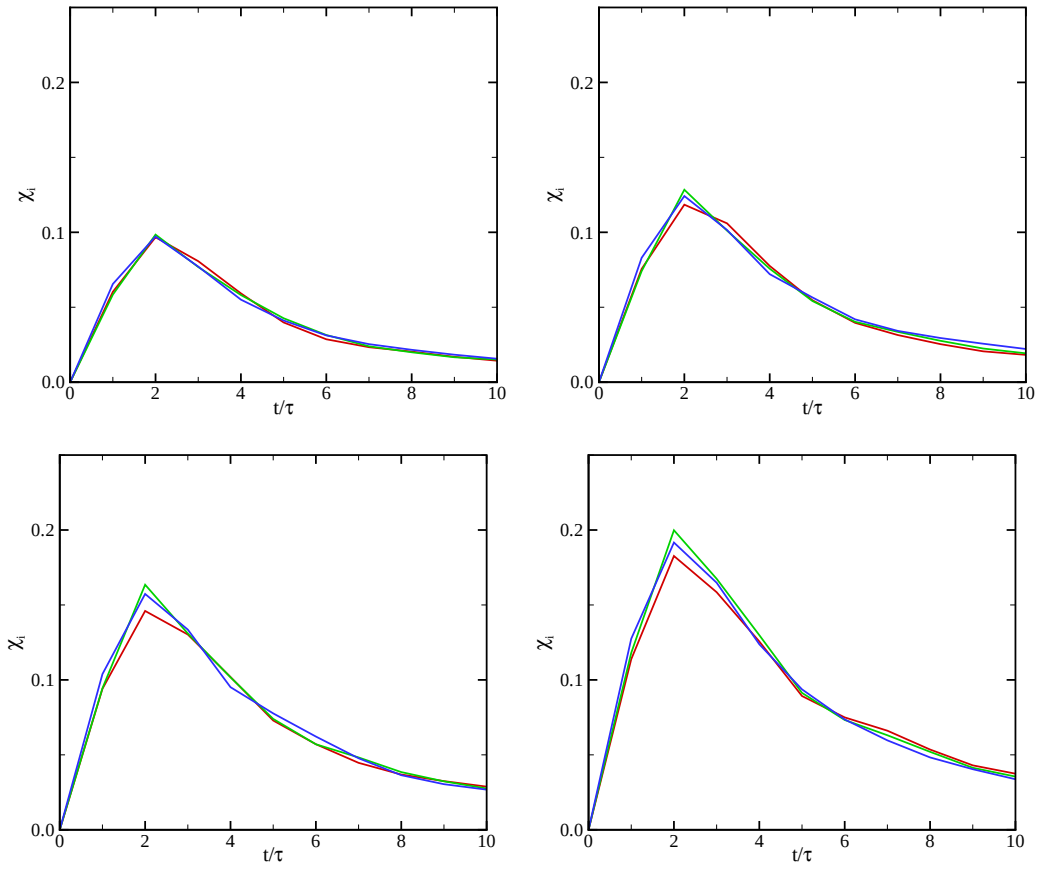

Figure 4.22: Time evolution of the directional turbulent scalar dissipation as defined in equation 4.44 for $Re_{\lambda,o} = 100$, and $\rho_2/\rho_1 = 3$ (top left), 5 (top right), 8 (bottom left) and 12 (bottom right). Red: x-component; green: y-component; blue: z-component.

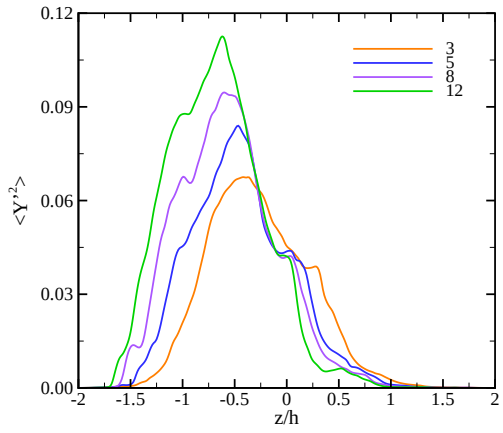

Figure 4.23: Average scalar fluctuation field in the $x - y$ plane at $t/\tau = 5$ for $Re_{\lambda,o} = 100$, and $\rho_2/\rho_1 = 3$, 5, 8, and 12.

4.4.4 Flow Intermittency

Small-scale intermittency of the velocity field is considered by measuring the directional skewness S and kurtosis K of the velocity derivatives in the mixing region ($0.25 \leq \langle Y \rangle \leq 0.75$), also measured in Tordella *et al.* (2008) and Cabot & Zhou (2013). These quantities are defined as

$$S_{\frac{\partial u_i}{\partial x_i}} = \left[\frac{\left\langle \left(\frac{\partial u_i}{\partial x_i} \right)^3 \right\rangle}{\left\langle \left(\frac{\partial u_i}{\partial x_i} \right)^2 \right\rangle^{1.5}} \right]_{mz}, \qquad K_{\frac{\partial u_i}{\partial x_i}} = \left[\frac{\left\langle \left(\frac{\partial u_i}{\partial x_i} \right)^4 \right\rangle}{\left\langle \left(\frac{\partial u_i}{\partial x_i} \right)^2 \right\rangle^2} \right]_{mz}, \tag{4.45}$$

where it is implied that there is no sum in i. The skewness of the velocity derivatives remains at the same level ($S \approx -0.5$) in all directions despite the different density ratios, corresponding to that reported in past grid turbulence experiments (Sreenivasan & Antonia, 1997); the same behavior is observed in the kurtosis (figure 4.24) and suggests that the higher derivatives of the velocity field also remain isotropic. This result lies in contrast to Level-1 mixing simulations with a jump in kinetic energy, which leads to anisotropy in the skewness of the velocity derivatives due to the set-up (Tordella & Iovieno, 2011). Results from our simulations and past studies indicate that the small-scale intermittency depends on the turbulence dynamics. Figure 4.24 indicates that the mass fraction field is more intermittent than the velocity field based on the higher values of the kurtosis and the higher negative value of the skewness of the mass fraction in the direction of the anisotropy. These results are consistent with grid experiments of Tong & Warhaft (1994), in which the temperature is found more intermittent than the velocity field, with a value of -1.8 ± 0.2 for the skewness of the (passive) temperature fluctuation derivative in the direction of the mean gradient.

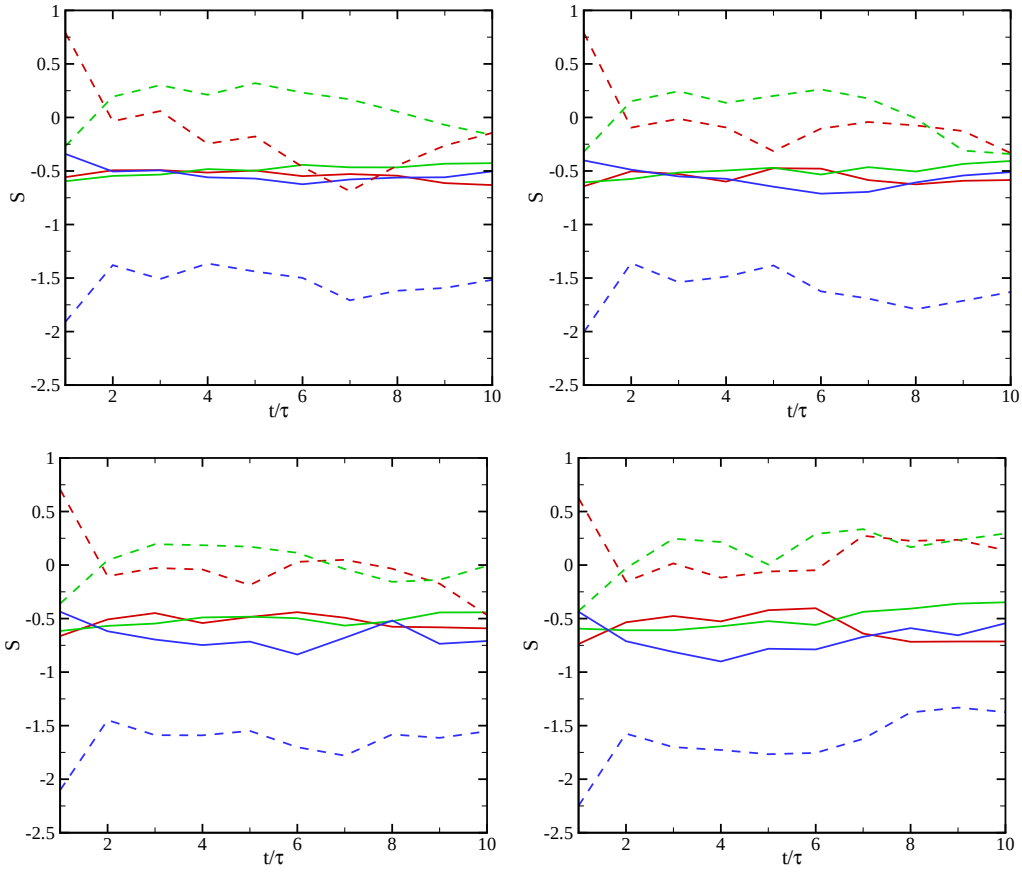

Figure 4.24: Time evolution of skewness of the velocity derivatives (solid) and the mass fraction derivatives (dashed) for $Re_{\lambda,o} = 100$ and $\rho_2/\rho_1 = 3$ (top left), 5 (top right), 8 (bottom left) and 12 (bottom right). Red: x-component; green: y-component; blue: z-component.

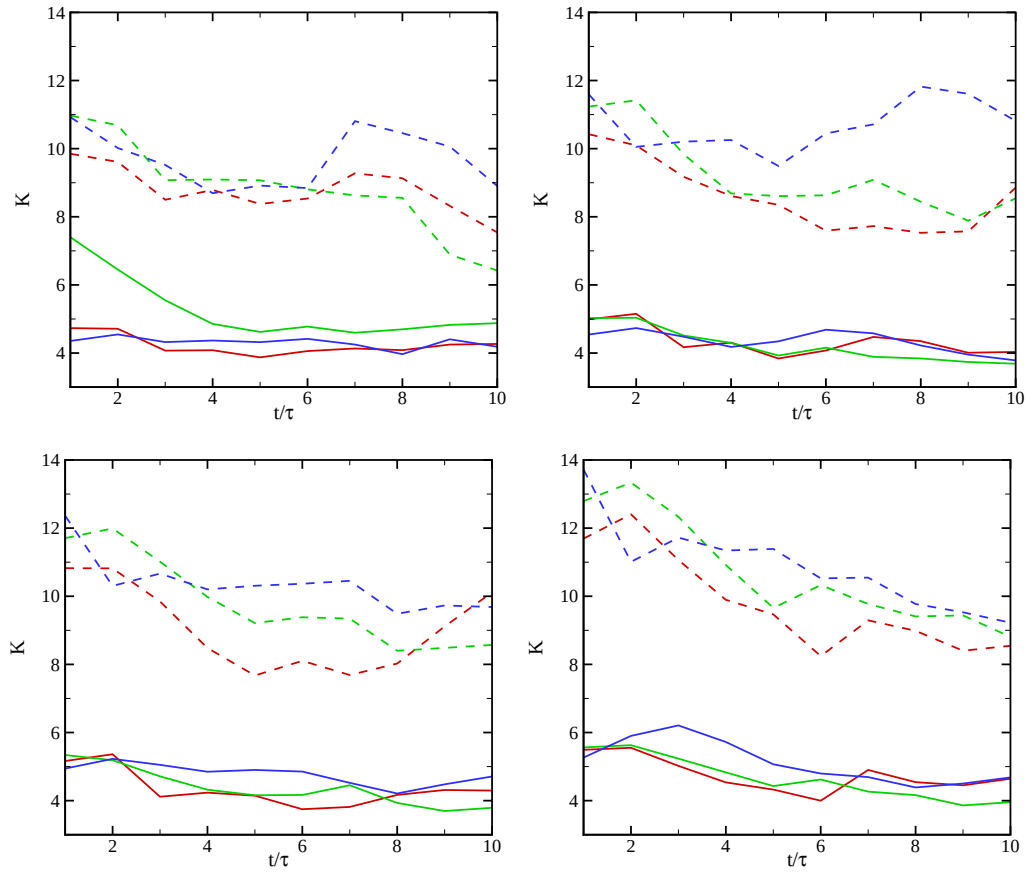

Figure 4.25: Time evolution of kurtosis of the velocity derivatives (solid) and the mass fraction derivatives (dashed) for $Re_{\lambda,o} = 100$ and $\rho_2/\rho_1 = 3$ (top left), 5 (top right), 8 (bottom left) and 12 (bottom right). Red: x-component; green: y-component; blue: z-component.

CHAPTER V

Turbulent mixing in the presence of gravitational field, with application to the Rayleigh-Taylor instability

5.1 Introduction

The Rayleigh-Taylor (RT) instability occurs in a variety of applications at different scales, ranging from inertial confinement fusion to supernova explosion (Landen *et al.*, 2012; Drake, 2006). The Rayleigh-Taylor instability (RTI) occurs when a heavy fluid is accelerated into a light one or, alternatively, when the light fluid supports the heavy fluid in the presence of gravity (Taylor, 1950). In RT unstable configurations, initial perturbations along an interface may grow due to the instability. Based on linear theory, small perturbations of amplitude h_0 and wavenumber k grow exponentially in time (neglecting viscosity and surface tension)

$$h = h_0 \cosh\left(\sqrt{Agkt}\right), \qquad \text{where } A = \frac{\rho_2 - \rho_1}{\rho_1 + \rho_2} \tag{5.1}$$

until the mixing region amplitude becomes comparable to the wavelength (Taylor, 1950; Ramaprabhu *et al.*, 2006). For multi-mode RTI, the mixing region becomes self-similar after an initial transient period. In the self-similar regime, the dominant

length scale associated with the perturbations inside the mixing region grows with time as different modes interact with each other. The memory of the initial conditions is expected to be lost and the growth is traditionally assumed to be quadratic in time. This growth can simply be obtained by momentum considerations: assuming the growth of the mixing region to be the result of a buoyancy force scaled by the density difference across the mixing region front suggests (Cook & Dimotakis, 2001)

$$\bar{\rho}\frac{du_i}{dt} = \bar{\rho}\frac{d\dot{h}}{dt} \simeq \alpha\Delta\rho g, \quad \bar{\rho} = \frac{\rho_1 + \rho_2}{2}, \quad \Delta\rho = \rho_2 - \rho_1. \tag{5.2}$$

Integrating twice yields

$$h \simeq \alpha A g \left(t + t_{i0}\right)^2 + h_{i0}. \tag{5.3}$$

A more complicated momentum argument including the drag forces similarly suggests (Dimonte & Schneider, 2000)

$$\frac{d\dot{h}}{dt} \simeq \beta_i A g - C_i \frac{\dot{h}|\dot{h}|}{h}, \tag{5.4}$$

where β_i and C_i are the model coefficients. For constant model coefficients, the above equation yields (Dimonte & Schneider, 2000)

$$h \simeq \alpha A g \left[t + (1 - \psi)\, t_{i0}\right]^2, \quad t_{i0} = \sqrt{\frac{h_{i0}}{\alpha A g}}. \tag{5.5}$$

Cook *et al.* (2004) used a mass flux and energy argument while Ristorcelli & Clark (2004) used similarity assumptions to obtain

$$\dot{h}^2 = 4\alpha A g h, \tag{5.6}$$

which yields

$$h = \alpha A g t^2 + 2\left(\alpha A g h_0\right)^{1/2} + h_0. \tag{5.7}$$

Cook & Dimotakis (2001) used the following assumptions to obtain the quadratic growth based on dimensional analysis:

- Diffusion effects may be neglected in the limit of $Re \gg 1$ and $Sc \approx 1$.
- The density ratio effect is captured by the RTI characteristic time scale defined as $\tau = \sqrt{L/(Ag)}$.
- The ratio of the dominant-mode wavelength and the mixing region height to the transverse extent is small.

The last bullet enables pure mode coupling by supposing that there is little energy contained at low wavenumbers. This condition is difficult to achieve in experiments and resolved numerical simulations. The initial perturbations are poorly characterized in accelerated tank experiments (Read, 1984; Dimonte & Schneider, 2000) while retracting plates experiments (Duff *et al.*, 1962; Dalziel *et al.*, 1999) suffer from large-scale disturbances. Unlike experiments, the initial conditions are well-characterized in numerical simulations and the initial energy can be put at high wavenumbers to remain in the pure mode coupling regime. Although appropriate initial conditions are readily designed in simulations, resolving the small-scale structures requires extremely fine grids, which consequently increases the computational time significantly.

While the mixing region growth is of great engineering interest, the physics governing this growth and flow characteristics inside the mixing region are also important. In RT-unstable configurations, initial perturbations at a heavy-light interface may evolve to a turbulent mixing region, as the initial potential energy feeds the instability growth. In this process, baroclinic vorticity is generated due to the misalignment of the density and the pressure gradients. The local density gradient depends on how

well mixed the different fluids are due to large-scale entrainment and dispersion by turbulent eddies. In addition, mass diffusion in miscible fluids acting at small scales tends to smoothen sharp interfaces between the heavy and light fluids resulting in molecularly mixed regions. Thus, turbulent mixing processes affect the local density gradient and consequently the local rate of baroclinic vorticity generation. A better understanding of turbulent mixing, which plays an important role on flow dynamics inside the mixing region in RT flows, is desired. Particularly, measures of flow isotropy at different scales in different directions are of great interest. Due to the presence of the gravitational field and the large-scale density gradient across the mixing region, the resulting turbulence is expected to be anisotropic at the Taylor microscale while flow may remain isotropic at the Kolmogorov microscale (Cook & Dimotakis, 2001). However, these two effects (density gradient and gravity) are generally coupled, such that it is difficult to assess each one individually.

In the previous chapter, we focused on anisotropy caused by density and composition gradients alone in a freely decaying turbulent field with zero mean velocity. We determined the extent to which the large-scale anisotropy in fluid density/composition modifies the phenomenology of the turbulence at different scales. In this chapter, we revisit our set-up in the presence of gravity. Our goal is to determine how large- and small-scales are affected by gravity. We consider two cases. First, an isotropic velocity field extending in approximately the whole domain is used to initialize the problem. Second, we restrict the perturbations just to the interface similar to classical RT simulations. Current simulations are done at $Re_{\lambda,o} = 60, 100$ and $k_o = 4, 8, 16$.

5.2 Physical model

The focus of this chapter is on mixing mechanisms between two different gases in a turbulent field in the presence of a gravitational field. The same problem set-up, initial conditions and governing equations as those in the previous chapter are used, except

for one important difference: that gravity is included in the momentum and energy equations. Gravity gives rise to a hydrostatic pressure field, which in turn implies that either that the density in each fluid is constant and the temperature varies according to pressure (constant density set-up), or vice-versa (isothermal set-up). The focus of the present study lies in the former; the latter is briefly discussed in Section 5.6. The initial set-up is described in greater detail in the next section. The two fluids can have different density, pressure, temperature, molecular weight, viscosity, and thermal conductivity based on the initial set-up. The light-fluid density, ρ_1, the length $l = L/(2\pi)$ where L is the computational domain width, the velocity $u_{ref} = \sqrt{gl}$, the pressure $p = \rho_1 u_{ref}^2$, the light-fluid gas constant, R_1, and the temperature of unity are used to non-dimensionalize equation 4.1. The specific heats ratio, γ, is set to 1.4 for both fluids; the Schmidt number is unity corresponding to a gas-gas mixture; the Prandtl number, Pr, is set to 0.7 in both fluids and the non-dimensional gravity vector is $(0, 0, -1)$ corresponds to a Froude number, Fr, of unity, where the Froude number is defined as

$$Fr = \frac{u_{ref}}{\sqrt{gl}}. \tag{5.8}$$

The numerical method is the same as that used in the previous chapter, with two minor difference: (i) gravity now appears in the equations and is treated explicitly, and (ii) non-reflecting boundary conditions in the z-direction are modified due to gravity as described in Thompson (1990).

5.3 Initial set-up

The computational domain consists of a rectangular parallelepiped of size $L \times L \times 10L$, with $L = 2\pi$ and N points per L on a uniform Cartesian grid. The initial mass

fraction field is generated in z without any perturbations in the x-y plane:

$$Y_1(z) = \frac{1}{2}\left[1 - \text{erf}\left(\frac{z - z_0}{H}\right)\right], \tag{5.9}$$

where $z_0 = 0$ is the mid-plane location separating the two fluids corresponding to $Y_1 = 0.5$. The value $H = \frac{8}{128}L$ corresponds to the steepest interface profile that central differences are capable of resolving in a satisfactory fashion on a $N = 128$ points per L grid, thus preventing the use of shock capturing and minimizing numerical dissipation that would otherwise overwhelm the small turbulent scales (Johnsen *et al.*, 2010). Because of this, the mixing region has a finite initial size.

In the mixing region, the initial density profile is obtained from the mass fraction field:

$$\frac{1}{\rho} = \frac{Y_1}{\rho_1} + \frac{Y_2}{\rho_2}. \tag{5.10}$$

The density in the light fluid, ρ_1, is the reference density and $\rho_2 = 3\rho_1$ corresponding to the Atwood number of $A = 0.5$. Pressure is obtained by considering the hydrostatic equilibrium and setting the pressure at the mid-plane as the reference pressure.

$$\frac{dp}{dz} = \rho g, \quad p_{mid-plane} = T_{mid-plane} = 2\pi L\left(\rho_1 + \rho_2\right). \tag{5.11}$$

To prevent generation of unphysical waves at the interface in the presence of finite mass physical diffusion, the following mean velocity is prescribed at the interface (see Chapter III),

$$u_i = -\frac{1}{ReSc}\frac{1}{\rho}\frac{\partial \rho}{\partial x_i}. \tag{5.12}$$

The initial molecular weight and the density are related as

$$\frac{R_2}{R_1} = \frac{M_1}{M_2} = \frac{\rho_1}{\rho_2}. \tag{5.13}$$

This results in an isothermal field in the absence of gravity as seen in the previous chapter. In the presence of gravity, the pressure is not uniform in the field anymore. Consequently, the temperature also varies in the domain.

Numerical simulations of the RTI are traditionally initialized by perturbing the interface either through the density or by transforming density perturbations to velocity perturbations using linear theory (Dimonte *et al.*, 2004). In this study, the interface separating the light and heavy fluids is initially unperturbed but the random velocity fluctuations serve as the perturbation source to initialize the RTI. We will consider the following two approaches to initialize the velocity field:

- ***RT-turb set-up***: the velocity field described in Section 4.2.3 is used to initialize the problem. The initial conditions consist of a random solenoidal velocity field inside a triple periodic box of size $2\pi \times 2\pi \times 2\pi$ that satisfies a Batchelor spectrum $E(k) \approx k^4 \exp\left(\frac{-2k^2}{k_0^2}\right)$, where k_0 is the most energetic wavenumber and $\lambda_0 = 2/k_0$ is the initial Taylor microscale (Lee *et al.*, 1991; Johnsen *et al.*, 2010; Movahed & Johnsen, 2013*c*). The initial velocity spectrum for $k_0 = 4$, 8, and 16 studied here are shown in figure 5.1. Taking advantage of periodicity, ten such isotropic boxes are juxtaposed in the z-direction to make up the full domain. Boundary conditions are periodic in the x- and y- directions, and non-reflecting with one-sided differences in the $z-$direction. Although the approach of Thompson (1987) is followed for non-reflecting conditions, numerical errors may be generated as turbulence reaches the boundaries. To avoid such difficulties, an error function is used to damp the turbulent fluctuations close to the boundaries. The long domain ($10L$) in the z-direction further minimises boundary effects on the evolution of the mixing region near $z = 0$.

- ***Classical RT set-up***: we investigate the problem in a similar set-up where velocity perturbations are restricted only to the mixing region. We use exactly the same initial field as discussed above and multiply it by $\exp(-k_0|z - z_0|)$

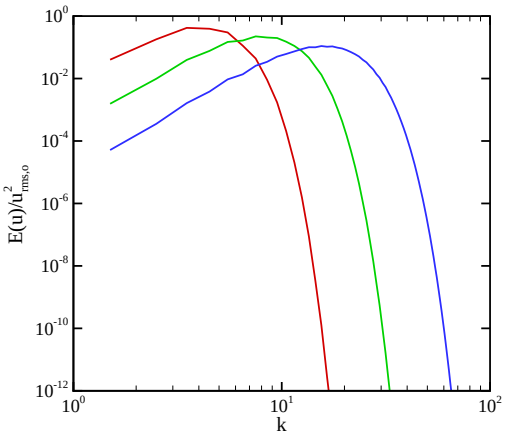

Figure 5.1: Initial velocity spectra for $k_0 = 4$ (red), 8 (green), and 16 (blue).

such that the perturbations decay exponentially in agreement with the linear theory.

The turbulent Mach number and Taylor-scale Reynolds number are defined as

$$M_t = \frac{\sqrt{\langle u_i u_i \rangle_{vol}}}{\langle c \rangle_{vol}}, \quad Re_\lambda = \frac{\langle \rho \rangle_{vol} \, u_{rms} \lambda}{\langle \mu \rangle_{vol}}, \tag{5.14}$$

where

$$u_{rms} = \sqrt{\frac{\langle u_i u_i \rangle_{vol}}{3}}, \qquad \lambda^2 = \frac{\langle u_i^2 \rangle_{vol}}{\left\langle \left(\frac{\partial u_i}{\partial x_i} \right)^2 \right\rangle_{vol}}. \tag{5.15}$$

Here, c is the sound speed, λ is the time-varying Taylor microscale, and $\langle \cdot \rangle_{vol}$ denotes spatial averages over the whole domain. The initial velocity field corresponds to the turbulent Mach number of 0.1 in the light fluid where $p = p_{mid-plane}$ and $\rho = \rho_1 = 1$ is used to calculate the sound speed. The amplitude of the added perturbations is large in this study ($M_t = 0.1$) compared to previous RT multi-mode studies (Youngs, 1991; Dimonte *et al.*, 2004; Cook & Dimotakis, 2001; Cook *et al.*, 2004; Cabot & Cook, 2006), so that the initial growth is not expected to follow linear theory. In addition, in order to remain in the pure-mode coupling regime, it is necessary to add perturbations with small amplitude such that the linear theory holds initially. As

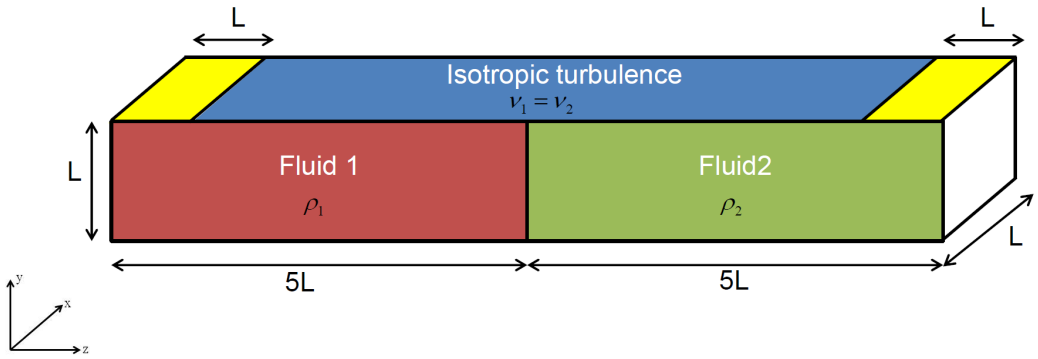

Figure 5.2: Schematic of the initial computational set-up. Two fluids of different densities are initially separated by a diffuse unperturbed material interface in the presence of an initially isotropic turbulent velocity field.

a consequence of the large amplitude perturbations added here, we do not expect our results to match previous multi-mode simulations in which the goal has been to remain in the mode-coupling regime.

In the problem under consideration, there are two important time scales. One is associated with the decay of the initial turbulent field (τ_{turb}) and the second with the development of the Rayleigh-Taylor instability (τ_{RT}). By choosing the initial Taylor microscale as the dominant length scale of the initial perturbations, we obtain

$$\tau_{RT} = \sqrt{\frac{\lambda_o}{Ag}} = \sqrt{\frac{2\pi}{k_0 Ag}}. \tag{5.16}$$

The initial eddy turn-over time is the important time scale for the initially decaying turbulent field, and is defined as

$$\tau_{turb} = \frac{\lambda_0}{u_{rms,o}} = \frac{2/k_0}{M_t\sqrt{\gamma p/3}} = \frac{2}{k_o M_t}\sqrt{\frac{3}{\gamma\left(2\pi\right)^2\left(\rho_1+\rho_2\right)}}. \tag{5.17}$$

Thus the ratio of the two important time scales of the problem can be related as

$$\frac{\tau_{RT}}{\tau_{turb}} = M_t\sqrt{\frac{\gamma k_0\left(2\pi\right)^3\left(\rho_1+\rho_2\right)}{3Ag}}, \tag{5.18}$$

Table 5.1: Summary of the simulations runs and relevant parameters.

	ρ_2/ρ_1	μ_2/μ_1	k_o	$Re_{\lambda,i}$	N
RT-turb & RT-classical	3	3	4	60	256
RT-turb & RT-classical	3	3	4	100	256
RT-turb & RT-classical	3	3	8	60	256
RT-turb & RT-classical	3	3	8	100	512
RT-turb & RT-classical	3	3	16	60	256
RT-turb & RT-classical	3	3	16	100	512

Table 5.2: Final time of our simulations based on different important time scales of the problem for different initial most energetic wavenumbers k_o.

k_o	τ_{RT}/τ_{turb}	t_{final}/τ_{turb}	t_{final}/t_{RT}
4	3.04	20	6.58
8	4.29	40	9.32
16	6.08	80	13.16

where $M_t = 0.1$, $\rho_1 = 1$, $\rho_2 = 3$, $\gamma = 1.4$, $A = 0.5$, $g = 1$ in our set-up. Therefore $\tau_{RT}/\tau_{turb} = 1.52\sqrt{k_o}$. A summary of the simulation runs and relevant parameters are provided in table 5.1. Table 5.2 summarizes the final time of our computations for different k_0. All of the simulations are run until the same final time in the physical space. Since the initial turbulent field decays rapidly compared to the time required for the RTI to develop, we chose a high initial Mach number ($M_t = 0.1$) in this study to increase the ratio of τ_{RT} to τ_{turb}. Thus, gravity effects become important before the decay of the initial turbulent field.

The scaled Reynolds number can be obtained in terms of the initial Taylor-scale

Table 5.3: Scaled Reynolds number for different initial most energetic wavenumbers k_0 and the initial Taylor-scale based Reynolds number $Re_{\lambda,o}$.

$Re_{\lambda,o}$	k_o	Re_o
60	4	139.7874
	8	279.5748
	16	559.1496
100	4	232.9790
	8	465.9580
	16	931.9159

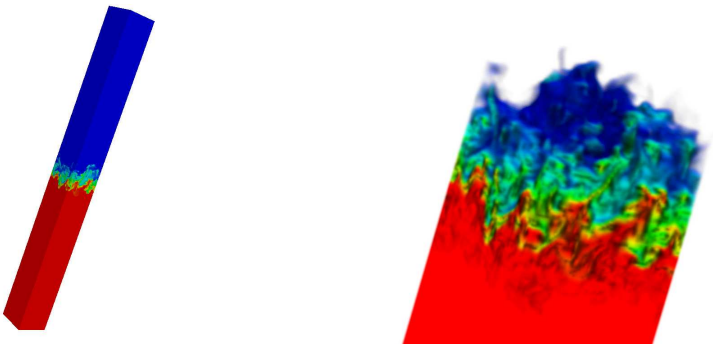

(a) Full domain. (b) Zoomed in.

Figure 5.3: Mass fraction contours from the new Rayleigh-Taylor set-up for $Re_{\lambda,o} = 60$, $k_0 = 4$, $t/\tau_{turb} = 5$.

Reynolds number as

$$Re = Re_\lambda \left[\frac{\rho u_{rms,0} \lambda_0}{\mu} \right]^{-1}. \tag{5.19}$$

In the simulations with no gravity from the previous chapter, the important Reynolds number was $Re_{\lambda,o}$. For RT turbulence, the scaled Reynolds number is also important because of the relative importance of gravity to viscous terms. Particularly, for the same initial Taylor-scale Reynolds number in our set-up, the scaled Reynolds number is larger for higher k_o, as shown in table 5.3.

5.4 Results: dynamics of the large scales in the mixing region

5.4.1 Qualitative behavior of the large scales

Figure 5.3 shows detailed plots of the mixing region in this problem after five eddy turn-over times. The initial fluctuating velocity field perturbs the interface and the baroclinic vorticity generated in the mixing region due to the instability provides energy for the growth of the instability. As observed in the mass fraction field, spikes/bubbles of the heavier/lighter fluid penetrate into the lighter/heavier fluid (figure 5.4).

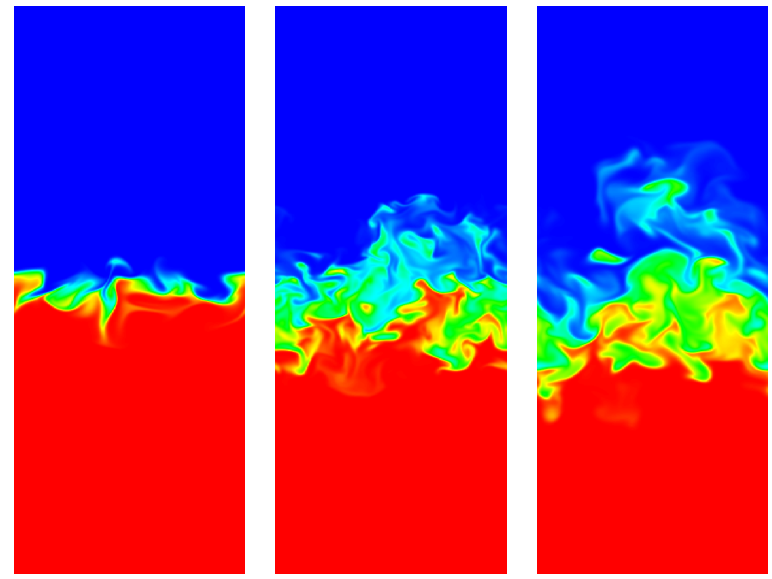

(a) $t/\tau_{turb} = 1.$ (b) $t/\tau_{turb} = 5.$ (c) $t/\tau_{turb} = 10.$

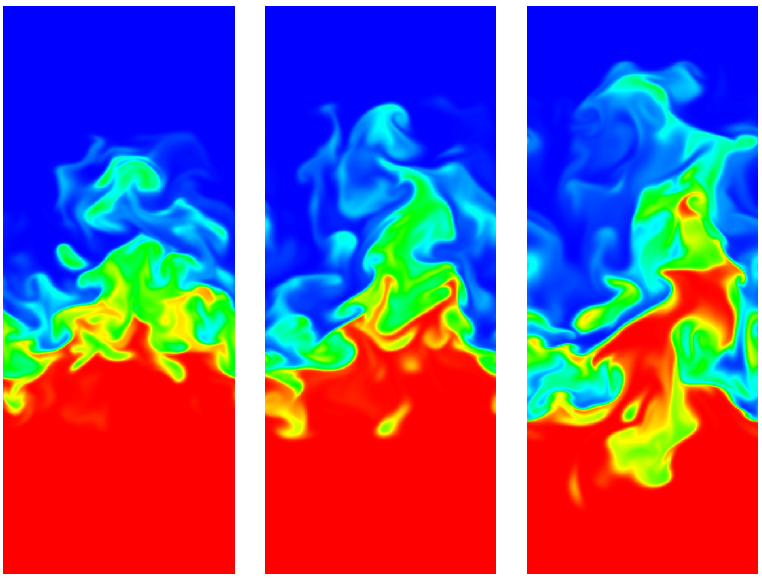

(d) $t/\tau_{turb} = 11.$ (e) $t/\tau_{turb} = 15.$ (f) $t/\tau_{turb} = 20.$

Figure 5.4: Two-dimensional contours of mass fraction in the $x - z$ plane for $Re_{\lambda,o} = 100$ and $k_0 = 4$. The vertical direction corresponds to the direction of anisotropy in the composition ($z-$ direction). Each plot covers an area of $L \times 3L$ and the initial mid-plane ($z = 0$) is located in the middle of the vertical direction. Red: light fluid; blue: heavy fluid.

5.4.2 Temporal evolution of the thermodynamic quantities

Figures 5.5 & 5.6 show the temporal evolution of the pressure, temperature, and density. The mixing region grows initially due to turbulence diffusion. The density field also gets perturbed due to the velocity field. The density perturbations inside the mixing region initiate the Rayleigh-Taylor instability. The loss of potential energy manifests itself as decrease in the pressure. The potential energy is converted to turbulent kinetic energy providing energy for the mixing region to grow. The decrease in pressure and increase in the density of light fluid result in a decrease of temperature in the light fluid, while the decrease in the pressure and the density of the heavy fluid result in a slight increase in the temperature in the heavy fluid.

5.4.3 Bubble and spike growth

The spike (bubble) amplitude h_s (h_b) is defined as the distance between $\langle Y \rangle \leq 0.99$ ($\langle Y \rangle \geq 0.01$) and the initial mid-plane ($z = 0$). The spikes (bubbles) amplitude growth is due to the penetration of the heavy (light) fluid into the light (heavy) fluid. The amplitude of the mixing region, h_{amp} is defined as the average of h_b and h_s:

$$h_{amp} = \frac{h_s + h_b}{2}. \tag{5.20}$$

Figures 5.7 (5.8) show the evolution of the bubble, spike and amplitude of the mixing region for the RT-turb set-up (classical RT set-up). The initial growth in the RT-turb set-up is due to turbulence diffusion. This results in a higher growth rate especially during the first five eddy turn-over times. The initial curvature of the growth in this set-up is clearly different from that in the classical RT set-up due to this turbulent diffusion. While the current measure of the amplitude is prone to noise, the amplitude is found to be slightly higher for the RT-turb for k_0 =8 and 16. The spike growth is higher than the bubble growth, as expected for $A = 0.5$ (Dimonte *et al.*, 2004). As a

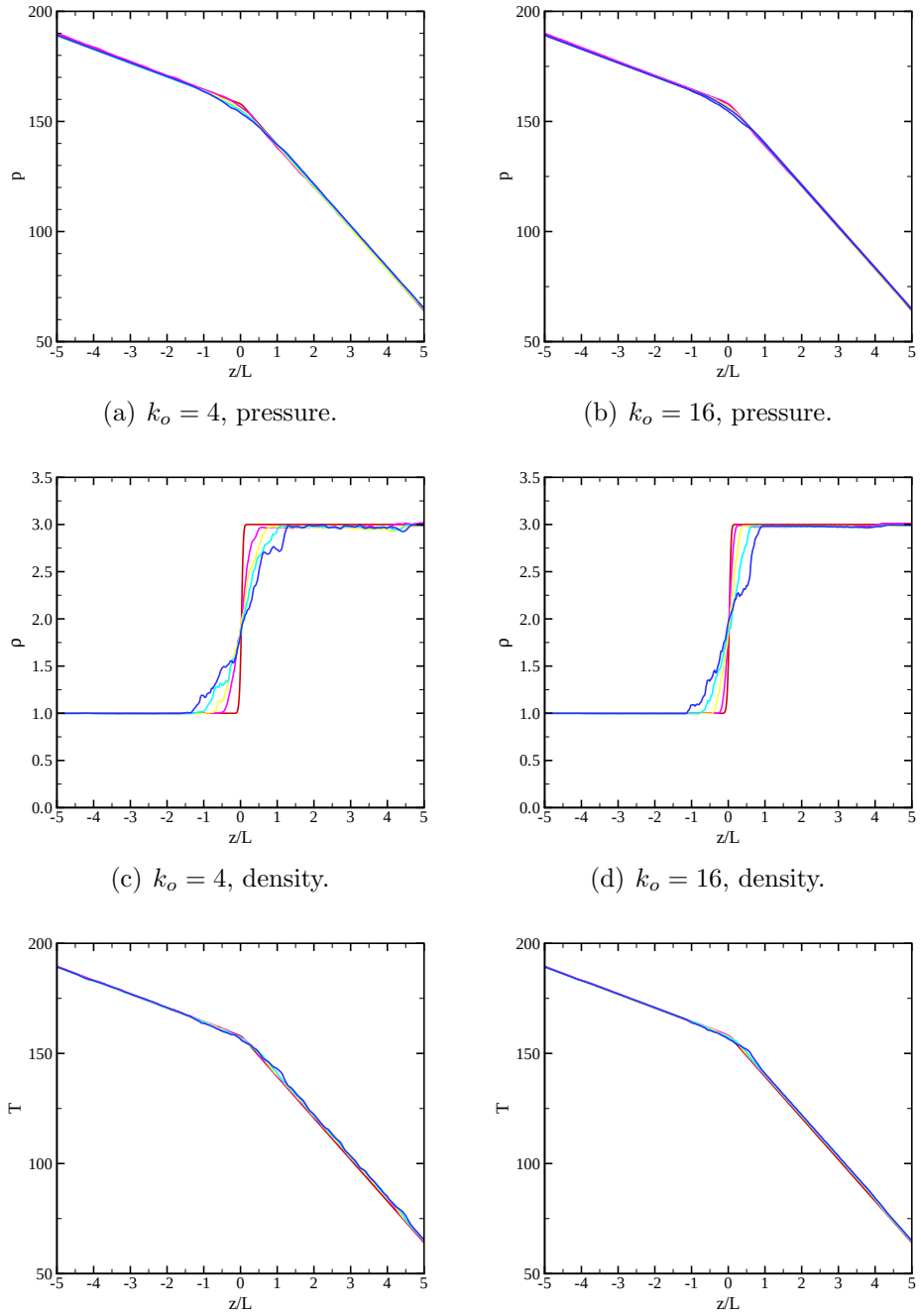

(a) $k_o = 4$, pressure.

(b) $k_o = 16$, pressure.

(c) $k_o = 4$, density.

(d) $k_o = 16$, density.

(e) $k_o = 4$, temperature.

(f) $k_o = 16$, temperature.

Figure 5.5: Average fields in the x-y plane for $Re_{\lambda,o} = 100$, and at $t/\tau = 0$ (red), 5 (pink), 10 (yellow), 15 (cyan), 20 (blue) for $k_o = 4$, and $t/(4\tau) = 0$ (red), 5 (pink), 10 (yellow), 15 (cyan), 20 (blue) for $k_o = 16$. RT-turb set-up.

result, the mean position of the interface moves towards the light fluid, an observation confirmed by monitoring the location in z of the $\langle Y \rangle = 0.5$ plane (figure 5.9).

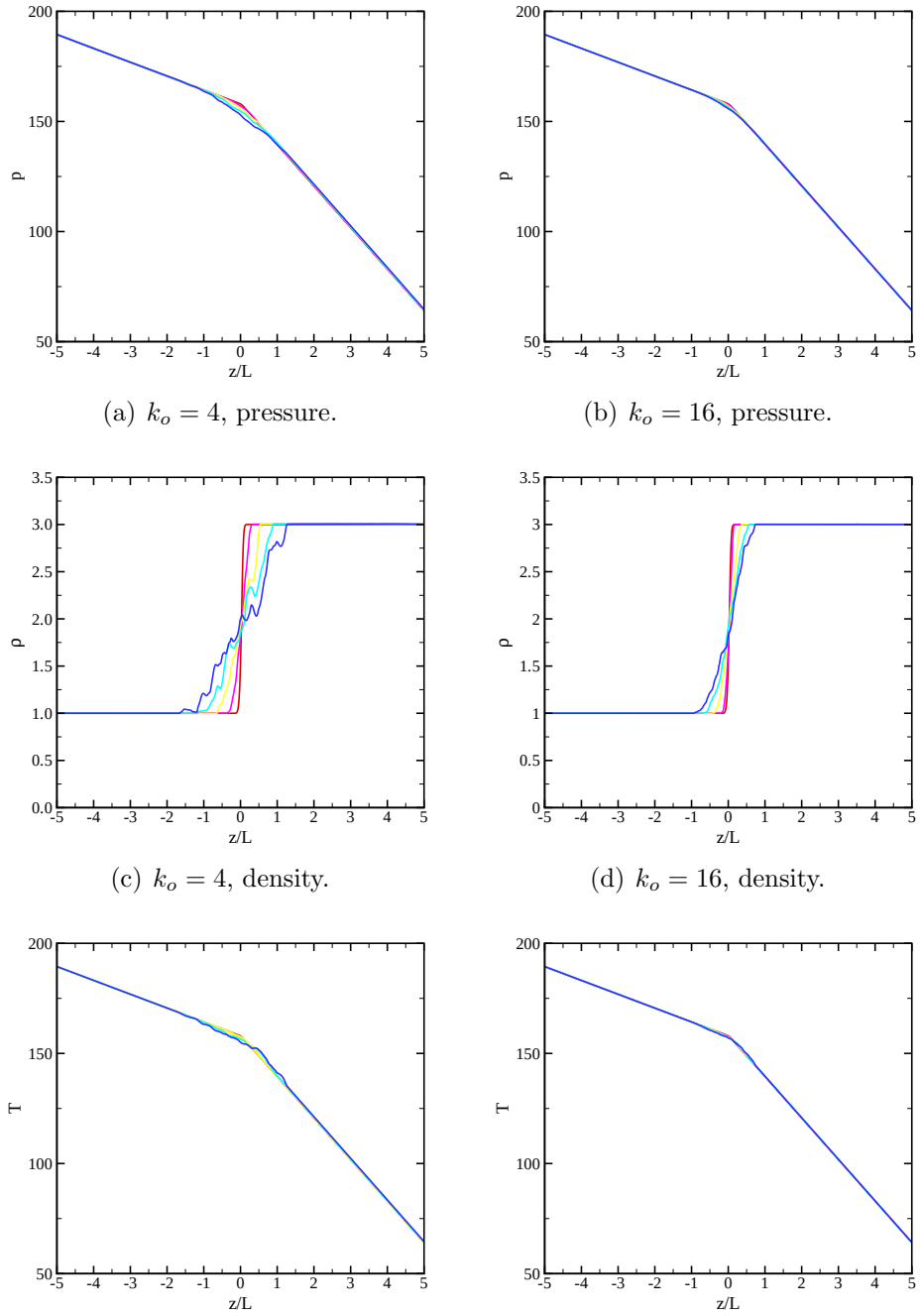

(a) $k_o = 4$, pressure.

(b) $k_o = 16$, pressure.

(c) $k_o = 4$, density.

(d) $k_o = 16$, density.

(e) $k_o = 4$, temperature.

(f) $k_o = 16$, temperature.

Figure 5.6: Average fields in the x-y plane for $Re_{\lambda,o} = 100$, and at $t/\tau = 0$ (red), 5 (pink), 10 (yellow), 15 (cyan), 20 (blue) for $k_o = 4$ (left), and $t/(4\tau) = 0$ (red), 5 (pink), 10 (yellow), 15 (cyan), 20 (blue) for $k_o = 16$ (right). Classical RT set-up.

5.4.4 Self-similarity

Figure 5.10 shows the average mass fraction field vs. similarity variable z/h for the RT-turb set-up. During the first 5 (20) eddy turn-over times for $k_0 = 4$ (16) the mass

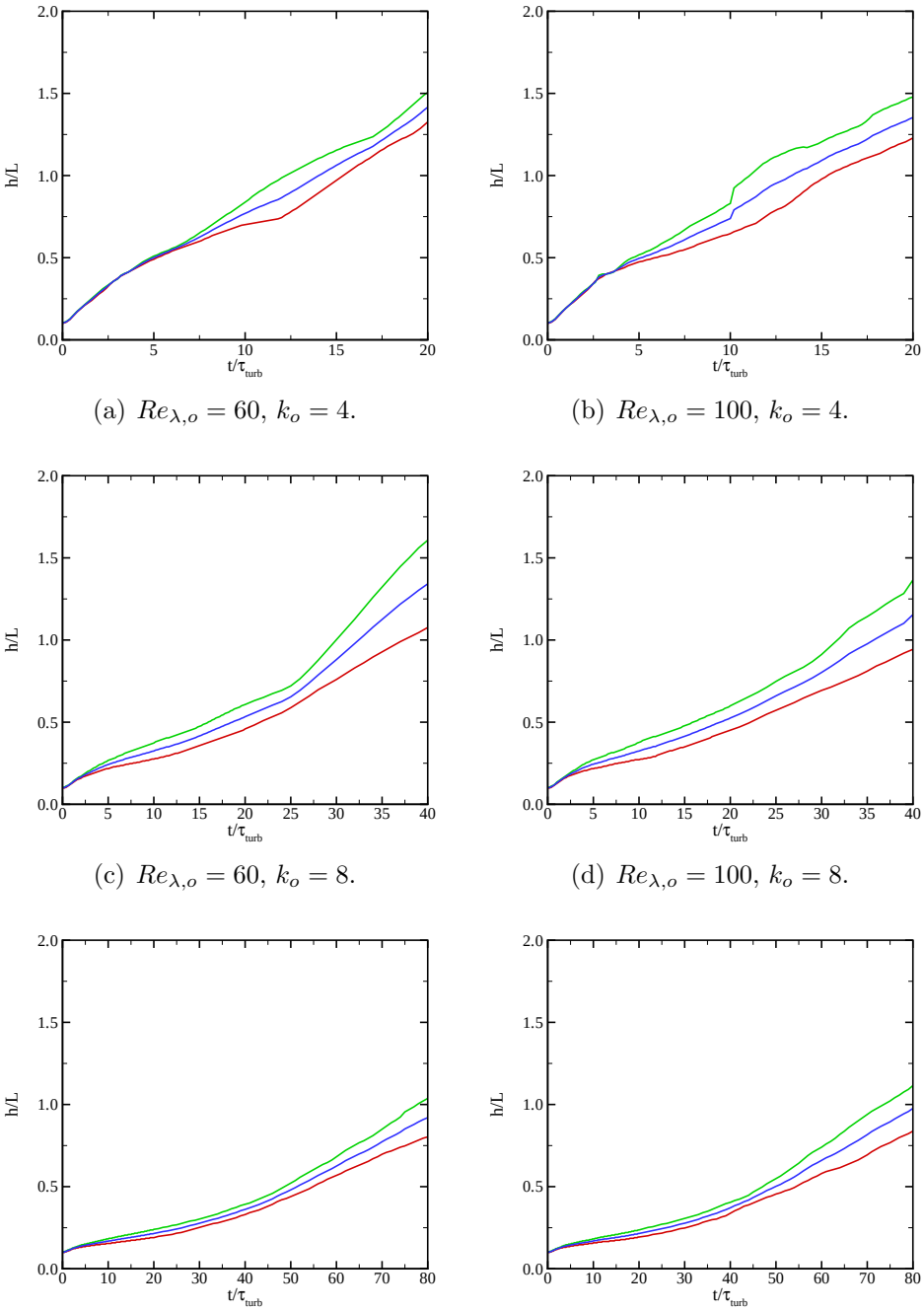

(a) $Re_{\lambda,o} = 60$, $k_o = 4$.

(b) $Re_{\lambda,o} = 100$, $k_o = 4$.

(c) $Re_{\lambda,o} = 60$, $k_o = 8$.

(d) $Re_{\lambda,o} = 100$, $k_o = 8$.

(e) $Re_{\lambda,o} = 60$, $k_o = 16$.

(f) $Re_{\lambda,o} = 100$, $k_o = 16$.

Figure 5.7: Time evolution of the bubble, spike, and amplitude for $Re_{\lambda,o} = 60$ (left), and 100 (right), and $k_o = 4$ (top), 8 (middle), and 16 (bottom). Red: bubble; green: spike; blue: amplitude. RT-turb set-up.

fraction field moves toward to the light fluid. This movement can be described by momentum arguments as follows. An eddy in the heavy fluid has higher momentum

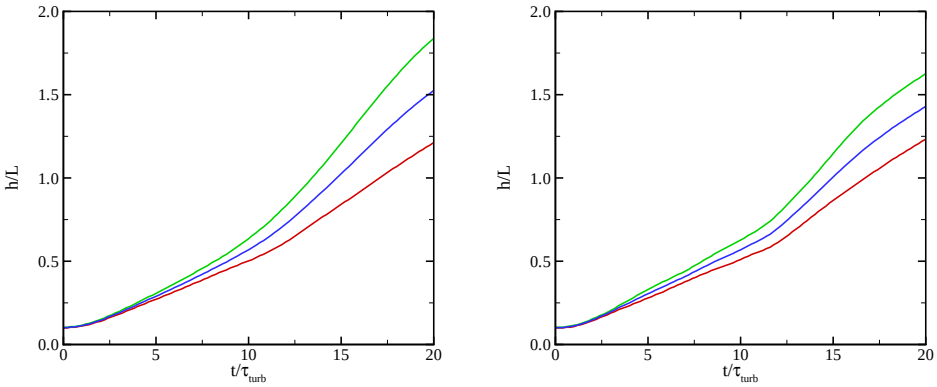

(a) $Re_{\lambda,o} = 60$, $k_o = 4$.

(b) $Re_{\lambda,o} = 100$, $k_o = 4$.

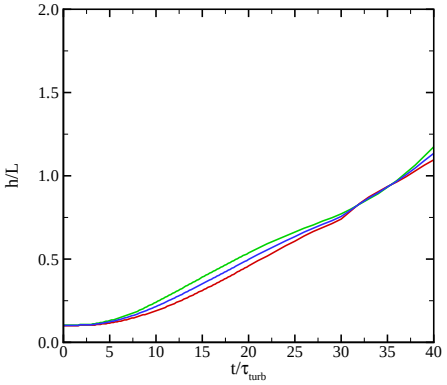

(c) $Re_{\lambda,o} = 60$, $k_o = 8$.

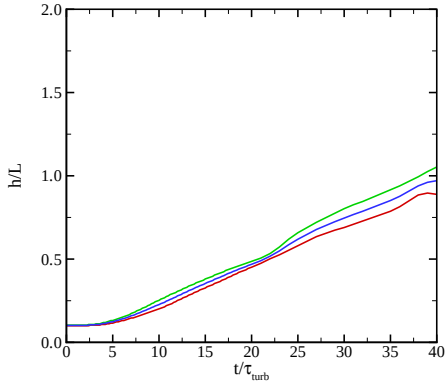

(d) $Re_{\lambda,o} = 100$, $k_o = 8$.

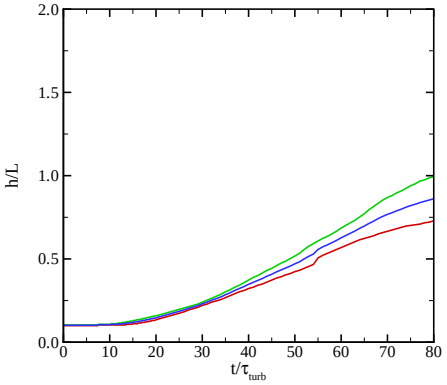

(e) $Re_{\lambda,o} = 60$, $k_o = 16$.

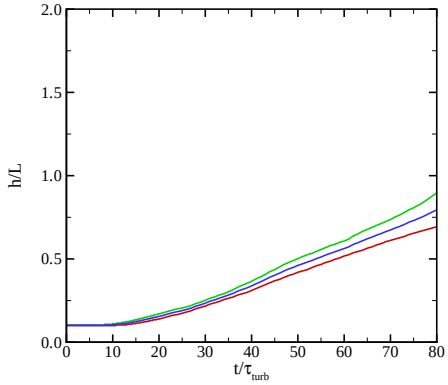

(f) $Re_{\lambda,o} = 100$, $k_o = 16$.

Figure 5.8: Time evolution of the bubble, spike, and amplitude for $Re_{\lambda,o} = 60$ (left), and 100 (right), and $k_o = 4$ (top), 8 (middle), and 16 (bottom). Red: bubble; green: spike; blue: amplitude. Classical RT set-up.

than the corresponding volume of light fluid, such that it is easier for the heavy fluid to displace the light fluid and penetrate it. Thereafter, the mixing region width

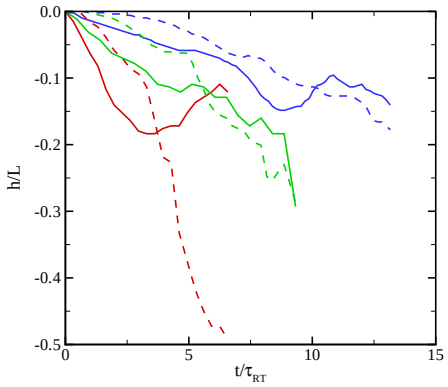

Figure 5.9: Time evolution of the mid-plane for $Re_{\lambda,o} = 100$. Red: $k_o = 4$; green: $k_o = 8$; blue: $k_o = 16$. Solid: RT-turb set-up; dashed: Classical RT set-up.

increases and exhibits self-similarity as the average mass fraction curves collapse onto each other.

Figure 5.11 shows the average mass fraction field vs. similarity variable z/h for the classical RT set-up. During the first 15 (60) eddy turn-over times for $k_0 = 4$ (16) the mass fraction field moves toward to the light fluid in agreement with momentum arguments. Thereafter, the mixing region width increases and exhibits self-similarity. It is interesting to note that it takes a longer time for the classical RT set-up to show a self-similar behaviour than it does with the RT-turb set-up. As researchers are typically more interested to study the RTI in the self-similar regime, the current proposed set-up (the RT-turb set-up) has the advantage of reaching this self-similar regime faster than the classical RT set-up.

5.4.5 Mixing region growth analysis

Another measure of mixing region width,

$$h = 2 \int_{-\infty}^{\infty} \min\left(\langle Y_1 \rangle, \langle Y_2 \rangle\right), \tag{5.21}$$

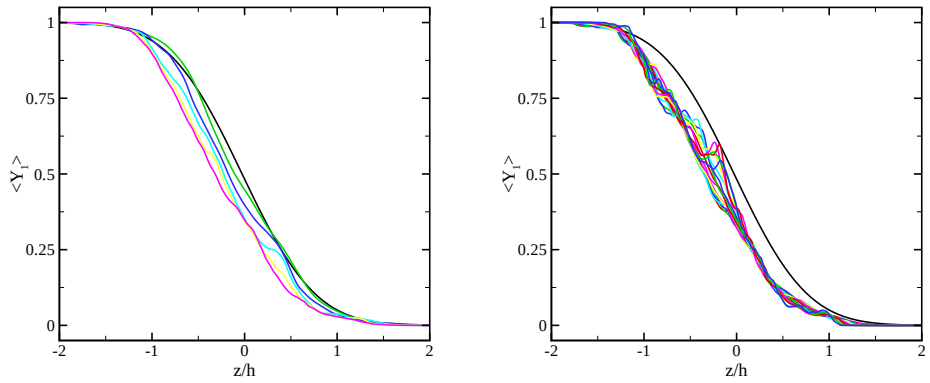

(a) $k_o = 4$, $t/\tau_{turb} = 0, 1, 2, 3, 4, 5$. (b) $k_o = 4$, $t/\tau_{turb} = 0, 5 - 20$.

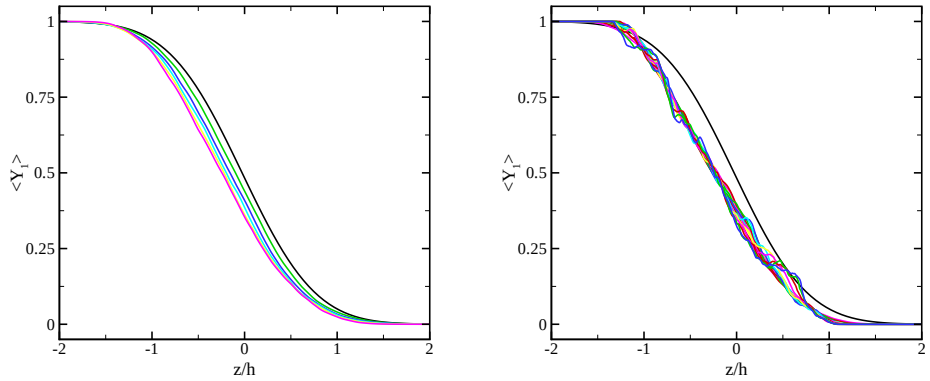

(c) $k_o = 16$, $t/(4\tau_{turb}) = 0, 1, 2, 3, 4, 5$. (d) $k_o = 16$, $t/(4\tau_{turb}) = 0, 5 - 20$.

Figure 5.10: Average mass fraction field in the x-y plane at different times for $Re_{\lambda,o}$ = 100, and $k_o = 4$ (left), and 16 (right). RT-turb set-up.

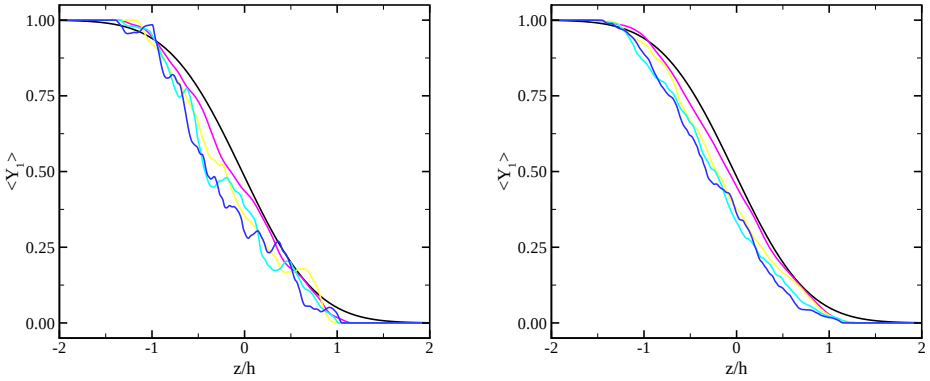

(a) $k_o = 4$, $t/\tau_{turb} = 0, 5, 10, 15, 20$. (b) $k_o = 16$, $t/(4\tau_{turb}) = 0, 5, 10, 15, 20$.

Figure 5.11: Average mass fraction field in the x-y plane at different times for $Re_{\lambda,o}$ = 100, and $k_o = 4$ (left), and 16 (right). Classical RT set-up.

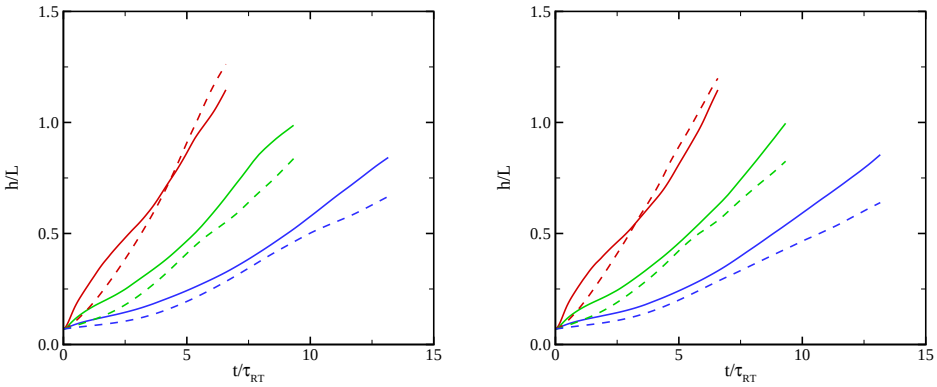

(a) $Re_{\lambda,o} = 60$. (b) $Re_{\lambda,o} = 100$.

Figure 5.12: Temporal evolution of the mixing region width, h based on equation 5.21. Red: $k_o = 4$; green: $k_o = 8$; blue: $k_o = 16$. Solid: RT-turb set-up; dashed: Classical RT set-up.

is more quantitative, in that it represents the region in which the flow is well mixed. This definition has the advantage of avoiding dependence on statistical fluctuations (Cook & Dimotakis, 2001; Cabot & Cook, 2006; Cabot & Zhou, 2013). Figure 5.12 shows the time evolution of the mixing width. Considering that the final time of all of the simulations are the same, the growth is found to decrease monotonically as k_0 increases. The initial curvature of the plots are different for the RT-turb set-up as the initial growth is dominated by turbulence diffusion. The mixing width remains larger during the whole simulation for $k_0 = 8$ and 16 for the RT-turb set-up. The mixing region growth shows small sensitivity to the Reynolds number for the range of the Reynolds number considered here. Although only two Taylor-scale Reynolds numbers (60 and 100) are considered here, the scaled Reynolds number varies significantly, from 140 to 940 (recall table 5.3).

The mixing region growth rate is obtained from the mixing region width. A fourth-order accurate central scheme is used to calculate the time derivative. The growth rate is higher initially for the RT-turb set-up due to turbulence diffusion. The larger initial Taylor scales for smaller values of k_0 result in a higher initial growth rate as the two fluids are dispersed by larger eddies. After the initial peak, the growth

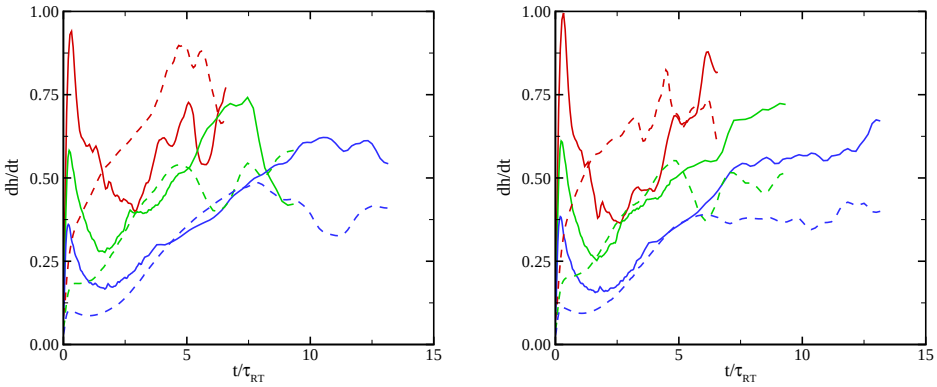

(a) $Re_{\lambda,o} = 60$. (b) $Re_{\lambda,o} = 100$.

Figure 5.13: Temporal evolution of the mixing region growth rate, $\dot{h}$. Red: $k_o = 4$; green: $k_o = 8$; blue: $k_o = 16$. Solid: RT-turb set-up; dashed: classical RT set-up

rate decreases as the initial turbulent field decays. The growth rate increases again due to the baroclinic vorticity generation by the RTI. At late times, the growth rate saturates as the mixing region width becomes comparable to the box size.

For the RTI in the pure-mode coupling regime, Cook *et al.* (2004) used a mass flux and energy argument while Ristorcelli & Clark (2004) used similarity assumptions to obtain

$$\dot{h}^2 = 4\alpha A g h, \tag{5.22}$$

which yields

$$h = \alpha A g t^2 + 2\left(\alpha A g h_0\right)^{1/2} + h_0. \tag{5.23}$$

Thus α can be measured in two ways. In the first approach,

$$\alpha_A = \frac{h}{Atgt^2} - \left(\frac{\alpha h_o}{Atg}\right)^{1/2} \frac{2}{t} - \frac{h_o}{Atgt^2}, \tag{5.24}$$

and for late times where a self-similar growth is obtained simplifies to

$$\alpha_A = \frac{h}{Atgt^2}. \tag{5.25}$$

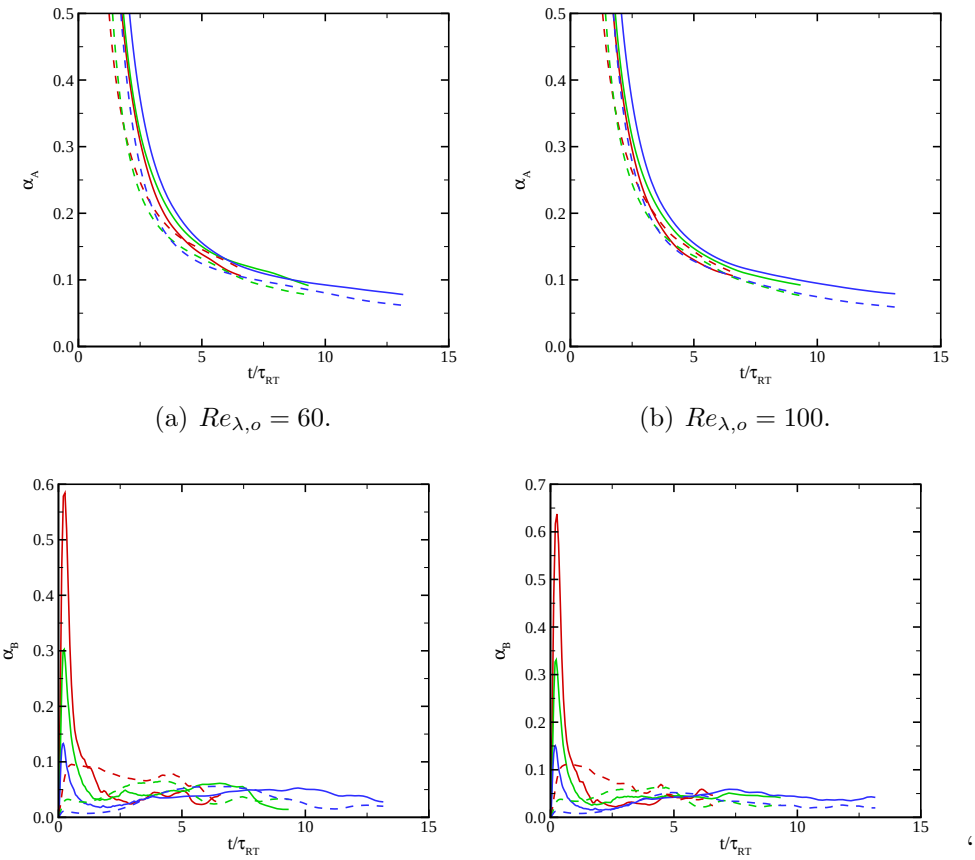

(a) $Re_{\lambda,o} = 60$. (b) $Re_{\lambda,o} = 100$.

(c) $Re_{\lambda,o} = 60$. (d) $Re_{\lambda,o} = 100$.

Figure 5.14: Temporal evolution of α_A and α_B for $Re_{\lambda,o} = 60$ (left), and 100 (right). Red: $k_o = 4$; green: $k_o = 8$; blue: $k_o = 16$. Solid: RT-turb set-up; dashed: classical RT set-up.

In the second approach α is measured as,

$$\alpha_B = \frac{\dot{h}^2}{4Atgh}. \tag{5.26}$$

Assuming that the mixing region grows at t^2, we can use our data to measure α (figure 5.14). Based on the first measure, α_A does not reach a steady state by the end of the simulation, especially for lower k_0. The measured value of α_B are almost converged and in a better agreement with previous studies (Dimonte *et al.*, 2004). For $k_0 = 16$, $\alpha_B \approx 0.04 \pm 0.015$ in our study. While α can be measured, the reported value of α is misleading and perhaps meaningless if the mixing region does not scale as t^2.

As discussed in Section 5.3, our initial condition does not satisfy the requirements to achieve the pure-mode coupling regime. Thus, we investigate the growth exponent directly from our DNS data. Assuming that $h \sim t^n$, n can be measured as,

$$n = \frac{\ln\left[\frac{h(t-t_0+\Delta t)}{h(t-t_0-\Delta t)}\right]}{\ln\left[\frac{t-t_0+\Delta t}{t-t_0-\Delta t}\right]}, \tag{5.27}$$

where $t_0 = 0.0$ is the virtual point of origin. The measured values of n are shown in figure 5.15. For the RT-turb set-up, the growth exponent increases initially and stays at the same level for a short while. The growth is dominated by turbulence diffusion over this time period. As τ_{RT}/τ_{turb} increases with k_0, this initial period is longer for lower values of k_0. After this initial period, the growth exponent increases due to the RTI up to 1.5. At late times, the growth exponent reduces, possibly due to box size effects. For the classical RT set-up the growth exponent increases continuously up to 1.5 and again decreases slightly due to box size effects. For $Re_{\lambda_0} = 100$ and $k_0 = 16$, n converges to approximately 1.3 for the RT-turb set-up and to 1.1 for the classical RT set-up. The current analysis suggests that the growth exponent indeed does not reach 2. Thus the reported values of α are not meaningful for our set-up as the t^2 growth is not achieved.

The effective Atwood number is defined as (Cook *et al.*, 2004)

$$At_e \equiv \frac{\rho_{rms}|_{z=z_0}}{\langle\rho\rangle\,|_{z=z_0} A}, \tag{5.28}$$

and is a measure of how fast the two fluids are mixed compared to the rate of pure fluids entrained to the mid-plane. For immiscible fluids, $At_e \approx A$ assuming $\langle\rho\rangle\,|_0 \approx (\rho_1 + \rho_2)/2$ (Cook *et al.*, 2004). The temporal evolution of the effective Atwood number is shown in figure 5.16. At_e increases initially as pure fluids are entrained through the mid-plane. The increase stops at later times as the two fluids start to diffuse and even results in a slight decrease of At_e for some cases. At_e is found to be

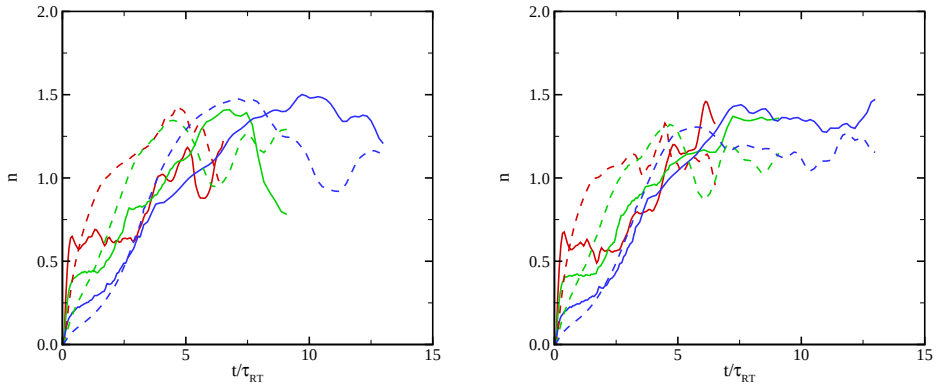

(a) $Re_{\lambda,o} = 60$. (b) $Re_{\lambda,o} = 100$.

Figure 5.15: Temporal evolution of the mixing region width exponent for $Re_{\lambda,o} = 60$ (left), and 100 (right). Red: $k_o = 4$; green: $k_o = 8$; blue: $k_o = 16$. Solid: RT-turb set-up; dashed: classical RT set-up.

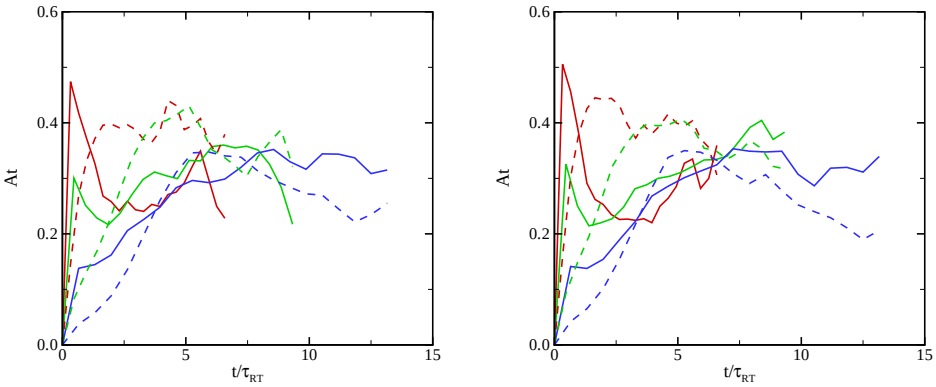

(a) $Re_{\lambda,o} = 60$. (b) $Re_{\lambda,o} = 100$.

Figure 5.16: Temporal evolution of the effective Atwood number for $Re_{\lambda,o} = 60$ (left), and 100 (right). Red: $k_o = 4$; green: $k_o = 8$; blue: $k_o = 16$. Solid: RT-turb set-up; dashed: classical RT set-up.

less than 0.5 for all of the cases. The fluctuations in At_e can be responsible for the fluctuations seen in the exponent growth component (figure 5.15).

The outer-scale Reynolds number is defined as

$$Re_h = 4Re\frac{\langle\rho\rangle\,|_{z=z_0} h\dot{h}}{\mu|_{z=z_0}}, \tag{5.29}$$

and is plotted in figure 5.17. In the literature, the distance between the bubble and spike fronts has been used previously to define the outer-scale Reynolds number (Cook

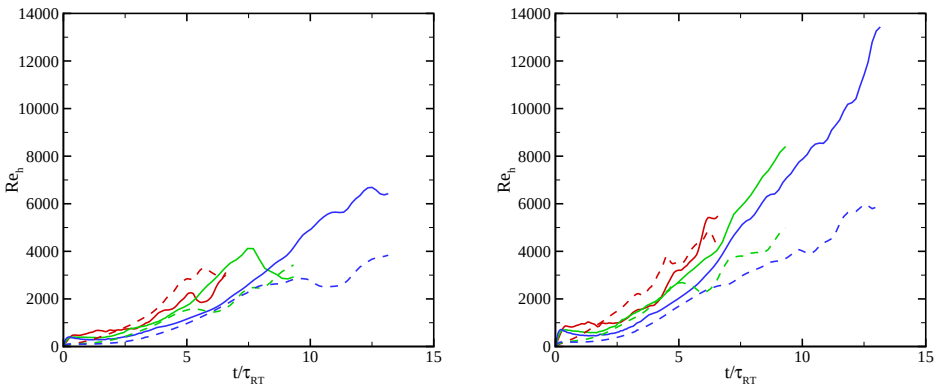

(a) $Re_{\lambda,o} = 60$. (b) $Re_{\lambda,o} = 100$.

Figure 5.17: Temporal evolution of Re_h for $Re_{\lambda,o} = 60$ (left), and 100 (right). Red: $k_o = 4$; green: $k_o = 8$; blue: $k_o = 16$. Solid: RT-turb set-up; dashed: classical RT set-up.

& Dimotakis, 2001; Cabot & Cook, 2006). As h represents half of the distance between the bubble and spike fronts, we included a factor of 4 in the outer-scale Reynolds number definition to be consistent with previous RT studies (Cook & Dimotakis, 2001; Cabot & Cook, 2006). Re_h increases with k_0 and $Re_{\lambda,o}$. The highest outer-scale Reynolds number achieved in our simulations is 13,000 for $k_0 = 16$, and $Re_{\lambda,o} = 100$.

5.4.6 Mixedness

Mixing can be quantified by considering a hypothetical reaction between two pure fluids where the fully mixed fluid is the product corresponding to a stoichiometric mixture of the two fluids (Cook & Dimotakis, 2001). The mass fraction of the mixed fluid is

$$Y_m(Y) = \begin{cases} 2Y & \text{if} \quad Y \leq 0.5, \\ 2(1-Y) & \text{if} \quad Y > 0.5, \end{cases} \tag{5.30}$$

where the stoichiometric coefficient is taken as 0.5. The mixing region width (entrainment length) is defined as

$$h_m = \int_{-\infty}^{\infty} Y_m \left(\langle Y \rangle \right) dz, \tag{5.31}$$

where h_m represents the maximum thickness of the product fluid (mixed fluid) if the fluid entrained into the mixing region is perfectly mixed in each x-y plane, thus implying that there are no perturbations from the mean. For a stoichiometric coefficient of 0.5, equation 5.31 reduces to equation 5.21. A measure of mixedness, Ξ, can be defined by comparing the total amount of the product with the maximum possible product as

$$\Xi = \frac{\int_{-\infty}^{\infty} \langle Y_m \rangle \, dz}{h_m}. \tag{5.32}$$

Figure 5.18 shows the temporal evolution of the mixedness of the mixing region. Since no mass fraction perturbation exists in any x-y plane initially, Ξ starts from unity and decreases as the velocity perturbs the mass fraction field and entrains one fluid into the other, thus creating inhomogeneous regions in x-y. The sudden initial decrease is greater for lower k_0 for the RT-turb set-up as the larger eddies for lower k_0 cause higher fluctuations in the mass fraction field. After this drop in Ξ, the mixedness increases as the mean kinetic energy and enstrophy decrease, such that the fluid newly entrained into the mixing region is not sufficiently energetic to perturb the mass fraction field. Next, Ξ decreases again as the set-up is RT unstable and the energy provided by the instability results in higher mass fraction fluctuations. At late times, Ξ reaches a nearly steady state. At this stage, the rate of generation of mass fluctuations is balanced by the scalar dissipation. A similar trend is also observed for the classical RT set-up. As the instability develops, mass fraction fluctuations are generated. It takes a longer time for higher k_0 to reach the minimum. At later times, Ξ increases, thus suggesting a balance between molecular diffusion and entrainment

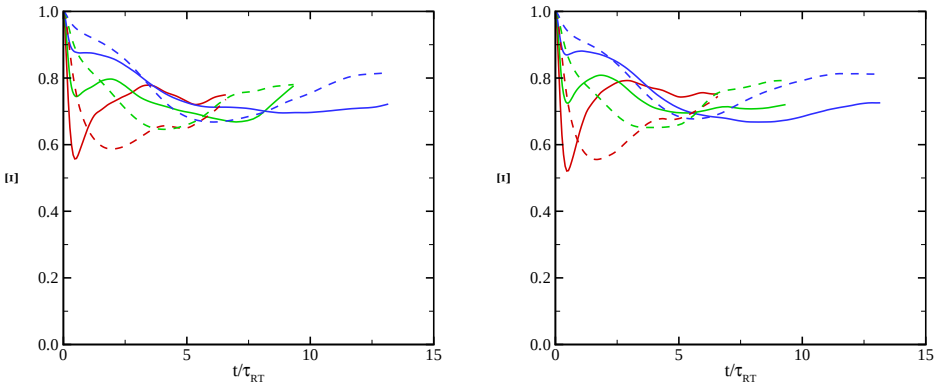

(a) $Re_{\lambda,o} = 60$. (b) $Re_{\lambda,o} = 100$.

Figure 5.18: Temporal evolution of the mixedness for $Re_{\lambda,o} = 60$ (left), and 100 (right). Red: $k_o = 4$; green: $k_o = 8$; blue: $k_o = 16$. Solid: RT-turb set-up; dashed: classical RT set-up.

from the "edges" of the mixing region.

5.5 Results: dynamics of the small scales in the mixing region

We now shift our focus to the small scales. To quantify flow isotropy across the different turbulent scales in the mixing region, energy spectra are first considered in Section 5.5.1. Then anisotropy at different length scales is investigated (Section 5.5.2), followed by an examination of intermittency in Section 5.5.3. All of the quantities reported in this section are measured well within the mixing zone, in range $0.25 \leq \langle Y \rangle \leq 0.75$.

5.5.1 Two-dimensional energy spectra

At each x-y plane in the mixing region, the two-dimensional energy spectra for each fluctuating field $\phi' = \phi - \langle \phi \rangle$ is calculated and averaged in the $z-$direction inside the mixing region. Figure 5.19 (5.20) shows the energy spectra of the RT-turb set-up (classical RT set-up) for the density, mass fraction, and z-velocity fluctuating fields for

$Re_{\lambda,o} = 100$ and $k_0 = 8$. For the RT-turb set-up, the initial velocity field perturbs the density and mass fraction fields. During the first 12 eddy turn-over times, the energy at large wave numbers decreases monotonically, but increases at small wavenumbers. In the absence of gravity, the turbulent fluctuations decay with time. For the present RT-unstable set-up, baroclinic vorticity is continuously generated throughout the mixing region due to the misalignment between the (hydrostatic) pressure and density gradients, which provides energy to drive the turbulence and maintain fluctuations inside the mixing region. It is interesting to note that the spectra profiles almost collapse on each other after 12 eddy turn-over times. This suggests that the rate of energy transfer to the small scales is similar to the dissipation rate.

For the classical RT set-up, the initial behaviour is different. The density, mass fraction and velocity fields get perturbed as the RTI develops. The energy at small wavenumbers increases in a fashion similar to that of the RT-turb set-up, but by a larger amount. Unlike the RT-turb set-up, the energy at high wavenumbers increases between 2-12 eddy turn-over times. Between 20-40 eddy turn-over times, the spectra almost collapse, particularly at high wavenumbers as in the classical RT set-up.

5.5.2 Temporal evolution of the Taylor and Kolmogorov scales

The flow in the mixing region is expected to become anisotropic at least at large scales due to the presence of both the large scale density gradient across the mixing region and the directed gravitational force. To study anisotropy at different scales, directional Taylor and Kolmogorov scales are defined as λ_i and η_i, respectively, in the ith direction (Cook & Dimotakis, 2001; Cabot & Zhou, 2013):

$$\lambda_i(z,t) = \left[\frac{\langle u_i^2 \rangle}{\left\langle \left(\frac{\partial u_i}{\partial x_i}\right)^2 \right\rangle}\right]_{mz}^{1/2}, \quad \eta_i(z,t) = \left[\frac{(\nu/Re)^3}{\epsilon_i}\right]_{mz}^{1/4}, \tag{5.33}$$

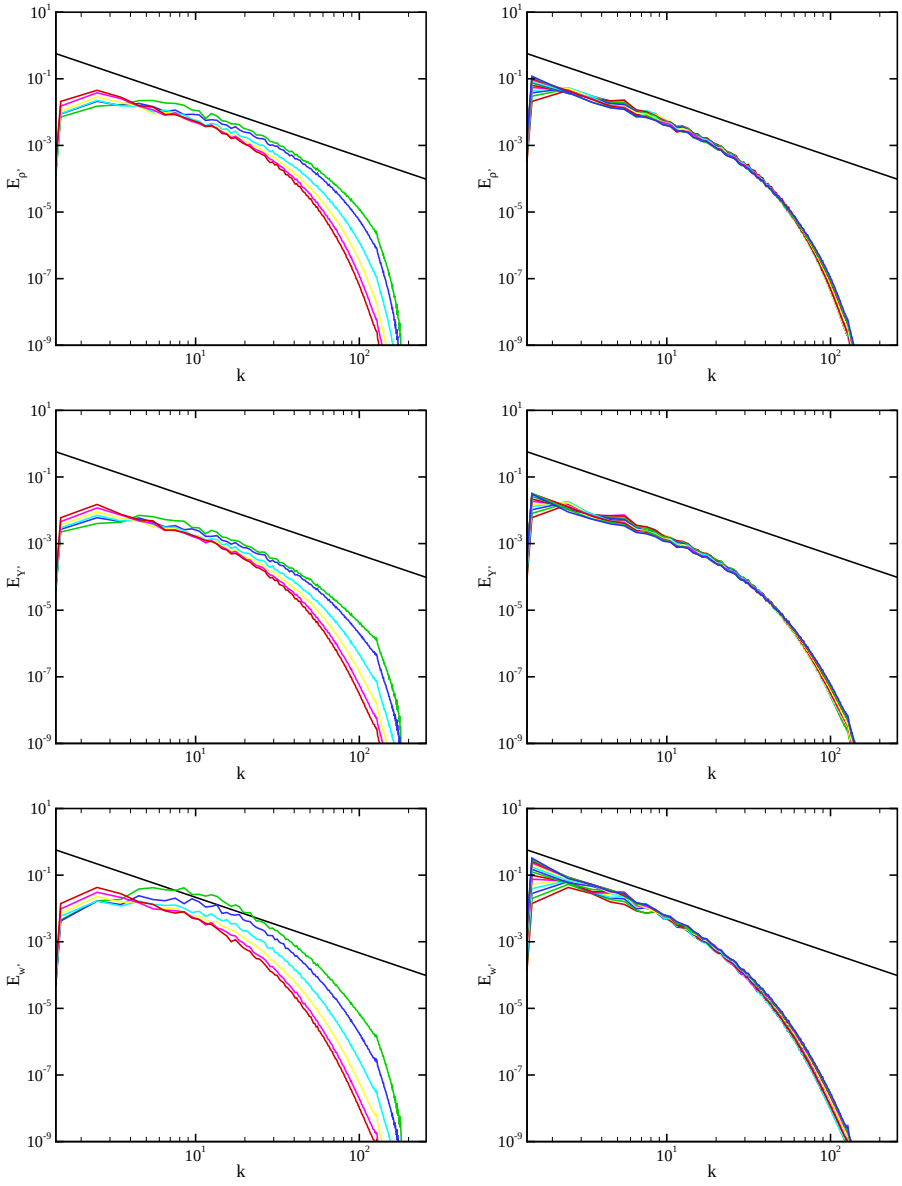

Figure 5.19: Two-dimensional spectra of density, mass fraction and vertical velocity fluctuations of the RT-turb set-up for $Re_{\lambda,o} = 100$, $k_0 = 8$. $t/\tau = 2$ (green), 4 (blue), 6 (cyan), 8 (yellow), 10 (pink), 12 (red) on the left; $t/\tau =$ 12-40 on the right.

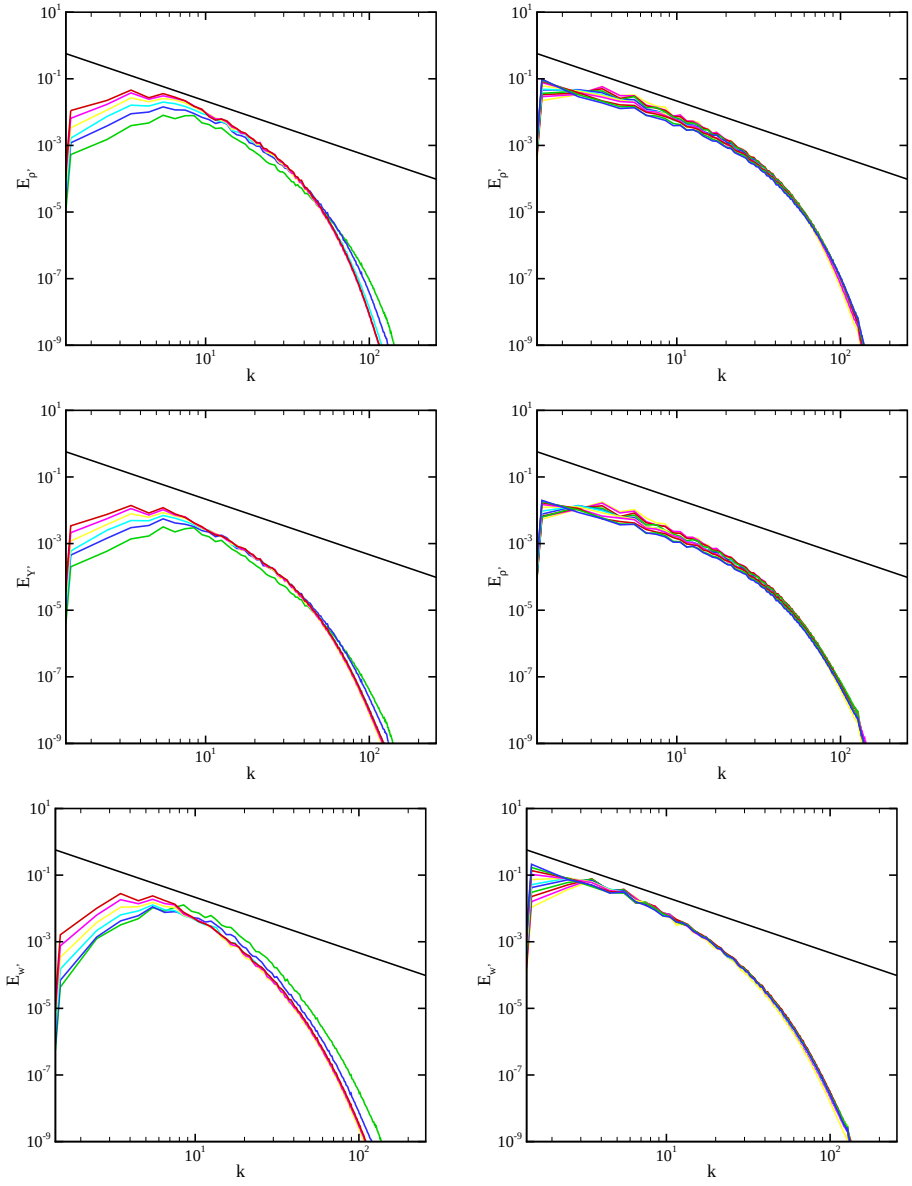

Figure 5.20: Two-dimensional spectra of density, mass fraction and vertical velocity fluctuations of the classical RT set-up for $Re_{\lambda,o} = 100$, $k_0 = 8$. $t/\tau =$ 2 (green), 4 (blue), 6 (cyan), 8 (yellow), 10 (pink), 12 (red) on the left; $t/\tau =$ 20-40 on the right.

where

$$\epsilon_i(z,t) = \frac{15\nu}{Re}\left\langle \left(\frac{\partial u_i}{\partial x_i}\right)^2 \right\rangle \tag{5.34}$$

is the directional dissipation rate and $[\cdot]_{mz}$ is average in the z-direction well within the mixing zone, in range $0.25 \leq \langle Y \rangle \leq 0.75$. By contrast, the overall dissipation is defined

$$\epsilon = \frac{2\nu}{Re} S^*_{ij} S^*_{ij}, \tag{5.35}$$

where

$$S^*_{ij} = S_{ij} - \frac{\delta_{ij}}{3} S_{kk}, \quad S_{ij} = \frac{1}{2}\left(\frac{\partial u_i}{\partial x_j} + \frac{\partial u_j}{\partial x_i}\right), \tag{5.36}$$

and S_{ij} is the strain-rate tensor.

Figure 5.21 shows the temporal evolution of the Taylor microscale. In contrast to the results in the absence of gravity, the flow is anisotropic in the z-direction in the presence of gravity at $\rho_2/\rho_1 = 3$. The temporal evolution in the x- and y-directions are similar for both the RT-turb and the classical RT set-ups. After an initial transient, the Taylor scale increases more rapidly in the z-direction. This result is in agreement with previous RT simulations. The initial most energetic wavenumber used here to perturb the initial interface is the same as that used in DNS by Cook & Dimotakis (2001), who reported an increase in the Taylor scale following a decrease, especially at late times for low k_0. Our results suggest that the initial rate of increase in the Taylor microscale decreases by the time that the mixing width becomes comparable to the box size. The Taylor-scale Reynolds number is plotted in figure 5.22. Re_λ exceeds the mixing transition Reynolds number for $Re_{\lambda,o} = 100$. Higher Re_λ are achieved at higher k_0.

The directional Kolmogorov scales are plotted in figures 5.23 & 5.24. Previous RT simulations, where the initial energy is put at high wavenumbers and the amplitude of the perturbations are small, suggest that the flow remains isotropic at the Kolmogorov microscale. We observed a similar behavior in the absence of gravity (previous chap-

ter). By contrast, the present RT results suggest that the flow exhibits anisotropy at the Kolmogorov scale over a certain time period, before becoming isotropic again. The general trend suggests that initially the dissipation rate is similar in all directions. Subsequently, the dissipation rate increases in the z-direction, resulting in a smaller Kolmogorov scale in this direction. The anisotropy observed at the Kolmogorov scale may be due to a process that is not self-similar during that period.

5.5.3 Flow intermittency

The directional skewness S and kurtosis K of the velocity derivatives in the mixing region ($0.25 \leq \langle Y \rangle \leq 0.75$) are defined as (Cabot & Zhou, 2013)

$$S_{\frac{\partial u_i}{\partial x_i}} = \left[\frac{\left\langle \left(\frac{\partial u_i}{\partial x_i} \right)^3 \right\rangle}{\left\langle \left(\frac{\partial u_i}{\partial x_i} \right)^2 \right\rangle^{1.5}} \right]_{mz}, \qquad K_{\frac{\partial u_i}{\partial x_i}} = \left[\frac{\left\langle \left(\frac{\partial u_i}{\partial x_i} \right)^4 \right\rangle}{\left\langle \left(\frac{\partial u_i}{\partial x_i} \right)^2 \right\rangle^2} \right]_{mz}, \tag{5.37}$$

where it is implied that there is no sum in i. These quantities are representative of small-scale intermittency of the velocity field. In Chapter IV, we observed that in the absence of gravity, the skewness is approximately -0.5 in all directions, in agreement with previous grid turbulence experiments (Sreenivasan & Antonia, 1997). In the presence of gravity, skewness in the $z-$direction decreases with time until a value close to -1 is reached (figure 5.25). Subsequently, skewness in the x- and y-directions increases slightly. The measured values do not vary significantly across the different set-ups, $Re_{\lambda,o}$ and k_o. While the average skewness in the mixing region is close to that of grid turbulence, the measured values depart significantly from -0.5 at the bubble and spike fronts (figures 5.26 & 5.26). The skewness decreases significantly in the z-direction, but increases in the x- and y-directions. The level of intermittency also increases significantly at the bubble and spike fronts at higher k_0 (figure 5.28). The high level of intermittency can potentially be used to measure the mixing region width. Given the range over which S and K vary, the average skewness shows clear

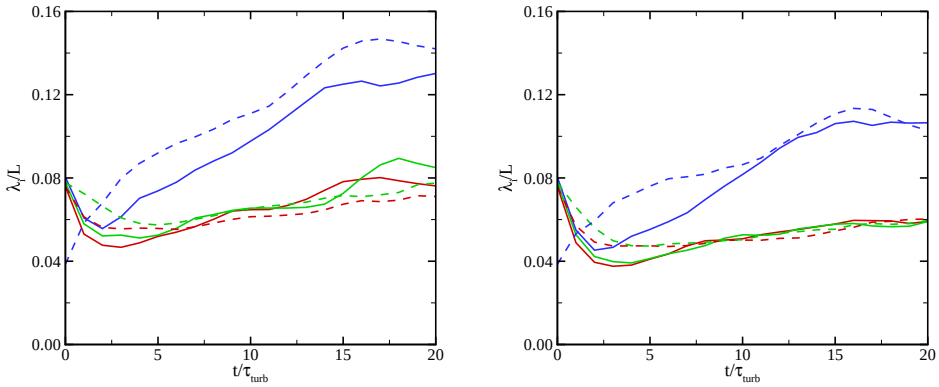

(a) $Re_{\lambda,o} = 60$, $k_o = 4$.

(b) $Re_{\lambda,o} = 100$, $k_o = 4$.

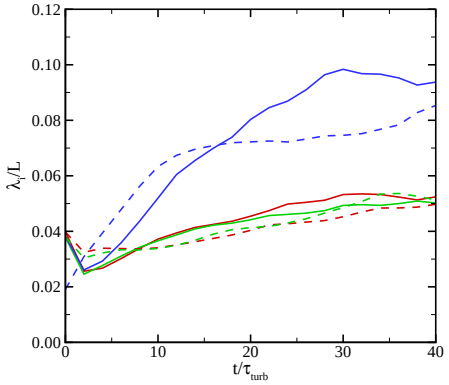

(c) $Re_{\lambda,o} = 60$, $k_o = 8$.

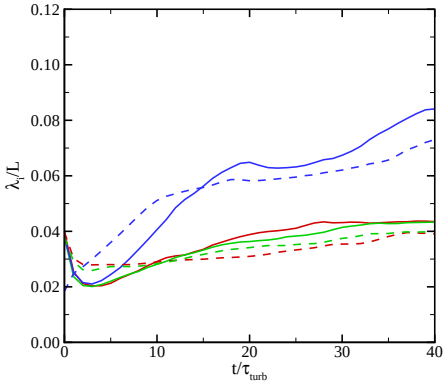

(d) $Re_{\lambda,o} = 100$, $k_o = 8$.

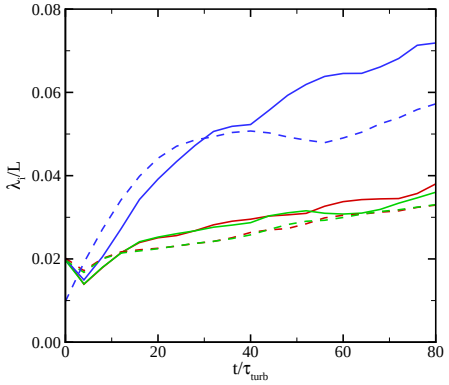

(e) $Re_{\lambda,o} = 60$, $k_o = 16$.

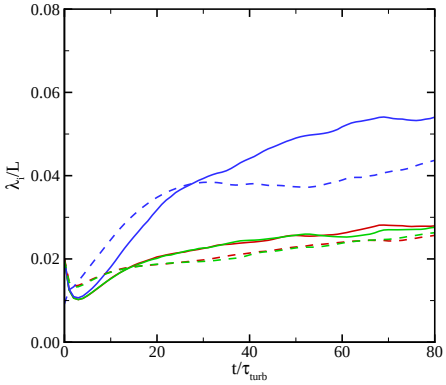

(f) $Re_{\lambda,o} = 100$, $k_o = 16$.

Figure 5.21: Time evolution of the directional Taylor scales for $Re_{\lambda,o} = 60$ (left), and 100 (right), and $k_o = 4$ (top), 8 (middle), and 16 (bottom). Red: x-component; green: y-component; blue: z-component. Solid: RT-turb set-up; dashed: classical RT set-up.

anisotropy in the statistics measured in the z-direction. The discrepancy between different directions is lower for the kurtosis in the mixing region (figure 5.29). The

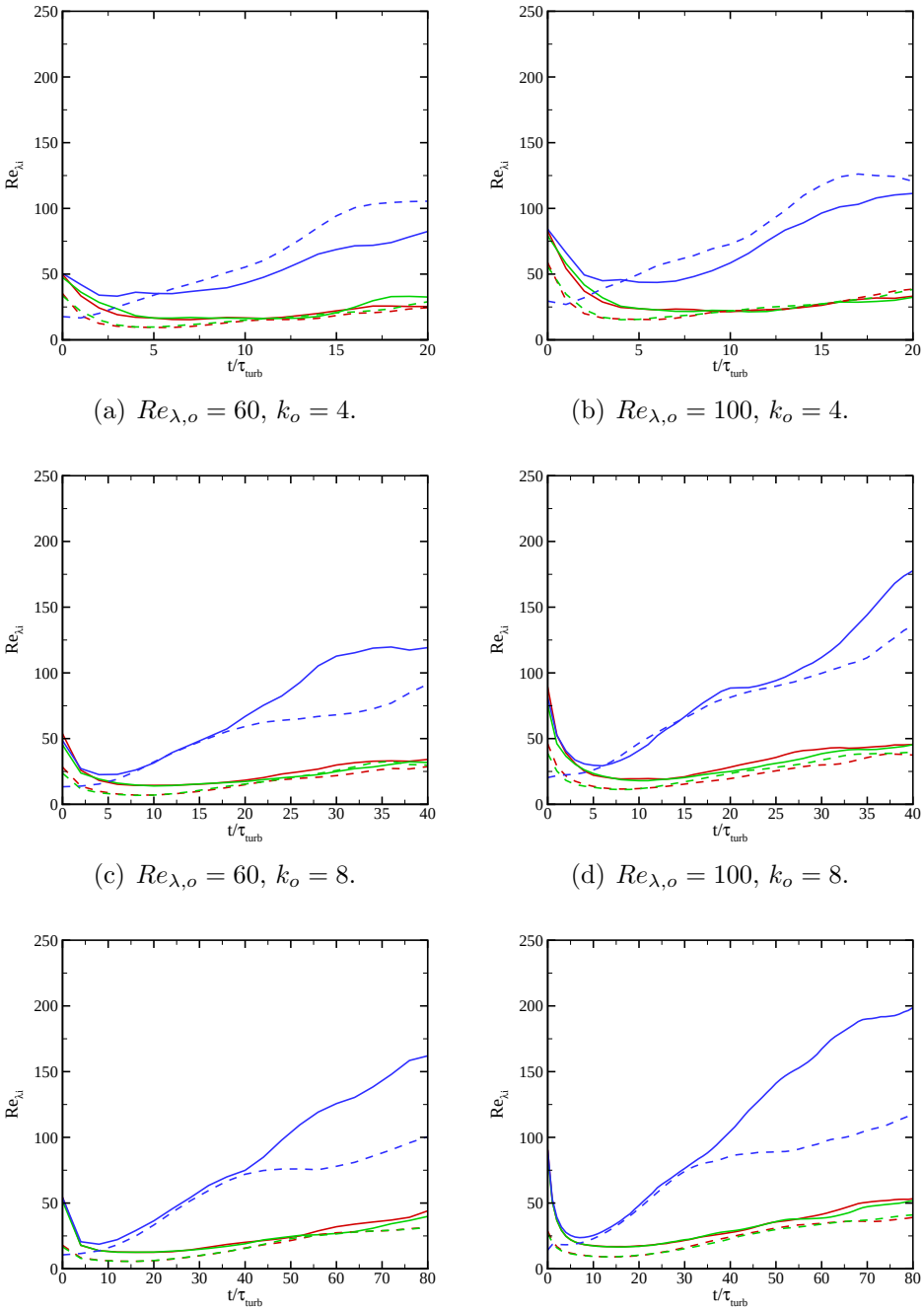

(a) $Re_{\lambda,o} = 60$, $k_o = 4$.

(b) $Re_{\lambda,o} = 100$, $k_o = 4$.

(c) $Re_{\lambda,o} = 60$, $k_o = 8$.

(d) $Re_{\lambda,o} = 100$, $k_o = 8$.

(e) $Re_{\lambda,o} = 60$, $k_o = 16$.

(f) $Re_{\lambda,o} = 100$, $k_o = 16$.

Figure 5.22: Temporal evolution of Re_λ in different directions for $Re_{\lambda,o} = 60$ (left), and 100 (right), and $k_o = 4$ (top), 8 (middle), and 16 (bottom). Red: x-component; green: y-component; blue: z-component. Solid: RT-turb set-up; dashed: classical RT set-up.

kurtosis is on average slightly higher in the z-direction compared to the x- and y-directions. The measured values are similar for both the RT-turb and the classical

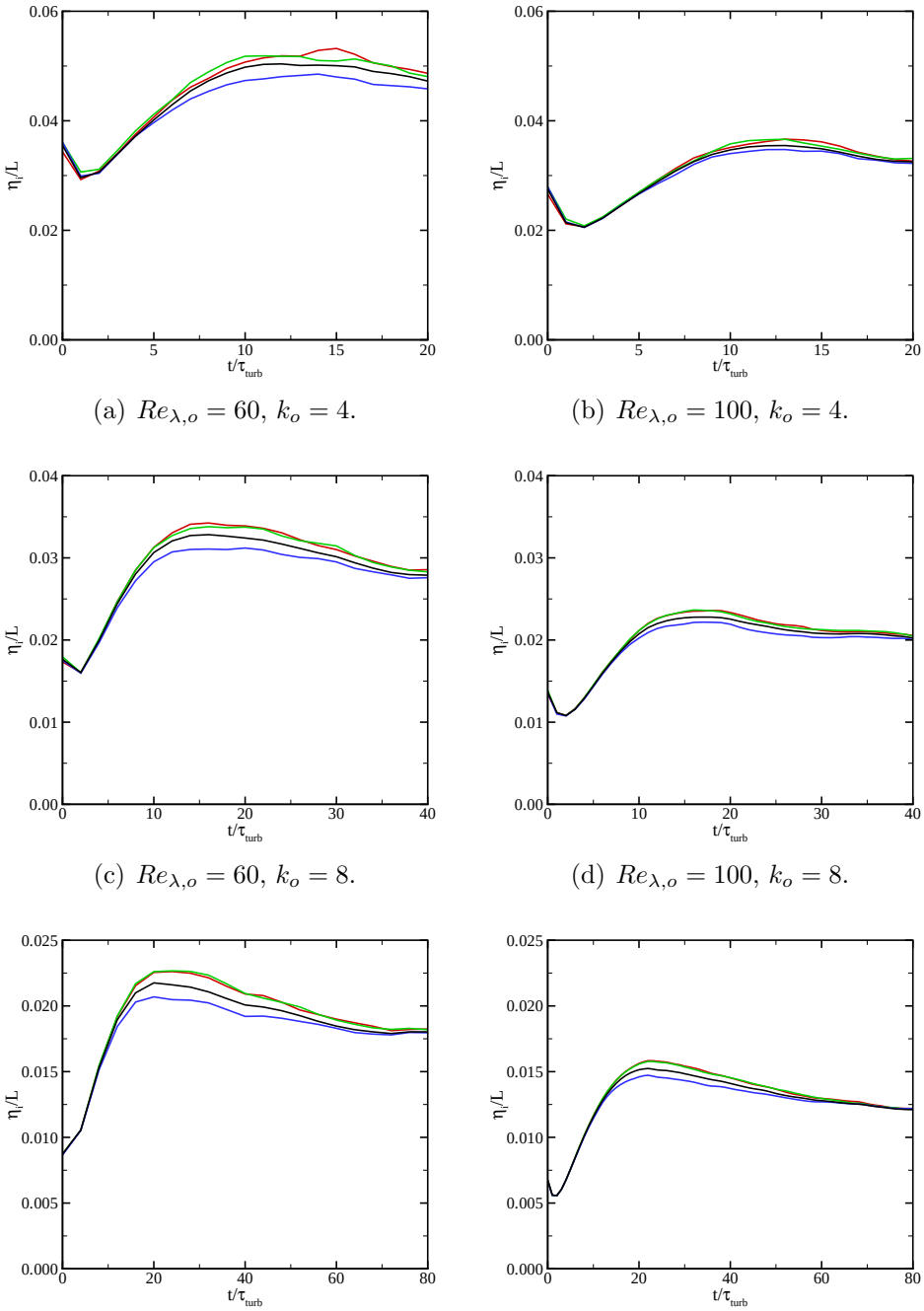

(a) $Re_{\lambda,o} = 60$, $k_o = 4$.

(b) $Re_{\lambda,o} = 100$, $k_o = 4$.

(c) $Re_{\lambda,o} = 60$, $k_o = 8$.

(d) $Re_{\lambda,o} = 100$, $k_o = 8$.

(e) $Re_{\lambda,o} = 60$, $k_o = 16$.

(f) $Re_{\lambda,o} = 100$, $k_o = 16$.

Figure 5.23: Time evolution of the directional Kolmogorov scales for $Re_{\lambda,o} = 60$ (left), and 100 (right), and $k_o = 4$ (top), 8(middle), and 16 (bottom). Red: x-component; green: y-component; blue: z-component; The Kolmogorov scale used by measuring the full dissipation is also plotted in black. RT-turb set-up.

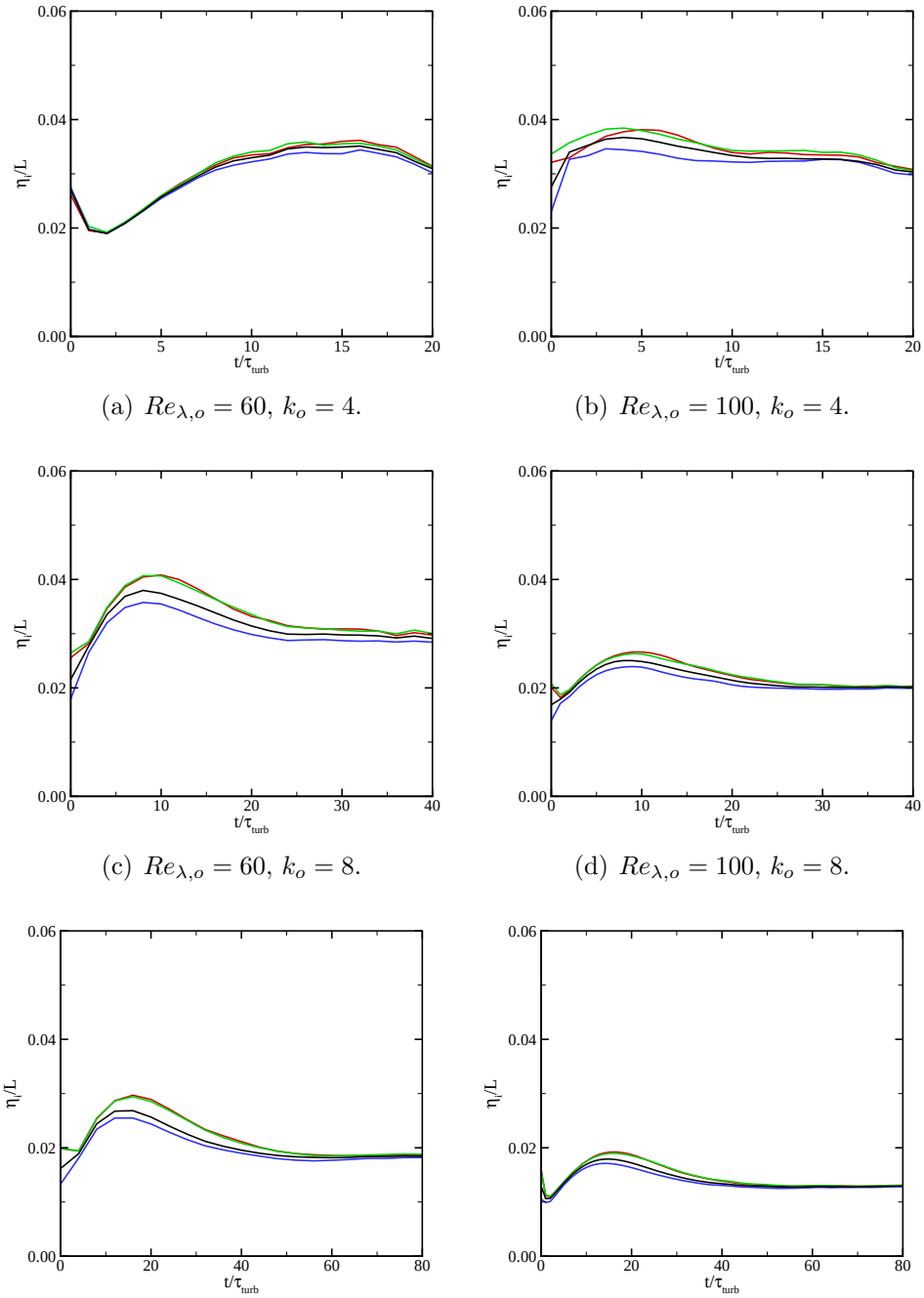

(a) $Re_{\lambda,o} = 60$, $k_o = 4$.

(b) $Re_{\lambda,o} = 100$, $k_o = 4$.

(c) $Re_{\lambda,o} = 60$, $k_o = 8$.

(d) $Re_{\lambda,o} = 100$, $k_o = 8$.

(e) $Re_{\lambda,o} = 60$, $k_o = 16$.

(f) $Re_{\lambda,o} = 100$, $k_o = 16$.

Figure 5.24: Time evolution of the directional Kolmogorov scales for $Re_{\lambda,o} = 60$ (left), and 100 (right), and $k_o = 4$ (top), 8 (middle), and 16 (bottom). Red: x-component; green: y-component; blue: z-component; The Kolmogorov scale used by measuring the full dissipation is also plotted in black. Classical RT set-up.

RT set-up for the given $Re_{\lambda,o}$ and k_0. High levels of kurtosis are observed at the bubble and spike fronts representing high intermittency (figure 5.30). The average kurtosis in the mixing region increases slightly with time. This increase can be related to the increase of Re_λ, since kurtosis is expected to increase with Re_λ (Sreenivasan & Antonia, 1997). The sudden increase at the bubble/spike fronts is not related to Re_λ and is mainly due to the abrupt change of turbulence characteristics inside and outside of the mixing region. A similar increase of intermittency has also been observed in jet flows outside the self-similar region (Stanley *et al.*, 2002).

The skewness and kurtosis of the mass fraction fluctuation field is plotted in figures 5.31 and 5.32. The average skewness in the x- and y-direction remains close to 0 as expected. In the z-direction, S decreases until it reaches a value of -3 for all set-ups. Similar to the velocity field, K increases with time. Higher values of K are observed in the z-direction. The mass fraction field is more intermittent than the velocity field.

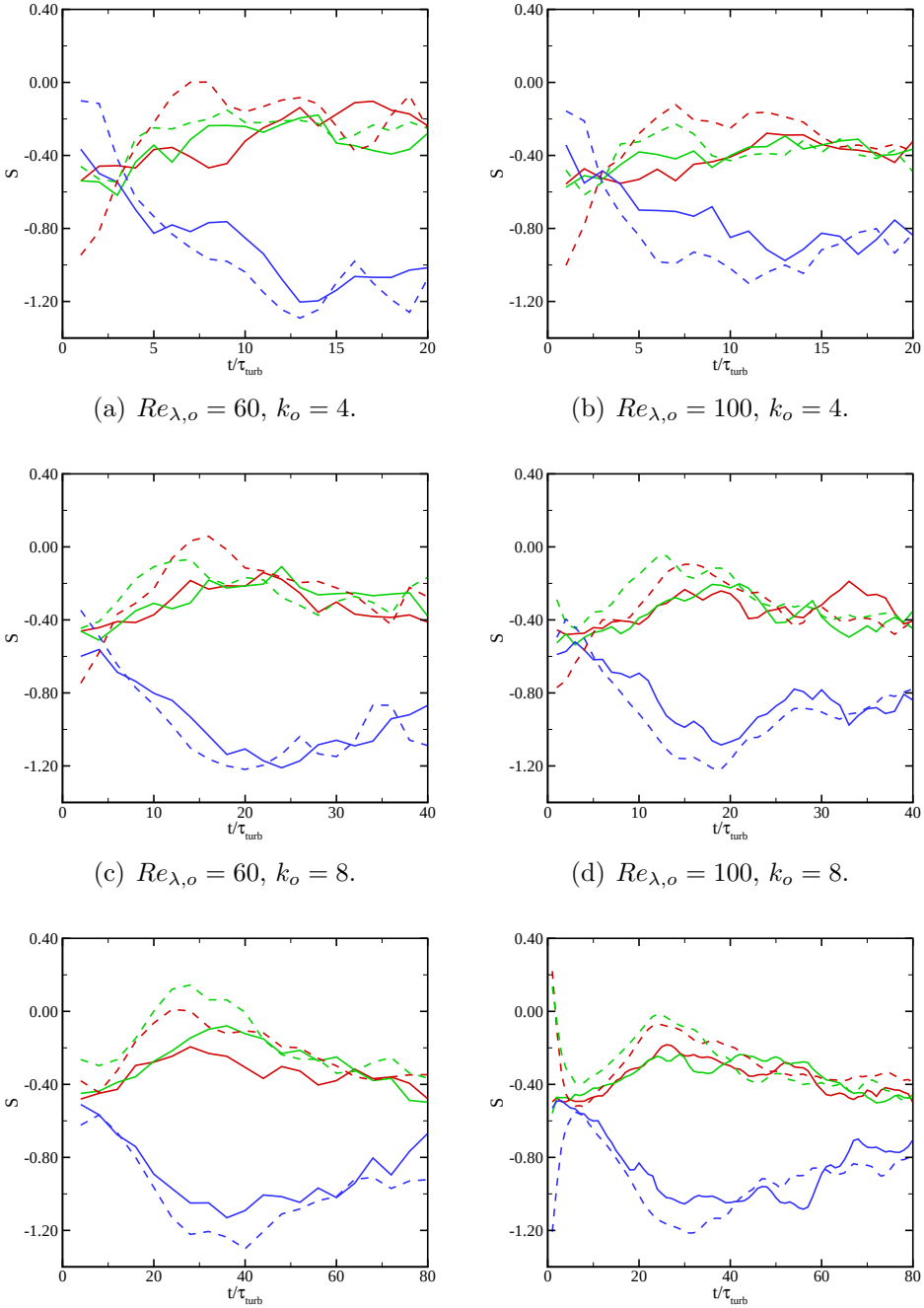

(a) $Re_{\lambda,o} = 60$, $k_o = 4$.

(b) $Re_{\lambda,o} = 100$, $k_o = 4$.

(c) $Re_{\lambda,o} = 60$, $k_o = 8$.

(d) $Re_{\lambda,o} = 100$, $k_o = 8$.

(e) $Re_{\lambda,o} = 60$, $k_o = 16$.

(f) $Re_{\lambda,o} = 100$, $k_o = 16$.

Figure 5.25: Time evolution of skewness of the velocity derivatives for $Re_{\lambda,o} = 60$ (left), and 100 (right), and $k_o = 4$ (top), 8 (middle), and 16 (bottom). Red: x-component; green: y-component; blue: z-component. Solid: RT-turb set-up; dashed: classical RT set-up.

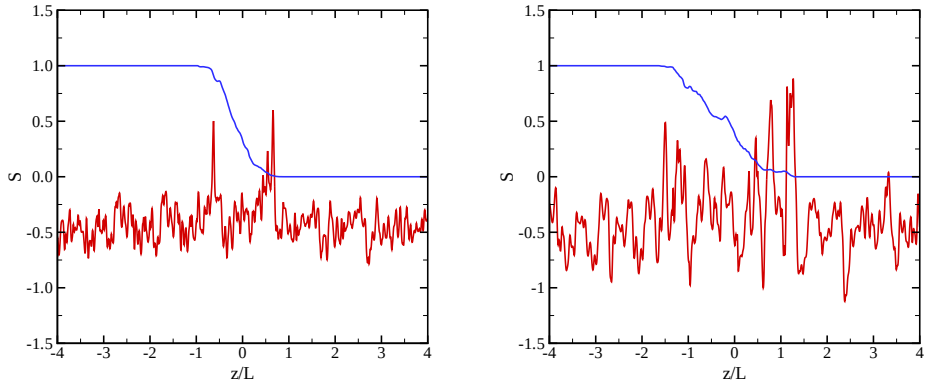

(a) $t = 10\tau$. (b) $t = 20\tau$.

Figure 5.26: Average skewness of the $x-$velocity derivative in the x-direction and mass fraction fields in the x-y plane at different times for $Re_{\lambda,o} = 100$, and $k_o = 4$.

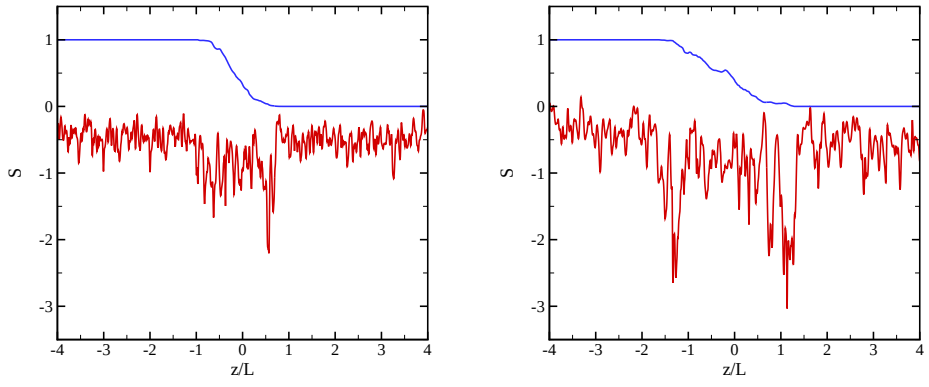

(a) $t = 10\tau$. (b) $t = 20\tau$.

Figure 5.27: Average skewness of the z-velocity derivative in the z-direction and mass fraction fields in the x-y plane at different times for $Re_{\lambda,o} = 100$, and $k_o = 4$.

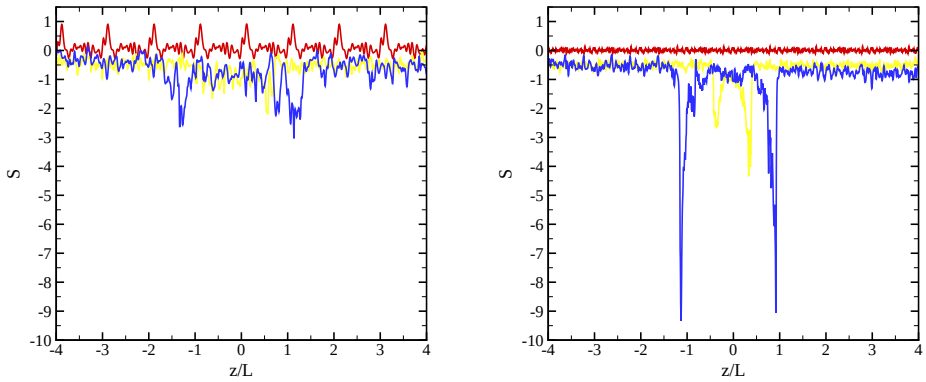

(a) $t = 0, 10, 20\tau_{turb}$. (b) $t = 0, 40, 80\tau_{turb}$.

Figure 5.28: Average skewness of the z-velocity derivative in the z-direction in the x-y plane at different times for $Re_{\lambda,o} = 100$, and $k_o = 4$, and 16.

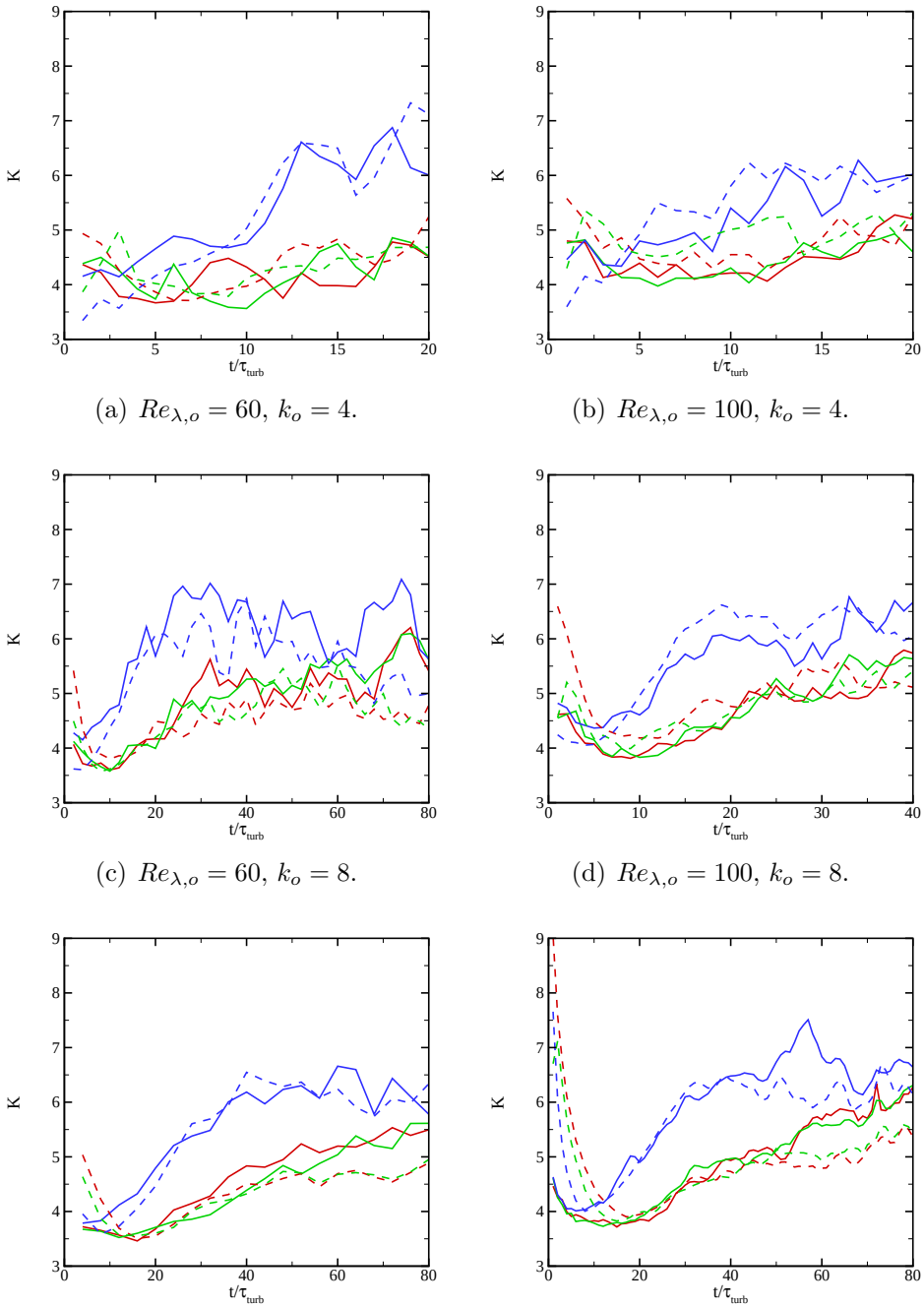

(a) $Re_{\lambda,o} = 60$, $k_o = 4$.

(b) $Re_{\lambda,o} = 100$, $k_o = 4$.

(c) $Re_{\lambda,o} = 60$, $k_o = 8$.

(d) $Re_{\lambda,o} = 100$, $k_o = 8$.

(e) $Re_{\lambda,o} = 60$, $k_o = 16$.

(f) $Re_{\lambda,o} = 100$, $k_o = 16$.

Figure 5.29: Time evolution of kurtosis of the velocity derivatives for $Re_{\lambda,o} = 60$ (left), and 100 (right), and $k_o = 4$ (top), 8 (middle), and 16 (bottom). Red: x-component; green: y-component; blue: z-component. Solid: RT-turb set-up; dashed: classical RT set-up.

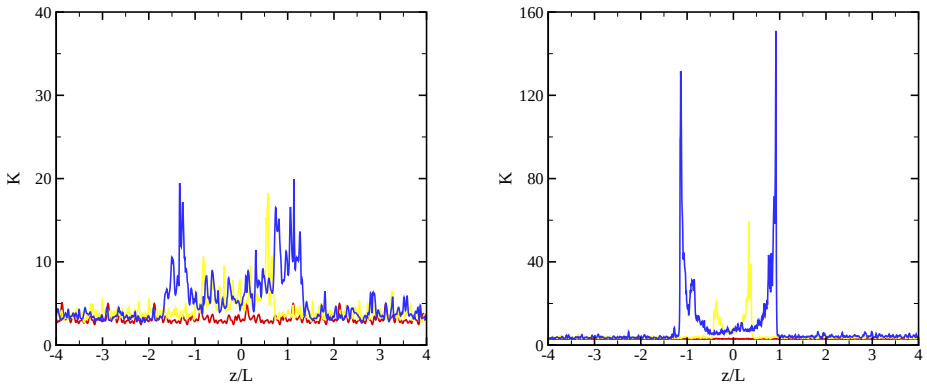

(a) $k_o = 4$, $t = 0, 10, 20\tau_{turb}$. (b) $k_o = 16$, $t = 0, 40, 80\tau_{turb}$.

Figure 5.30: Average kurtosis of the z-velocity derivative in the z-direction in the x-y plane at different times for $Re_{\lambda,o} = 100$, and $k_o = 4$ (left), and 16 (right).

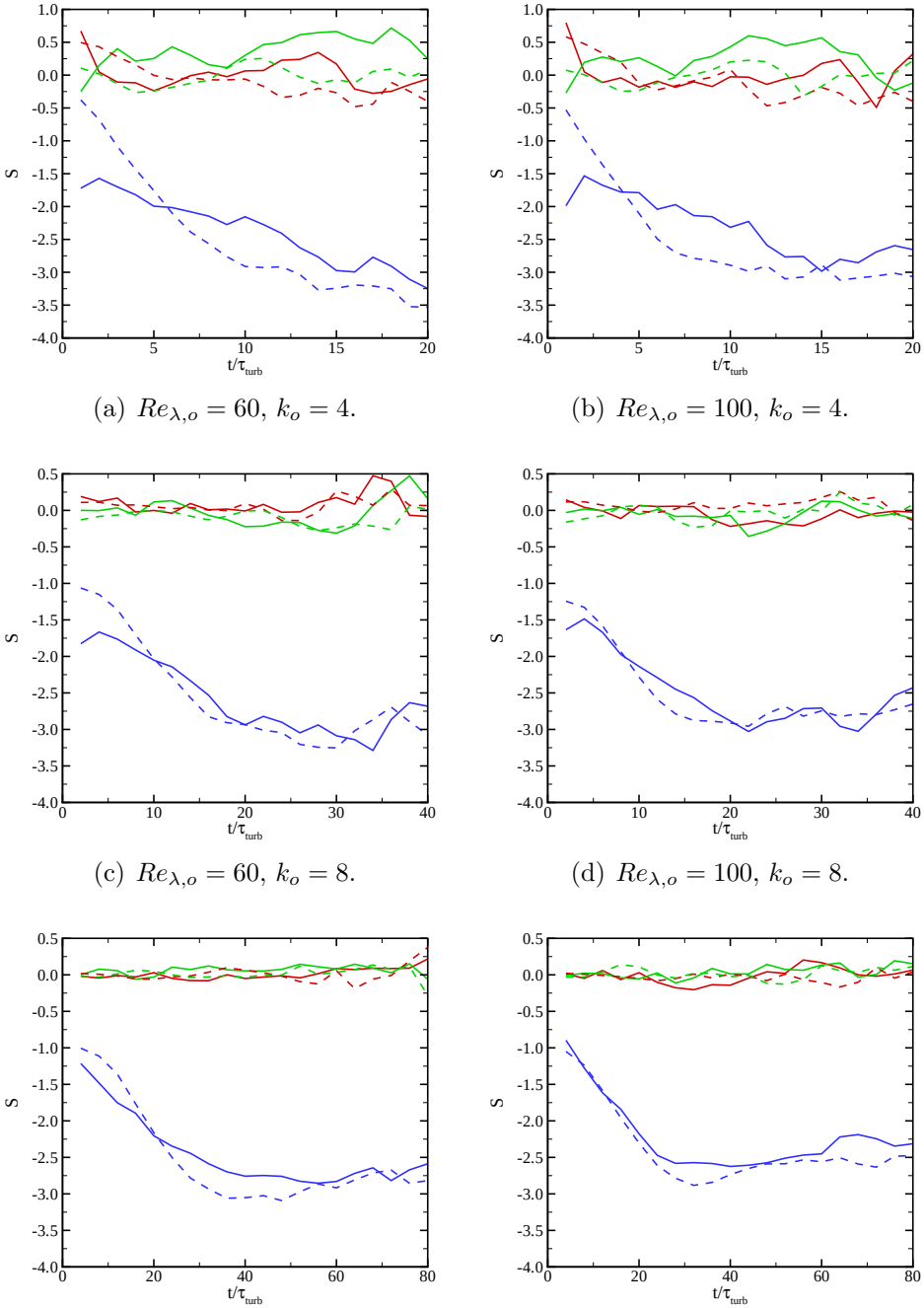

(a) $Re_{\lambda,o} = 60$, $k_o = 4$.

(b) $Re_{\lambda,o} = 100$, $k_o = 4$.

(c) $Re_{\lambda,o} = 60$, $k_o = 8$.

(d) $Re_{\lambda,o} = 100$, $k_o = 8$.

(e) $Re_{\lambda,o} = 60$, $k_o = 16$.

(f) $Re_{\lambda,o} = 100$, $k_o = 16$.

Figure 5.31: Time evolution of skewness of the mass fraction derivatives for $Re_{\lambda,o}$ = 60 (left), and 100 (rright), and k_o = 4 (top), 8 (middle), and 16 (bottom). Red: x-component; green: y-component; blue: z-component. Solid: RT-turb set-up; dashed: classical RT set-up.

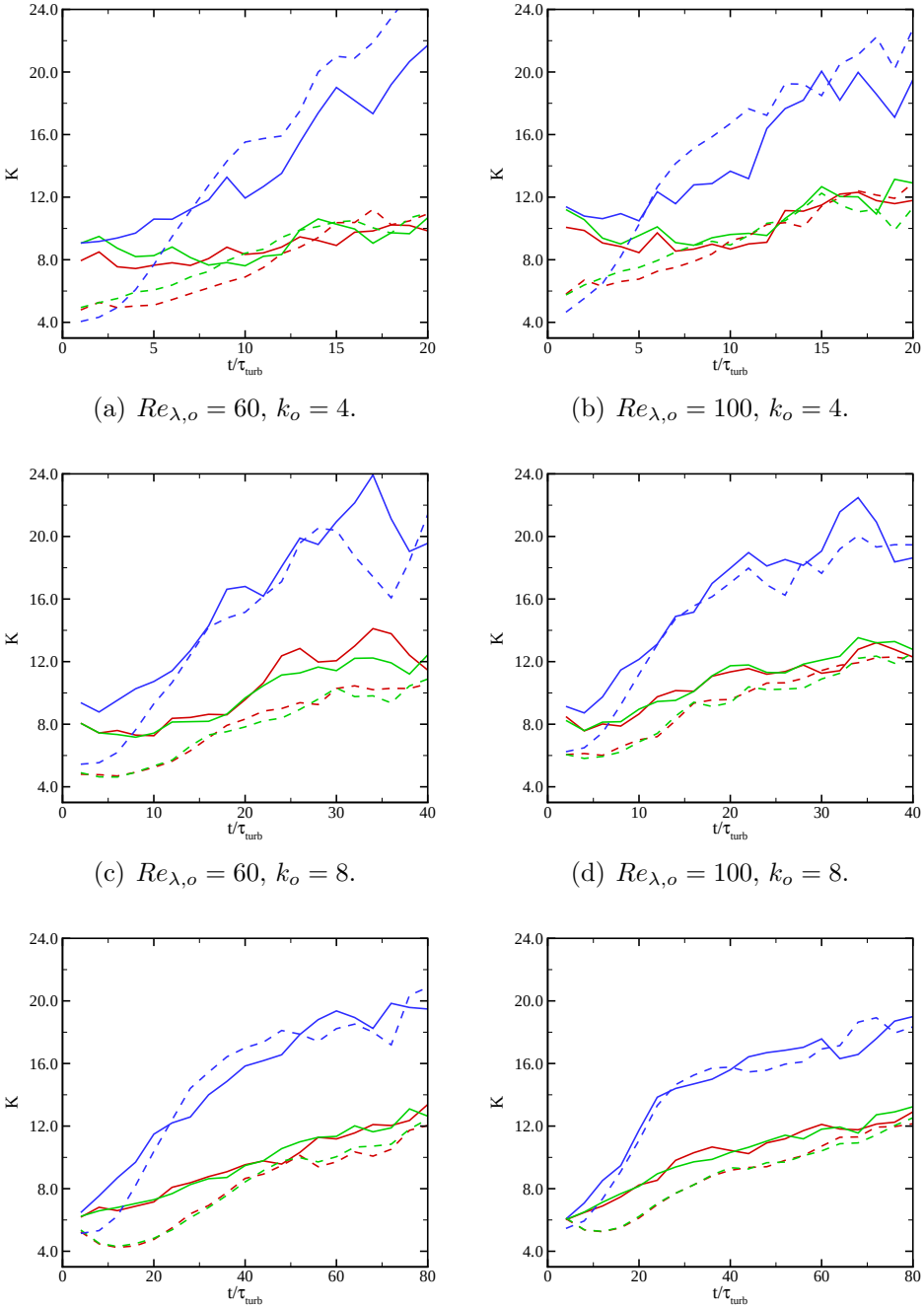

(a) $Re_{\lambda,o} = 60$, $k_o = 4$.

(b) $Re_{\lambda,o} = 100$, $k_o = 4$.

(c) $Re_{\lambda,o} = 60$, $k_o = 8$.

(d) $Re_{\lambda,o} = 100$, $k_o = 8$.

(e) $Re_{\lambda,o} = 60$, $k_o = 16$.

(f) $Re_{\lambda,o} = 100$, $k_o = 16$.

Figure 5.32: Time evolution of kurtosis of the mass fraction derivatives for $Re_{\lambda,o} = 60$ (left), and 100 (right), and $k_o = 4$ (top), 8 (middle), and 16 (bottom). Red: x-component; green: y-component; blue: z-component. Solid: RT-turb set-up; dashed: classical RT set-up.

5.6 Comparison with other relevant set-ups

In this section, my goal is to investigate how gravity affects the evolution of the mixing region in configurations different from the constant-density RT-unstable set-up considered here. In the previous sections of this chapter, the role of gravity was studied in a RT unstable configuration. In the absence of gravity, the evolution of the mixing region was studied in Chapter IV.

5.6.1 RT stable set-up

Sharp density interfaces are frequently present in stably stratified turbulent environments such as the base of the oceanic thermocline and at the top of the convective mixed layers of the atmospheric boundary layer (Huq & Britter, 1995*b*). Several experiments studied the evolution of a sharp density interface between two homogeneous stably stratified layers of different densities in a grid-generated turbulence. Part of the kinetic energy is used in these flows to mix the two fluids, which requires work against buoyancy forces (Linden, 1980; Turner, 1968). Subsequently, the vertical velocity component is suppressed, particularly a higher dissipation rate is observed for the vertical velocity component compared to the other components (Huq & Britter, 1995*b*; Itsweire *et al.*, 1986). In addition, buoyancy forces retard the growth of the Taylor microscale in the direction of gravity and the mixing region (Huq & Britter, 1995*b*; Lienhard & Van Atta, 1990; Hannoun & List, 1988).

To complete my study, I have done an additional run in a RT stable configuration here. In this configuration, the set-up is the same as that discussed in Section 5.3 except that the direction of gravity is reversed; Thus the set-up is no longer RT unstable. Consequently, the initial pressure and temperature are different such that the initial conditions are in hydrostatic equilibrium (equation 5.11).

Due to buoyancy, growth of the Taylor scale in the z-direction is suppressed after a certain time period and is clearly anisotropic(figure 5.33). The flow becomes

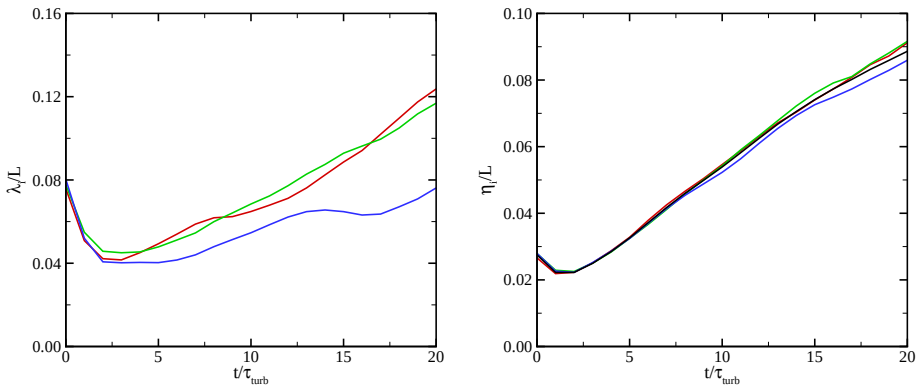

Figure 5.33: Time evolution of the directional Taylor (left) and Kolmogorov scales (right) for the RT stable configuration. Red: x-component; green: y-component; blue: z-component. The Kolmogorov scale used by measuring the full dissipation is also plotted in black.

anisotropic at the Kolmogorov scale after 15 eddy turn-over times. This suggests that the dissipation rate measured in the z-direction is higher compared to the other two directions.

The temporal evolution of the skewness and kurtosis of the velocity field and the mass fraction fields are shown in figure 5.34. Kurtosis decreases with time similar to the results without gravity. The skewness of the velocity field is approximately -0.5 corresponding to the decaying isotropic turbulence problem during the first 14 eddy turn-over times. Afterwards, skewness of the velocity field in the z-direction increases slightly, reaching zero by the end of the simulation. This effect is due to buoyancy as this behaviour was not observed in the runs without gravity. While the skewness of the mass fraction in the z-direction takes negative values due to anisotropy in the z-direction, it shows again lower levels of intermittency compared to the case without gravity due to buoyancy.

Now, we compare the results for the three different set-ups (RT stable, RT unstable and no gravity). The initial Taylor-sclae Reynolds number and the initial kinetic energy are 100 and 4, respectively. The initial mixing region evolves starting from an unperturbed material interface in a pre-existing turbulent field. Figure 5.36 shows the

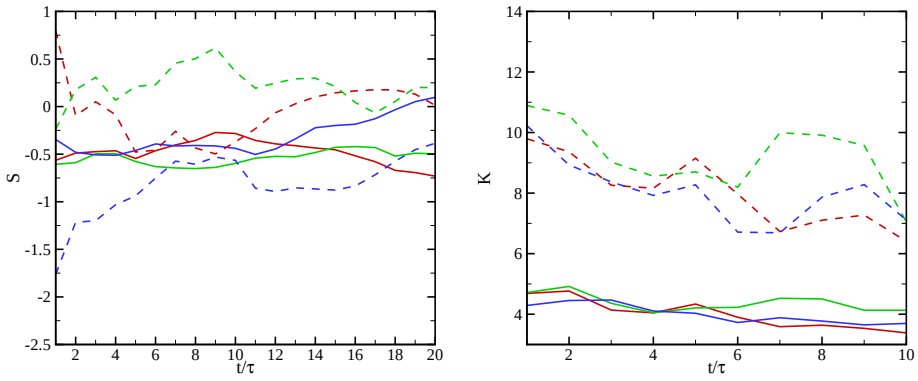

Figure 5.34: Temporal evolution of skewness (left) and kurtosis (right) of the velocity field (solid) and the mass fraction field (dashed) for the RT stable configuration. Red: x-component; green: y-component; blue: z-component.

temporal evolution of the mixing region width. The mixing region grows initially due to turbulence diffusion for all cases. As the initial velocity field decays, the growth rate decreases in the absence of gravity. In the RT unstable configuration, the potential energy gets converted to the kinetic energy and provides energy for the turbulence. This results in the highest growth compared to the other cases, as expected. In the RT stable configuration, the mixing region width stops growing after 5 eddy turnover times and even decreases slightly afterwards due to buoyancy. This result is in agreement with water tunnel experiments of Huq & Britter (1995*b*). Gravity has a similar effect on the temporal evolution of the Taylor scale in the $z-$direction as shown in figure 5.36. The Taylor scale increases for the RT unstable configuration compared to the no gravity case while decreases for the RT stable configuration compared to the no gravity case.

5.6.2 Isothermal set-up

I finish my RT study by considering one more RT unstable set-up. In the set-up discussed in Section 5.3, the density is uniform in each fluid, but the temperature varies also due to the hydrostatic pressure as shown in figure 5.5. Here I consider a set-up where the temperature is uniform in the whole domain. An isothermal

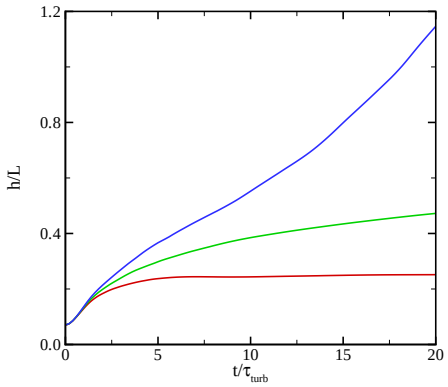

Figure 5.35: Temporal evolution of the mixing region width, h based on equation 5.21 for $Re_{\lambda,o} = 100$ and $k_o = 4$. Red: RT stable; green: no gravity; blue: RT unstable.

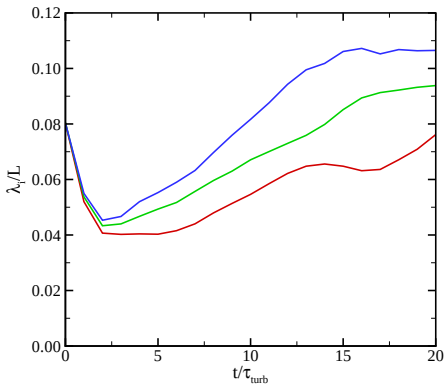

Figure 5.36: Temporal evolution of the Taylor scale in the $z-$direction for $Re_{\lambda,o} = 100$ and $k_o = 4$. Red: RT stable; green: no gravity; blue: RT unstable.

initial field is chosen such that heat conduction terms do not perturb the hydrostatic equilibrium (Mellado *et al.*, 2005). The following equations are combined to obtain the pressure and density in both fluids (Olson & Cook, 2007):

$$R = R_0 \sum_{i=1}^{2} \frac{Y_i}{M_i}, \quad p = \rho R T, \quad \frac{dp}{dz} = -\rho g, \tag{5.38}$$

where the same mass fraction field is obtained from equation 5.9. The initial density and pressure fields are shown in figure 5.37. The temporal evolution of the mixing region width and the effective Atwood number for the isothermal set-up and the RT-turb set-up are shown in figure 5.38. It is interesting to note that while the initial

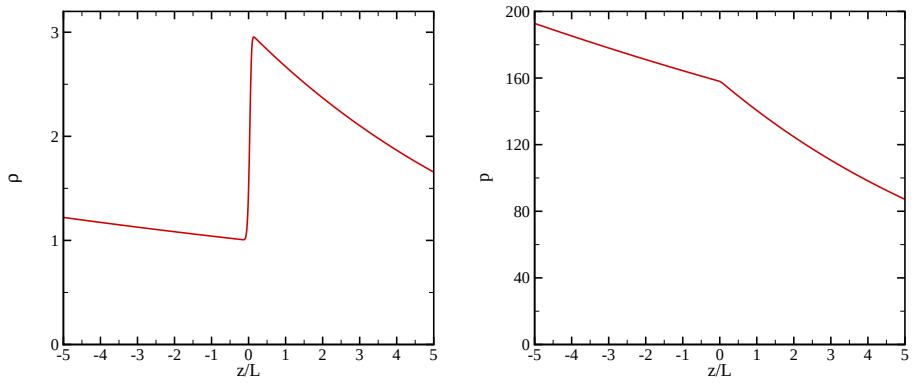

Figure 5.37: The initial density (left) and pressure (right) profiles for the isothermal set-up.

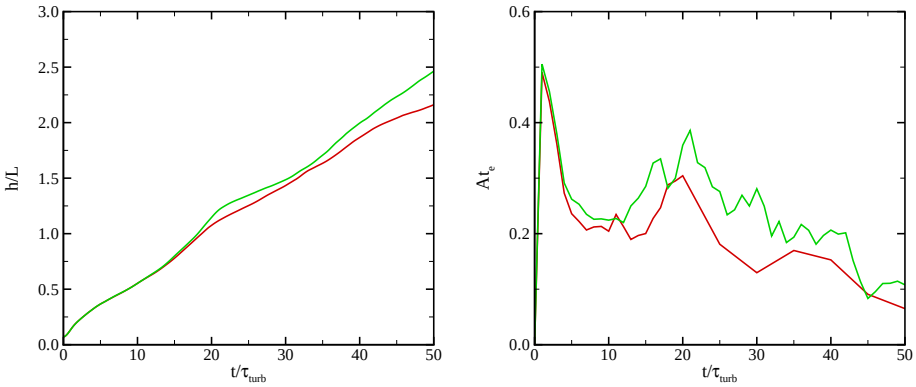

Figure 5.38: Temporal evolution of the mixing region width (left) and the effective Atwood number (right) for $Re_{\lambda,o} = 100$ and $k_o = 4$. Red: isothermal set-up; green: constant density.

density and pressure fields are different for the two set-ups, the mixing region width is almost the same for the first 15 eddy turn-over times. Afterwards, the mixing region grows faster for the RT-turb set-up. This higher growth is due to the higher effective Atwood number for the RT-set-up.

CHAPTER VI

Concluding remarks

This chapter summarizes the work conducted in the present research and provides an outlook for possible future directions.

6.1 Summary and conclusions

First, a solution-adaptive central/shock-capturing finite difference scheme is proposed for efficient high-fidelity simulations of multicomponent flows. The following key conclusions are made in this study:

- A new shock sensor based on the deviation between the WENO weights and the ideal weights is developed to discriminate between smooth and discontinuous regions. In smooth regions, an energy-preserving scheme is used, which is shown to prevent spurious pressure oscillations for varying distributions of specific heats ratio. Specifically, the Blaisdell form (Blaisdell *et al.*, 1996) must be used.

- High-order WENO schemes are used at discontinuities, either in their standard finite difference form at shocks and contacts or using a reconstruction of the primitive variables (Johnsen & Colonius, 2006) at interfaces to prevent spurious pressure oscillations. Thus, the resulting hybrid framework also prevents these errors in finite difference and finite volume formulations.

- One-dimensional test problems with smooth distributions of varying specific heats ratio, sharp interfaces and shocks verify the present analysis. The two-dimensional single-mode inviscid and viscous Richtmyer-Meshkov instability is simulated to highlight the efficiency and accuracy of the method by considering various key quantities related to the late-time behavior.

- Although pointwise convergence is not achieved at the resolutions and Reynolds numbers considered here, the results appear to converge, at least in the integral sense. These quantitative metrics provide a starting point for high-fidelity simulations (direct numerical simulation, explicit large eddy simulation) of shock-accelerated multi-material turbulence.

Second, we study the temporal evolution of an isolated material interface in the presence of physical mass diffusion. It is shown that based on physical arguments a velocity depending on the mass fraction profile should be prescribed initially to prevent the generation of spurious waves in the presence of physical mass diffusion. The initial prescribed velocity is a consequence of physical mass diffusion between the two fluids. The following key conclusions are made in this study:

- Our current study is consistent with Euler simulations with no prescribed velocity, as the initial proposed velocity goes to zero as the Reynolds number goes to infinity.

- The spurious waves travel faster in the light fluid, due to the higher sound speed, and with a lower amplitude. The amplitude of these waves increases as the grid resolution is increased.

- In the presence of gravity, the pressure varies in the direction of gravity to maintain hydrostatic equilibrium. In isothermal configurations, this also results in a change of density, in which case no velocity needs to be added, since density

changes are due to compressibility rather than mass diffusion. Thus, the initial prescribed velocity is adjusted in the presence of gravity for these set-ups.

Third, direct numerical simulation (DNS) is conducted using a novel set-up to investigate Level-2 turbulent mixing, with a focus on anisotropy generated solely by a density gradient. The velocity is initialised by a random solenoidal field that produces homogeneous isotropic turbulence with zero mean velocity, which decays freely in the absence of kinetic energy production mechanisms, e.g., shear in the Kelvin-Helmholtz instability or gravity in the Rayleigh-Taylor instability. Superposed onto this velocity field, an interface initially separates a heavy fluid from a light one. The fluid properties are selected such that the kinematic viscosity, and thus the dissipation rate, is the same in both fluids despite their different densities. Since, the mean kinetic energy per unit volume is the same in each fluid, anisotropy initially lies in the density gradient only. Thus, anisotropy observed at later times can be attributed to this gradient, such that the effect of large-scale density differences on the turbulence can be considered, independently from any other contribution. As the flow evolves, mixing occurs between the heavy and light fluids. We explore how the mixing region grows for different density ratios and Reynolds numbers and examine both the large- and small-scale dynamics. From this study, we can make the following key conclusions:

- As the initial random field evolves to a turbulent state, energy gets transferred to higher wavenumbers. Over approximately the first two eddy turnover times, the dynamics exhibit little dependence on the density ratio. After this initial transient and once decay becomes important, the distribution of energy reverses as the small scales dissipate faster.

- After the initial transient, the mixing region grows self-similarly. Several theoretical arguments (one-dimensional turbulent diffusion, energy considerations) are proposed to describe how the mixing region width scales with time, in agree-

ment with the simulations results and past work. For higher density ratios, it takes a longer time to achieve self-similar growth.

- Bubbles and spikes grow in an asymmetric fashion due to the higher momentum of heavier eddies in the mixing region. As a result, the mid-plane corresponding to $\langle Y \rangle = 0.5$ shifts toward the lighter fluid as the density ratio is increased. This observation is important in the context of the Rayleigh-Taylor instability, as the temporal evolution of turbulence statistics is often reported at the $z = 0$ plane.

- While a wider mixing region is achieved at higher density ratios, the flow is found to be less molecularly mixed therein.

- At the Taylor scale, the turbulence remains almost isotropic at modest density ratios ($\rho_2/\rho_1 = 1$ and 3), while it becomes clearly anisotropic at higher density ratios ($\rho_2/\rho_1 = 8$ and 12). The fact that flow is almost isotropic at the Taylor scale for $\rho_2/\rho_1 = 3$ is particularly important in terms of Rayleigh-Taylor turbulence, as many past DNS have been performed at this density ratio (Cook & Dimotakis, 2001; Cabot & Cook, 2006); typically the anisotropy in the composition is also considered as one of the main sources of anisotropy in addition to gravity in these flows. The scalar field appears to remains almost isotropic up to the Corrsin scale, even for high density ratios.

- Flow intermittency is investigated by measuring the skewness and kurtosis of the velocity and the scalar derivatives in different directions. The intermittency of the velocity field remains the same in different directions and takes expected values corresponding to grid turbulence. The scalar field is more intermittent than the velocity, and exhibits larger intermittency in the direction of the scalar gradient, in agreement with past grid-turbulence experiments.

Finally, DNS is conducted using a novel set-up to investigate Level-2 turbulent mixing in the presence of gravitational field, with application to the Rayleigh-Taylor (RT) instability. We study the temporal evolution of the mixing region starting from an unperturbed material interface in a pre-existing turbulent field with zero mean velocity in the presence of gravity. Both RT stable and unstable configurations are considered. As for the problem with no gravity, the fluid properties are selected such that the kinematic viscosity, and thus the dissipation rate, is initially almost the same in both fluids, despite different densities. As the flow evolves, mixing occurs between the heavy and light fluids. We explore how the mixing region grows for different initial most energetic wave numbers and Reynolds numbers and examine both the large- and small-scale dynamics. From this study, we can make the following key conclusions:

- The current set-up does not satisfy the requirements for being in the mode-coupling regime. Consequently, the mixing region does not grow quadratically. The maximum exponent of time for the mixing region growth achieved is 1.5 during our simulations. Assuming a quadratic growth, $\alpha \approx 0.04 \pm 0.015$ for $k_0 = 16$, the highest energetic wave number considered here. The maximum outer-scale Reynolds number achieved in our simulations is 13,000.

- The mid-plane corresponding to $\langle Y \rangle = 0.5$ shifts toward the lighter fluid due to the higher momentum of heavier eddies in the mixing region. This results in asymmetric growth of bubbles and spikes.

- The mixing region becomes self-similar faster for the RT-turb set-up compared to the classical RT set-up. The two-dimensional spectra of density, mass fraction and velocity fluctuations collapse at high and modest wave numbers on each other after an initial transition. This suggests that the rate of energy transfer to the small scales from large scales is similar to the dissipation rate at those

scales.

- The flow becomes anisotropic at the Taylor microscale in the direction of gravity. The Taylor scale increases more rapidly in the direction of gravity in RT unstable configurations while increases more slowly in RT stable configurations. The flow does not remain isotropic at the Kolmogorov scale in the direction of gravity during the whole simulation.

- Flow intermittency is investigated by measuring the skewness and kurtosis of the velocity and scalar derivatives in different directions. The mass fraction field is more intermittent than the velocity field. High levels of small-scale intermittency is observed at the bubble and spike fronts.

- An additional set-up is also considered where the temperature is uniform initially in the whole domain. The initial growth is the same as the RT-turb set-up. At late times, the mixing region grows more rapidly for the RT-turb set-up due to higher effective Atwood numbers.

6.2 Future work

Numerical simulation of compressible multifluid problems. The numerical framework developed in this research can be used to simulate the advection terms in any compressible flow solver for problems that involve material interfaces. Some of the areas areas in multicomponent and multiphase fluid mechanics that can take advantage of the proposed scheme are: Richtmyer-Meshkov instability, shock-bubble interaction, bubble-turbulence interaction, compressible turbulence, shock-turbulence and shock-turbulent boundary layer interaction, and high-speed reacting flows (e.g., scramjets).

Reduced order modeling. Due to the high cost of DNS, RANS and LES are used in practice for design purposes. Both of these approaches rely on some sort of closure to model the unresolved scales. Particularly, the Reynolds stresses (the subgrid-scale stress tensors) need to be modeled. There are several assumptions behind these models typically based on physical arguments that may not necessarily be valid for multifluid problems. The modeled terms are related to the resolved scales. DNS data has the advantage that all of the scales involved in the problem are accurately resolved. Consequently, the DNS data can be used to exactly measure the terms that need to be modeled in low-fidelity simulations and also investigate how these terms are correlated to the resolved scales in RANS or LES. This allows us to study the validity of the assumptions in RANS and LES.

A more interesting and challenging study is to pick a problem with a specific initial condition and try to obtain the same late-time solution using either DNS, LES or RANS. This scenario is not practical in many cases since flow needs to transition to turbulence and RANS and LES models are not suitable to represent this phenomenon. Thus the hope of achieving the same late-time behavior is impractical and it makes it impossible to make an "apple to apple" comparison between the DNS and RANS/LES data. The novel set-up proposed in this research has a great potential for such studies as the problem is started with a pre-existing isotropic turbulent field in contrast with the classical RT simulations (perturbations just at the interface), where RANS/LES approaches are also expected to perform well in this regime.

APPENDICES

APPENDIX A

Parallel scaling

A.1 Weak and strong scaling

Extreme Science and Engineering Discovery Environment (XSEDE) is a program sponsored by the National Science Foundation (NSF) and provides computational time on NSF supercomputers to researchers. Using our XSEDE allocation, we have performed weak and strong scaling analysis on the Lonestar and Ranger machines. The isotropic turbulence problem from Chapter IV was used as a test case. In summary, the code runs efficiently on both Lonestar and Ranger.

For weak scaling, figure A.1 shows the time for each sub-time step on a triple periodic box problem with 32^3 grid points per core, which is typical of large-scale production runs. The weak scaling is defined as how the compute time varies with the number of processors for a fixed problem size per core. The full time step and the communication times are recorded; the compute time is obtained by subtracting the latter from the former. The most obvious result is that the code scales well: the weak scaling efficiency is above 90% for Lonestar and above 86% for Ranger. The results show good efficiency, given the 512-fold increase in the number of cores compared to

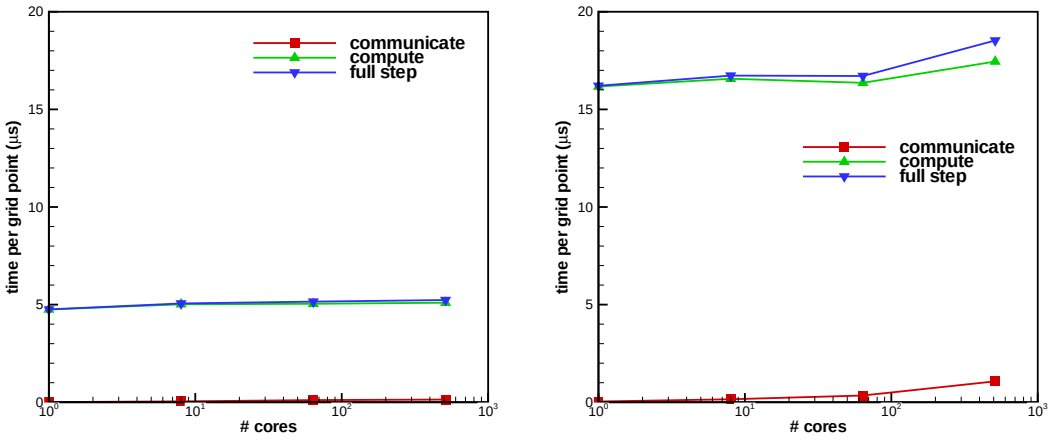

Figure A.1: Weak scaling on a periodic box problem with 32^3 points per core on Lonestar (left) and Ranger (right). Time for full step (Blue), all communications (red), and compute time (green).

the single-core run. The difference in the clock-speed between the two machines is visible; the code runs approximately three times faster on Lonestar.

The strong scaling results performed on a grid of 256^3 are reported in figure A.2. The strong scaling is defined as how the compute time varies with the number of cores for a fixed total problem. The parallel efficiency stays above 80% up to 2048 cores, *i.e.*, an 2048-fold increase in the number of cores compared to the single-core run. Note that very few points (only 8192 grid points per core) are used for the final data point, which is exceedingly coarse.

A.2 Input/output performance and storage requirements

The reading and writing of restartfiles is done using the parallel HDF5 library to a single file. We output six primitive variables in double precision format. We compute many other statistics on-the-fly during every run, but for additional post-processing and visualization We store a couple of restartfiles. Parallel I/O was performed successfully using up to 2048 cores. In addition, we were able to read our restartfiles directly using VisIt. VisIt is an open source, scalable, visualization tool developed by

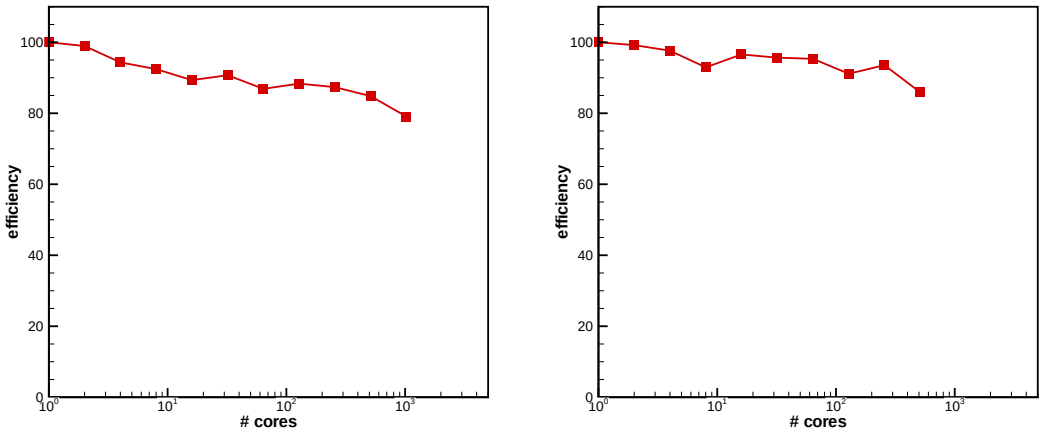

Figure A.2: Strong scaling on periodic box problem with 256^3 grid points on Lonestar machine (left) and Ranger (right).

the Department of Energy Advanced Simulation and Computing Initiative. We successfully used Globus Online to transfer more than 20TB of data to our local storage facility at the Computational Flow Physics Laboratory, University of Michigan.

APPENDIX B

Symmetry-breaking issues

In simulations of inviscid interfacial instabilities, asymmetric solutions are often observed at late times despite nearly perfectly symmetric initial set-ups (Latini *et al.*, 2007; Mosedale & Drikakis, 2007; Houim & Kuo, 2011), thus highlighting the sensitivity of the Richtmyer-Meshkov instability (RMI, considered in Chapter II) to initial conditions. These asymmetries become more prominent when increasing the number of points or order of the scheme, *i.e.*, when reducing the numerical dissipation. We suggest that these asymmetries stem from round-off errors generated when subtracting large numbers in the convective terms. In particular, although the pressure is supposed to be constant across an interface, the specific heats ratios are different, such that the pressure calculation from the total energy may be contaminated by round-off errors. To confirm this hypothesis, figure B.1 shows density plots with perfectly symmetric initial conditions of the RMI for three different non-dimensionalizations using pure WENO. In the first, the dimensional equations are solved. In the second, the variables and equations are non-dimensionalized using a pressure of 10^4 Pa. In the third, the sound speed is used for non-dimensionalization. The dimensional simulations are most sensitive to round-off errors, which generate small-scale Kelvin-Helmholtz instability; these features are not present on the non-

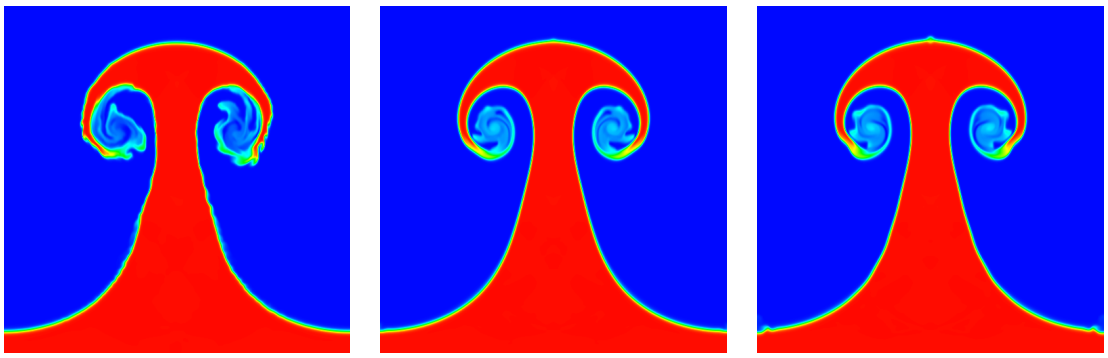

(a) Dimensional. (b) Non-dimensionalized by pressure (10^4) Pa. (c) Non-dimensionalized by sound speed.

Figure B.1: Density plots at $t = 0.006$s right before re-shock for 512 cells per wavelength for the inviscid Richtmyer-Meshkov instability.

dimensionalized plots. In the dimensional simulations, the base pressure is of order 10^5 Pa, which causes an error of order 10^{-11} when calculating the pressure difference term in the momentum equations near the interface. Although still small, such an error is no longer at round-off level. At the present resolutions, these problems are not observed in the non-dimensional cases, since the pressure is $O(1)$. In the simulations non-dimensionalized by the sound speed, shock anomalies (Pandolfi & D'Ambrosio, 2001) manifest themselves at the tips of the bubble and spike; although not shown here, the HLL solver removes these errors at this resolution.

While these issues do not significantly alter the physics of the problem at early times, they may affect the amount of baroclinic vorticity deposed after re-shock due to an amplification of asymmetries already present in the results. Figure B.2 shows density plots at $t = 0.010$ s (well after re-shock) for 128 and 512 points per wavelength. The overall flow structure looks similar for all three cases at the lower resolution. However, for the higher resolutions, very different results are achieved, even for the most symmetric cases. Although pointwise convergence should not be expected for the Euler equations (Samtaney & Pullin, 1996), it is striking to note that only slightly different non-dimensionalizations lead to very different morphologies at late times in the Richtmyer-Meshkov instability. Such errors are no longer important for

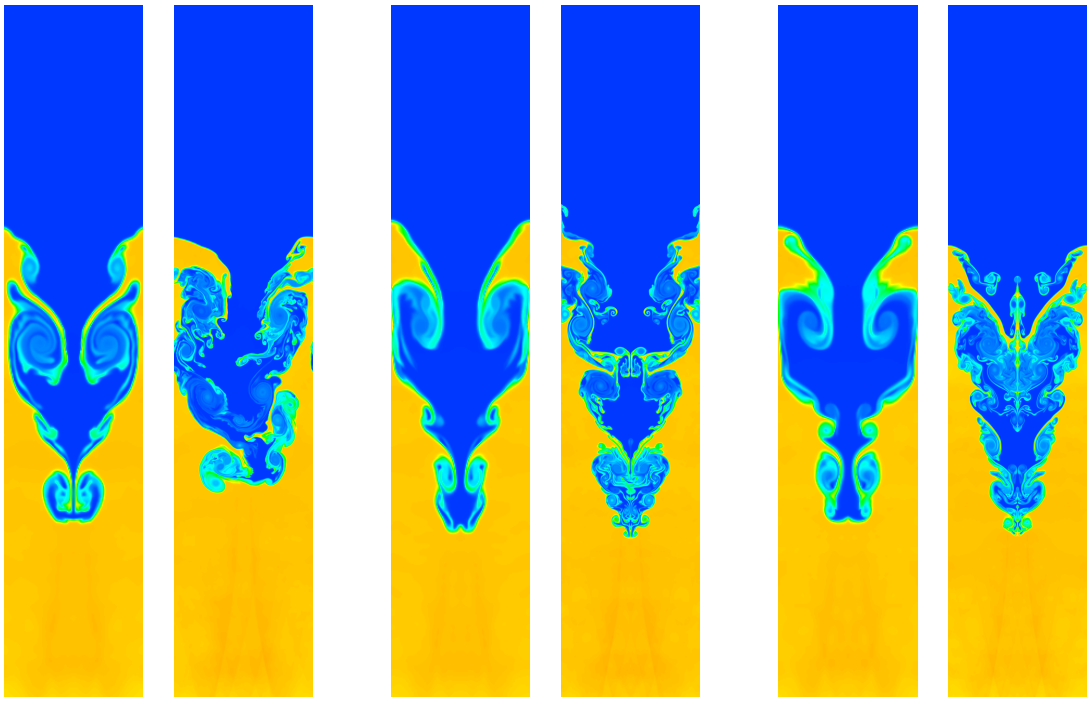

(a) $N = 128$. (b) $N = 512$. (c) $N = 128$. (d) $N = 512$. (e) $N = 128$. (f) $N = 512$.

Figure B.2: Density contours at late time ($t = 0.010$ s) on different resolutions (number of cells per wavelength) for the inviscid Richtmyer-Meshkov instability. Dimensional results: (a) & (b); results non-dimensionalized by pressure (10^4) Pa: (c) & (d); results non-dimensionalized by sound speed: (e) & (f).

sufficiently resolved viscous calculations (see figure 2.14).

APPENDIX C

List of publications

Journal articles

- Movahed, P. & Johnsen, E. 2013*a* A solution-adaptive method for efficient compressible multifluid simulations, with application to the Richtmyer-Meshkov instability. *J. Comput. Phys.* **239**, 166–186

- Movahed, P. & Johnsen, E. 2014*a* The mixing region in freely decaying variable-density turbulence. *submitted to J. Fluid Mech.*

- Henry de Frahan, M. T., Movahed, P. & Johnsen, E. 2014 Numerical simulations of a shock interacting with successive interfaces using the Discontinuous Galerkin method: the multilayered Richtmyer-Meshkov and Rayleigh-Taylor instabilities. *submitted*

- Movahed, P. & Johnsen, E. 2014*b* On the treatment of material interfaces in the presence of finite mass physical diffusion. *in preparation*

- Movahed, P. & Johnsen, E. 2014*c* Turbulent mixing in the presence of gravity, with application to the Rayleigh-Taylor instability. *in preparation*

AIAA conference presentations and proceedings

- Movahed, P. & Johnsen, E. 2013*c* Turbulence diffusion effects at material interfaces, with application to the Rayleigh-Taylor instability. 43^{rd} *AIAA Fluid Dynamics Conference and Exhibit* pp. 2013–3121

- Movahed, P. & Johnsen, E. 2011*b* Numerical simulations of the Richtmyer-Meshkov instability with reshock. 20^{th} *AIAA Computational Fluid Dynamics Conference* pp. 2011–3689

APS conference presentations

- Movahed, P. & Johnsen, E. 2013*b* Free shearless multi-material turbulent mixing in the presence and absence of gravity. *Bulletin of the American Physical Society* **58**

- Movahed, P., Fryxell, B. & Johnsen, E. 2012 Numerical investigations of Rayleigh-Taylor instability development from an initially isotropic turbulent velocity field. *Bulletin of the American Physical Society* **57**

- Movahed, P., Varadan, S. & Johnsen, E. 2011 Turbulence characteristics of the mixing region in the planar Richtmyer-Meshkov Instability. *Bulletin of the American Physical Society* **56**

- Movahed, P. & Johnsen, E. 2011*a* Low-dissipation hybrid schemes for simulations of compressible multicomponent flows. *Bulletin of the American Physical Society* **56**

BIBLIOGRAPHY

BIBLIOGRAPHY

Abarzhi, S. I. 2010 On fundamentals of Rayleigh-Taylor turbulent mixing. *Europhys. Lett.* **91**, 35001.

Abarzhi, S. I., Gorobets, A. & Sreenivasan, K. R. 2005 Rayleigh-Taylor turbulent mixing of immiscible, miscible and stratified fluids. *Phys. Fluids* **17**, 081705.

Abgrall, R. 1996 How to prevent pressure oscillations in multicomponent flow calculations: A quasi conservative approach. *J. Comput. Phys.* **125**, 150–160.

Abgrall, R. & Karni, S. 2001 Computations of compressible multifluids. *J. Comput. Phys.* **169**, 594–623.

Anand, M.S. & Pope, S. B. 1983 Diffusion behind a line source in grid turbulence. *Turbulent shear flows* **4**, 46–61.

Antonia, R. A., Lee, S. K., Djenidi, L., Lavoie, P. & Danaila, L. 2013 Invariants for slightly heated decaying grid turbulence. *J. Fluid Mech.* **727**, 379–406.

Aure, R. & Jacobs, J. W. 2008*a* Particle image velocimetry study of the shock-induced single mode Richtmyer–Meshkov instability. *Shock Waves* **18**, 161–167.

Aure, R. & Jacobs, J. W. 2008*b* Particle image velocimetry study of the shock-induced single mode Richtmyer-Meshkov instability. *Shock Waves* **18**, 161–167.

Bakewell Jr, H. P. & Lumley, J. L. 2004 Viscous sublayer and adjacent wall region in turbulent pipe flow. *Phys. Fluids* **10**, 1880–1889.

Batchelor, G.K. 1959 Small-scale variation of convected quantities like temperature in turbulent fluid .1. general discussion and the case of small conductivity. *J. Fluid Mech.* **5**, 113–133.

Batchelor, G. K. & Proudman, I. 1956 The large-scale structure of homogeneous turbulence. *Phil. Trans. R. Soc. A* **248**, 369–405.

Bernardini, M., Pirozzoli, S. & Grasso, F. 2011 The wall pressure signature of transonic shock/boundary layer interaction. *J. Fluid Mech.* **671**, 288–312.

Bhagatwala, A. & Lele, S. K. 2011 Interaction of a Taylor blast wave with isotropic turbulence. *Phys. Fluids* **23**, 035103.

Bhagatwala, A. & Lele, S. K. 2012 Interaction of a converging spherical shock wave with isotropic turbulence. *Phys. Fluids* **24**, 085102.

Blaisdell, G. A., Spyropoulos, E. T. & Qin, J. H. 1996 The effect of the formulation of nonlinear terms on aliasing errors in spectral methods. *Appl. Numer. Math.* **21**, 207–219.

Bogey, C. & Bailly, C. 2004 A family of low dispersive and low dissipative explicit schemes for flow and noise computations. *J. Comput. Phys.* **194**, 194–214.

Brouillette, M. 2002 The Richtmyer-Meshkov instability. *Annu. Rev. Fluid Mech.* **34**, 445–468.

Cabot, W. & Zhou, Y. 2013 Statistical measurements of scaling and anisotropy of turbulent flows induced by Rayleigh-Taylor instability. *Phys. Fluids* **25**, 015107.

Cabot, W. H. & Cook, A. W. 2006 Reynolds number effects on Rayleigh-Taylor instability with possible implications for type-Ia supernovae. *Nature Phys.* **2**, 562–568.

Chandrasekhar, S. 1961 *Hydrodynamic and Hydromagnetic Stability*. Oxford: University Press.

Collins, B. D. & Jacobs, J. W. 2002 PLIF flow visualization and measurements of the Richtmyer-Meshkov instability of an air/SF_6 interface. *J. Fluid Mech.* **464**, 113–136.

Comte-Bellot, G. & Corrsin, S. 1966 Use of a contraction to improve isotropy of grid-generated turbulence. *J. Fluid Mech.* **25**, 657–682.

Cook, A.W. & Dimotakis, P.E. 2001 Transition stages of Rayleigh-Taylor instability between miscible fluids. *J. Fluid Mech.* **443**, 69–99.

Cook, A. W., Cabot, W. & Miller, P. L. 2004 The mixing transition in Rayleigh–Taylor instability. *J. Fluid Mech.* **511**, 333–362.

Corrsin, S. 1951 On the spectrum of isotropic temperature fluctuations in an isotropic turbulence. *J. Appl. Phys.* **22**, 469–473.

Dalziel, S. B., Linden, P. F. & Youngs, D. L. 1999 Self-similarity and internal structure of turbulence induced by Rayleigh–Taylor instability. *J. Fluid Mech.* **399**, 1–48.

Danckwerts, P. V. 1952 The definition and measurement of some characteristics of mixtures. *Appl. Sci. Res.* **3**, 279–296.

Danckwerts, P. V. 1958 The effect of incomplete mixing on homogeneous reactions. *Chem. Eng. Sci.* **8**, 93–102.

Davidson, P. A. 2004 *Turbulence: An Introduction for Scientists and Engineers*. Oxford University Press.

Dimonte, G. & Schneider, M. 2000 Density ratio dependence of Rayleigh–Taylor mixing for sustained and impulsive acceleration histories. *Phys. Fluids* **12**, 304–321.

Dimonte, G., Youngs, D. L., Dimits, A., Weber, S., Marinak, M., Wunsch, S., Garasi, C., Robinson, A., Andrews, M. J., Ramaprabhu, P., Calder, A. C., Fryxell, B., Biello, J., Dursi, L., MacNeice, P., Olson, K., Ricker, P., Rosner, R., Timmes, F., Tufo, H., Young, Y. N. & Zingale, M. 2004 A comparative study of the turbulent Rayleigh-Taylor instability using high-resolution three-dimensional numerical simulations: The Alpha-Group collaboration. *Phys. Fluids* **16**, 1668–1693.

Dimotakis, P. E. 2000 The mixing transition in turbulent flows. *J. Fluid Mech.* **409**, 69–98.

Dimotakis, P. E. 2005 Turbulent mixing. *Annu. Rev. Fluid. Mech* **37**, 329–356.

Dong, S 2007 Direct numerical simulation of turbulent Taylor–Couette flow. *J. Fluid Mech.* **587**, 373–393.

Dowling, D. R. & Dimotakis, P. E. 1990 Similarity of the concentration field of gas-phase turbulent jets. *J. Fluid Mech.* **218**, 109–141.

Drake, R. P. 2006 *High-Energy Density Physics*, 1st edn. Springer-Verlag, Berlin.

Ducros, F., Laporte, F., Souleres, T., Guinot, V., Moinat, P. & Caruelle, B. 2000 High-order fluxes for conservative skew-symmetric-like schemes in structured meshes: Application to compressible flows. *J. Comput. Phys.* **161**, 114–139.

Duff, R. E., Harlow, F. H. & Hirt, C. W. 1962 Effects of diffusion on interface instability between gases. *Phys. Fluids* **5**, 417–425.

Fedkiw, R. P., Merriman, B. & Osher, S. 2000 Simplified discretization of systems of hyperbolic conservation laws containing advection equations. *J. Comput. Phys.* **157**, 302–326.

Feiereisen, W. J., Reynolds, W. C. & Ferziger, J. H. 1981 Numerical simulation of a compressible, homogeneous, turbulent shear flow. *Tech. Rep.* Report TF 13. Stanford.

Henry de Frahan, M. T., Movahed, P. & Johnsen, E. 2014 Numerical simulations of a shock interacting with successive interfaces using the Discontinuous Galerkin method: the multilayered Richtmyer-Meshkov and Rayleigh-Taylor instabilities. *submitted* .

George, W. K. 1992 The decay of homogeneous isotropic turbulence. *Phys. Fluids A, Fluid Dyn.* **4**, 1492–1509.

Gottlieb, S. & Shu, C. W. 1998 Total variation diminishing Runge-Kutta schemes. *Math. Comp.* **67**, 73–85.

Grinstein, F. F., Margolin, L. G. & Rider, W. J. 2007 *Implicit large eddy simulation*. Cambridge: University Press.

Hannoun, I. A. & List, E. J. 1988 Turbulent mixing at a shear-free density interface. *J. Fluid Mech.* **189**, 211–234.

Helmholtz, H. V. 1868 On discontinuous movements of fluids. *The London, Edinburgh, and Dublin Philosophical Magazine and Journal of Science* **36**, 337–346.

Henrick, A. K., Aslam, T. D. & Powers, J. M. 2005 Mapped weighted essentially non-oscillatory schemes: Achieving optimal order near critical points. *J. Comput. Phys.* **207**, 542–567.

Hill, D. J. & Pullin, D. I. 2004 Hybrid tuned center-difference-WENO method for large eddy simulations in the presence of strong shocks. *J. Comput. Phys.* **194**, 435–450.

Honein, A. E. & Moin, P. 2004 Higher entropy conservation and numerical stability of compressible turbulence simulations. *J. Comput. Phys.* **201**, 531–545.

Houim, R. W. & Kuo, K. K. 2011 A low-dissipation and time-accurate method for compressible multi-component flow with variable specific heat ratios. *J. Comput. Phys.* **230**, 8527–8553.

Huq, P. & Britter, R. E. 1995*a* Mixing due to grid-generated turbulence of a two-layer scalar profile. *J. Fluid Mech.* **285**, 17–40.

Huq, P. & Britter, R. E. 1995*b* Turbulence evolution and mixing in a two-layer stably stratified fluid. *J. Fluid Mech.* **285**, 41–67.

Itsweire, E. C., Helland, K. N. & Van Atta, C. W. 1986 The evolution of grid-generated turbulence in a stably stratified fluid. *J. Fluid Mech.* **162**, 299–338.

Jacobs, J. W. & Sheeley, J. M. 1996 Experimental study of incompressible Richtmyer-Meshkov instability. *Phys. Fluids* **8**, 405.

Jayesh, Tong, C. N. & Warhaft, Z. 1994 On temperature spectra in grid turbulence. *Phys. Fluids* **6**, 306–312.

Jiang, G. S. & Shu, C. W. 1996 Efficient implementation of weighted ENO schemes. *J. Comput. Phys.* **126**, 202–228.

Jin, S. & Liu, J. G. 1996 The effects of numerical viscosities. I. Slowly moving shocks. *J. Comput. Phys.* **126**, 373–389.

Johnsen, E. 2011 On the treatment of contact discontinuities using WENO schemes. *J. Comput. Phys.* **230**, 8665–8668.

Johnsen, E. 2013 Analysis of numerical errors generated by shock waves moving slowly relative to the grid. *AIAA J.* **51**, 1269–1274.

Johnsen, E. & Colonius, T. 2006 Implementation of WENO schemes in compressible multicomponent flow problems. *J. Comput. Phys.* **219**, 715–732.

Johnsen, E. & Ham, F. 2012 Preventing numerical errors generated by interface-capturing schemes in compressible multi-material flows. *J. Comput. Phys.* **231**, 5705–5717.

Johnsen, E., Larsson, J., Bhagatwala, A. V., Cabot, W. H., Moin, P., Olson, B. J., Rawat, P. S., Shankar, S. K., Sjogreen, B., Yee, H. C., Zhong, X. & Lele, S. K. 2010 Assessment of high-resolution methods for numerical simulations of compressible turbulence with shock waves. *J. Comput. Phys.* **229**, 1213–1237.

Joseph, D. D. 1990 Fluid dynamics of two miscible liquids with diffusion and gradient stresses. *Eur J Mech B-Fluid* **9**, 565–596.

Kennedy, C. A. & Gruber, A. 2008 Reduced aliasing formulations of the convective terms within the navier-stokes equations for a compressible fluid. *J. Comput. Phys.* **227**, 1676–1700.

Kifonidis, K., Plewa, T., Janka, H. T. & Muller, E. 2003 Non-spherical core collapse supernovae. *Astron. Astrophys.* **408**, 621–649.

Kifonidis, K., Plewa, T., Scheck, L., Janka, H. T. & Muller, E. 2006 Non-spherical core collapse supernovae - II. The late-time evolution of globally anisotropic neutrino-driven explosions and their implications for SN 1987 A. *Astron. Astrophys.* **453**, 661–678.

Kolmogorov, A.N. 1962 A refinement of previous hypotheses concerning the local structure of turbulence in a viscous incompressible fluid at high Reynolds number. *J. Fluid Mech.* **13**, 82–85.

Koochesfahani, M. M. & Dimotakis, P. E. 1986 Mixing and chemical-reactions in a turbulent liquid-mixing layer. *J. Fluid Mech.* **170**, 83–112.

Krogstad, P. A. & Davidson, P. A. 2010 Is grid turbulence Saffman turbulence? *J. Fluid Mech.* **642**, 373–394.

Lamriben, C., Cortet, P. & Moisy, F. 2011 Direct measurements of anisotropic energy transfers in a rotating turbulence experiment. *Phys. Rev. Lett.* **107**, 024503.

Landen, O. L., Benedetti, R., Bleuel, D., Boehly, T. R., Bradley, D. K., Caggiano, J. A., Callahan, D. A., Celliers, P. M., Cerjan, C. J., Clark, D., Collins, G. W., Dewald, E. L., Dixit, S. N., Doeppner, T., Edgell, D., Eggert, J., Farley, D., Frenje, J. A., Glebov, V., Glenn, S. M., Glenzer, S. H., Haan, S. W., Hamza, A., Hammel, B. A., Haynam, C. A., Hammer, J. H., Heeter, R. F., Herrmann, H. W., Hicks, D. G., Hinkel, D. E., Izumi, N., Johnson, M. Gatu, Jones, O. S., Kalantar, D. H., Kauffman, R. L., Kilkenny, J. D., Kline, J. L., Knauer, J. P., Koch, J. A., Kyrala, G. A., LaFortune, K., Ma, T., Mackinnon, A. J., Macphee, A. J., Mapoles, E., Milovich, J. L., Moody, J. D., Meezan, N. B., Michel, P., Moore, A. S., Munro, D. H., Nikroo, A., Olson, R. E., Opachich, K., Pak, A., Parham, T., Patel, P., Park, H-S, Petrasso, R. P., Ralph, J., Regan, S. P., Remington, B. A., Rinderknecht, H. G., Robey, H. F., Rosen, M. D., Ross, J. S., Salmonson, J. D., Sangster, T. C., Schneider, M. B., Smalyuk, V., Spears, B. K., Springer, P. T., Suter, L. J., Thomas, C. A., Town, R. P. J., Weber, S. V., Wegner, P. J., Wilson, D. C., Widmann, K., Yeamans, C., Zylstra, A., Edwards, M. J., Lindl, J. D., Atherton, L. J., Hsing, W. W., MacGowan, B. J., Van Wonterghem, B. M. & Moses, E. I. 2012 Progress in the indirect-drive national ignition campaign. *Plasma Phys. Contr. F.* **54**.

Larsson, J. & Gustafsson, B. 2008 Stability criteria for hybrid difference methods. *J. Comput. Phys.* **227**, 2886–2898.

Larsson, J. & Lele, S. K. 2009 Direct numerical simulation of canonical shock/turbulence interaction. *Phys. Fluids* **21**, 126101.

Latini, M., Schilling, O. & Don, W. S. 2007 Effects of WENO flux reconstruction order and spatial resolution on reshocked two-dimensional Richtmyer-Meshkov instability. *J. Comput. Phys.* **221**, 805–836.

Lawrie, A. G. W. & Dalziel, S. B. 2011 Turbulent diffusion in tall tubes. I. Models for Rayleigh-Taylor instability. *Phys. Fluids* **23**, 085109.

Lee, S., Lele, S. K. & Moin, P. 1991 Eddy shocklets in decaying compressible turbulence. *Phys. Fluids* **3**, 657–664.

Lesieur, M. & Metais, O. 1996 New trends in large-eddy simulations of turbulence. *Ann. Rev. Fluid Mech.* **28**, 45–82.

Lienhard, J. H. & Van Atta, C. W. 1990 The decay of turbulence in thermally stratified flow. *J. Fluid Mech.* **210**, 57–112.

Linden, P. F. 1980 Mixing across a density interface produced by grid turbulence. *J. Fluid Mech.* **100**, 691–703.

Lindl, J. 1995 Development of the indirect-drive approach to inertial confinement fusion and the target physics basis for ignition and gain. *Phys. Plasmas* **2**, 3933–4024.

Liu, X. D., Osher, S. & Chan, T. 1994 Weighted essentially non-oscillatory schemes. *J. Comput. Phys.* **115**, 200–212.

Livescu, D., Jaberi, F. A. & Madnia, C. K. 2000 Passive-scalar wake behind a line source in grid turbulence. *J. Fluid Mech.* **416**, 117–149.

Lo, S. C., Blaisdell, G. A. & Lyrintzis, A. S. 2010 High-order shock capturing schemes for turbulence calculations. *Int. J. Numer. Meth. Fluids* **62**, 473–498.

Lombardini, M., Hill, D. J., Pullin, D. I. & Meiron, D. I. 2011 Atwood ratio dependence of Richtmyer-Meshkov flows under reshock conditions using large-eddy simulations. *J. Fluid Mech.* **670**, 439–480.

Mellado, J. P., Sarkar, S. & Zhou, Y. 2005 Large-eddy simulation of Rayleigh-Taylor turbulence with compressible miscible fluids. *Phys. Fluids* **17**, 076101.

Meshkov, E. E. 1969 Instability of the interface of two gases accelerated by a shock wave. *Fluid Dynamics* **4**, 101–104.

Meyer, K. A. & Blewett, P. J. 1972 Numerical investigation of the stability of a shock-accelerated interface between two fluids. *Phys. Fluids* **15**, 753.

Misra, A. & Pullin, D. I. 1997 A vortex-based subgrid stress model for large-eddy simulation. *Phys. Fluids* **9**, 2443–2454.

Monin, A. S. & Yaglom, A. M. 1975 *Statistical Fluid Mechanics*. MIT Press, Cambridge, MA.

Morinishi, Y. 2010 Skew-symmetric form of convective terms and fully conservative finite difference schemes for variable density low-mach number flows. *J. Comput. Phys.* **229**, 276–300.

Mosedale, A. & Drikakis, D. 2007 Assessment of very high order of accuracy in implicit les models. *J. Fluids Eng.* **129**, 1497–1503.

Movahed, P., Fryxell, B. & Johnsen, E. 2012 Numerical investigations of Rayleigh-Taylor instability development from an initially isotropic turbulent velocity field. *Bulletin of the American Physical Society* **57**.

Movahed, P. & Johnsen, E. 2011*a* Low-dissipation hybrid schemes for simulations of compressible multicomponent flows. *Bulletin of the American Physical Society* **56**.

Movahed, P. & Johnsen, E. 2011*b* Numerical simulations of the Richtmyer-Meshkov instability with reshock. 20^{th} *AIAA Computational Fluid Dynamics Conference* pp. 2011–3689.

Movahed, P. & Johnsen, E. 2013*a* A solution-adaptive method for efficient compressible multifluid simulations, with application to the Richtmyer-Meshkov instability. *J. Comput. Phys.* **239**, 166–186.

Movahed, P. & Johnsen, E. 2013*b* Free shearless multi-material turbulent mixing in the presence and absence of gravity. *Bulletin of the American Physical Society* **58**.

Movahed, P. & Johnsen, E. 2013*c* Turbulence diffusion effects at material interfaces, with application to the Rayleigh-Taylor instability. 43^{rd} *AIAA Fluid Dynamics Conference and Exhibit* pp. 2013–3121.

Movahed, P. & Johnsen, E. 2014*a* The mixing region in freely decaying variable-density turbulence. *submitted to J. Fluid Mech.* .

Movahed, P. & Johnsen, E. 2014*b* On the treatment of material interfaces in the presence of finite mass physical diffusion. *in preparation* .

Movahed, P. & Johnsen, E. 2014*c* Turbulent mixing in the presence of gravity, with application to the Rayleigh-Taylor instability. *in preparation* .

Movahed, P., Varadan, S. & Johnsen, E. 2011 Turbulence characteristics of the mixing region in the planar Richtmyer-Meshkov Instability. *Bulletin of the American Physical Society* **56**.

Mueschke, N. J. & Schilling, O. 2009 Investigation of Rayleigh-Taylor turbulence and mixing using direct numerical simulation with experimentally measured initial conditions. I. Comparison to experimental data. *Phys. Fluids* **21**, 014106.

Mydlarski, L. & Warhaft, Z. 1998 Passive scalar statistics in high-Peclet-number grid turbulence. *J. Fluid Mech.* **358**, 135–175.

Nagarajan, S., Lele, S. K. & Ferziger, J. H. 2003 A robust high-order compact method for large eddy simulation. *J. Comput. Phys.* **191**, 392–419.

Nonomura, T., Morizawa, S., Terashima, H., Obayashi, S. & Fujii, K. 2012 Numerical (error) issues on compressible multicomponent flows using a high-order differencing scheme: Weighted compact nonlinear scheme. *J. Comput. Phys.* **231**, 3181–3210.

Obukhov, A. M. 1949 Structure of the temperature field in turbulent flows. *Izv. Akad. Nauk SSSR, Ser. Geogr. Geofiz* **13**, 58.

Olson, B. J. & Cook, A. W. 2007 Rayleigh-Taylor shock waves. *Phys. Fluids* **19**, 128108.

Pandolfi, M. & D'Ambrosio, D. 2001 Numerical instabilities in upwind methods: Analysis and cures for the carbuncle phenomenon. *J. Comput. Phys.* **166**, 271–301.

Park, N., Yoo, J. Y. & Choi, H. C. 2004 Discretization errors in large eddy simulation: on the suitability of centered and upwind-biased compact difference schemes. *J. Comput. Phys.* **198**, 580–616.

Peng, G., Zabusky, N. J. & Zhang, S. 2003 Vortex-accelerated secondary baroclinic vorticity deposition and late-intermediate time dynamics of a two-dimensional Richtmyer-Meshkov interface. *Phys. Fluids* **15**, 3730–3744.

Pirozzoli, S. 2010 Generalized conservative approximations of split convective derivative operators. *J. Comput. Phys.* **229**, 7180–7190.

Pirozzoli, S. 2011 Numerical methods for high-speed flows. *Annu. Rev. Fluid Mech.* **43**, 163–194.

Pope, S. 2000 *Turbulent flows*. Cambridge: University Press.

Poujade, O. 2006 Rayleigh-Taylor turbulence is nothing like Kolmogorov turbulence in the self-similar regime. *Phys. Rev. Lett.* **97**, 185002.

Prasad, A. & Williamson, C. H. K. 1997 Three-dimensional effects in turbulent bluff-body wakes. *J. Fluid Mech.* **343**, 235–265.

Ramaprabhu, P., Dimonte, G., Woodward, P., Fryer, C., Rockefeller, G., Muthuraman, K., Lin, P.-H & Jayaraj, J. 2012 The late-time dynamics of the single-mode Rayleigh-Taylor instability. *Phys. Fluids* **24**, 074107.

Ramaprabhu, P., Dimonte, G., Young, Y., Calder, A. C. & Fryxell, B. 2006 Limits of the potential flow approach to the single-mode Rayleigh-Taylor problem. *Phys. Rev. E* **74**, 066308.

Ramaprabhu, P., Karkhanis, V. & Lawrie, A. G. W. 2013 The Rayleigh-Taylor instability driven by an accel-decel-accel profile. *Phys. Fluids* **25**, 115104.

Read, K. I. 1984 Experimental investigation of turbulent mixing by Rayleigh-Taylor instability. *Phys. D* **12**, 45–58.

Reid, R. C., Prausnitz, J. M. & Poling, B. E. 1987 *The Properties of Gases and Liquids*, 4th edn. McGraw-Hill, New York.

Richardson, L. F. 1926 Atmospheric diffusion shown on a distance-neighbour graph. In *Proc. R. Soc. London, Ser. A*, , vol. 110, pp. 709–737.

Richtmyer, R. D. 1960 Taylor instability in shock acceleration of compressible fluids. *Comm. Pure Appl. Math.* **13**, 297–319.

Ristorcelli, J. R. & Clark, T. T. 2004 Rayleigh–Taylor turbulence: self-similar analysis and direct numerical simulations. *J. Fluid Mech.* **507**, 213–253.

Roe, P. L. 1981 Approximate Riemann solvers, parameter vectors, and difference-schemes. *J. Comput. Phys.* **43**, 357–372.

Romick, C. M., Aslam, T. D. & Powers, J. M. 2012 The effect of diffusion on the dynamics of unsteady detonations. *J. Fluid Mech.* **699**, 453–464.

Ryutov, D., Drake, R. P., Kane, J., Liang, E., Remington, B. A. & Wood-Vasey, W. M. 1999 Similarity criteria for the laboratory simulation of supernova hydrodynamics. *Astrophys. J.* **518**, 821–832.

Sadot, O., Erez, L., Alon, U., Oron, D., Levin, L. A., Erez, G., Ben-Dor, G. & Shvarts, D. 1998 Study of nonlinear evolution of single-mode and two-bubble interaction under Richtmyer-Meshkov instability. *Phys. Rev. Lett.* **80**, 1654.

Saffman, P. J. 1967 The large-scale structure of homogeneous turbulence. *J. Fluid Mech.* **27**, 581–593.

Samtaney, R. & Pullin, D. I. 1996 Initial-value and self-similar solutions of the compressible Euler equations. *Phys. Fluids* **8**, 2650–2655.

Samtaney, R., Pullin, D. I. & Kosovic, B. 2001 Direct numerical simulation of decaying compressible turbulence and shocklet statistics. *Phys. Fluids* **13**, 1415–1430.

Samtaney, R. & Zabusky, N. J. 1994 Circulation deposition on shock-accelerated planar and curved density-stratified interfaces: Models and scaling laws. *J. Fluid Mech.* **269**, 45–78.

Sandoval, D.L. 1995 The dynamics of variable-density turbulence. Phd thesis, University of Washington.

Sawford, B. 2001 Turbulent relative dispersion. *Annu. Rev. Fluid Mech.* **33**, 289–317.

Sayadi, T., Hamman, C. W. & Moin, P. 2013 Direct numerical simulation of complete h-type and k-type transitions with implications for the dynamics of turbulent boundary layers. *J. Fluid Mech.* **724**, 480–509.

Schilling, O. & Latini, M. 2010 High-order weno simulations of three-dimensional reshocked Richtmyer-Meshkov instability to late times: dynamics, dependence on initial conditions, and comparisons to experimental data. *Acta. Math. Sci.* **30**, 595–620.

Schilling, O., Latini, M. & Don, W. S. 2007 Physics of reshock and mixing in single-mode Richtmyer-Meshkov instability. *Phys. Rev. E* **76**, 026319.

Shu, C. W. & Osher, S. 1989 Efficient implementation of essentially non-oscillatory shock-capturing schemes II. *J. Comput. Phys.* **83**, 32–78.

Shyue, K. M. 1998 An efficient shock-capturing algorithm for compressible multicomponent problems. *J. Comput. Phys.* **142**, 208–242.

Sod, G. A. 1978 Survey of several finite-difference methods for systems of non-linear hyperbolic conservation laws. *J. Comput. Phys.* **27**, 1–31.

Soulard, O. & Griffond, J. 2012 Inertial-range anisotropy in Rayleigh-Taylor turbulence. *Phys. Fluids* **24**, 025101.

Sreenivasan, K. R. & Antonia, R. A. 1997 The phenomenology of small-scale turbulence. *Annu. Rev. Fluid Mech.* **29**, 435–472.

Stanley, S. A., Sarkar, S. & Mellado, J. P. 2002 A study of the flow-field evolution and mixing in a planar turbulent jet using direct numerical simulation. *J. Fluid Mech.* **450**, 377–407.

Stapountzis, H., Sawford, B. L., Hunt, J. C. R & Britter, R. E. 1986 Structure of the temperature-field downwind of a line source in grid turbulence. *J. Fluid Mech.* **165**, 401–424.

Stolz, S., Schlatter, P. & Kleiser, L. 2005 High-pass filtered eddy-viscosity models for large-eddy simulations of transitional and turbulent flow. *Phys. Fluids* **17**, 065103.

Swinney, H. L. & Gollub, J. P. 1985 *Hydrodynamic Instabilities and the Transition to Turbulence*, 2nd edn. Springer-Verlag, Berlin.

Taylor, E. M., Wu, M. & Martin, M. P. 2007 Optimization of nonlinear error for weighted essentially non-oscillatory methods in direct numerical simulations of compressible turbulence. *J. Comput. Phys.* **223**, 384–397.

Taylor, G. 1950 The instability of liquid surfaces when accelerated in a direction perpendicular to their planes .1. *Proc. R. Soc. A* **201**, 192–196.

Thomas, V. A. & Kares, R. J. 2012 Drive Asymmetry and the Origin of Turbulence in an ICF Implosion. *Phys. Rev. Lett.* **109**, 075004.

Thompson, K. W. 1987 Time-dependent boundary-conditions for hyperbolic systems. *J. Comput. Phys.* **68**, 1–24.

Thompson, K. W. 1990 Time-dependent boundary conditions for hyperbolic systems, ii. *J. Comput. Phys.* **89**, 439–461.

Thomson, W. 1871 Hydrokinetic solutions and observations. *The London, Edinburgh, and Dublin Philosophical Magazine and Journal of Science* **42**, 362–377.

Thornber, B., Drikakis, D., Williams, R. J. R. & Youngs, D. 2008*a* On entropy generation and dissipation of kinetic energy in high-resolution shock-capturing schemes. *J. Comput. Phys.* **227**, 4853–4872.

Thornber, B., Drikakis, D., Youngs, D. L. & Williams, R. J. R. 2011 Growth of a Richtmyer-Meshkov turbulent layer after reshock. *Phys. Fluids* **23**, 095107.

Thornber, B., Mosedale, A., Drikakis, D., Youngs, D. & Williams, R. J. R. 2008*b* An improved reconstruction method for compressible flows with low mach number features. *J. Comput. Phys.* **227**, 4873–4894.

Titarev, V. A. & Toro, E. F. 2004 Finite-volume WENO schemes for three-dimensional conservation laws. *J. Comput. Phys.* **201**, 238–260.

Tong, C. N. & Warhaft, Z. 1994 On passive scalar derivative statistics in grid turbulence. *Phys. Fluids* **6**, 2165–2176.

Tordella, D. & Iovieno, M. 2006 Numerical experiments on the intermediate asymptotics of shear-free turbulent transport and diffusion. *J. Fluid Mech.* **549**, 429–441.

Tordella, D. & Iovieno, M. 2011 Small-scale anisotropy in turbulent shearless mixing. *Phys. Rev. Lett.* **107**, 194501.

Tordella, D. & Iovieno, M. 2012 Decaying turbulence: What happens when the correlation length varies spatially in two adjacent zones. *Phys. D* **241**.

Tordella, D., Iovieno, M. & Bailey, P. R. 2008 Sufficient condition for Gaussian departure in turbulence. *Phys. Rev. E* **77** (1).

Turner, J. S. 1968 The influence of molecular diffusivity on turbulent entrainment across a density interface. *J. Fluid Mech.* **33**, 639–656.

Varadan, S. & Johnsen, E. 2014 A recovery-based discontinuous galerkin method for compressible turbulence with shocks p. in preparation.

Vasilyev, O. V., Lund, T. S. & Moin, P. 1998 A general class of commutative filters for les in complex geometries. *J. Comput. Phys.* **146**, 82–104.

Ward, G. M. & Pullin, D. I. 2011 A study of planar Richtmyer-Meshkov instability in fluids with Mie-Gruneisen equations of state. *Phys. Fluids* **23**.

Warhaft, Z. 1984 The interference of thermal fields from line sources in grid turbulence. *J. Fluid Mech.* **144**, 363–387.

Warhaft, Z. 2000 Passive scalars in turbulent flows. *Annu. Rev. Fluid Mech.* **32**, 203–240.

Watanabe, T. & Gotoh, T. 2006 Intermittency in passive scalar turbulence under the uniform mean scalar gradient. *Phys. Fluids* **18**, 058105.

Watanabe, T. & Gotoh, T. 2007 Inertial-range intermittency and accuracy of direct numerical simulation for turbulence and passive scalar turbulence. *J. Fluid Mech.* **590**, 117–146.

Yang, J., Kubota, T. & Zukoski, E.E. 1993 Applications of shock-induced mixing to supersonic combustion. *AIAA Journal* **31**, 854–862.

Youngs, D. L. 1991 Three-dimensional numerical simulation of turbulent mixing by Rayleigh-Taylor instability. *Phys. Fluids A* **3**, 1312–1320.

Zhang, Q. & Sohn, S. I. 1997 Nonlinear theory of unstable fluid mixing driven by shock wave. *Phys. Fluids* **9**, 1106.